

HEAT TRANSFER ENHANCEMENT OF NANOFUID FLOW IN CHANNEL  
THROUGH SINUSOIDAL WAVY BAFFLES

WATCHARIN NOOTHONG

A THESIS SUBMITTED IN PARTIAL FULFILLMENT  
OF THE REQUIREMENT FOR THE DEGREE OF  
DOCTOR OF ENGINEERING IN MECHANICAL ENGINEERING  
FACULTY OF ENGINEERING  
KING MONGKUT'S INSTITUTE OF TECHNOLOGY LADKRABANG

2014

KMITL-2014-EN-D-058-208

การเพิ่มการถ่ายเทความร้อนของการไหลของไหลนาโนในช่องขนานผ่านแผ่นกั้น  
รูปคลื่นไซน์

HEAT TRANSFER ENHANCEMENT OF NANOFLUID FLOW IN CHANNEL  
THROUGH SINUSOIDAL WAVY BAFFLES

วัชรินทร์ หนูทอง  
WATCHARIN NOOTHONG

วิทยานิพนธ์นี้เป็นส่วนหนึ่งของการศึกษาตามหลักสูตรปริญญาวิศวกรรมศาสตรดุษฎีบัณฑิต  
สาขาวิชาวิศวกรรมเครื่องกล  
คณะวิศวกรรมศาสตร์  
สถาบันเทคโนโลยีพระจอมเกล้าเจ้าคุณทหารลาดกระบัง  
พ.ศ.2557  
KMITL-2014-EN-D-058-208

HEAT TRANSFER ENHANCEMENT OF NANOFUID FLOW IN CHANNEL  
THROUGH SINUSOIDAL WAVY BAFFLES

WATCHARIN NOOTHONG

A THESIS SUBMITTED IN PARTIAL FULFILLMENT  
OF THE REQUIREMENT FOR THE DEGREE OF  
DOCTOR OF ENGINEERING IN MECHANICAL ENGINEERING  
FACULTY OF ENGINEERING  
KING MONGKUT'S INSTITUTE OF TECHNOLOGY LADKRABANG  
2014

KMITL-2014-EN-D-058-208

COPYRIGHT 2014

FACULTY OF ENGINEERING

KING MONGKUT'S INSTITUTE OF TECHNOLOGY LADKRABANG

หัวข้อวิทยานิพนธ์	การเพิ่มการถ่ายเทความร้อนของการไหลของไหลนาโนในช่อง ขนานผ่านแผ่นกั้นรูปคลื่นไซน์
นักศึกษา	นายวัชรินทร์ หนูทอง
รหัสนักศึกษา	49069153
ปริญญา	วิศวกรรมศาสตรดุษฎีบัณฑิต
สาขาวิชา	วิศวกรรมเครื่องกล
พ.ศ.	2557
อาจารย์ที่ปรึกษาวิทยานิพนธ์	รศ.ดร.พงษ์เจต พรหมวงศ์

### บทคัดย่อ

วิทยานิพนธ์นี้นำเสนอแบบจำลองเชิงตัวเลขสำหรับการไหลสามมิติแบบปั่นป่วนที่มีลักษณะการไหลแบบพัฒนาอย่างสมบูรณ์และช้าเป็นช่วง แบบจำลองนี้พัฒนาขึ้นโดยมีวัตถุประสงค์เพื่อศึกษาพฤติกรรมและคุณลักษณะของการไหลแบบอัดตัวไม่ได้และการถ่ายเทความร้อนในช่องขนานที่มีการติดตั้งแผ่นกั้นรูปคลื่นไซน์ โดยทำการศึกษาผลกระทบของความสูง แอมปริจูด ระยะห่างและการจัดเรียงของรูปคลื่นไซน์ที่มีต่อการสูญเสียความดันตกคร่อม การถ่ายเทความร้อน และสมรรถนะเชิงความร้อน การคำนวณเชิงตัวเลขใช้ระเบียบวิธีปริมาตรสี่เหลี่ยม การคู่ควบของความเร็วและความดันใช้วิธีแบบ SIMPLE และใช้แบบจำลอง RNG  $k-\epsilon$  เป็นแบบจำลองความปั่นป่วน โดยใช้แบบแผนการคำนวณแบบ SOU และ QUICK และใช้อากาศ น้ำและของไหลนาโนอะลูมิเนียมออกไซด์เป็นของไหลทดสอบ จากการตรวจสอบแบบจำลองกับสมการสหสัมพันธ์และข้อมูลจากการทดลองพบว่าผลที่ได้มีความสอดคล้อง ผลจากการคำนวณเชิงตัวเลขพบว่า เมื่อเลขเรย์โนลด์เพิ่มขึ้นค่าตัวประกอบความเสียดทานค่อยๆ ลดลง เมื่อเพิ่มความสูงแผ่นกั้นค่าเลขนัสเซิลท์เพิ่มขึ้นมากแต่ค่าตัวประกอบความเสียดทานเพิ่มขึ้นด้วยทำให้สมรรถนะเชิงความร้อนลดลง เมื่อเพิ่มขนาดแอมปริจูดค่าตัวประกอบความเสียดทานลดลงมาก จากผลการคำนวณพบว่าค่าสมรรถนะเชิงความร้อนสูงสุดมีค่าเท่ากับ  $1.53 - 2.15$  ที่แผ่นกั้นแบบ  $a/H=0.75$   $b/H=0.05$   $p/H=1.00$  ขึ้นกับช่วงของเลขเรย์โนลด์ที่ทำการทดสอบ

เมื่อนำแผ่นกั้นที่ให้ค่าสมรรถนะเชิงความร้อนสูงสุดไปทำการทดสอบกับของไหลนาโนอะลูมิเนียมออกไซด์เพื่อศึกษาผลกระทบของการเพิ่มขนาดและความเข้มข้นของอนุภาคนาโนที่ผสมให้กระจายตัวในน้ำ จากผลการคำนวณเชิงตัวเลขพบว่าขนาดของอนุภาคนาโนมีผลเล็กน้อยต่อค่าตัวประกอบความเสียดทานที่ความเข้มข้นเดียวกัน เมื่อเพิ่มความเข้มข้นค่าตัวประกอบความเสียดทานมีค่าเพิ่มขึ้น ค่าเลขนัสเซิลท์เพิ่มขึ้นมากเมื่อเพิ่มความเข้มข้นและลดขนาดอนุภาคนาโน ดังนั้นค่าสมรรถนะเชิงความร้อนเพิ่มขึ้นเมื่อลดขนาดและเพิ่มความเข้มข้นอนุภาคนาโน จากการทดสอบกับแผ่นกั้นที่นำเสนอพบว่าค่าสมรรถนะเชิงความร้อนสูงสุดมีค่าเท่ากับ  $90.1 - 2.68$  ที่ขนาดอนุภาค 30 นาโนเมตรและความเข้มข้น 5% ขึ้นกับช่วงของเลขเรย์โนลด์ที่ทำการทดสอบ

<b>Thesis Title</b>	Heat Transfer Enhancement of Nanofluid Flow in Channel through Sinusoidal Wavy Baffles
<b>Student</b>	Mr.Watcharin Noothong
<b>Student ID</b>	49069153
<b>Degree</b>	Doctor of Engineering
<b>Program</b>	Mechanical Engineering
<b>Year</b>	2014
<b>Thesis Advisor</b>	Assoc.Prof.Dr.Pongjet Promvongse

## **ABSTRACT**

This thesis presents a numerical simulation of periodical three-dimensional steady-state incompressible turbulent flow and heat transfer. The primary objectives were to investigate the fluid flow and heat transfer characteristics of sinusoidal wavy baffle in a channel using air, water, and  $\text{Al}_2\text{O}_3$ -water nanofluid as working fluids. The RNG  $k-\varepsilon$  turbulence model and the finite volume method with SOU and QUICK schemes were used to solve the governing equations. First, the numerical simulation was carried out to examine the influence of baffle's geometries and arrangements on thermal performance using the air. The investigation revealed that the extending baffle height enhanced both pressure loss and heat transfer while reduced the thermal performance. An increment of baffle amplitude reduced the friction factor noticeably whereas Nusselt number declined slightly. Based on numerical solutions, depending on Reynolds number, the maximum thermo-hydraulic performance was found to be 1.53 – 2.15 corresponding to the baffle 'a/H=0.75 b/H=0.05 p/H=1.00'.

Then, the investigation of water and  $\text{Al}_2\text{O}_3$ -water nanofluid were conducted to examine the effects of nanoparticle sizes of 30 to 80nm and volume fractions of 1 to 5% on the thermal performance with the optimum baffle geometry from the air flow study. The numerical results indicated that, for the same concentration, the nanoparticle sizes had a little influence on the pressure loss. However, the friction factor increased moderately with adding volume fraction. Nusselt number increased substantially with adding volume fraction and also improved moderately with decreasing nanoparticle size. The thermo-hydraulic performance increased with reducing nanoparticle size. Therefore, the addition of concentration had strong influence on the thermal performance. According to the numerical solutions, depending on Reynolds number, the maximum thermo-hydraulic performance was found to be 1.90 – 2.68 corresponding to nanoparticle size of 30nm and volume fraction of 5% for the proposed baffle channel.

## ACKNOWLEDGEMENT

I would like to express my deepest gratitude to my thesis advisor, Assoc.Prof.Dr.Pongjet Promvong, for the valuable advices, enlightening, and encouragement.

I would like to give my gratitude to Asst.Prof.Dr.Somchai Sripattanapipat for the suggestions and discussions on the heat transfer and computational fluid dynamics.

I extend my sincere thanks to Mr.Supattarachai Suwannapan, Mr.Suriya Chokphoemphun, Mr.Sombat Tamna, and other member staffs at the Thermal Laboratory, Department of Mechanical Engineering, King Mongkut's Institute of Technology Ladkrabang, and my appreciations to my colleagues and my research students at Mahanakorn University of Technology.

I gratefully acknowledge the course funding received towards my D.Eng. from Mahanakorn University of Technology and the partial financial support for my research from the Energy Policy and Planning Office (EPPO), Ministry of Energy, Thailand.

My most sincere and very deepest thanks are to my parents, my family, and my lovely wife for continuous encouragements and supports.

Watcharin Noothong

# TABLE OF CONTENTS

	Page
THAI ABSTRACT.....	I
ENGLISH ABSTRACT.....	II
ACKNOWLEDGEMENT .....	III
TABLE OF CONTENTS .....	IV
LIST OF TABLES .....	VIII
LIST OF FIGURES.....	IX
NOMENCLATURE.....	XII
CHAPTER 1 INTRODUCTION.....	1
1.1 Statement of the problem.....	1
1.2 Research objectives.....	2
1.3 Scope of the study.....	2
1.4 Research methodology .....	2
1.5 Assumptions.....	3
1.6 Thesis structure .....	3
CHAPTER 2 LITERATURE REVIEW .....	5
2.1 Experimental heat transfer enhancement of air flow .....	6
2.1.1 Using of roughen surfaces, ribs and baffles .....	6
2.1.2 Using extended and dimpled surfaces.....	9
2.1.3 Using displaced inserts and swirl flow devices .....	10
2.1.4 Combinations of different roughness elements .....	13
2.2 Numerical heat transfer enhancement of air flow.....	14
2.3 Nanofluids.....	18
2.3.1 Synthesis of nanofluids.....	18
2.3.2 Thermophysical properties of nanofluids .....	19
2.3.3 Heat transfer enhancement of nanofluids flow .....	20
CHAPTER 3 MATHEMATICAL FORMULATION .....	23
3.1 Governing equations .....	23
3.1.1 Conservation of mass .....	23
3.1.2 Conservation of momentum .....	24
3.1.3 Conservation of energy.....	24
3.2 Turbulence modeling .....	25
3.2.1 Reynolds-averaged Navier-Stokes (RANS).....	26

## TABLE OF CONTENTS (CONT'D)

	Page
3.2.2 The law of the wall.....	27
3.2.3 The RNG $k - \varepsilon$ model .....	28
3.3 Finite volume method .....	30
3.3.1 The second order upwind scheme .....	32
3.3.2 The QUICK scheme .....	33
3.4 Boundary conditions .....	35
3.4.1 Wall boundary condition .....	35
3.4.2 Periodicity .....	35
3.5 Solution algorithm.....	35
3.5.1 Pressure-velocity coupling with SIMPLE algorithm.....	35
3.5.2 User-defined function.....	38
3.5.3 Solution procedure .....	38
3.5.4 Key quantifying performance factors.....	39
3.6 Thermophysical properties of nanofluid .....	41
3.6.1 Nanofluid dynamic viscosity .....	41
3.6.2 Nanofluid mass density and heat capacity .....	41
3.6.3 Nanofluid thermal conductivity .....	42
3.7 Flow topology and coherent structure .....	43
3.7.1 Flow topology .....	43
3.7.2 Coherent structure .....	43
3.7.3 Q criterion.....	44
 CHAPTER 4 NUMERICAL SOLUTION PROCEDURE .....	 45
4.1 Computational details of the baffle channel.....	45
4.1.1 Baffle geometry and arrangement for numerical simulation .....	45
4.1.2 Computational domain.....	46
4.1.3 Grid generation.....	48
4.1.4 Boundary conditions.....	49
4.1.5 Computational schemes and convergence criteria .....	49
4.2 Verification of numerical simulation .....	50
4.2.1 Grid independence.....	50
4.2.2 Grid convergence index .....	51
4.2.3 Verification of smooth channel.....	52
4.3 Validation of numerical simulation .....	53
4.3.1 Preliminary experiment of air flow.....	53

# TABLE OF CONTENTS (CONT'D)

	Page
4.3.2 Experimental setup and procedure of air flow .....	54
CHAPTER 5 VERIFICATION AND VALIDATION OF NUMERICAL SIMULATION .....	57
5.1 Preliminary experimental results and discussion.....	57
5.1.1 Verification of smooth channel for experimental setup .....	57
5.1.2 Experimental flow characteristics .....	59
5.1.3 Experimental heat transfer characteristics .....	60
5.1.4 Experimental thermo-hydraulic performance .....	62
5.2 Verification of numerical simulation .....	63
5.2.1 Grid refinement study.....	63
5.2.2 Estimation of grid convergence index .....	66
5.2.3 Verification of smooth channel for numerical simulation.....	66
5.3 Validation of numerical simulation .....	68
5.3.1 Comparison of friction characteristics .....	68
5.3.2 Comparison of heat transfer characteristics .....	69
CHAPTER 6 NUMERICAL INVESTIGATION OF AIR FLOW.....	71
6.1 The baffle channel computation of air flow .....	71
6.2 Flow characteristics of air .....	74
6.2.1 Effects of Reynolds number and longitudinal pitch.....	74
6.2.2 Effects of baffle height .....	77
6.2.3 Effects of baffle amplitude .....	87
6.3 Heat transfer characteristics of air flow.....	96
6.3.1 Effects of Reynolds number and longitudinal pitch.....	96
6.3.2 Effects of baffle height .....	101
6.3.3 Effects of baffle amplitude .....	109
6.4 Thermo-hydraulic performance of air flow.....	115
6.4.1 Effects of Reynolds number and longitudinal pitch.....	115
6.4.2 Effects of baffle height .....	117
6.4.3 Effects of baffle amplitude .....	120
6.5 Empirical correlations of air flow.....	122
CHAPTER 7 NUMERICAL INVESTIGATION OF NANOFUID FLOW.....	125
7.1 The baffle channel computation of nanofluid flow .....	125
7.2 Flow characteristics of nanofluid.....	126

## TABLE OF CONTENTS (CONT'D)

	Page
7.3 Heat transfer characteristics of nanofluid flow .....	128
7.4 Thermo-hydraulic performance of nanofluid flow.....	134
7.5 Empirical correlation of nanofluid flow .....	135
CHAPTER 8 CONCLUSIONS AND SUGGESTIONS .....	138
8.1 Conclusions .....	138
8.2 Suggestions for future work.....	139
REFERENCES.....	140
APPENDIX .....	149
Appendix A User defined function for nanofluids.....	150
Appendix B Author publications .....	154
AUTHOR BIOGRAPHY .....	156

# LIST OF TABLES

Table	Page
3.1 Central coefficient and neighbor coefficients for the SOU scheme .....	33
3.2 Central coefficient and neighbor coefficients for the QUICK scheme.....	34
4.1 Numerical scheme/method used in the computation.....	49
4.2 Residual monitors and convergence criteria .....	50
4.3 Measurement uncertainties of the experimental setup.....	55
5.1 Geometric parameters and flow conditions for preliminary experiment.....	57
5.2 Grid refinement study at $Re=10,000$ .....	64
5.3 Grid convergence index .....	66
6.1 Geometric parameters and flow condition of air flow.....	72
6.2 Reference values used in computations of air flow.....	72
6.3 Specified mass flow rates in computation of air flow .....	73
7.1 Study parameters and flow conditions of nanofluid flow.....	126
7.2 Reference values used in computations of nanofluid flow .....	126

## LIST OF FIGURES

Figure	Page
3.1 A typical velocity of one-dimensional turbulent flow.....	26
3.2 A typical velocity profile for a turbulent boundary layer .....	28
3.3 A control volume around node P .....	31
3.4 Linear profile used in the SOU scheme.....	32
3.5 Quadratic profiles used in the QUICK scheme.....	34
3.6 Pressure-based segregated algorithm flowchart.....	36
3.7 Pressure-based segregated with SIMPLE algorithm flowchart .....	37
3.8 Pressure-based segregated with UDF function flowchart.....	38
4.1 Baffle geometry and arrangement for computation .....	46
4.2 Two-dimensional computational domain .....	47
4.3 Three-dimensional computational domain .....	47
4.4 Hexahedral grid structure for numerical simulation .....	48
4.5 Baffle geometry and arrangement for experiment .....	53
4.6 A sample photo of baffle arrangement for experiment.....	54
4.7 Schematic diagram of the experimental setup.....	55
5.1 Comparison of experimental $f_0$ and corresponding correlations .....	58
5.2 Comparison of experimental $Nu_0$ and corresponding correlations.....	59
5.3 Variations of experimental $f$ with $Re$ at $p/H=1.00$ .....	59
5.4 Variations of experimental $f$ with $Re$ at $p/H=2.00$ .....	60
5.5 Variations of experimental $Nu$ with $Re$ at $p/H=1.00$ .....	61
5.6 Variations of experimental $Nu$ with $Re$ at $p/H=2.00$ .....	61
5.7 Variations of experimental $\eta$ with $Re$ at $p/H=1.00$ .....	62
5.8 Variations of experimental $\eta$ with $Re$ at $p/H=2.00$ .....	63
5.9 Absolute error of $f$ from grid refinement study .....	64
5.10 Absolute error of $Nu$ from grid refinement study.....	65
5.11 The $y^+$ values from grid refinement study.....	65
5.12 Comparison of predicted $f_0$ and corresponding correlations.....	67
5.13 Comparison of predicted $Nu_0$ and corresponding correlations.....	67
5.14 Comparison of experimental and numerical $f$ .....	68
5.15 Comparison of experimental and numerical $f$ .....	69
5.16 Comparison of experimental and numerical $Nu$ .....	70
5.17 Comparison of experimental and numerical $Nu$ .....	70
6.1 Locations of cross-sectional transverse plane of interest.....	73
6.2 Variation of $f/f_0$ with $Re$ for varied $p/H$ at $b/H=0.05$ .....	74
6.3 Variation of $f/f_0$ with $Re$ for varied $p/H$ at $b/H=0.10$ .....	75

## LIST OF FIGURES (CONT'D)

Figure	Page
6.4 Variation of $f/f_0$ with Re for varied $p/H$ at $b/H=0.15$ .....	76
6.5 Streamlines released from the crest of baffles at $Re=10,000$ .....	77
6.6 Secondary flow patterns for varied $b/H$ at $Re=10,000$ .....	78
6.7 Pressure distribution for varied $b/H$ at $Re=10,000$ .....	80
6.8 The Q isosurface for varied $b/H$ at $Re=10,000$ .....	82
6.9 Variation of $f/f_0$ with Re for varied $b/H$ at $p/H=0.50$ .....	84
6.10 Variation of $f/f_0$ with Re for varied $b/H$ at $p/H=1.00$ .....	84
6.11 Variation of $f/f_0$ with Re for varied $b/H$ at $p/H=1.50$ .....	85
6.12 Variation of $f/f_0$ with $b/H$ for various Re at $a/H=0.25$ .....	85
6.13 Variation of $f/f_0$ with $b/H$ for various Re at $a/H=0.50$ .....	86
6.14 Variation of $f/f_0$ with $b/H$ for various Re at $a/H=0.75$ .....	86
6.15 Variation of $f/f_0$ with $b/H$ for various Re at $a/H=1.00$ .....	87
6.16 Secondary flow patterns for varied $a/H$ at $Re=10,000$ .....	88
6.17 Pressure distribution for varied $a/H$ at $Re=10,000$ .....	90
6.18 The Q isosurface for varied $a/H$ at $Re=10,000$ .....	92
6.19 Variation of $f/f_0$ with $a/H$ for various Re at $b/H=0.05$ .....	95
6.20 Variation of $f/f_0$ with $a/H$ for various Re at $b/H=0.10$ .....	95
6.21 Variation of $f/f_0$ with $a/H$ for various Re at $b/H=0.15$ .....	96
6.22 Nu contours of varied Re .....	97
6.23 Nu contour of varied $p/H$ .....	98
6.24 Variation of $Nu/Nu_0$ with Re for varied $p/H$ at $b/H=0.05$ .....	100
6.25 Variation of $Nu/Nu_0$ with Re for varied $p/H$ at $b/H=0.10$ .....	100
6.26 Variation of $Nu/Nu_0$ with Re for varied $p/H$ at $b/H=0.15$ .....	101
6.27 Temperature distributions for varied $b/H$ at $Re=10,000$ .....	102
6.28 Nu contour of varied $b/H$ at $Re=10,000$ .....	104
6.29 Variation of $Nu/Nu_0$ with Re for varied $b/H$ at $p/H=0.50$ .....	105
6.30 Variation of $Nu/Nu_0$ with Re for varied $b/H$ at $p/H=1.00$ .....	106
6.31 Variation of $Nu/Nu_0$ with Re for varied $b/H$ at $p/H=1.50$ .....	106
6.32 Variation of $Nu/Nu_0$ with $b/H$ for various Re at $a/H=0.25$ .....	107
6.33 Variation of $Nu/Nu_0$ with $b/H$ for various Re at $a/H=0.50$ .....	107
6.34 Variation of $Nu/Nu_0$ with $b/H$ for various Re at $a/H=0.75$ .....	108
6.35 Variation of $Nu/Nu_0$ with $b/H$ for various Re at $a/H=1.00$ .....	108
6.36 Temperature distribution for varied $a/H$ at $Re=10,000$ .....	109
6.37 Nu contour of varied $a/H$ at $Re=10,000$ .....	112
6.38 Variation of $Nu/Nu_0$ with $a/H$ for various Re at $b/H=0.05$ .....	114

## LIST OF FIGURES (CONT'D)

Figure	Page
6.39 Variation of $Nu/Nu_0$ with $a/H$ for various $Re$ at $b/H=0.10$ .....	114
6.40 Variation of $Nu/Nu_0$ with $a/H$ for various $Re$ at $b/H=0.15$ .....	115
6.41 Variation of $\eta$ with $Re$ for varied $pL/H$ at $b/H=0.05$ .....	116
6.42 Variation of $\eta$ with $Re$ for varied $pL/H$ at $b/H=0.10$ .....	116
6.43 Variation of $\eta$ with $Re$ for varied $pL/H$ at $b/H=0.15$ .....	117
6.44 Variation of $\eta$ with $b/H$ for various $Re$ at $a/H=0.25$ .....	118
6.45 Variation of $\eta$ with $b/H$ for various $Re$ at $a/H=0.50$ .....	118
6.46 Variation of $\eta$ with $b/H$ for various $Re$ at $a/H=0.75$ .....	119
6.47 Variation of $\eta$ with $b/H$ for various $Re$ at $a/H=1.00$ .....	119
6.48 Variation of $\eta$ with $a/H$ for various $Re$ at $b/H=0.05$ .....	120
6.49 Variation of $\eta$ with $a/H$ for various $Re$ at $b/H=0.10$ .....	121
6.50 Variation of $\eta$ with $a/H$ for various $Re$ at $b/H=0.15$ .....	121
6.51 Comparison of correlation and numerical $f$ .....	123
6.52 Comparison of correlation and numerical $Nu$ .....	123
6.53 Comparison of correlation and numerical $\eta$ .....	124
7.1 Variation of $f$ with $Re$ for varied $d_p$ and $\phi$ .....	127
7.2 Variation of $f/f_0$ with $Re$ for varied $d_p$ and $\phi$ .....	128
7.3 $Nu$ contour of water as base fluid at $Re=10,000$ .....	129
7.4 $Nu$ contours of varied $d_p$ at $\phi=1\%$ .....	129
7.5 $Nu$ contours of varied $\phi$ at $d_p=30nm$ .....	131
7.6 Variation of $Nu$ with $Re$ for varied $d_p$ and $\phi$ .....	133
7.7 Variation of $Nu/Nu_0$ with $Re$ for varied $d_p$ and $\phi$ .....	133
7.8 Variation of $\eta$ with $Re$ for varied particle sizes and volume fractions.....	134
7.9 Comparison of correlation and numerical $f$ .....	136
7.10 Comparison of correlation and numerical $Nu$ .....	136
7.11 Comparison of correlation and numerical $\eta$ .....	137

# NOMENCLATURE

## Symbol, definition, SI units

a	Baffle amplitude: m
A	Heat transfer area: $m^2$
b	Baffle height: m
B	Empirical constant in the law of the wall
$c_p, c_v$	Specific heat capacity at constant pressure, volume: $J/(kg \cdot K)$
$d_f$	Equivalent diameter of base fluid: nm
$d_p$	Nanoparticle size, diameter: nm
D	Tube inside diameter, diameter: m
$D_h$	Hydraulic diameter: m
f	Friction factor
g	Gravitational acceleration: $m/s^2$
h	Heat transfer coefficient: $W/(m^2 \cdot K)$
H	Channel height: m
i	Internal energy: m
k	Thermal conductivity: $W/(m \cdot K)$
k	Turbulent kinetic energy
K	Mean kinetic energy
L	Length: m
$\dot{m}$	Mass flow rate: $kg/s$
M	Molecular weight: $g/mol$
N	Avogadro number: $6.022 \times 10^{23} \text{ mol}^{-1}$
Nu	Nusselt number
pl	Longitudinal pitch: m
pt	Transverse pitch: m
P	Pressure: Pa, $N/m^2$
Pr	Prandtl number
$\Delta P$	Pressure drop: Pa, $N/m^2$
q	Heat transfer rate: W
$q_s$	Surface heat flux: $W/m^2$
Q	Heat transfer rate: W
T	Temperature: $^{\circ}C$ , K
$\Delta T$	Temperature difference: $^{\circ}C$ , K
t	Time: s
u, v, w	Velocity component in x, y, z directions in rectangular coordinates: m/s

## NOMENCLATURE (CONT'D)

### Symbol, definition, SI units

U	Velocity vector: m/s
W	Channel width: m
x, y, z	Rectangular Cartesian coordinates: m

### Greek

$\beta$	Empirical function in correlations of nanofluids
$\delta$	Boundary layer thickness: m
$\varepsilon$	Viscous dissipation
$\eta$	Thermo-hydraulic performance
$\kappa_B$	Boltzmann constant: $1.3807 \times 10^{-23}$ J/K
$\kappa$	Kármán constant
$\mu$	Dynamic viscosity: Pa·s
$\nu$	Kinematic viscosity: $\text{m}^2/\text{s}$
$\rho$	Fluid density: $\text{kg}/\text{m}^3$
$\tau$	shear stress: Pa, $\text{N}/\text{m}^2$
$\varphi$	Arbitrary variable, component
$\phi$	Particle volume fraction: %
$\phi$	Arbitrary quantity
$\Phi$	Viscous dissipation function

### Subscripts

b	Bulk mean
eff	Effective
f	Base fluid
in	Inlet
m	Mean value
nf	Nanofluid
out	Outlet
p	Nanoparticle
ref	Reference
s	Surface value
x, y, z	The x, y, z components
w	Wall value
0	Smooth channel

## NOMENCLATURE (CONT'D)

### Superscripts

- + Sublayer-scaled value
- ' Fluctuating quantity

### Mathematical operation symbols

- $d/dx$  Derivative with respect to  $x$ :  $m^{-1}$
- $\partial/\partial t$  Partial time derivative operator:  $s^{-1}$

# CHAPTER 1

## INTRODUCTION

### 1.1 Statement of the problem

One of the most important energy is the heat which has been consumed in a broad range of applications and industries. When the heat is in use, heat transfer occurs either in heating or cooling mode due to the temperature differences. Heat transfer is the transport of thermal energy from the higher temperature region to the lower temperature region. A practical use of this phenomenon is a heat exchanger which is a device that exchange thermal energy between fluids or solids with thermal contact to working fluids at different temperatures. The examples of heat exchanger are the cooling tower, evaporators, condensers, car radiators, solar heaters, etc.

For decades, there are several researches and developments to improve the thermal performance of the heat exchangers such as extending the surface area, adapting the surface geometries, using fluid additives, using the external power to stimulate the flow modification, etc. Moreover, there are still the needs to make the heat exchangers become more compact and yield higher thermal performance with greater reliability. These requirements are challenges because it becomes more difficult to meet the energy efficiency while trying to reduce the size and cost of thermal equipment.

Therefore, a numerical simulation is introduced to investigate the fluid flow and heat transfer behaviors in a small hydraulic diameter channel which represents the compact heat exchanger. The numerical simulation is very useful to examine the temperature and flow fields which are very difficult or impossible to measure directly. The numerical simulation is also a cost effective solution that avoids the cost of numerous prototyping experiments.

In the present study, a numerical simulation was conducted to study the effects of sinusoidal wavy baffle's geometries and arrangements on the fluid flow and heat transfer characteristics in a channel. The working fluids investigated in this study were the traditional air fluid, water, and the innovative  $Al_2O_3$ -water nanofluid. The nanofluid was introduced since it attractively provided higher thermal conductivity compared to the traditional fluid. In order to evaluate the thermal performance, the key quantitative performance factors were defined. The fluid flow and heat transfer characteristics were examined extensively. The thermo-hydraulic performances of the baffle channel using those fluids were determined with respect to the smooth channel.

## 1.2 Research objectives

The main objectives of the present study were:

1. To perform a numerical simulation to investigate the fluid flow and heat transfer characteristics in a channel with sinusoidal wavy baffles having different geometries and arrangements using the air as a working fluid.
2. To evaluate the optimum thermal performance of the baffle channel using the air as a working fluid.
3. To further investigate the fluid flow and heat transfer behaviors in a channel using water and  $\text{Al}_2\text{O}_3$ -water nanofluid as working fluids.
4. To evaluate the optimum thermal performance of  $\text{Al}_2\text{O}_3$ -water nanofluid.

## 1.3 Scope of the study

The present study conducted a numerical simulation to investigate the effects of sinusoidal wavy baffles' geometries and arrangements on the fluid flow and heat transfer characteristics in a channel. The pressure loss, heat transfer characteristic, and thermal performance were described in terms of the friction factor, Nusselt number, and the thermo-hydraulic performance, respectively. First, the traditional air fluid was used as a working fluid to determine the geometrical configuration that yielded the highest thermal performance. After that, water and an innovative  $\text{Al}_2\text{O}_3$ -water nanofluid were adopted with the optimum baffle geometry from the air flow study to further enhance the heat transfer rate. The influences of nanoparticle size and volume fraction were examined. For all working fluids, the constant surface heat fluxes as thermal boundary conditions were applied to the principal walls of the channel. The numerical simulation was carried out by assumed the periodical fully-developed turbulent flow inside the baffle channel. The range of observed Reynolds number was varied from 5,000 to 18,000.

## 1.4 Research methodology

For the present work, a three-dimensional steady-state fluid flow and heat transfer analysis was accomplished using a commercial ANSYS Workbench. In the preprocessor process, the DesignModeler application was used to create the sinusoidal wavy baffle's geometries and arrangements. The Meshing application was used to generate the grid structure which was the computational domain. In the FLUENT application, the RNG  $k$ - $\epsilon$  turbulence model was employed. The finite volume method was used with SOU and QUICK schemes to solve for the numerical solutions with different baffle geometries and arrangements. First, the key quantifying performance factors were evaluated to determine the optimum geometrical configuration of the baffle using air as a working fluid that provided the highest

thermo-hydraulic performance. This optimum solution was further studied to enhance the heat transfer rate using water and  $\text{Al}_2\text{O}_3$ -water nanofluid. Finally, in the post-processing, the flow visualization was introduced. The flow topology and coherent structure were adapted to study the fluid flow and heat transfer characteristics of the baffle channel.

## 1.5 Assumptions

In the present study, a numerical simulation of fluid flow and heat transfer in a channel was developed under the following major assumptions:

- Steady three-dimensional fluid flow and heat transfer.
- Turbulent and incompressible flow.
- Negligible body forces.
- Negligible viscous dissipation.
- Negligible radiation heat transfer.
- No thermal energy sources within the fluid.

## 1.6 Thesis structure

This thesis is organized in 8 chapters, the contents of which are briefly described below:

Chapter 1 introduces the statement of the problem and the objectives of the study. The scope of the study is prescribed. The research methodology is proposed. The major assumptions used in the study are clarified.

Chapter 2 reviews the published literatures on the heat transfer enhancement. The surveys on experimental and numerical investigations using the air as a working fluid are presented. The recent development of nanoparticles and the using of nanofluids to augment the heat transfer rate are also reviewed.

Chapter 3 provides the mathematical formulations employed as the governing equations in the numerical simulation. The turbulence model is introduced to represent the physics of fluid flow. The finite volume method is briefly described to solve the algebraic equations which discretized from the governing equations. The solution algorithm, the solution procedure, and the boundary conditions are explained. The key quantifying performance parameters are defined to evaluate the thermal performance. Moreover, the mathematical models to specify the nanofluids' thermophysical properties are also introduced.

Chapter 4 describes the construction of numerical model and the computational details to represent the domain of interest. The geometries and arrangements of the sinusoidal wavy baffle in the channel are prescribed. The grid

generation, the boundary conditions, and the computational schemes are presented. The verification and validation methods are described and discussed. The preliminary experimental investigation is also introduced to validate the numerical model.

Chapter 5 presents the verification and validation of the numerical model. The verification results are described and discussed. For validation purpose, first, the preliminary experimental data are presented. Then, the comparisons of numerical solutions with experimental results are described and discussed.

Chapter 6 presents the numerical solutions using the air as a working fluid. The flow topology and coherent structures of the air flow and details of heat transfer enhancement on the baffles are described and discussed. The effects of the baffle geometries and arrangements on the pressure loss, heat transfer enhancement and thermal performance are described and discussed. The optimum geometrical configuration that provides the highest thermo-hydraulic performance is also presented.

Chapter 7 presents the numerical results of the optimum baffle geometry using water and  $\text{Al}_2\text{O}_3$ -water nanofluid as working fluids. The effects of nanoparticle sizes and volume fractions are described and discussed.

Chapter 8 summarizes the numerical results compiled from the present computational study. The suggestions for future work are also included.

## CHAPTER 2

# LITERATURE REVIEW

The techniques for heat transfer enhancement can be generally classified into two groups which are the passive and the active techniques [1]. The passive technique exploits the modification of surface geometries or fluid additives to enhance the heat transfer rate. In this technique, the heat transfer coefficient can be improved by disturbing or altering the fluid flow behaviors except for the extended surface method which enlarges the surface area. The examples of the passive technique are implement of coated surfaces, roughen surfaces, extended surfaces, displaced inserts, coiled tubes, swirl flow devices, surface tension devices, fluid additives, etc.

On the other hand, the active technique requires the external power inputs such as mechanical aids, electric or magnetic fields, surface or fluid vibrations, and jet impingement to cause the desired flow alteration and improvement in the heat transfer rate. This technique has limited applications because of the need of external power. However, two or more of the passive and active techniques may be applied simultaneously to yield higher heat transfer enhancement. The simultaneous use is called the compound enhancement technique [2]. This combination method has limited applications because of its complex design.

Recently, there are developments in the new class of fluids that suspending the small solid particles in the ordinary fluids to enhance the heat transfer rate. With the advanced development of nanotechnology, the nanometer-size particles (1 - 100nm) have been studied and used for heat transfer enhancement. The term nanofluid used for nanoparticle suspension was introduced by Choi from Argonne National Laboratory (U.S.A.) in 1995 [3]. Because the high thermal conductivity of nanofluids has made this innovative fluids become more interesting and attractive, a ceramic nanofluid was considered as an alternative working fluid in the present study.

Since the present study relates to heat transfer enhancement using a special surface geometry with the air, water, and a nanofluid, therefore, the following literature reviews are focused mainly on relevant passive techniques for the air and the nanofluids. The reviews are divided into three parts. First, the articles of experimental researches are surveyed due to the extensive studies in the field of heat transfer enhancement. Second, the published literatures of numerical investigations are reviewed and discussed. Finally, the articles of convective heat transfer enhancement using nanofluids are reviewed and discussed.

## 2.1 Experimental heat transfer enhancement of air flow

### 2.1.1 Using of roughen surfaces, ribs, and baffles

Surface roughness is one of the first techniques used to increase the forced convective heat transfer. The artificial surface roughness may be produced by traditional manufacturing processes such as machining, forming, casting, welding, and so on. For single-phase flow, this technique has often been chosen to promote the mixing in boundary layer near the surface rather than to increase the surface area. The boundary layer or the laminar sublayer between the surface and the fluid flow is considered as thermal resistance.

Ribs and baffles are mostly used to enhance the heat transfer rate. They break the laminar sublayer and create the turbulence due to the flow separation and reattachment between the consecutive ribs or baffles. Consequently, the thermal resistance is reduced and the heat transfer rate is increased. Furthermore, since the turbulence is desirable only in the region very close to the surface, the height of ribs or baffles are usually designed to be small [4]. The using of artificial roughness techniques to enhance the heat transfer is exemplified as following reviews:

Verma and Prasad [5] carried out an outdoor experiment using transverse continuous ribs and circular cross-sectional ribs. They determined the thermo-hydraulic optimization of the roughness and flow parameters for Reynolds number ranging from 5,000 to 20,000. Their studied geometries were relative roughness pitch of 10 - 40 and relative roughness height of 0.01 - 0.03. The optimal value of relative roughness was found to be 24. Corresponding to this value, the optimal thermo-hydraulic performance was reported to be 71%. Heat transfer enhancement factor was found to vary between 1.25 and 2.08 for the range of parameters investigated. Correlations for the heat transfer and friction factor were developed.

Karwa et al. [6] experimentally investigated the chamfered rib and roughness on the air flow side of absorber plates in the solar air heater. Their roughened elements had a relative roughness pitch of 4.58 and 7.09 while the rib's chamfered angle was fixed at 15°. The duct's height was varied among 21.8, 21.5, and 16 mm. The relative roughness height was varied among 0.0197, 0.0256, and 0.0441, respectively. Reynolds number was ranged from 3,750 to 16,350. Their study showed the substantial enhancement in thermal performance around 10 to 40% over smooth plate due to the increase in Nusselt number approximately 50 to 120% with the enlargement in friction factor about 80 to 290%.

Momin et al. [7] conducted an experiment to study the effects of geometric parameters of v-shaped ribs on heat transfer and fluid flow characteristics in a rectangular duct. The investigation covered Reynolds number of 2,500 - 18,000, relative roughness height of 0.02 - 0.034, and angle of attack at 30° - 90° for a fixed

relative roughness pitch of 10. The increased rate of Nusselt number was observed to be lower than the increase rate of friction factor through the increment in Reynolds number. For an angle of attack at  $60^\circ$ , v-shaped ribs enhanced the Nusselt number by 1.14 over inclined ribs and 2.30 times over smooth plate. They also developed the correlations for Nusselt number and friction factor.

Bhagoria et al. [8] experimentally studied the heat transfer and fluid flow characteristics in a solar air heater having the absorber plate roughened with wedge shaped transverse ribs. The investigation covered Reynolds number of 3,000 - 18,000, relative roughness height of 0.015 - 0.033 and rib wedge angle at  $8^\circ$  -  $12^\circ$ . They reported that Nusselt number and friction factor were increased by 2.4 and 5.3 times over the smooth duct in the range of parameters investigated, respectively. They also derived the correlations for Nusselt number and friction factor. Lau et al. [9] studied the effects of different holes geometry in the blockage. They reported that the blockages with round holes enhanced more heat transfer on the channel walls but caused larger pressure drop than the blockages with square holes. However, the square holes blockage had 27% larger cross-sectional area of the flow.

Karwa [10] again carried out a comparative experimental study of rectangular cross-section ribs in rectangular duct with aspect ratio of 7.19 - 7.75. The studied ribs were arranged in v-continuous and v-discrete patterns. The configuration had relative roughness pitch of 10, relative roughness height of 0.0467 - 0.050 and Reynolds number of 2,800 - 15,000. The enhancement in the Stanton number over smooth duct was reported to be in range of 102 - 137%, 110 - 147%, 93 - 134%, and 102 - 142% for the transverse, inclined, v-up continuous, v-down continuous, v-up discrete, and v-down discrete rib arrangements, respectively. The friction factor ratios corresponding to these arrangements were found to be 3.02 - 3.42, 3.40 - 3.92, 3.32 - 3.65, 2.35 - 2.47 and 2.46 - 2.58, respectively. The performance of v-down ribs was better than the v-up ribs.

Sahu and Bhagoria [11] investigated the effect of  $90^\circ$  broken ribs on the thermal performance of a solar air heater. They fixed the roughness height at 1.5 mm with duct's aspect ratio of 8. They varied roughness pitch of 10 - 30 mm, and Reynolds number of 3,000 - 12,000. They found that roughened absorber plate increased the heat transfer coefficient by 1.25 - 1.4 times compared to the smooth plate under similar operating conditions. The maximum value of Nusselt number was obtained at the roughness pitch of 20 mm. Based on the experimental results, the thermal performance of roughened solar air heater was found to be in the range of 51 - 83.5% depending upon the flow conditions.

Aharwal et al. [12] conducted an experiment to study the effects of width and position of a gap in the inclined split-ribs on heat transfer and friction

characteristics in a rectangular duct. The duct had an aspect ratio of 5.84. The ribs had relative roughness pitch of 10, relative roughness height of 0.0377, angle of attack at  $60^\circ$ , relative gap width of 0.5 - 2.0, and relative gap position of 0.1667 - 0.667. Reynolds number was ranging from 3,000 to 18,000. The enhancement in heat transfer was reported to be in the range of 1.71 - 2.59 times for the split-rib and 1.48 - 2.26 times for continuous rib over smooth duct under similar operating conditions. The maximum values of heat transfer, friction factor ratio and thermo-hydraulic parameter were corresponding to relative gap width of 1.00 and relative gap position of 0.25. The Particle Image Velocimetry (PIV) system was also used to visualize the effects of inclination angle of ribs on the flow behavior. Based on experimental results, correlations for Nusselt number and friction factor were also developed.

Saini and Saini [13] studied the effects of arc shaped ribs on heat transfer coefficient and friction factor of rectangular duct with Reynolds number, relative roughness height, and relative arc angle varying from 2,000 to 17,000, 0.0213 to 0.0422 and 0.3333 to 0.6666, respectively. They reported that Nusselt number increased while friction factor decreased with decreasing in relative arc angle value. Nusselt number ratio and friction factor ratio were reported to be 3.6 and 1.75, respectively over smooth duct for relative arc angle of 0.3333 and relative roughness height of 0.0422. Based on the experimental results, correlations for Nusselt number and friction factor were also developed.

Promvongse and Thianpong [14] conducted the forced convection experiments to examine the heat transfer and friction loss behaviors with different shaped ribs: triangular, wedge, and rectangular shapes arranged in-line and staggered. They reported that the in-line ribs provided higher heat transfer and friction loss than the staggered ribs for similar mass flow rate. The wedge rib pointing downstream yielded the highest Nusselt number and also friction factor while the staggered triangular rib showed a better thermal performance than the others.

Bopche and Tandale [15] performed an experiment using inverted U shaped turbulators as the roughness element. They found that even at relatively low Reynolds number ( $Re < 5000$ ), there was a considerable increase in heat transfer. The maximum increase in friction factor and Nusselt number ratios were 2.50 and 2.388, respectively. When compared with smooth duct, the maximum increase in friction factor and Nusselt number values were 3.72 and 2.82, respectively.

Promvongse [16] again conducted an experiment to assess the heat transfer and friction loss behaviors for the air flow through a channel fitted with a multiple  $60^\circ$  V-baffle turbulator. Three different baffle blockage ratios and three baffle pitch spacing ratios were observed. He reported that the V-baffle provides the drastic increase in Nusselt number, friction factor and thermal enhancement factor values

over the smooth wall channel due to better flow mixing from the formation of secondary flows induced by vortex flows generated by the V-baffle. He concluded that the use of the V-baffle with pitch ratio of 1.00 and blockage ratio of 0.10 gave a maximum thermal enhancement factor of about 1.87 at lowest Reynolds number of 5,000.

### **2.1.2 Using extended and dimpled surfaces**

The extended and dimpled surfaces are used in many heat exchangers. Heat transfer coefficient may be increased by enlarging the surface area with the formation of special shape of the extended surfaces. The dimpled surfaces are designed to enlarge the surface area while trying to reduce the pressure drop. The examples of using these techniques are reviewed as following.

Afanasyev et al. [17] experimentally studied the friction and heat transfer on surfaces shaped by systems of spherical cavities streamlined by turbulent flows. Experimental data on heat transfer were generalized and a correlation of heat transfer and the geometric parameters used were obtained. They attributed the heat transfer enhancement to a slight decrease in the thickness of the viscous sublayer and also the three dimensional nature of the cavities which produce a wall pressure gradient that determines the mechanism of heat transport in the region. Heat transfer enhancement of about 30 - 40 percent was reported without appreciable pressure losses.

Bilen et al. [18] performed the experimental investigation using cylindrical fins arranged both in-line and staggered. The parameters for study were Reynolds number of 3,700 - 30,000, the distances between fins in the flow direction of 1.96 - 4.41, and fin arrangements. They found that the maximum heat transfer occurred at distance of 2.94 with the heat transfer enhancement 33% over smooth channel. The correlations for Nusselt number and friction factor were also developed.

Chandra et al. [19] reported an experimental study of surface heat transfer and friction characteristics of a fully developed turbulent air flow in a square channel with transverse ribs on one, two, three, and four walls. They varied Reynolds numbers from 10,000 to 80,000. The pitch-to-rib height ratio, rib-height-to-channel and hydraulic diameter ratio were kept constant. Heat transfer coefficient and friction factor results were enhanced with the increase in the number of ribbed walls. The friction roughness function was almost constant. The heat transfer roughness function increased with roughness Reynolds number.

Karmare and Tikekar [20] experimentally investigated the heat transfer and friction characteristics of a rectangular duct having absorber plate roughened with a defined grit of metal ribs of circular cross-section. The investigation considered relative roughness height of 0.035 - 0.044, relative roughness pitch of 12.5 - 36,

relative grit length of 1 - 1.72, and Reynolds number range of 4,000 - 17,000. Enhancement in Nusselt number was found to be 187% and the friction factor increased by 213%. The optimum performance was observed for relative grit length of 1.72, relative roughness height of 0.044 and relative roughness pitch value of 17.5 for the range of parameters studied. Based on the experimental results, correlations for Nusselt number and friction factor were developed.

Saini and Verma [21] studied the effect of roughness and operating parameters on heat transfer and friction factor in a roughened duct provided with dimple-shape roughness geometry for the range of Reynolds number of 2,000 - 12,000, relative roughness height of 0.018 - 0.037 and relative pitch of 8 - 12. For the range of parameters investigated, Nusselt number was found to be maximum corresponding to relative roughness height of 0.0379 and relative roughness pitch of 10. For fixed value of relative roughness pitch of 10, friction factor attained the maximum and minimum values corresponding to relative roughness height values of 0.0289 and 0.0189, respectively. Correlations for Nusselt number and friction factor have been developed.

Change et al. [22] comparatively examined the heat transfer characteristics of dimpled fin channels with Reynolds number ranging from 1500 to 11,000. They studied the effects of dimple arrangement and fin length ( $L$ ) to channel hydraulic diameter ( $d$ ) ratio of 8.9, 6.2 and 3.5 on heat transfer over the dimpled fin channel. They reported the heat transfer correlations for spatially averaged Nusselt number using  $Re$  and  $L/d$  as the controlling parameters. A set of design criteria for determining the optimal  $L/d$  that offers the maximum cooling power was also reported.

Yu et al. [23] carried out an experimental study on friction and heat transfer performances of a transitional airflow in a rectangular channel with stagger-arrayed short pin fins. They reported that, in the transitional flow region, the pin fin channels of the proposed geometrical configuration could lead to a significant improvement of an overall thermal performance. The convective heat transfer performance was increased by at least 68%. In the fully turbulent flow region, the ability of the proposed pin fin channels to increase heat transfer performances decreased as the Reynolds number increased. When  $Re > 6,000$ , the overall thermal performance became lower than the others.

### **2.1.3 Using displaced inserts and swirl flow devices**

Displaced inserts are put into the flow channel to improve the energy transport at the heated surface indirectly. They are placed at the edge of the boundary layer to promote the mixing within the boundary layer without significantly affecting the main flow. Various inserts placing adjacent to the surface can be used

to provide surface protuberances. Swirl flow devices include a number of geometrical arrangements or tube inserts that create rotating or secondary flow. These devices mostly swirl the flow in clockwise and counterclockwise directions.

Fiebig et al. [24] reviewed the vortex generators. He carried out a number of investigations both experimental as well as computational to understand the basic mechanism of heat transfer enhancement by longitudinal vortices and also to predict quantitatively the extent of heat transfer augmentation which could be achieved by using different types of vortex generators viz., delta wings, delta winglet pairs, and rectangular wings. The vortex generator obstructs the flow and hence adds to the pumping cost. However, the additional pressure loss due to the use of longitudinal vortex generators is very modest, because the form drag for these slender bodies is low. Further, this increase in pumping power will be insignificant when the complete ducting of the equipment is considered.

Gentry and Jacobi [25] investigated the impact of a single delta-wing vortex generator on the flow and heat transfer in a laminar boundary layer. The experiments were performed for Reynolds numbers 600, 800, and 1000 with aspect ratios 0.5, 1, 1.5, and 2 and angles of attack of the delta wings equal to 10°, 25°, 40°, and 55°. They visualized the flow by smoke illuminated by a laser sheet, and obtained the plate average heat transfer coefficient by conducting naphthalene sublimation experiments. Optimized delta-wing geometries for maximum heat transfer enhancement for all three Reynolds numbers were presented in this study. A 50 to 60% enhancement of average heat transfer was reported for these geometries, with an estimated pressure drop penalty of 50 to 100%. Flow visualization showed that the two vortices generated by the delta wing spread apart and lifted away from the surface as they moved downstream. Based on the flow visualization images, the plate-to-core, and the core-to-core distances were obtained for the tip vortices. It was suggested that the streamwise vortices should be strong and located near the edge of the boundary layer for the best performance.

Gentry and Jacobi [26] performed experiments for a variety of fin and vortex generator configurations over a range of flow conditions for laminar, flat-plate and laminar developing channel flows. The objective behind the study was to obtain an increased understanding of the flow structure, heat transfer enhancement, and pressure drop encountered in wing based VG's. The local and average measurements of the convection coefficients were obtained using naphthalene sublimation, and the structure of the vortices was studied using flow visualization and vortex strength measurements. The pressure drop penalty associated with the heat transfer enhancement of the channel flow was also investigated. It was found that in the regions where a vortex induces a surface-normal inflow, the local heat transfer

coefficients augmented by 300 % over the baseline flow, depending on vortex strength and location relative to the boundary layer. Vortex strength amplified with Reynolds number, wing aspect ratio, and wing attack angle. It was observed that the vortex strength decayed as the vortex was carried downstream. For the complete channel surface, the largest spatially averaged heat transfer enhancement was found to be 55%; along with 100 percent increase in the pressure drop relative to the same channel flow with no vortex generator.

Kim and Yang [27] experimentally studied the flow and heat transfer characteristics for a pair of embedded counter-rotating vortices. The heat transfer measurements were made using thermo-chromatic liquid crystal to provide the local surface distributions of heat transfer coefficients. In order to control the strength of longitudinal vortices, angle of attack of the vortex generators was varied from  $20^\circ$  to  $45^\circ$ , and the spacing between the vortex generators was taken 4 cm apart. It was concluded that for the common-flow-down cases, two maximum values in the local heat transfer distribution exists for the three angles of attack. With the common-flow-up cases, only one highest value exists. The common-flow-down cases showed better heat transfer characteristics than the common flow-up cases.

Dupont et al. [28] investigated an isothermal flow in a model channel of a plate-fin heat exchanger with periodically arranged embossed-like vortex generators. Velocity measurements were performed by LDA in the transitional regime (Reynolds number from 1000 up to 5000). Strong longitudinal vortices were observed downstream of each generator. The vortex rollup process was highlighted by the evolution of the velocity vector field in the cross-section of the flow. The modifications of the vortex characteristics after successively encountered generators were investigated. This work showed that these smooth shaped vortex generators were very promising for enhanced heat exchangers.

Joardar and Jacobi [29] experimentally evaluated the effectiveness of delta-wing type vortex generators by full-scale wind-tunnel testing of a compact heat exchanger, used in automotive systems. The important mechanisms to vortex enhancement methods were discussed, and a basis for selecting a delta-wing design as a vortex generator was established. The heat transfer and pressure drop performance were assessed at full scale under both dry- and wet-surface conditions for a louvered-fin baseline and for a vortex-enhanced louvered-fin heat exchanger. An average heat transfer increase over the baseline case of 21% for dry conditions and 23.4% for wet conditions was achieved with a pressure drop penalty smaller than 7%. It was concluded that vortex generation provided an improved thermal-hydraulic performance in the compact heat exchangers for an automotive system.

Joardar and Jacobi [30] experimentally evaluated the potential of winglet type vortex generator (VG) arrays, for air-side heat transfer enhancement, by full scaled wind tunnel testing of a plain fin and tube heat exchanger. The effectiveness of a 3VG alternate-tube inline array of vortex generators was compared to a single-row vortex generator design and the baseline configuration.

#### **2.1.4 Combinations of different roughness elements**

Jaurker et al. [31] experimentally investigated heat transfer and friction characteristics of rib-groove roughened rectangular duct. The effect of relative roughness pitch, relative roughness height and relative groove position on the heat transfer coefficient and friction factor had been studied. The presence of rib-grooved artificial roughness yielded Nusselt number and friction factor up to 2.7 and 3.6 times, respectively compared to smooth absorber plate. The maximum heat transfer occurred for a relative roughness pitch of about 6 and relative groove position of 0.4. Correlations for Nusselt number and friction factor were developed.

Layek et al. [32] carried out an experimental investigation to study heat transfer and friction for repeated transverse compound rib-groove arrangement on absorber plate of a solar air heater. The relative rib-groove positions of 0.3 - 0.6 were investigated for fixed relative roughness height and relative roughness pitch of 0.03 and 10, respectively. They found that corresponding to relative roughness pitch of 10, relative groove position of 0.4 provided about 2.42 and 2.6 times increase in the Nusselt number and friction factor, respectively. Correlations for Nusselt number and friction factor were developed.

Varun et al. [33] carried out an experimental study on heat transfer and friction characteristics by using a combination of inclined and transverse ribs on the absorber plate of a solar air heater with Reynolds number of 2,000 - 14,000, relative roughness pitch of 3.8, relative roughness height of 0.03, duct aspect ratio of 10 and roughness height of 1.6 mm. for relative roughness pitch of 8, the best thermal performance was reported. Correlations for Nusselt number and friction factor were developed.

Promvonge et al. [34] proposed the combined ribs and winglet type vortex generators (WVGs) to enhance the heat transfer on forced convection. They conducted the experiments to study heat transfer and friction loss behaviors. The isosceles triangle shape ribs were placed inside the opposite channel walls to create a reverse flow. Two pairs of the WVGs with various attack angles of 60°, 45°, and 30° were also mounted on the entrance to create a longitudinal vortex flow through the test channel. They found that the values of Nusselt number and friction factor for utilizing both the ribs and the WVGs were found to be considerably higher than those for using the rib or the WVGs alone. The larger the attack angle value led to higher

heat transfer and friction loss than the lower one. The in-line rib with the WVGs provided the higher heat transfer and friction loss than the staggered one. In common with the WVGs, the in-line rib yields the highest increase in both Nusselt number and friction factor. The rib with staggered array shows better thermal performance than the others.

## 2.2 Numerical heat transfer enhancement of air flow

Patankar et al. [35] reported the first work on the numerical analysis of flow and forced convective heat transfer in a duct. They also presented the concept of periodically fully developed flow. Webb and Ramadhyani [36] investigated the fluid flow and heat transfer in a parallel plate channel with staggered baffles. Their computational model was based on the periodically fully developed flow conditions proposed by Patankar.

Cheng and Huang [37] analyzed laminar forced convection flows in the entrance region of a horizontal channel. Computations for the semi-infinite channel within which one or two pairs of baffles were symmetrically attached to the respective walls in the entrance region were performed. Cheng and Huang [38] investigated the case where the transverse baffles are not symmetrically placed. Their results indicated that the relative position of the baffle arrays is an influential factor on the flow field, especially for baffles with a large height.

Biswas and Chattopadhyay [39] further extended this numerical model by including a hole under the delta wing for forced convection heat transfer. A comparison of the results was performed by varying a number of design parameters such as (channel dimensions, wing dimensions, angle of attack, placement, etc.). For a long channel at Reynolds number of 500, with a wing at an angle of attack  $26^\circ$  having no hole underneath it, the average Nusselt number increased by 34% while the friction factor increased by 79% over the plain channel geometry. For otherwise same conditions with a hole under the wing, the average Nusselt number increased by 10% and the friction factor increased by 48% over the plain channel geometry.

Brockmeier [40] made a comparative assessment of five different heat transfer configurations for operation in the compact heat exchangers. Two plain fins (rectangular fins and triangular fins), an offset strip and louvered fin geometry and one surface with wing type vortex generator mounted (attached) on the surface plate were considered. It was reported that the vortex generator surface provided the least heat exchanger surface area. The stamping was not considered in this geometry.

Zhu et al. [41] presented simulations of a delta wing, a rectangular wing, a delta winglet pair, and a rectangular winglet pair in a developing turbulent channel flow. The computational results showed the overall heat transfer enhancements of

16 - 19%. There was 300 - 400% increase in the flow loss. It was concluded that the heat transfer augmentation in turbulent channel flows with longitudinal vortex generators is caused by an elevation of the turbulent kinetic energy level near the wall and an exchange of fluid in the near wall and core regions of the channel. They found that the location of the vortex depends on the generator size and geometry, and it was more useful to generate a vortex near the wall so that it disturbs the laminar sublayer. They also presented computations on three-dimensional turbulent flows and heat transfer in a rectangular channel with rows of longitudinal vortex generators on one wall and distributed rib-roughness elements on the other wall modeled by the  $k - \varepsilon$  model and law of the wall [42]. The rectangular winglets were used as vortex generators. Flow structure and heat transfer was analyzed. It was found that the combined effect of rib-roughness and vortex generators enhanced the average Nusselt number by nearly 450% at Reynolds number of 150,000.

Biswas et al. [43] predicted the laminar flow and heat transfer characteristics in a rectangular channel containing built-in vortex generators. They used both the wing and winglet-pair. They concluded that the winglet was more attractive augmentation technique. Next, they numerically investigated the staggered array of tube rows with a punched-out delta winglet pair [44]. They reported that the local heat transfer was found to increase by more than 240% at a location about 12 times the channel height downstream of the inlet. After that, they also numerically investigated the flow structure and heat transfer of a built-in-winglet type vortex generator [45]. The computed flow structure was compared with the experimentally obtained flow structure measured by hot-wire-anemometer. The performance was summarized and observed that the performance of the winglet was best for an angle of attack 15°.

The hydraulic and thermal effects of placing normal baffles inside a three-dimensional channel were studied numerically by Lopez et al. [46]. A numerical investigation of laminar forced convective heat transfer was performed in a three-dimensional channel with baffles in which a uniform heat flux was applied to the top and bottom walls, and the sidewalls were considered adiabatic. They presented that three-dimensional effects on the friction factor of a channel with unity aspect ratio and a blockage ratio of 0.5 increased with an increasing in Reynolds number.

Guo and Anand [47] studied the three-dimensional heat transfer in a channel with a single baffle in the entrance region. Yang and Hwang [48] performed an interesting work to consider both solid and porous baffles in a two dimensional channel for the turbulent flow regime and reported their results for both the solid and porous cases. Bazdid-Tehrani and Naderi-Abadi [49] presented a numerical solution for the fluid flow and heat transfer in a duct with inline baffles. They

reported that the heat transfer behavior of this type of baffles is somewhat inefficient for large values of the blockage ratio.

Mousavi and Hooman [50] studied the fluid flow and heat transfer in a rectangular channel with segmented baffles that are staggeringly arranged on both the top and bottom walls of the channel. Their results were reported for fixed baffle spacing and different values of Reynolds number, blockage ratio and Prandtl number. They found that the Reynolds number is influential on the location of the periodically fully developed condition, as well as the blockage ratio. These two parameters were found to affect the development in such a way that increasing any of the two can postpone the development and consequently increase the Nusselt number since the flow reattachment to the channel wall causes the washing of the wall and, hence, results in greater values of the local Nusselt number. They indicated that not only the two aforementioned parameters but also the Prandtl number should be taken into account for determining the precise location of the fully developed region and the higher the Prandtl number is, the longer the entry length will be. Also, the results were observed that while increasing the Reynolds number and the blockage ratio increases the Nusselt number, it simultaneously increases the pressure drop. It was observed that moving from blockage ratios nearly equal to 0.25 to those of 0.5 will lead to significant changes in both friction factor and the Nusselt number.

Chaube et al. [51] carried out a computational analysis using FLUENT software to investigate the flow and heat transfer characteristics of two-dimensional rib roughened rectangular ducts with one wall subjected to uniform heat flux of  $1,100 \text{ W/m}^2$ . They compared the predictions of different turbulence models with experimental results available in the literature and reported good matching of experimental results and predictions of shear stress transport (SST)  $k - \varepsilon$  turbulence model. They used SST  $k - \varepsilon$  turbulence model for analyzing the performance of nine different roughness elements and compared the predictions on the basis of heat transfer enhancement, friction characteristics and performance index. The results obtained from two-dimensional model were reported to be closer to the experimental results and these models required less memory and computational time as compared to three-dimensional models. The highest heat transfer was reported in case of chamfered ribs, however, the best performance index was found to be with rectangular rib of size  $3 \times 5 \text{ mm}^2$  within the range of parameters investigated.

Wu and Tao [52] performed a numerical simulation on laminar flow heat transfer on a fin and tube surface with vortex generators for Reynolds numbers range of 800 to 2000 and angle of attack  $30^\circ$  and  $45^\circ$ . The results were analyzed from the

view point of the field synergy principal. The delta winglet with an angle of attack  $45^\circ$  produced better heat transfer enhancement, with increased pressure drop.

Wu et al. [53] also presented numerical computation on laminar convection heat transfer in a rectangular channel with a pair of rectangular winglet type and longitudinal vortex generator punched out from the lower wall of the channel. They found that the punched holes had more heat transfer enhancement in the region near to the vortex generator and lower average flow frictional coefficient compared with the no-punched holes. The thickness of rectangular winglet caused less heat transfer enhancement in the region near to the vortex generator and almost had no significant effect on the total pressure drop of the channel. Longitudinal vortices improved the synergy between the velocity and temperature field in the large downstream region of the longitudinal vortex generator. Transverse vortices only improved the synergy in the region near the vortex generator. They also further presented the influence of the main parameters of the longitudinal vortex generator on the heat transfer enhancement and flow resistance in a rectangular channel [54]. They found that the increase of heat transfer enhancement was always accompanied with the decrease of field synergy angle between the velocity and temperature gradient when the parameters of longitudinal vortex generator were changed.

Chu et al. [55] numerically studied the heat transfer characteristics and fluid flow structure of fin-and-oval-tube heat exchangers with longitudinal vortex generators. They reported that the average Nusselt number for the three-row fin-and-oval-tube heat exchanger with longitudinal vortex generators increased by 13.6 - 32.9% and the corresponding pressure loss increased by 29.2 - 40.6%. They confirmed that the reduction of the intersection angle between the velocity field and the temperature field was one of the essential factors influencing the heat transfer enhancement. They found that the longitudinal vortex generator with downstream placement and angles of attack  $30^\circ$  provided the best heat transfer performance. They also numerically investigated the flow structure and heat transfer enhancement in a full scale fin and tube heat exchanger with a rectangular winglet pair [56]. They reported that the heat transfer coefficient increased when using their proposed winglets. The inline one row winglet pair obtained the best overall performance.

Promvonge et al. [57] presented a numerical investigation on periodic laminar flow and heat transfer behaviors in a three-dimensional isothermal wall square-channel fitted with  $45^\circ$  staggered V-Baffles. The V-baffles were mounted periodically and staggered to generate the vortex pair of main streamwise vortex flows. They reported that the optimum thermal performance was around 2.75 at relative baffle height of 0.2 with V-baffle pointing downstream. After that, they also

conducted a numerical investigation on periodic laminar flow of the 30° angled baffles [58]. The 30° angled baffles were mounted periodically and inline arrangement to generate a pair of streamwise counter-rotating vortex flows. They showed that the pair vortex flows helped to induce impinging flows over the baffle leading end side and the inter-baffle cavity walls resulting in drastic increase in heat transfer rate over the test channel. They reported that the maximum thermal enhancement factors for the baffle with pitch ratio of 2 were found to be about 4.0 at blockage ratio of 0.15.

## 2.3 Nanofluids

The recent development in nanotechnology has made the production of nanometer-size solid particles (1 - 100nm) properly possible. This advancement has generated the great interest in using the suspended solid nanoparticles as an additive to improve the thermal properties and also to enhance the heat transfer of the traditional working fluids. The concept of using nanofluids is to improve the thermal conductivity of the working fluids. Because the nanometer-size solid particles have higher thermal conductivity than the ordinary fluids, the suspended nanoparticles in the base fluids can improve the thermal conductivity of the working fluids.

This section briefly describes the preparation of nanofluids. Nevertheless, for the computational purpose, the reviews focus mainly on the development of mathematical models to estimate the thermophysical properties of nanofluids and also emphasizes on the forced convective heat transfer enhancement using potential nanofluids.

### 2.3.1 Synthesis of nanofluids

In the experimental study, the preparation of nanofluids requires special techniques since the nanofluids are not simply solid-liquid mixtures. In general, the synthesis of nanofluids is divided into two methods. There are the two-step and the single-step methods [3].

The two-step method is widely used in preparation of nanofluids. In this method, the first step is to produce the nanometer-size solid particles such as  $\text{Al}_2\text{O}_3$ ,  $\text{CuO}$ ,  $\text{TiO}_2$ ,  $\text{SiC}$ ,  $\text{TiC}$ ,  $\text{Ag}$ ,  $\text{Au}$ ,  $\text{Cu}$ , and  $\text{Fe}$  in the powder forms. The examples of technique used to make the nanopowders are the inert-gas condensation (IGC) process, the direct evaporation condensation (DEC) method, the laser vapor deposition method, and the multi-walled carbon nanotubes (MWCNTs). By using these techniques, the nanopowders can be produced in mass quantities. The second step is to disperse the nanoparticles into the base fluids such as water, ethylene glycol (EG), oils, etc. In the synthesis of nanofluids, the tendency to form agglomerates is a major problem. Therefore, the ultrasonic equipment is often used

and regularly combined with stabilizing agents to thoroughly disperse the nanoparticles and also reduce the agglomeration.

The single-step method is directly producing nanofluids to reduce the chance of agglomeration. An example of this method is the single-step direct evaporation approach which the metallic vapor is directly condensed into nanoparticles by contact with a flowing low-vapor-pressure liquid such as ethylene glycol. This method is used to produce the metallic nanofluids. However, due to its complication, the single-step method is currently not suitable for mass production.

### 2.3.2 Thermophysical properties of nanofluids

Many experimental and theoretical studies have been conducted to predict the thermal conductivity of nanofluids. In the experimental, the transient hotwire method, the steady-state parallel-plate technique and the temperature oscillation technique are employed to measure the thermal conductivity of nanofluids. In the theoretical, the Maxwell model is the first model to estimate the effective thermal conductivity of solid-liquid mixtures given for micro/millimeter-size particles suspended in the base fluids [59]. Hamilton and Crosser model further extended the Maxwell model for non-spherical particles by combine the shape factor into the model. However, these models fail to predict the thermal conductivity of nanofluids because they were developed to predict the thermal conductivity of micro/millimeter-size particles suspended in the base fluids.

Many researchers proposed the theoretical models to explain and predict the thermal conductivity of nanofluids. For instance, Yu and Choi model further modified Hamilton and Crosser model to include the effect of interfacial layer surrounding the nanoparticles [60]. Koblinski et al. [61] explored the possible explanations for anomalous increase of the thermal conductivity of nanofluids. There were the Brownian motion of particles, molecular level layering of the fluid at the solid-liquid interface, the nature of heat transport in nanoparticles, and the effects of nanoparticle clustering. Recently, Khoo and Kleinstreuer [62] developed a model to estimate the effective thermal conductivity. The model included the effects of particle size, particle volume fraction, and temperature dependence as well as the properties of base fluids and the Brownian motion effect.

Only few investigations have been presented on viscosity of nanofluids. For example, Chandrasekar et al. [63] observed the Newtonian behavior in  $\text{Al}_2\text{O}_3$ -water nanofluid. Longo and Zilio [64] observed the Newtonian behavior in the investigated ranges of temperature (1 - 40°C) and particle volume fraction (1 - 6%). Chen et al. [65] reported the Newtonian behavior at room temperature for nanoparticle volume fraction less than 1.5%. Nguyen et al. [66] conducted experimental study the viscosity of  $\text{Al}_2\text{O}_3$ -water and CuO-water nanofluids under ambient conditions with

different volume fractions and particle diameters. Recently, Corcione [67] proposed an empirical correlation to determine the effective dynamic viscosity related to nanoparticle volume fraction, nanoparticle diameter and equivalent diameter of base fluids.

### 2.3.3 Heat transfer enhancement of nanofluids flow

Pak and Cho [68] conducted an experiment to investigate the convective turbulent heat transfer characteristics of  $\gamma\text{-Al}_2\text{O}_3$ -water and  $\text{Ti}_2\text{O}$ -water with volume concentration 1 - 3%. They found that the heat transfer coefficient increased with an increasing volume concentration and Reynolds number. Xuan and Li [69] carried out an experiment to study the single-phase heat transfer of Cu-water nanofluid in tubes with volume concentration 0.3 - 2.0% and varying Reynolds number between 10,000 and 25,000. They showed that the convective heat transfer coefficient increased considerably with volume concentration and Reynolds number with a negligible penalty in pumping power.

Zhou [70] studied the single-phase heat transfer enhancement of Cu-acetone particles had averaged sizes 80 to 100nm and concentrations of 0.0 to 4.0 g/l with and without acoustic cavitation. He indicated that the copper nanoparticles and acoustic cavitation had significant influence on heat transport in the fluid. Yang et al. [71] studied the convective heat transfer of graphite nanoparticles dispersed in liquid in laminar regime. They reported that at 2.5 wt% the heat transfer coefficient of nanofluids increased 22 and 15% compared with base fluid at 50 and 70°C, respectively.

Wen and Ding [72] carried out an experiment on  $\text{TiO}_2$ -water nanofluid with volume fraction 0 - 1%. They used two horizontally positioned aluminum discs with 10 mm gap filled with nanofluid. The lower disc was heated at the bottom surface and the upper surface was opened to the atmosphere. They reported that the time to reach steady-state was shorter compared to micro-size particles. The heating surface was found to increase with nanoparticle concentrations. Heris et al. [73] investigated the laminar convective heat transfer of  $\text{Al}_2\text{O}_3$ -water under constant wall temperature with volume concentration 0.2 - 2.5% for Reynolds number ranging between 700 and 2050. They reported that the heat transfer coefficient increased with an increase in particle volume concentration.

Duangthongsuk and Wongwises [74] presented the heat transfer enhancement of  $\text{TiO}_2$ -water at low volume concentration of 0.2%. They [75] also conducted an experiment to study the forced convective heat transfer using  $\text{TiO}_2$ -water with volume concentration of 0.2% and particle size of 21nm under varied heat flux conditions in a double-tube counter flow heat exchanger. They reported that the convective heat transfer coefficient of nanofluid is higher than the base fluid

about 6 - 11%. They also observed that the use of oxide nanofluid had a little penalty in pressure drop.

Williams et al. [76] experimentally investigated the turbulent convective heat transfer behavior of alumina-water ( $\text{Al}_2\text{O}_3$ ) and zirconia-water ( $\text{ZrO}_2$ ) nanofluids in smooth horizontal tubes. They varied the flow rates, temperatures, heat fluxes, and particle concentrations. They compared the experimental data with predictions made using traditional single-phase convective heat transfer and viscous pressure loss correlations for fully-developed turbulent flow. They showed that the convective heat transfer and pressure loss behavior of the alumina-water and zirconia-water nanofluids can be predicted by the traditional correlations.

Fotukian and Esfahany [77] studied the turbulent convective heat transfer of very dilute CuO/water nanofluid. They reported that increasing the volume fraction of CuO particles in nanofluid had negligible effect on the heat transfer enhancement. Sajadi and Kazemi [78] experimentally investigated the turbulent heat transfer behavior of  $\text{TiO}_2$ -water nanofluid in a circular pipe. The volume fraction was less than 0.25%. They indicated that addition of small amounts of nanoparticles to the base fluid increased the heat transfer about 22% compared to base fluid.

Syam Sundar and Sharma [79] conducted an experiment to study the turbulent heat transfer and friction factor of  $\text{Al}_2\text{O}_3$ -water nanofluid in circular tube with different twist ratios in the range of  $0 < H/D < 83$ . The Reynolds number was ranging from 10,000 to 22,000. They reported that at volume concentration of 0.5% and twist ratio of 5, the heat transfer coefficient and friction factor increased 33.5% and 1.1 times compared with water, respectively. Wongcharee and Eiamsa-ard [80] studied the heat transfer and friction factor of CuO-water for volume concentration from 0.3% to 0.7% and Reynolds number from 830 to 1,990. The nanofluid was employed in a circular tube equipped with modified twisted tape having twisted ratio of 3 and with alternate axis.

Salman et al. [81] conducted a numerical study to examine the fluid flow and heat transfer characteristics in a two-dimensional microtube. They examined the effects of  $\text{Al}_2\text{O}_3$ , CuO,  $\text{SiO}_2$ , and ZnO nanoparticles suspended in ethylene glycol for the Reynolds number of 10-5,000 with concentration of 0 - 4% and the nanoparticle diameters of 25 - 85nm. They found that using  $\text{SiO}_2$ -ethylene glycol with volume concentration of 4% and nanoparticle diameter of 25nm at Reynolds number of 1,500 gave the highest heat transfer enhancement.

Mohammed et al. [82] numerically investigated the thermo-hydraulic performance of two-dimensional turbulent forced convective using nanofluids in a rib-groove channel. They reported that the  $\text{SiO}_2$ -glycerin gave the highest heat transfer coefficient. Abbasian Arani and Amani [83] experimentally studied the effect

of TiO<sub>2</sub>-water nanofluid on convective heat transfer and pressure drop. They varied the volume fraction between 0.002 and 0.02 and Reynolds number between 8,000 and 51,000 with fixed particle diameter of 30nm. They observed that by increasing volume fraction or Reynolds number, the Nusselt number increased. By used the nanofluid at Reynolds number greater than 30,000, more power needed to compensate the pressure drop of nanofluid but the Nusselt number were not obviously changed.

In the case of numerical study on nanofluids, some studies considered nanofluids as single-phase homogeneous mixtures, while others used the two-phase approaches. Lotfi et al. [84] compared the single-phase with the Mixture and Eulerian two-phase models for forced convection flow of Al<sub>2</sub>O<sub>3</sub>-water nanofluid with temperature independent properties. They compared the Nusselt number predictions for volume concentration of 1% with several correlations and a set of experimental values. Based on their available data, they concluded that the Mixture model was more precise than other two models. They also observed that the single-phase and the Eulerian two-phase models underestimated the Nusselt number.

Akbari et al. [85] conducted a numerical analysis to compare the single-phase model and the three different two-phase models (VOF, Mixture, and Eulerian) of laminar mixed convection of Al<sub>2</sub>O<sub>3</sub>-water nanofluid. They found that all models predicted almost identical hydrodynamic fields but different in the thermal results. They reported that, for the considered problem, the two-phase models gave closer predictions to the available experimental data than the single-phase model. However, the two-phase models over predicted the heat transfer coefficients. They also suggested that these models are still needed to compare with other experimental data for different flow conditions.

Next chapter details the mathematical formulations deployed to govern a numerical model. The governing equations used behind the numerical simulation are described. The turbulence model and the finite volume method employed in the computations are also introduced. The boundary conditions are prescribed. The solution algorithm, the numerical solution procedure, and key quantifying performance factors are described. The mathematical models to specify the thermophysical properties of nanofluids are also explained.

## CHAPTER 3

# MATHEMATICAL FORMULATION

This chapter details the mathematical formulations exploited to construct and solve a numerical simulation of fluid flow and heat transfer. First, the governing equations derived from the basic conservation laws are described. The turbulence model used in the computation is introduced to represent the characteristics of the turbulent flow. Then, the finite volume method is briefly explained to solve the algebraic equations which were discretized from the governing equations. The boundary conditions as the essential components of the numerical simulation are prescribed. Next, the solution algorithm and solution procedure employed in this study are also described. The key quantifying parameters are defined to evaluate the thermal performances. Finally, the mathematical models for determining the thermophysical properties of nanofluid are also included.

### 3.1 Governing equations

The governing equations are fundamental for a numerical simulation of the fluid flow and heat transfer problem. These equations represent the mathematical statements of the principle conservation laws of physics. For an incompressible viscous fluid, the governing equations were derived from the conservation of mass, the conservation of momentum, and the conservation of energy.

In the present study, a numerical simulation of fluid flow and heat transfer in a channel was developed under the following major assumptions:

- Steady three-dimensional fluid flow and heat transfer.
- Turbulent and incompressible flow.
- Negligible body forces.
- Negligible viscous dissipation.
- Negligible radiation heat transfer.
- No thermal energy sources within the fluid.

#### 3.1.1 Conservation of mass

The conservation of mass equation or the continuity equation was derived by a mass balance of a fluid element entering and exiting a control volume in a flow field. The mass of a fluid must be conserved. The matter cannot be created or destroyed. The net rate of a mass that enters a differential control volume must equal zero. For a three-dimensional and incompressible fluid flow (constant density), the conservation of mass equation can be derived to

$$\frac{\partial \rho}{\partial t} + \text{div}(\rho \mathbf{U}) = 0 \quad (3.1)$$

Where  $\mathbf{U}$  is the velocity vector has the velocity components of  $u$ ,  $v$ , and  $w$  in the  $x$ ,  $y$ , and  $z$  directions, respectively.

### 3.1.2 Conservation of momentum

The conservation of momentum equations were derived using Newton's second law of motion. This law states that the external forces acting on a body in a given direction is equal to the mass times the acceleration in the same direction. The external forces are classified as surface forces and body forces. The surface forces are from the stresses acting on the control volume surface. The body forces include gravitational forces, magnetic and electric fields acting on the body of fluid. For a three-dimensional and incompressible fluid flow, the conservation of momentum equations in terms of velocity gradients can be derived to each direction as following equations.

x-momentum:

$$\frac{\partial(\rho u)}{\partial t} + \text{div}(\rho u \mathbf{U}) = -\frac{\partial P}{\partial x} + \text{div}(\mu \text{grad } u) \quad (3.2)$$

y-momentum:

$$\frac{\partial(\rho v)}{\partial t} + \text{div}(\rho v \mathbf{U}) = -\frac{\partial P}{\partial y} + \text{div}(\mu \text{grad } v) \quad (3.3)$$

z-momentum:

$$\frac{\partial(\rho w)}{\partial t} + \text{div}(\rho w \mathbf{U}) = -\frac{\partial P}{\partial z} + \text{div}(\mu \text{grad } w) \quad (3.4)$$

The terms on the left-hand side of the conservation of momentum equations are the rates of change of momentum and the inertia forces. The first term on the right-hand side is the pressure force and the second term within the bracket is the viscous forces. For the present study, the body force acting on the fluid element was negligible. Hence, there is no source term in the conservation of momentum equations.

### 3.1.3 Conservation of energy

The conservation of energy equation can be derived using the first law of thermodynamics for a differential control volume in a flow field. This law expresses that the rate of change of energy is equal to the sum of the rate of heat addition to

and the rate of work done on a fluid particle. For a three-dimensional and incompressible fluid flow, the conservation of energy equation can be derived to

$$\frac{\partial(\rho i)}{\partial t} + \text{div}(\rho i \mathbf{U}) = \text{div}(k \text{ grad } T) + \Phi \quad (3.5)$$

Where  $i$  is the internal energy of the control volume ( $i = c_v T$ ). The viscous dissipation ( $\Phi$ ) was defined as

$$\Phi = \mu \left\{ 2 \left[ \left( \frac{\partial u}{\partial x} \right)^2 + \left( \frac{\partial v}{\partial y} \right)^2 + \left( \frac{\partial w}{\partial z} \right)^2 \right] + \left( \frac{\partial u}{\partial y} + \frac{\partial v}{\partial x} \right)^2 + \left( \frac{\partial u}{\partial z} + \frac{\partial w}{\partial x} \right)^2 + \left( \frac{\partial v}{\partial z} + \frac{\partial w}{\partial y} \right)^2 \right\} \quad (3.6)$$

The left-hand side of the energy equation represents the convective heat transfer. The first term on the right-hand side represents the conductive heat transfer. The second term represents the viscous dissipation owing to friction in the fluid which may usually be neglected except in systems with large velocity gradients [1]. Therefore, the energy equation can be simplified to

$$\frac{\partial(\rho i)}{\partial t} + \text{div}(\rho i \mathbf{U}) = \text{div}(k \text{ grad } T) \quad (3.7)$$

In numerical simulation, these partial differential equations as the governing equations were integrated over all of the control volumes in the region of interest or the computational domain. This is equivalent to applying the basic conservation laws to each control volume. The discretization approach is described in subsequent section of the finite volume method.

### 3.2 Turbulence modeling

The fluid flows are considered as laminar at low Reynolds numbers. When Reynolds number increases, flows are observed to become turbulent. The turbulent flows are characterized by a highly unsteady and random state of three-dimensional motion which the velocity and pressure change continuously on a broad range of time and length scales [86]. A typical one-dimensional velocity of turbulent flow can be illustrated in Figure 3.1. The term  $u'(t)$  is the instantaneous velocity at time  $t$ . Denoted  $U$  is an averaged flow velocity over time.

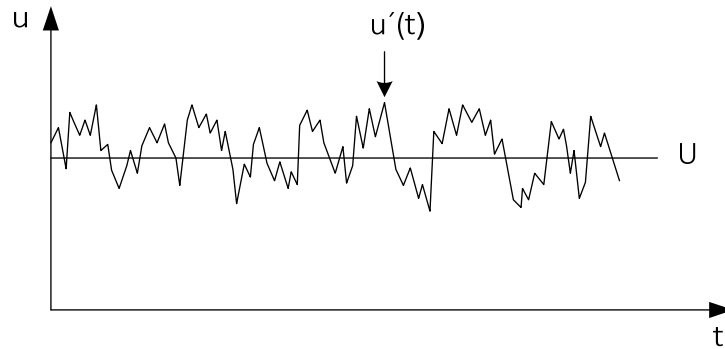


**Figure 3.1** A typical velocity of one-dimensional turbulent flow

There are many approaches to numerically predict the turbulent flows such as Reynolds-averaged Navier-Stokes (RANS), direct numerical simulation (DNS), and large eddy simulation (LES). Each method requires different computational efforts and time. In the present study, the RANS approach was employed to simulate the turbulent flow.

### 3.2.1 Reynolds-averaged Navier-Stokes (RANS)

The turbulent flow can be predicted by an approximation method. This method is based on averaging the equations of motion over time by assumed that the flow is statistically steady. This time-averaging method is appropriate for stationary turbulence which the mean flow velocity does not vary with time. By averaging, all of unsteadiness in the flow is regarded as a part of the turbulence. This approach leads to a set of partial differential equations which are called the Reynolds-averaged Navier-Stokes (RANS) equations. In a statistically steady flow, every variable can be written as the sum of a time-averaged component,  $\bar{\varphi}$  and a fluctuating component,  $\varphi'(t)$  with zero mean value as expressed in following equation.

$$\varphi(t) = \bar{\varphi} + \varphi'(t) \quad (3.8)$$

The time-averaged component is defined as

$$\bar{\varphi} = \lim_{T \rightarrow \infty} \frac{1}{T} \int_0^T \varphi(t) dt \quad (3.9)$$

Here  $t$  is the time and  $T$  is the averaging time interval. This interval must be large enough compared to the typical time scale of the fluctuations. Therefore, the component  $\bar{\varphi}$  does not depend on the time that the averaging is started. However,

if the flow is unsteady, the ensemble averaging method is used instead. The ensemble averaging is expressed as

$$\bar{\varphi} = \lim_{N \rightarrow \infty} \frac{1}{N} \sum_{n=1}^N \varphi(t) \quad (3.10)$$

Where  $N$  is number of members of the ensemble and  $N$  must be large enough to eliminate the effects of the fluctuations [86]. The ANSYS Fluent employs this ensemble averaging method. Nevertheless, technically, by applying either averaging methods to the Navier-Stokes equations yields the Reynolds-averaged Navier-Stokes (RANS) equations.

### 3.2.2 The law of the wall

For the flow in a channel, the characteristics of turbulent flow near solid wall are significantly different from the free turbulent flow because of the presence of solid boundary. In the flow far away from the wall, the inertia forces are larger than the viscous forces. To examine the near wall characteristics, a Reynolds number based on a distance  $y$  away from the wall is formed as  $\mathbf{Re}_y = Uy/\nu$ . As the distance  $y$  is decreased to zero, a Reynolds number based on  $y$  will also reduce to zero. At the distance  $y$  very close to zero, the viscous forces will be larger or equal to the inertia forces. Therefore, the flow at the near wall region is mainly influenced by viscous effects. The mean flow velocity depends only on the distance  $y$  from the wall, fluid density, fluid viscosity, and the wall shear stress. From dimensional analysis, the law of the wall is defined as

$$u^+ = \frac{U}{u_\tau} = f\left(\frac{\rho\tau_w y}{\mu}\right) = f(y^+) \quad (3.11)$$

Where  $\tau_w$  is the wall shear stress and the appropriate velocity scale or the friction velocity is defined as  $u_\tau = \sqrt{\tau_w/\rho}$ .

Figure 3.2 exhibits a typical velocity profile for a turbulent boundary layer. The graph shows the dimensionless velocity  $u^+$  and distance normal to the wall  $y^+$ . The fluid is stationary at the solid wall surface. The fluid's behavior closest to the wall is dominated by the viscous effects. In practice, this viscous sublayer is extremely thin ( $y^+ < 5$ ). The shear stress is approximately constant and equal to the wall shear stress throughout the layer. This region is also called linear sublayer since the velocity  $u^+$  is equal to the distance  $y^+$ . In the viscous sublayer, the relationship between  $u^+$  and  $y^+$  is expressed as

$$u^+ = y^+ \quad (3.12)$$

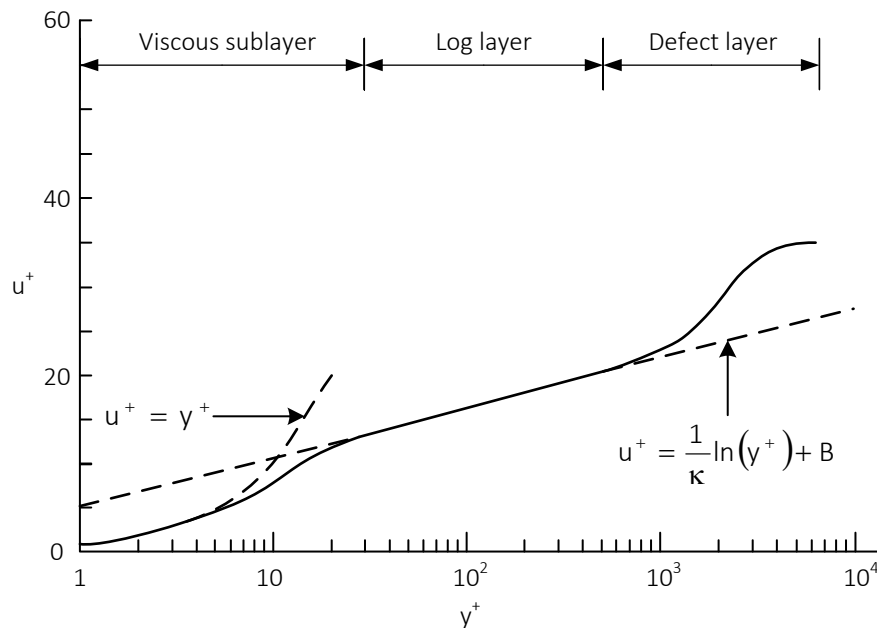


**Figure 3.2** A typical velocity profile for a turbulent boundary layer

Next to the viscous sublayer ( $30 < y^+ < 500$ ), there is a region where viscous and turbulent effects are both important. The shear stress varies slowly with distance from the wall. The shear stress is almost constant and equal to the wall shear stress. A functional relationship between  $u^+$  and  $y^+$  can be derived to

$$u^+ = \frac{1}{\kappa} \ln(y^+) + B \quad (3.13)$$

Where  $\kappa$  is Kármán's constant ( $\kappa \approx 0.4$ ) and  $B$  is an empirical constant related to the thickness of the viscous sublayer ( $B \approx 5.5$ , for smooth surface). Because of the logarithmic relationship, this region is often called the log-law layer. Furthermore, outside the log-law layer, there is a region where the core flow far from the wall is dominated by inertia forces. The flow is free from viscous effects. This outer region is called defect layer or law-of-the-wake layer.

### 3.2.3 The RNG $k - \varepsilon$ model

The turbulence models are introduced to represent the characteristics of turbulence. They are employed to compute the turbulent flows with the RANS equations. The turbulent models are used to predict the Reynolds stresses and the scalar transport terms and to close the system of mean flow equations. For each

turbulent model, additional transport equations are needed to be solved along with the RANS equations. The  $k - \varepsilon$  model is the most popular two-equation model which considering the dynamics of turbulence, production and destruction of turbulence as closures to complete the turbulence model [87]. The turbulent kinetic energy ( $k$ ) is production term and the viscous dissipation ( $\varepsilon$ ) is destruction term in the turbulent kinetic energy equation. The  $k - \varepsilon$  model focuses on the mechanisms that affect the turbulent kinetic energy. The instantaneous kinetic energy,  $k(t)$  of a turbulent flow is the sum of the mean kinetic energy,  $K = \frac{1}{2}(U^2 + V^2 + W^2)$  and the turbulent kinetic energy,  $k = \frac{1}{2}(\overline{u'^2} + \overline{v'^2} + \overline{w'^2})$  as expressed in the following equation.

$$k(t) = K + k \quad (3.14)$$

The turbulent model used in the present study was the renormalization group (RNG)  $k - \varepsilon$  model. The RNG  $k - \varepsilon$  model was devised by Yakhot and Orszag in 1992 using a statistical technique called renormalization group theory. The RNG  $k - \varepsilon$  model is more accurate and reliable for a wide range of flows than the standard  $k - \varepsilon$  model. The RNG procedure systematically removes the small scales of motion from the governing equations by expressing their effects in terms of larger scale motions and a modified viscosity. The RNG  $k - \varepsilon$  model equations are expressed as following equations [88].

$$\frac{\partial(\rho k)}{\partial t} + \text{div}(\rho k \mathbf{U}) = \text{div}[\alpha_k \mu_{eff} \text{grad } k] + \tau_{ij} \cdot S_{ij} - \rho \varepsilon \quad (3.15)$$

$$\frac{\partial(\rho \varepsilon)}{\partial t} + \text{div}(\rho \varepsilon \mathbf{U}) = \text{div}[\alpha_\varepsilon \mu_{eff} \text{grad } \varepsilon] + C_{1\varepsilon}^* \frac{\varepsilon}{k} \tau_{ij} \cdot S_{ij} - C_{2\varepsilon} \rho \frac{\varepsilon^2}{k} \quad (3.16)$$

Where the Reynolds stresses,  $\tau_{ij} = -\rho \overline{u'_i u'_j} = 2\mu_t S_{ij} - \frac{2}{3}\rho k \delta_{ij}$ , the effective viscosity,  $\mu_{eff} = \mu + \mu_t$ , the eddy viscosity,  $\mu_t = \rho C_\mu \frac{k^2}{\varepsilon}$ , and the model constants,  $C_\mu = 0.0845$ ,  $\alpha_k = \alpha_\varepsilon = 1.39$ ,  $C_{1\varepsilon}^* = 1.42$ ,  $C_{2\varepsilon} = 1.68$ , respectively.

The first terms on the left-hand side of RNG  $k - \varepsilon$  model equations are rate of change in  $k$  or  $\varepsilon$  and the second terms are transport of  $k$  or  $\varepsilon$  by convection. The right-hand side of equations comprises transport of  $k$  or  $\varepsilon$  by diffusion, rate of  $k$  or  $\varepsilon$  production, and rate of  $k$  or  $\varepsilon$  destruction, respectively.

### 3.3 Finite volume method

The governing equations in terms of partial differential equations are transformed into discrete algebraic equations. The solution of discretized equations produces a set of values corresponding to the solution of the original equations. The discretization process can be divided into two steps which are the discretization of the solution domain and the discretization of the governing equation.

The discretization of the solution domain produces a numerical description of the computational domain. This process is also known as grid generation. The space is divided into a finite number of discrete regions which called control volumes (CVs) or cells. For transient simulations, the time interval is also split into a finite number of time steps. The discretization of the governing equations altogether with the domain discretization produces an appropriate transformation of the governing equations into a system of discrete algebraic equations. Then, the set of algebraic equations can be solved using any direct or iterative method.

The generic conservation equation for an arbitrary quantity ( $\phi$ ) can be written in the vector form as following.

$$\mathbf{div}(\rho u \phi) = \mathbf{div}(\Gamma \mathbf{grad} \phi) + S_{\phi} \quad (3.17)$$

The left-hand side of the equation is the convective term. The right-hand sides are the diffusive term and the source term, respectively. The finite volume method uses the integral form of the conservation equation as the starting point. Therefore, formal integration over a control volume gives

$$\int_A (\rho \phi u) \cdot n dA = \int_A (\Gamma \mathbf{grad} \phi) \cdot n dA + \int_{CV} S_{\phi} dV \quad (3.18)$$

This integral equation represents the flux balance in a control volume. The left-hand side gives the net convective flux. The right-hand side comprises the net diffusive flux and the production and destruction of the quantity  $\phi$  within the control volume, respectively. The integral conservation equation is applied to each control volume and to the entire solution domain. The integral conservation equations for all control volumes are summed to obtain the global conservation equations.

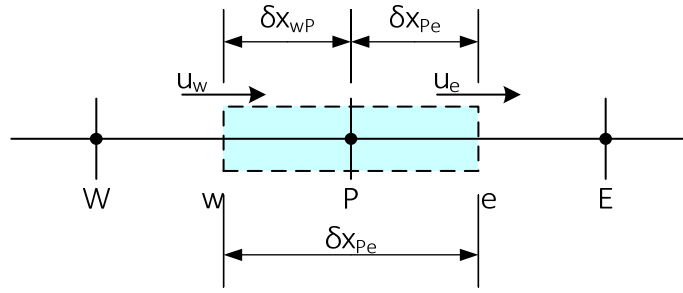


**Figure 3.3** A control volume around general node P

For simplicity, consider the one-dimensional control volume illustrated in Figure 3.3. Focusing on general node P, the neighboring nodes are identified by W and E nodes. The control volume faces are identified by w and e faces.

Integration of transport equation (Equation 3.17) over the control volume gives

$$(\rho u A \phi)_e - (\rho u A \phi)_w = \left( \Gamma A \frac{d\phi}{dx} \right)_e - \left( \Gamma A \frac{d\phi}{dx} \right)_w \quad (3.19)$$

Integration of continuity equation (3.1) yields

$$(\rho u A \phi)_e - (\rho u A \phi)_w = 0 \quad (3.20)$$

The variables  $F = \rho u$  and  $D = \Gamma / \delta x$  are defined to represent the convective mass flux per unit area and diffusion conductance at the cell faces, respectively. Assuming that the face area,  $A_w = A_e = A$ , the integrated convection-diffusion equation (Equation 3.19) can be written as

$$F_e \phi_e - F_w \phi_w = D_e (\phi_E - \phi_P) - D_w (\phi_P - \phi_W) \quad (3.21)$$

The integrated continuity equation (3.20) can be expressed as

$$F_e - F_w = 0 \quad (3.22)$$

Assuming that the velocity field is known and the quantity  $\phi$  at the e and w faces can be calculated, therefore the integrated convection-diffusion equation (Equation 3.21) can be solved.

### 3.3.1 The second order upwind scheme

The second order upwind (SOU) scheme was employed in the present study. The SOU scheme uses two-point upstream values to estimate the cell face values. The quantity  $\phi$  at cell faces between two bracketing nodes  $i$  and  $i-1$  and upstream node  $i-2$  can be estimated from the following expression.

$$\phi_{face} = \phi_{i-1} + \frac{1}{2}(\phi_{i-1} - \phi_{i-2}) \quad (3.23)$$

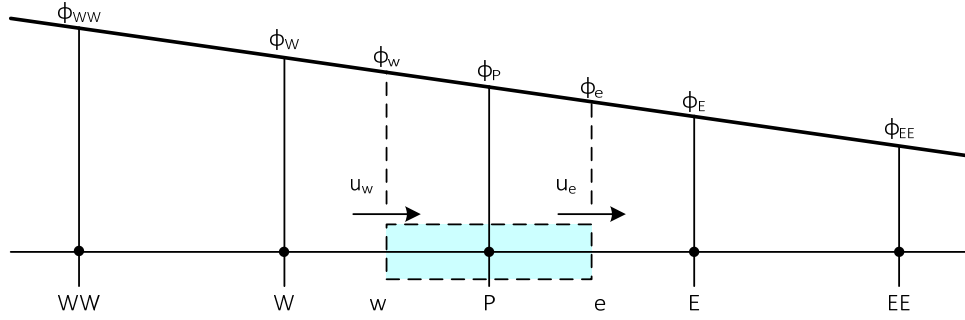


Figure 3.4 Linear profile used in the SOU scheme

For simplicity, the SOU scheme for one-dimensional convection-diffusion problem for a general node  $P$  is illustrated in Figure 3.4.

For positive flow,  $F_w > 0$  ( $u_w > 0$ ), the quantity  $\phi$  at the  $w$  face is

$$\phi_e = \phi_P + \frac{1}{2}(\phi_P - \phi_W) \quad (3.24)$$

When  $F_e > 0$  ( $u_e > 0$ ), the quantity  $\phi$  at the  $e$  face is

$$\phi_w = \phi_W + \frac{1}{2}(\phi_W - \phi_{WW}) \quad (3.25)$$

Substituting Equations 3.24 and 3.25 in the discretized convection-diffusion equation (Equation 3.21) and solving for central and neighboring coefficients, the quantity  $\phi$  at the cell faces can be calculated. The quantity  $\phi$  for negative flow directions can also be evaluated using the same method. The general SOU scheme for one-dimensional convection-diffusion problem can be expressed as

$$a_P \phi_P = a_W \phi_W + a_E \phi_E + a_{WW} \phi_{WW} + a_{EE} \phi_{EE} \quad (3.26)$$

The central and neighbor coefficients in Equation 3.26 can be estimated using the expressions in Table 3.1.

**Table 3.1** Central coefficient and neighbor coefficients for the SOU scheme

Central coefficient	Formula
$a_P$	$a_W + a_E + a_{WW} + a_{EE} + (F_e - F_w)$
Neighbor coefficients	Formula
$a_W$	$D_w + \frac{3}{2}\alpha_w F_w + \alpha_e F_e$
$a_{WW}$	$-\alpha_w F_w$
$a_E$	$D_e - \frac{3}{2}(1-\alpha_e)F_e - (1-\alpha_w)F_w$
$a_{EE}$	$(1-\alpha_e)F_e$
Note:	$\alpha_w = 1$ for $F_w > 0$ and $\alpha_e = 1$ for $F_e > 0$ $\alpha_w = 0$ for $F_w < 0$ and $\alpha_e = 0$ for $F_e < 0$

### 3.3.2 The QUICK scheme

The quadratic upstream interpolation for convective kinetics (QUICK) scheme introduced by Leonard in 1979 [88] was also employed in the present study. The QUICK scheme uses a three-point upstream-weighted quadratic interpolation for cell face values. The quantity  $\phi$  can be obtained from a quadratic function passing through two bracketing nodes on each side of the face and a node on the upstream side. For a uniform grid, the value of quantity  $\phi$  at the cell faces between two bracketing nodes  $i$  and  $i-1$ , and upstream node  $i-2$  can be estimated by

$$\phi_{face} = \frac{6}{8}\phi_{i-1} + \frac{3}{8}\phi_i - \frac{1}{8}\phi_{i-2} \quad (3.27)$$

For demonstration, the QUICK scheme for one-dimensional convection-diffusion problem for a general node  $P$  is illustrated in Figure 3.5. For positive flow,  $F_w > 0$  ( $u_w > 0$ ), the quantity  $\phi$  at the  $w$  face is

$$\phi_w = \frac{6}{8}\phi_W + \frac{3}{8}\phi_P - \frac{1}{8}\phi_{WW} \quad (3.28)$$

When  $F_e > 0$  ( $u_e > 0$ ), the quantity  $\phi$  at the  $e$  face is

$$\phi_e = \frac{6}{8}\phi_P + \frac{3}{8}\phi_E - \frac{1}{8}\phi_W \quad (3.29)$$

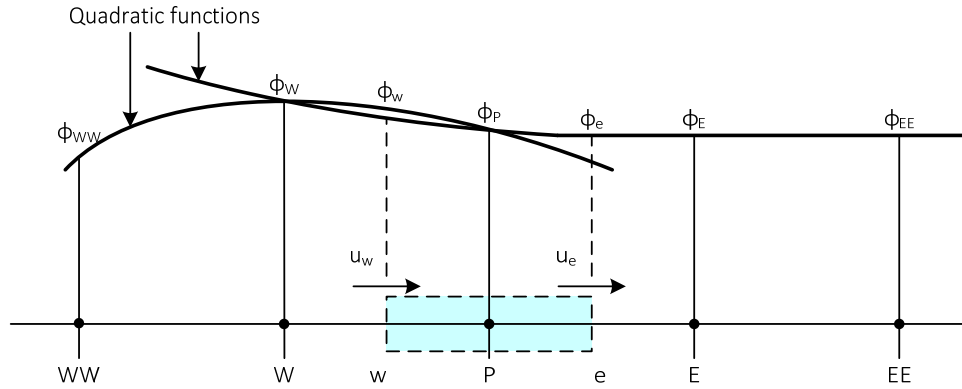


Figure 3.5 Quadratic profiles used in the QUICK scheme

Equations 3.26 and 3.27 were substituted in the discretized convection-diffusion equation (Equation 3.21) and solved for central and neighboring coefficients. Moreover, the quantity  $\phi$  for negative flow directions can be obtained using the same sequence. Therefore, the QUICK scheme for one-dimensional convection-diffusion problem can be expressed as

$$a_P \phi_P = a_W \phi_W + a_E \phi_E + a_{WW} \phi_{WW} + a_{EE} \phi_{EE} \quad (3.30)$$

The central and neighbor coefficients in equation 3.28 can be identified using the expressions in Table 3.2.

Table 3.2 Central coefficient and neighbor coefficients for the QUICK scheme

Central coefficient	Formula
$a_P$	$a_W + a_E + a_{WW} + a_{EE} + (F_e - F_w)$
Neighbor coefficients	Formula
$a_W$	$D_w + \frac{6}{8} \alpha_w F_w + \frac{1}{8} \alpha_e F_e + \frac{3}{8} (1 - \alpha_w) F_w$
$a_{WW}$	$-\frac{1}{8} \alpha_w F_w$
$a_E$	$D_e - \frac{3}{8} \alpha_e F_e - \frac{6}{8} (1 - \alpha_e) F_e - \frac{1}{8} (1 - \alpha_w) F_w$
$a_{EE}$	$\frac{1}{8} (1 - \alpha_e) F_e$
Note:	$\alpha_w = 1$ for $F_w > 0$ and $\alpha_e = 1$ for $F_e > 0$ $\alpha_w = 0$ for $F_w < 0$ and $\alpha_e = 0$ for $F_e < 0$

For the QUICK scheme, the cell face values of fluxes are always calculated by quadratic interpolation between two bracketing nodes and an upstream node. Since the scheme is based on a quadratic function, its accuracy in terms of Taylor series truncation error is third-order on a uniform mesh. The QUICK scheme has greater accuracy than the central differencing or hybrid schemes. Furthermore, the QUICK scheme is also suitable for quadrilateral and hexahedral meshes aligned with the flow direction.

### **3.4 Boundary conditions**

#### **3.4.1 Wall boundary condition**

The boundary conditions appropriate to a solid wall boundary must be specified for velocity and turbulence parameters. The wall boundary condition is treated between the fluid and solid regions. Since the viscous sublayer and buffer layer are extremely thin, the wall function which is a set of semi-empirical formulas must be used along with fine grid at the near-wall region [89]. In the present study, the no-slip condition was applied at the solid wall. The fluid velocity at the wall is equal to zero. For the RNG  $k - \varepsilon$  model, enhanced wall treatment method which combines the standard two-layer model with the enhanced wall function was also suggested to bridge the viscosity affected between the near-wall and the fully-turbulent regions.

#### **3.4.2 Periodicity**

The flow becomes periodical fully-developed in repetitive geometries. Since the geometry and arrangement of the sinusoidal wavy-baffle channel was successively repetitive, the flow became periodic far from the entrance region. The periodic boundary conditions were advisably used instead of inlet and outlet boundary conditions with a large number of repetitive modules. By using the periodic condition, the time and cost can be substantially saved for the computation of self-repeating modules. Therefore, the periodic module was used as the computational domain.

### **3.5 Solution algorithm**

#### **3.5.1 Pressure-velocity coupling with SIMPLE algorithm**

The pressure-based solver uses a solution algorithm to solve the governing equations. Since the governing equations are non-linear and coupled, the solution loop must be employed iteratively in order to obtain a converged numerical solution. The pressure-based segregated algorithm solves the individual governing equations sequentially for the solution variables as depicted in Figure 3.6. Since the governing

equations are solved in separated manner, the segregated algorithm is memory efficient. The discretized equations are stored in the memory one at a time.

The iteration procedure of the pressure-based segregated algorithm consists of the following steps.

1. Update fluid properties such as density, viscosity, specific heat, turbulent viscosity based on the current solution.
  2. Sequentially solve the momentum equations using the recently updated values of pressure and face mass fluxes.
  3. Solve the pressure correction equation using the recently obtained velocity field and the mass flux.
  4. Correct the face mass fluxes, pressure, and the velocity field using the pressure correction obtained from step 3.
  5. Solve the equations for additional scalars such as turbulent quantities and energy using the current values of the solution variables.
  6. Check for the convergence of the governing equations.
- These steps are continued until the convergence criteria are satisfied.

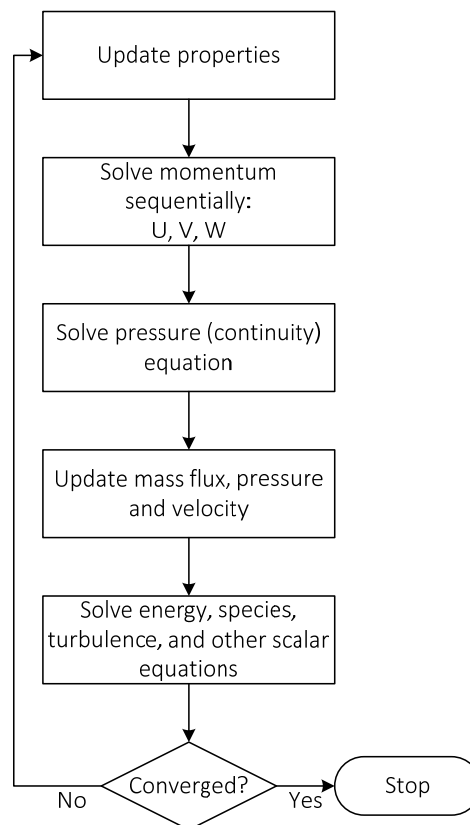


**Figure 3.6** Pressure-based segregated algorithm flowchart

The pressure-velocity coupling solver was employed with the SIMPLE (Semi-Implicit Method for Pressure Linked Equations) algorithm. The SIMPLE algorithm is a segregated algorithm that uses a relationship between velocity and pressure corrections to enforce the mass conservation and to obtain the pressure. The SIMPLE algorithm field as depicted in Figure 3.7 can be described as the following sequence.

1. Guess the pressure field.
2. Solve the momentum equations to obtain the velocity field.
3. Solve the pressure correction equation.
4. Calculate the new pressure from the pressure correction value.
5. Calculate the velocity field from their corrected values using the velocity correction formula. The corrected velocity field exactly satisfies the continuity equation.

6. Solve the discretization equation for other variables such as temperature and turbulence quantities if they influence the fluid properties.

Treat the corrected pressure as a new guessed pressure. Return to step 2 and repeat the whole procedure until the convergence criteria is satisfied.

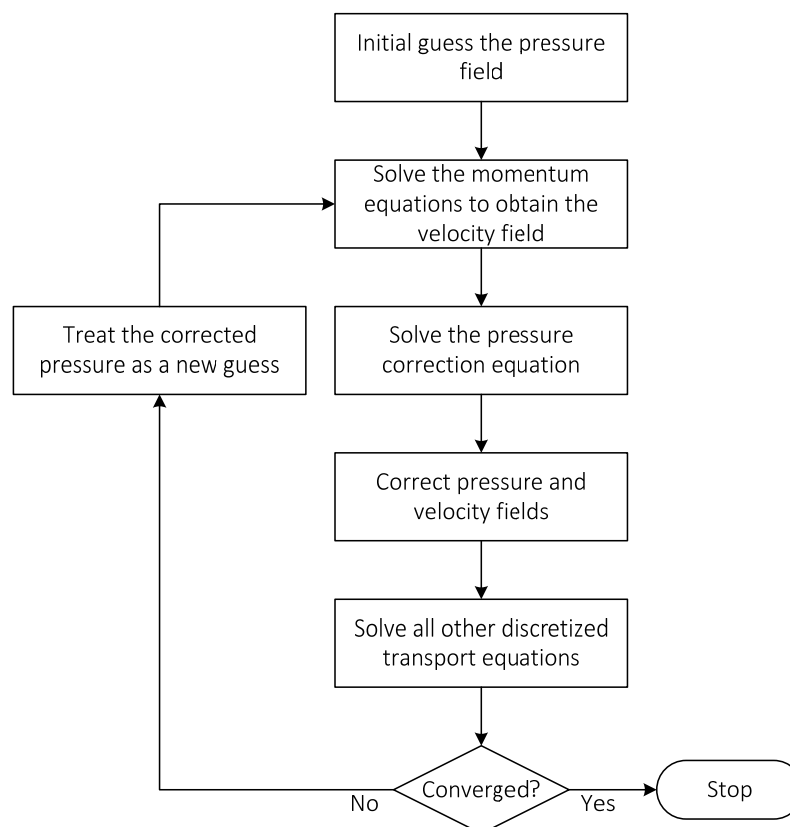


**Figure 3.7** Pressure-based segregated with SIMPLE algorithm flowchart

### 3.5.2 User-defined function

Since the thermophysical properties of nanofluids depend on the particle volume fraction and/or temperature, therefore the nanofluid properties cannot be assumed as constant thermophysical properties. Each thermophysical property must be estimated for each iterative calculation. The user-defined function (UDF) for calculating the nanofluid properties is introduced. The UDF is a C function that can be loaded dynamically in the ANSYS Fluent. The pressure-based segregated algorithm coupled with UDF is presented in Figure 3.8. An example of UDF code used to calculate the thermophysical properties of nanofluid in this study is provided in Appendix A.

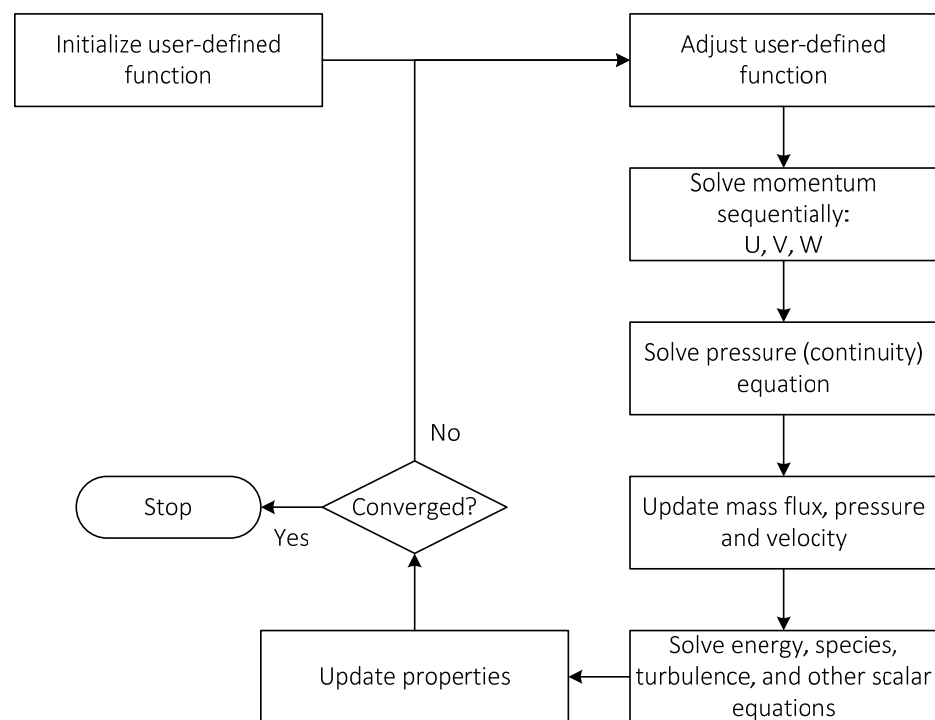


Figure 3.8 Pressure-based segregated with UDF function flowchart

### 3.5.3 Solution procedure

In the present study, the ANSYS Workbench was employed to numerically investigate the effects of sinusoidal wavy baffles on the heat transfer and fluid flow characteristics in a channel. First, the problem of interest and the assumptions were defined. Then, the computational domain and the boundary conditions were determined. The solid geometry of computational domain was constructed using the DesignModeler application. Next, the computational grid was generated using the Mesh application in the ANSYS Workbench. The turbulence model and the solution methods were established using the FLUENT application in the ANSYS Workbench. The flow and thermal boundary conditions were applied. The convergence criteria

were specified. After that, the computations were performed. Finally, the numerical solutions were examined and discussed. The flow topology and coherent structure were also introduced to visualize the fluid flow and heat transfer behaviors.

### 3.5.4 Key quantifying performance factors

The key quantifying performance factors were Reynolds number, the friction factor, Nusselt number and the thermo-hydraulic performance.

The Reynolds number is defined as a ratio of inertia to viscous forces and is derived as

$$\text{Re} = \frac{\rho U_m D_h}{\mu} \quad (3.31)$$

Where  $\rho$ ,  $\mu$ , and  $U_m$  are the fluid density, dynamic viscosity, and mean velocity, respectively. The hydraulic diameter is defined as  $D_h = 4WH/2(W + H)$ .

The friction factor is defined as the dimensionless pressure drop for internal flow. The friction factor can be calculated by evaluating the pressure drop ( $\Delta P$ ) across the length of test section or the length of periodic module ( $L$ ) for the numerical model. The friction factor is expressed as

$$f = \frac{(\Delta P/L)D_h}{(\rho U_m^2/2)} \quad (3.32)$$

In the experiments, the net heat is defined as

$$Q_{net} = Q_{supply} - Q_{loss} \quad (3.33)$$

Here,  $Q_{supply}$  is total electrical power that supplied to the heater and  $Q_{loss}$  is heat loss from the test section to the surroundings. The  $Q_{net}$  was obtained by estimating heat gained by the fluid or  $\dot{m}c_p(T_{out} - T_{in})$ . Since the channel was well insulated, in most cases, the estimated  $Q_{loss}$  was less than 10%. The surface heat flux was assumed to be uniform.

The surface heat flux is expressed as

$$q_s = \frac{Q_{net}}{A_s} \quad (3.34)$$

Where  $A_s$  is the heated surface area of the test section.

From the Newton's law of cooling, the local convective heat transfer coefficient ( $h_x$ ) is defined as

$$h_x = \frac{q_s}{(T_s - T_b)} \quad (3.35)$$

Where  $q_s$  is surface heat flux,  $T_s$  is surface temperature, and  $T_b$  is bulk fluid temperature.

The local Nusselt number is defined as a ratio of convective heat transfer to conduction in a fluid and is expressed as

$$\text{Nu}_x = \frac{h_x D_h}{k} \quad (3.36)$$

Where  $k$  is the thermal conductivity of the fluid.

The area-weighted average Nusselt number is defined as

$$\text{Nu} = \frac{1}{A} \int_A \frac{h_x D_h}{k} dA \quad (3.37)$$

To comparing the key quantifying performance factors of the baffle channel with based values of the smooth channel, the friction factor ratio and the Nusselt number ratio are introduced. The friction factor ratio is expressed as  $f/f_0$ . The Nusselt number ratio is given by  $\text{Nu}/\text{Nu}_0$ , where  $f$ ,  $f_0$ ,  $\text{Nu}$ , and  $\text{Nu}_0$  are the friction factor and Nusselt number for the baffle channel and the smooth channel, respectively.

To evaluate the thermal performance of the baffle channel, the thermo-hydraulic performance is introduced. The thermo-hydraulic performance is defined as the ratio of the heat transfer coefficient of an augmented channel ( $h$ ) to the smooth channel ( $h_0$ ) at the same pumping power criterion. The thermo-hydraulic performance ( $\eta$ ) is derived as

$$\eta = \frac{h}{h_0} \Big|_{pp} = \frac{\text{Nu}}{\text{Nu}_0} \Big|_{pp} = \frac{(\text{Nu}/\text{Nu}_0)}{(f/f_0)^{1/3}} \quad (3.38)$$

Where  $f$ ,  $f_0$ ,  $\text{Nu}$ , and  $\text{Nu}_0$  are the friction factor and Nusselt number for the baffle channel and the smooth channel, respectively.

### 3.6 Thermophysical properties of nanofluid

In the present study, nanofluid was considered as a homogeneous fluid. Therefore, the single-phase model was introduced. In order to obtain accurate results, it is crucial to use the most appropriate formulations for determining the nanofluid properties. Since, at present, there are no universal formulations that can accurately predict nanofluid properties for any combination of independent variables. However, for currently available formulations, nanofluid properties depend on the nanoparticles volume fraction, the properties of solid particles, and also the base fluids. Since the properties of base fluids are temperature dependent, the nanofluids are also temperature dependent. Most of the nanofluid properties are expressed as functions of the nanoparticle volume fraction excepted for the thermal conductivity which depends on both volume concentration and temperature.

#### 3.6.1 Nanofluid dynamic viscosity

The nanofluid dynamic viscosity ( $\mu_{nf}$ ) can be determined from the empirical correlation proposed by Corcione [67].

$$\mu_{nf} = \frac{\mu_f}{1 - 34.87(d_p/d_f)^{-0.3} \phi^{1.03}} \quad (3.39)$$

Where  $\mu_f$  is the dynamic viscosity of base fluid,  $d_p$  is the nanoparticle diameter, and  $d_f$  is the equivalent diameter of a base fluid molecule which is given by

$$d_f = 0.1 \left[ \frac{6M}{(\pi N \rho_f)} \right]^{1/3} \quad (3.40)$$

Where  $M$  is the molecular weight of the base fluid ( $M_{water} = 18.01528$  g/mol),  $N$  is the Avogadro number ( $6.022 \times 10^{23}$  mol<sup>-1</sup>), and  $\rho_f$  is the mass density of the base fluid ( $\rho_{water} = 998.26$  kg/m<sup>3</sup>) at the reference temperature ( $T_{ref} = 293$ K).

#### 3.6.2 Nanofluid mass density and heat capacity

The nanofluid mass density ( $\rho_{nf}$ ) and the specific heat capacity of the nanofluids can be calculated from theoretical equations derived by Pak and Cho [68]. The nanofluid mass density is given by

$$\rho_{nf} = (1 - \phi)\rho_f + \phi\rho_p \quad (3.41)$$

Where  $\varphi$  is the nanoparticle volume fraction and  $\rho_p$  is the mass density of the nanoparticle. The nanofluid heat capacity at constant pressure per unit volume of nanofluids is expressed as

$$(\rho c_p)_{nf} = (1 - \varphi)(\rho c_p)_f + \varphi(\rho c_p)_p \quad (3.42)$$

Where  $c_p$  is the specific heat at constant pressure, the terms  $(\rho c_p)_f$  and  $(\rho c_p)_p$  are the heat capacities at constant pressure per unit volume of the base fluid and the nanoparticles, respectively. Hence, the nanofluid specific heat at constant pressure of the nanofluid can be derived as

$$c_{p,nf} = \frac{(1 - \varphi)(\rho c_p)_f + \varphi(\rho c_p)_p}{(1 - \varphi)\rho_f + \varphi\rho_p} \quad (3.43)$$

### 3.6.3 Nanofluid thermal conductivity

The nanofluid thermal conductivity ( $k_{nf}$ ) can be determined from the proposed model of Koo and Kleinstreuer [62]. They combined the classical Maxwell's model of thermal conductivity with the effect of Brownian motion. The nanofluid thermal conductivity is expressed by

$$k_{nf} = k_{static} + k_{Brownian} \quad (3.44)$$

The Maxwell's model represents the thermal conductivity enhancement due to the higher thermal conductivity of nanoparticles. The term  $k_{static}$  is given by

$$k_{static} = \frac{k_p + 2k_f + 2(k_p - k_f)\varphi}{k_p + 2k_f - (k_p - k_f)\varphi} k_f \quad (3.45)$$

Where  $k_p$  is the thermal conductivity of nanoparticle and  $k_f$  is the thermal conductivity of base fluid. The term  $k_{Brownian}$  is expressed as

$$k_{Brownian} = 5 \times 10^{-4} \beta \varphi \rho_f c_{p,f} \sqrt{\frac{\kappa_B T}{\rho_p d_p}} f(T, \varphi) \quad (3.46)$$

Where  $\kappa_B$  is the Boltzmann constant ( $\kappa_B = 1.3807 \times 10^{-23}$  J/K), the additional factor  $\beta$  is a function of  $\varphi$  and is dependent on the type of nanoparticles. The term

$f(T, \varphi)$  is an empirical function of temperature and nanoparticle volume fraction. The empirical function of  $\beta$  for  $\text{Al}_2\text{O}_3$  and the function  $f(T, \varphi)$  developed by Vajjha and Das [90] are expressed in following equations, respectively.

$$\beta = 8.4407(100\varphi)^{-1.07304} \quad (3.47)$$

$$1\% \leq \varphi \leq 10\%, \quad 298 \leq T \leq 363$$

$$f(T, \varphi) = \left( 2.8217 \times 10^{-2} \varphi + 3.917 \times 10^{-3} \right) \left( T/T_{ref} \right) - \left( 3.0669 \times 10^{-2} \varphi + 3.91123 \times 10^{-3} \right) \quad (3.48)$$

### 3.7 Flow topology and coherent structure

#### 3.7.1 Flow topology

The topology in the case of periodic incompressible flow can be described by the two dimensional streamlines. The definitions of streamline, streamsurface, and vortex core are summarized in the followings:

- Streamline is a tool for visualizing the vector fields is to plot the location of streamlines, which are lines tangential to the vector field of the velocity vector field. The projection of streamlines to solid walls is very useful. The plotting is done using wall shear stress vectors, and their corresponding wall streamlines.
- Streamsurface is a set of streamlines passing through a fixed curve inside the flow field. This streamsurface is tangential to the velocity vector field. The streamsurface is very useful for the flow visualization.
- Vortex is a region of the flow where streamlines are closed and approximately circular.

#### 3.7.2 Coherent structure

By definition, a coherent structure is a three-dimensional region of the flow over which at least one fundamental flow variable (e.g. velocity component, temperature, etc.) exhibits significant correlation with itself or with another variable over a range of space and/or time that is significantly larger than the smallest local scale of the flow.

After the Reynolds decomposition, the fluctuating part is decomposed into the coherent motion and to the turbulent background. The coherent part has important impact on the dynamics of the flow. Therefore, the coherent structure concept is to develop separate model for the coherent part which can be used to describe the flow.

### 3.7.3 Q criterion

The Q is a fundamental variable that is able to detect a vortex. The Q is the second scalar invariant of the velocity gradient tensor and can be expressed for fluids with constant density as follow.

$$Q = \frac{1}{2}(\Omega_{ij}\Omega_{ji} - S_{ij}S_{ji}) \quad (3.49)$$

Where  $\Omega_{ij}$  is the anti-symmetrical part of the velocity gradient tensor,  $\partial_j u_i$  or the vorticity tensor, which is expressed as

$$\Omega_{ij} = \frac{1}{2}(\partial_i u_j - \partial_j u_i) \quad (3.50)$$

Where  $S_{ij}$  is the symmetrical part of the velocity gradient tensor,  $\partial_j u_i$  or the rate of strain tensor, which is expressed as

$$S_{ij} = \frac{1}{2}(\partial_i u_j + \partial_j u_i) \quad (3.51)$$

Equation 3.43 shows that the Q is the indicator of vorticity dominance over strain. The results of the flow topology and coherent structure for the air and nanofluid flows are presented in chapters 6 and 7, respectively.

The next chapter presents the construction of numerical model and the computational details to represent the given problem of interest. The geometries and arrangements of the sinusoidal wavy baffle are also described. The numerical model was verified and validated. After that, for the air flow numerical investigation, the effects of various geometrical configurations on the prescribed key quantifying performance factors are presented and discussed in Chapter 6. The effects nanofluid on the performance factors are presented and discussed in Chapter 7.

## CHAPTER 4

# NUMERICAL SOLUTION PROCEDURE

This chapter describes and discusses the construction of numerical simulation, the numerical verification and validation procedures. First, the computational details of the baffle geometry and arrangement are explained. Then, the computational domain and the grid generation are described. The boundary conditions are defined. Next, the computational schemes and methods used in the computation are presented. The convergence criteria are also specified. Finally, the verification and validation methods are also introduced.

### 4.1 Computational details of the baffle channel

This section describes the computational details used to create the numerical simulation to represent the problem of interest. First, the sinusoidal wavy baffle's geometry and its arrangement in the channel were defined. Then, computational domain and the grid structure were specified and generated. The boundary conditions based on prescribed major assumptions were applied. Finally, the computational schemes and the convergence criteria were determined.

#### 4.1.1 Baffle geometry and arrangement for numerical simulation

The problem of interest under this numerical study assumed a periodical fully-developed turbulent flow inside a channel with a constant heat flux applied on the principal walls. The sinusoidal wavy baffles were successively placed in line on the top and bottom surfaces inside the channel. The baffle's profile was defined by the general sinusoidal function:  $x = a \sin(2\pi z / pt)$  which subjected to corresponding spatial variables in the Cartesian coordinates as illustrated in Figure 4.1. The baffle's geometric parameters and its arrangements comprised the baffle amplitude ( $a$ ), the baffle height ( $b$ ), the longitudinal pitch ( $pl$ ), and the transverse pitch ( $pt$ ), respectively. In order to generalize the study parameters, all of geometries were designed in relative to channel height ( $H$ ). Hence, the baffle's geometric parameters under study had become dimensionless parameters.

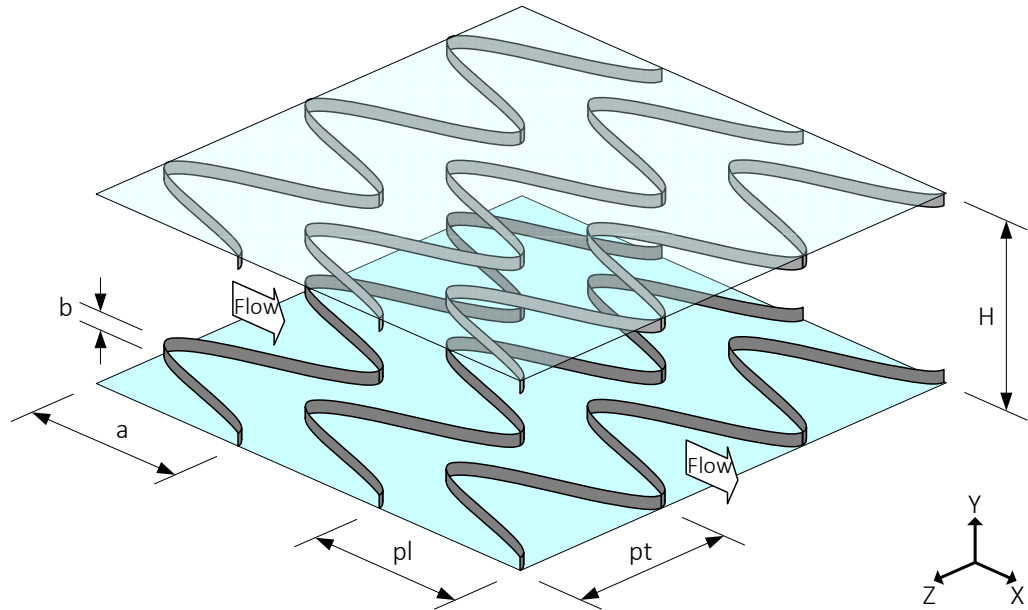


**Figure 4.1** Baffle geometry and arrangement for computation

#### 4.1.2 Computational domain

By using a periodicity characteristic of the given problem depicted in Figure 4.1, the confined two-dimensional periodic module as shown in Figure 4.2 was considered as the computational domain. A constant surface heat flux condition was applied at the top and bottom wall boundaries. The inlet and outlet planes were specified as periodic boundary. The side walls were also assigned as symmetry planes. Figure 4.3 depicts a three-dimensional schematic design of the periodic module for the computational domain employed in the present study.

The DesignModeler application in the ANSYS workbench was used to sketch and model the physical domain of solid geometry which was deployed as the computational domain. The geometry's extents, dimensions, and labeling had been followed the descriptions in Figure 4.1. It should be noted that, in the computational domain, the sinusoidal wavy baffle's profile had been intentionally projected to the x-z plane for the computational purpose. Consequently, the main fluid flow was specified to be in the x-direction as shown in subsequent figures.

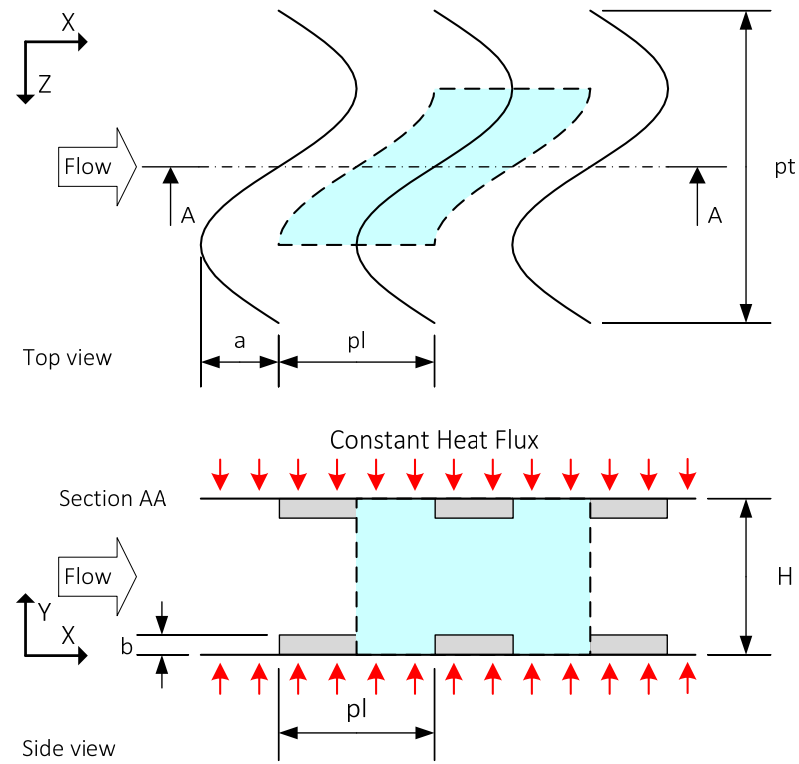


Figure 4.2 Two-dimensional computational domain

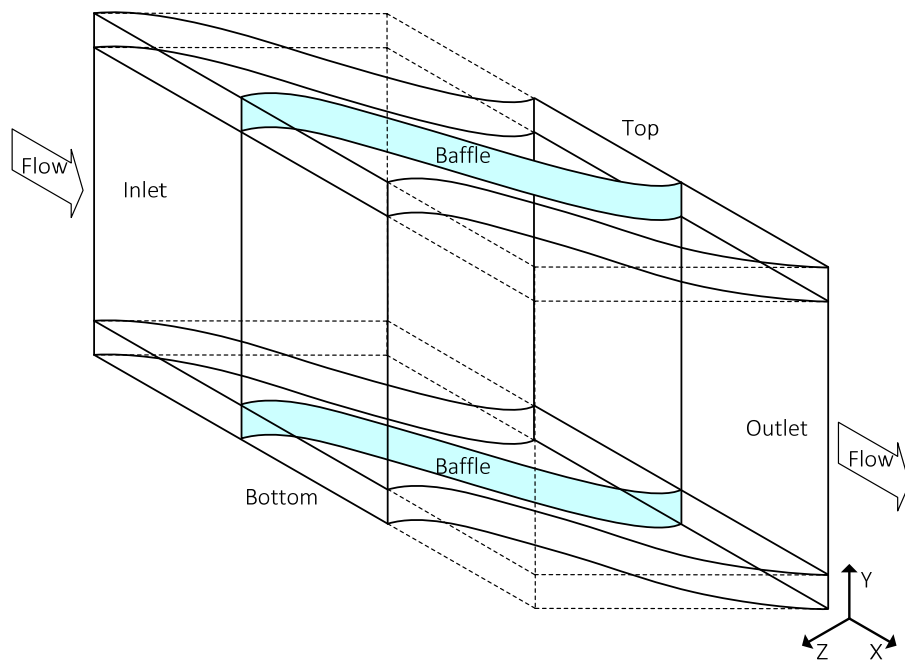


Figure 4.3 Three-dimensional computational domain

### 4.1.3 Grid generation

The numerical solution of the partial differential equations requires an arrangement of a discrete set of grids or meshes in the flow field. These differential equations are approximated by a set of algebraic equations on the discrete set of defined grids. Then, the system of algebraic equations can be solved to obtain a set of discrete values which is an approximated solution of the partial differential equations. The determination of grids for a given body is known as grid generation.

In the present study, the grid structure was generated by the Meshing application in the ANSYS Workbench. The computational domain created in previous section was meshed with quadrilateral-faced hexahedral elements. This selected grid type could provide high quality solution while reduces the numerical diffusion when the mesh is aligned with the flow.

A sample of hexahedral grid structure used for computation is presented in Figure 4.4. The grid structure was designed to be non-uniform for effective computation. As a matter of fact, a fine grid was required where the dependent variable changes sharply with corresponding coordinate [89]. Therefore, the grid structure was intentionally densely packed around the wavy baffles, at the wall boundaries, and at the periodic boundaries.

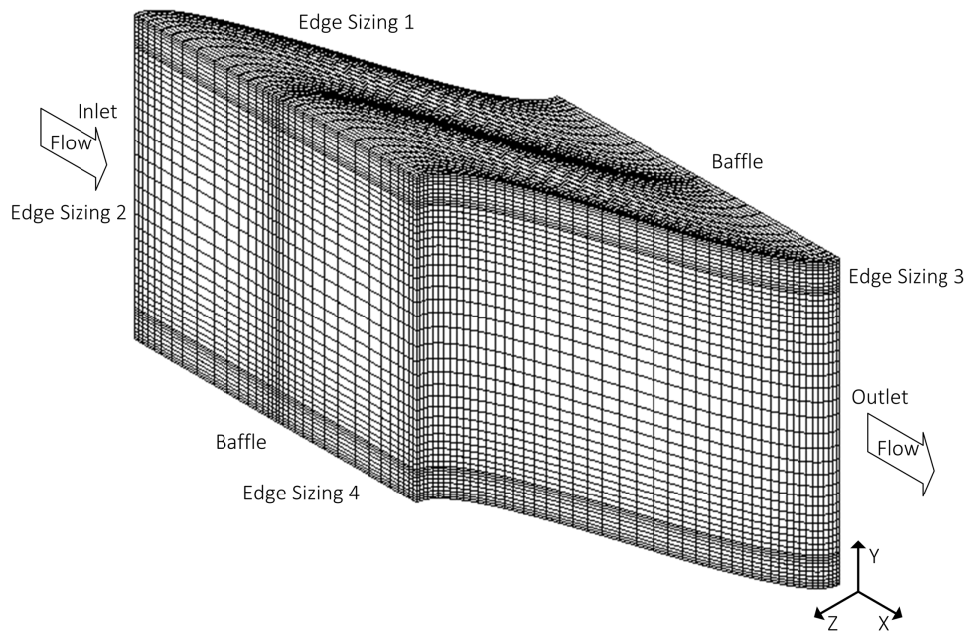


**Figure 4.4** Hexahedral grid structure for numerical simulation

#### 4.1.4 Boundary conditions

The following boundary conditions were imposed for the computations.

- Periodic boundary conditions were applied at the inlet and outlet of each periodic module.
- No-slip boundary conditions were imposed along the stationary solid wall of the channel.
- The top and bottom walls of the channel were assumed to be at a constant surface heat flux.
- The upstream bulk temperature of the fluid was specified to be 300K.

#### 4.1.5 Computational schemes and convergence criteria

Since the algebraic equations for steady flow were non-linear, an iteration scheme was used to solve the equations. The algebraic equations had to be modified using linearization process. Then, the linear systems could be solved by iteration techniques. The numerical scheme or methods employed in the present study are presented in Table 4.1.

**Table 4.1** Numerical scheme/method used in the computation

Spatial discretization	Numerical scheme/method
Pressure-velocity coupling	SIMPLE
Gradient	Least squares cell based
Pressure	Standard
Momentum	Second Order Upwind
Turbulent Kinetic Energy ( $k$ )	QUICK
Turbulent Dissipation Rate ( $\varepsilon$ )	QUICK
Energy	QUICK

For the iteration method, the convergence criteria had to be determined to end the iteration process. The residual was used as an indicator for the iterative convergence. The residual of the algebraic equation is the change in the equation over each step of iteration. It is usually scaled or normalized to eliminate the effect of magnitude of the flow variable. In order to minimize the iteration error, the normalized residual should be reduced until the first two or three most significant digits of the general flow variable will not change in further iterations.

The computations for each steady-state simulation were considered to have converged when the monitoring residuals for the continuity, momentum,  $k$  and  $\varepsilon$  equations had decreased to less than  $1 \times 10^{-7}$ . Except for the energy equation, the

convergence criterion was set to less than  $1 \times 10^{-10}$ . The monitoring residuals and their convergence criteria are also listed in Table 4.2.

**Table 4.2** Residual monitors and convergence criteria

Residual monitor	Absolute criteria
Continuity	$1 \times 10^{-7}$
x-velocity	$1 \times 10^{-7}$
y-velocity	$1 \times 10^{-7}$
z-velocity	$1 \times 10^{-7}$
Turbulent Kinetic Energy ( $k$ )	$1 \times 10^{-7}$
Turbulent Dissipation Rate ( $\epsilon$ )	$1 \times 10^{-7}$
Energy	$1 \times 10^{-10}$

Using the specified schemes and methods, numerical simulations were solved iteratively until the criteria were reached. Next subsequent sections describe and discuss the methods used for verification and validation process in construction of the numerical model.

## 4.2 Verification of numerical simulation

The verification is a process of determining that a computational model accurately represents the conceptual description of the domain of interest. This section presents the verification methods used to estimate the errors in the numerical model.

### 4.2.1 Grid independence

The quality of a numerical solution depends highly on the quality of generated grid. A high quality grid is critical to reliability and accuracy of the numerical solution. A low quality grid may lead to an incorrect solution. Therefore, it is important to test if the attained solution is grid independent. A simple method to test for the grid independence is to refine the resolution of the numerical model and repeat the simulation. If the results do not change significantly, the successive refined grid is probably adequate. If there are significant differences between two solutions, the successive grid is likely an inadequate. This method is often called a grid refinement study. For the present study, the grid refinement study was performed for various grid resolutions. The observed key parameters for the test of grid independence were the friction factor, the averaged Nusselt number, and the averaged  $y^+$  values. The settings and results of the grid refinement study are presented in the next chapter.

#### 4.2.2 Grid convergence index

The other method to examine the numerical error in a numerical solution is to determine the grid convergence index (GCI). This approach was originally proposed by Roached [91] for reporting the grid refinement study. The GCI is based on generalized Richardson extrapolation involving comparison of discrete solutions at two different grid sizes [92]. The objective is to provide a measure of uncertainty of the grid convergence. The GCI indicates how much the numerical solution would change with a further grid refinement. A small value of GCI indicates that the computation is within the asymptotic range of convergence.

The GCI on the fine grid is defined as [88]

$$GCI_U = F_s E_U \quad (4.1)$$

Here  $F_s$  is the safety factor and  $F_s = 3$  for a conservative value.  $E_U$  is the estimate error in a target quantity  $U$  as a function of a reference size  $h$  of the control volumes inside the mesh which is expressed as

$$E_U(h) = U_{exact} - U \approx Ch^p \quad (4.2)$$

Here  $C$  is a constant and  $p$  is the order of the numerical scheme.

For two meshes with refinement ratio  $r = h_2/h_1$  ( $r > 1$ ) and solutions  $U_1$  and  $U_2$ , the estimate of the discretization error can be written as

$$E_{U,1} = \frac{U_2 - U_1}{1 - r^p} \quad (4.3)$$

$$E_{U,2} = r^p \left( \frac{U_2 - U_1}{1 - r^p} \right)$$

Here  $E_{U,1}$  and  $E_{U,2}$  are the errors in the coarse and fine mesh solutions, respectively.

However, for three or more successively refined meshes and for constant refinement ratio,  $r = h_2/h_1 = h_3/h_2$ , the observed order  $\tilde{p}$  should be used in conjunction with a reduced safety factor,  $F_s = 1.25$ . The observed order of the numerical scheme is defined as

$$\tilde{p} = \ln \left( \frac{U_3 - U_2}{U_2 - U_1} \right) / \ln(r) \quad (4.4)$$

Here  $U_2 - U_1$  is the difference between the solutions on the medium and coarse mesh and  $U_3 - U_2$  is the difference between the solutions on the fine and medium mesh. The results of the calculated GCI are presented in the numerical verification section in the next chapter.

### 4.2.3 Verification of smooth channel

To verify the numerical model, at preliminary stage, computational experiments were repeatedly performed to quantify the averaged friction factor ( $f_0$ ) and averaged Nusselt number ( $Nu_0$ ) for smooth channel at given Reynolds number ranging from 5,000 to 18,000. Then, the calculated  $Nu_0$  and  $f_0$  were qualified with prominent classical correlations at the same given Reynolds numbers.

The averaged friction factor for smooth channel was compared with Blasius correlation [93] and Petukhov correlation [93] for fully developed turbulent flow in rectangular duct.

The Blasius correlation is expressed as

$$f = 0.316Re^{-1/4} \quad (4.5)$$

$$Re \leq 2 \times 10^4$$

The Petukhov correlation is given by

$$f = (0.790 \ln Re - 1.64)^{-2} \quad (4.6)$$

$$3,000 \leq Re \leq 5 \times 10^6$$

The averaged Nusselt number for smooth channel was compared with Dittus-Boelter correlation [94] and Gnielinski correlation [93] for fully developed turbulent flow in rectangular duct.

The Dittus-Boelter correlation is expressed as

$$Nu = 0.023 Re^{4/5} Pr^{2/5} \quad (4.7)$$

$$0.6 \leq Pr \leq 160, \quad Re \geq 1 \times 10^4$$

The Gnielinski correlation is given by

$$Nu = \frac{(f/8)(Re-1000)Pr}{1 + 12.7(f/8)^{1/2}(Pr^{2/3} - 1)} \quad (4.8)$$

$$0.5 \leq Pr \leq 2,000, \quad Re \geq 1 \times 10^4$$

### 4.3 Validation of numerical simulation

The experimental data was crucial for validation process. This section describes the experimental setup and procedure used to conduct a preliminary experiment. The experimental uncertainties were evaluated. The experimental results are presented in the next chapter. The obtained experimental data were used to validate the solution of numerical model.

#### 4.3.1 Preliminary experiment of air flow

In order to validate the numerical model, an experimental investigation was introduced. The baffle's profile used in this preliminary experiment was identical to the baffle defined in the computational detail section. Denoted again, the geometric parameters were baffle amplitude ( $a$ ), baffle height ( $b$ ), longitudinal pitch ( $pl$ ), and transverse pitch ( $pt$ ). The geometric parameters were similarly designed in relative to the channel height ( $H$ ). The baffle's geometry and its arrangement for the experiment are shown in Figure 4.5 and 4.6. The baffles were made of thin aluminum strip having a thickness of 0.3 mm identical to the numerical simulation. The baffles were consecutively placed on the top and bottom walls along the test section inside the channel. However, the experimental setup was originally designed for the solar air heater applications [95], the heat surface was applied only to the top wall in the test section.

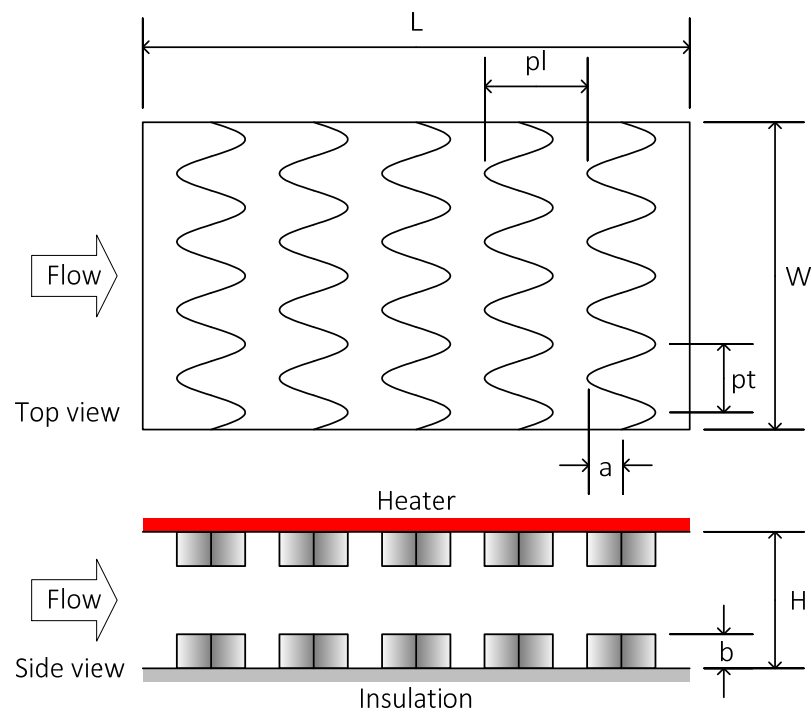


**Figure 4.5** Baffle geometry and arrangement for experiment

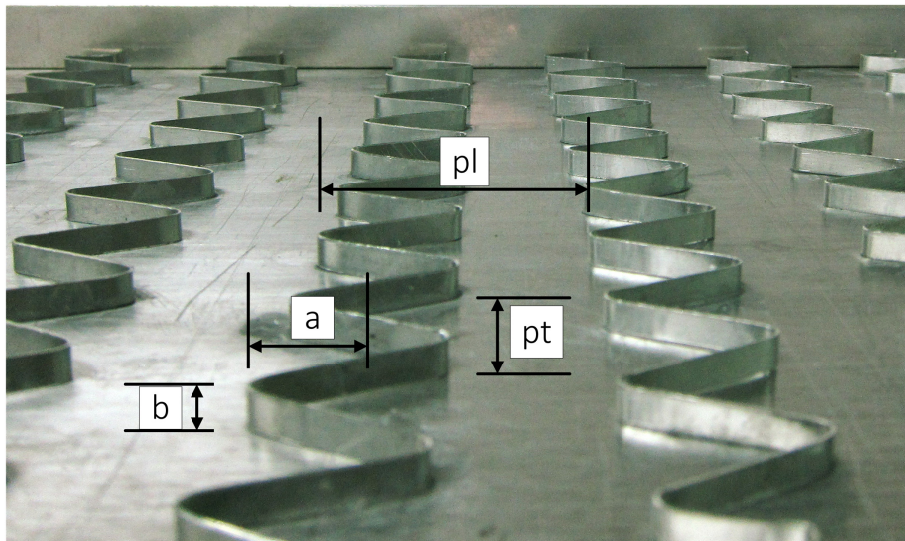


**Figure 4.6** A sample photo of baffle arrangement for experiment

#### 4.3.2 Experimental setup and procedure of air flow

A schematic diagram of experimental setup is illustrated in Figure 4.7. The flow system mainly composed of an entrance section, a test section, a mixing chamber, a flow meter and a high pressure blower. The entrance section, the test section, and the mixing chamber had an internal cross-section of 210 mm  $\times$  20 mm with lengths of 1,600 mm ( $42D_h$ ), 400 mm ( $10.5D_h$ ) and 200 mm ( $5.2D_h$ ), respectively. The channel walls were made of Plexiglas ( $k = 0.19$  W/m-K) except the top wall in the test section. The top wall was made of aluminum plate attached to an electrical plate heater. The backside of plate heater was insulated with glass wool, polyethylene foam ( $k = 0.42$  W/m-K), and thick wood plate to protect heat loss from the heater. Moreover, the entire channel was also insulated with polyethylene foam to prevent the heat loss to surroundings.

In the preliminary experiment, an inverter was used to control the 3-hp air blower to supply desired flow rates. A calibrated orifice meter was used to determine the air flow rate entering the test section. The orifice meter was also connected to a digital manometer linked with the data acquisition system. Another digital manometer was used to measure the pressure drop across the test section. The calibrated PT-100 resistance temperature detectors (RTDs) were used to measure the air inlet and outlet temperatures. The calibrated J-type thermocouples were used to measure the surface temperatures at selected locations along the top wall. A data acquisition system was employed to record the temperatures and pressure drops at steady state conditions. A power meter was used to measure total electrical power supplied to the plate heater. The heater was controlled by a power controller circuit to obtain the uniform heat flux condition.

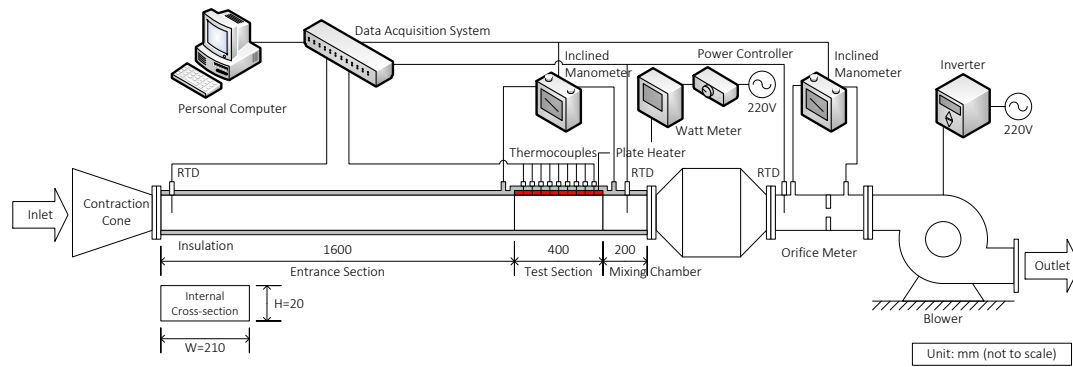


**Figure 4.7** Schematic diagram of the experimental setup

An uncertainty analysis for the experimental setup was performed on relevant parameters. If  $R$  is a given function of the independent variables  $x_1, x_2, x_3, \dots, x_n$  and  $\Delta x_1, \Delta x_2, \Delta x_3, \dots, \Delta x_n$ , are the uncertainties in these independent variables, the uncertainty of  $R$  can be evaluated by:

$$\frac{\Delta R}{R} = \left[ \frac{1}{R^2} \left( \frac{\partial R}{\partial x_1} \Delta x_1 \right)^2 + \frac{1}{R^2} \left( \frac{\partial R}{\partial x_2} \Delta x_2 \right)^2 + \frac{1}{R^2} \left( \frac{\partial R}{\partial x_3} \Delta x_3 \right)^2 + \dots + \frac{1}{R^2} \left( \frac{\partial R}{\partial x_n} \Delta x_n \right)^2 \right]^{1/2} \quad (4.9)$$

The maximum values of uncertainty were dominated by the dimensional measurements, an orifice meter, manometers, and the temperature measurements. The uncertainties for basic measured parameters are reported in Table 4.3. The uncertainties of estimated  $Re$ ,  $f$ , and  $Nu$  were 0.93%, 2.30%, and 6.33%, respectively.

**Table 4.3** Measurement uncertainties of the experimental setup

Parameters	Maximum uncertainty (%)
Hydraulic diameter, $D_h$	0.04
Mean velocity, $U_m$	0.86
Reynolds number, $Re$	0.93
Temperature, $T$	2.80
Temperature difference, $\Delta T$	3.96
Net heat specified, $Q_{net}$	0.04
Pressure difference, $\Delta P$	1.50
Friction factor, $f$	2.30
Nusselt number, $Nu$	6.33

The experimental setup was also verified with the classical correlations as expressed in the numerical verification section. After that, the experiments with various flow rates, different geometric parameters and arrangements were performed to evaluate the fluid flow and heat transfer characteristics in the sinusoidal wavy baffle's channel. The next chapter presents the results of preliminary experimental investigation, numerical verification, and validation of numerical simulation with the achieved experimental results.

# CHAPTER 5

## VERIFICATION AND VALIDATION OF NUMERICAL SIMULATION

This chapter describes and discusses the verification and validation results according to the procedures introduced in the previous chapter. First, the experimental results used for comparing with numerical solutions are reported. Next, the verification of numerical solutions is described. Sequentially, grid independence was tested. The numerical smooth channel's data were evaluated with the prominent classical correlations. Finally, to validate the computational model, comparison of numerical results with the obtained experimental data is discussed.

### 5.1 Preliminary experimental results and discussion

The experimental investigation was preliminarily conducted to observe the enhancements of pressure loss and heat transfer coefficient within the baffle channel [95]. The geometric parameters and flow conditions considered in the preliminary experiment are shown in Table 5.1.

**Table 5.1** Geometric parameters and flow conditions for preliminary experiment

Geometric parameters	Values
Relative amplitude, $a/H$	0.50, 0.75
Relative height, $b/H$	0.10, 0.20
Relative longitudinal pitch, $p/H$	1.0, 2.0
Relative transverse pitch, $pt/H$	1.0
Channel height, $H$	0.02 m
Channel width, $W$	0.21 m
Hydraulic diameter, $D_h$	0.04 m
Flow and thermal conditions	Values
Working fluid	Air
Reynolds number, $Re$	5,000 – 18,000
Surface heat flux on top wall, $q_s$	1,000 W/m <sup>2</sup>

#### 5.1.1 Verification of smooth channel for experimental setup

The experiments for smooth channel were repeatedly performed to verify the experimental setup. The smooth channel's friction factor (Experimental  $f_0$ ) and Nusselt number (Experimental  $Nu_0$ ) were calculated and compared with classical

correlations as expressed in the previous chapter. The averaged friction factor was compared with Blasius and Petukhov correlations and shown in Figure 5.1. The averaged Nusselt number was compared with Dittus-Boelter and Gnielinski correlation and presented in Figure 5.2.

From Figure 5.1 and 5.2, the results of the experimental smooth channel were in reasonably well agreement with the classical correlations for both averaged friction factor and Nusselt number. The maximum deviations of friction factor compared to Blasius and Petukhov correlations were 3.90% and 3.78%, respectively. Nusselt number had maximum deviations of 9.76% and 20.88% compared to Dittus-Boelter and Gnielinski correlations, respectively. Consequently, based on the verification results, the experimental setup was acceptable. For the pilot experiments, these smooth channel's data were used as references for evaluating the thermal performance over the smooth channel. The effects of wavy baffles on the key performance factors are presented in the subsequent section.

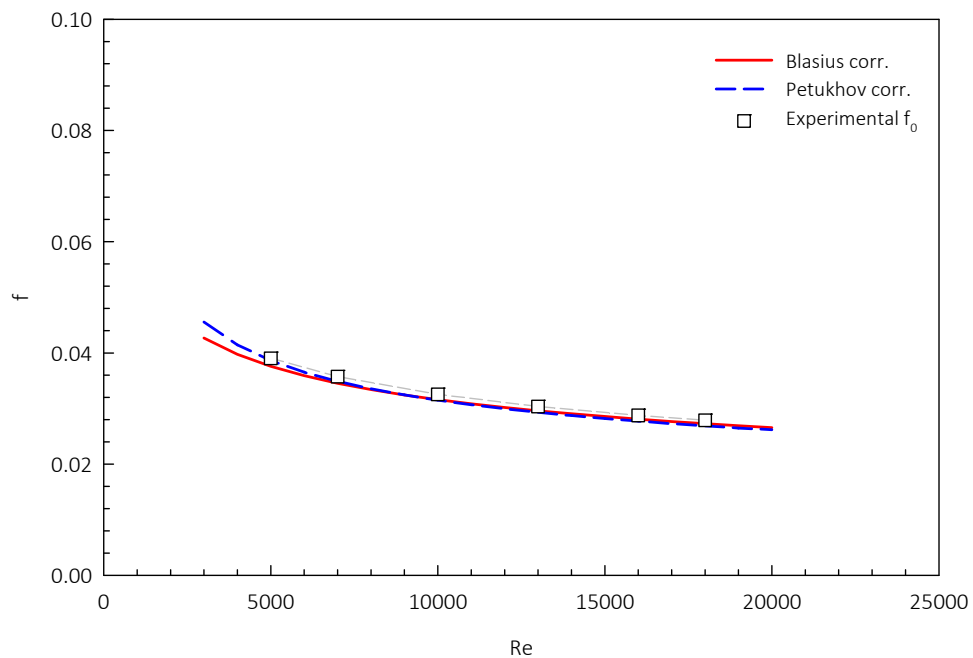


**Figure 5.1** Comparison of experimental  $f_0$  and corresponding correlations

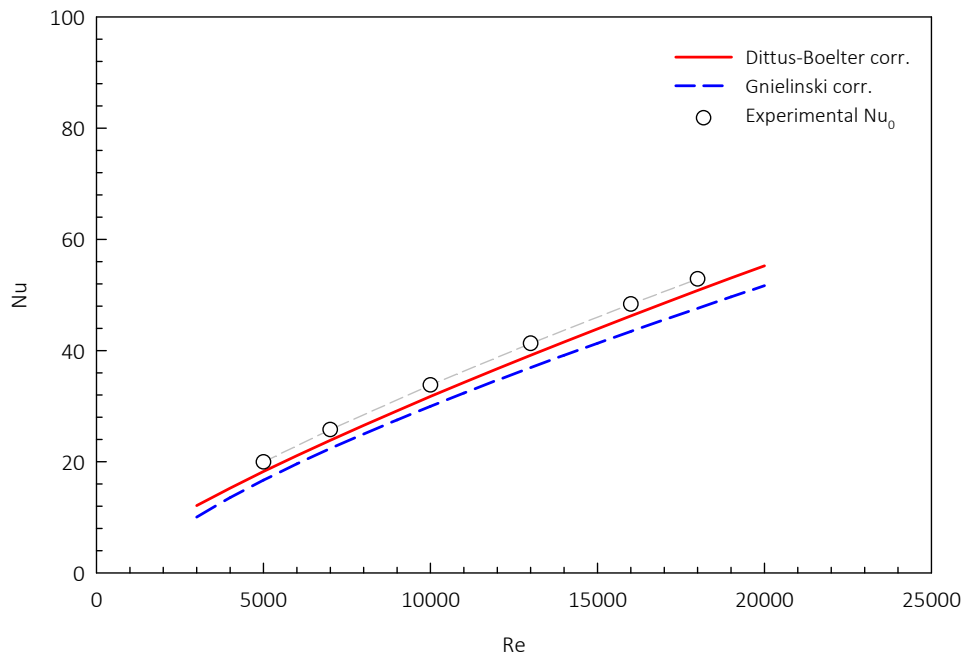


Figure 5.2 Comparison of experimental  $Nu_0$  and corresponding correlations

### 5.1.2 Experimental flow characteristics

The experimental friction factors of the air flow in the wavy baffle channel were calculated from the read out pressure drops across the test section along the flow direction. The observed range of Reynolds number was 5,000 to 18,000. The experimental results are shown in Figure 5.3 and 5.4.

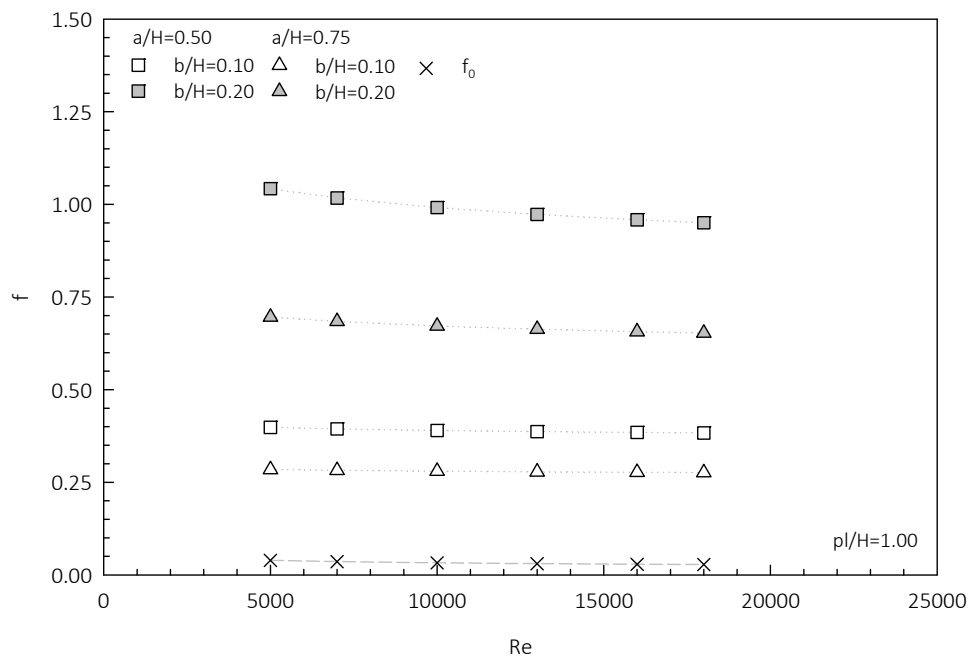
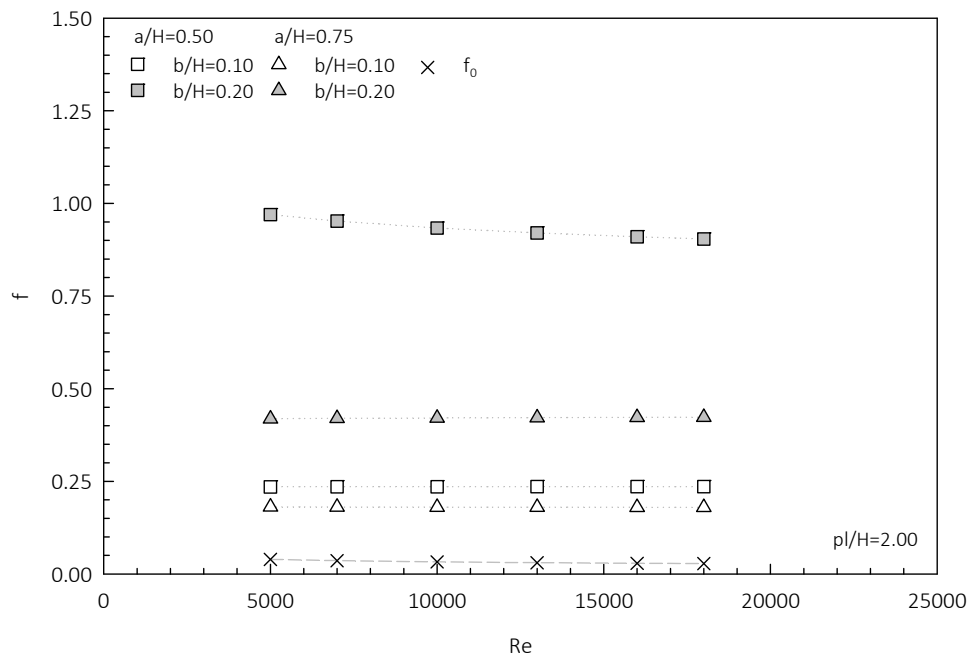


Figure 5.3 Variations of experimental  $f$  with  $Re$  at  $pL/H=1.00$



**Figure 5.4** Variations of experimental  $f$  with  $Re$  at  $pl/H=2.00$

Based on experimental results, the friction factor slightly decreased with increasing Reynolds number as expected. The values of friction factor for the wavy baffle channel were obviously higher than for the smooth channel at a given range of Reynolds numbers. Considering results for each fixed relative longitudinal pitch, the friction factor increased with enlarging the relative baffle height from 1.0 to 2.0 due to higher blockage ratio. However, the friction factor decreased with an increment in relative amplitude from 0.50 to 0.75.

### 5.1.3 Experimental heat transfer characteristics

The averaged Nusselt numbers for the preliminary experiment of the wavy baffle channel for the Reynolds number ranging from 5,000 to 1,8000 are presented in Figure 5.5 and 5.6. The Nusselt number moderately increased with an increase of Reynolds number as expected. At a given range of Reynolds numbers, Nusselt numbers for wavy baffle channel were noticeably higher than for the smooth channel. Considering Nusselt number results for each fixed relative longitudinal pitch, Nusselt number also increased with increasing the relative baffle height from 0.1 to 0.2. However, Nusselt number slightly decreased with an increment in the relative amplitude from 0.50 to 0.75.

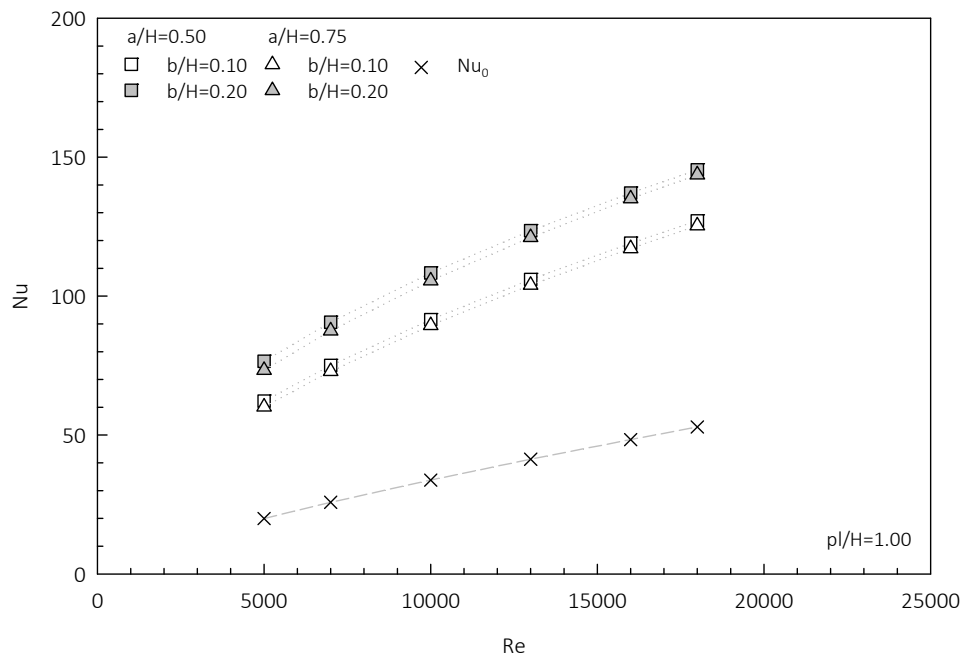


Figure 5.5 Variations of experimental Nu with Re at  $p/H=1.00$

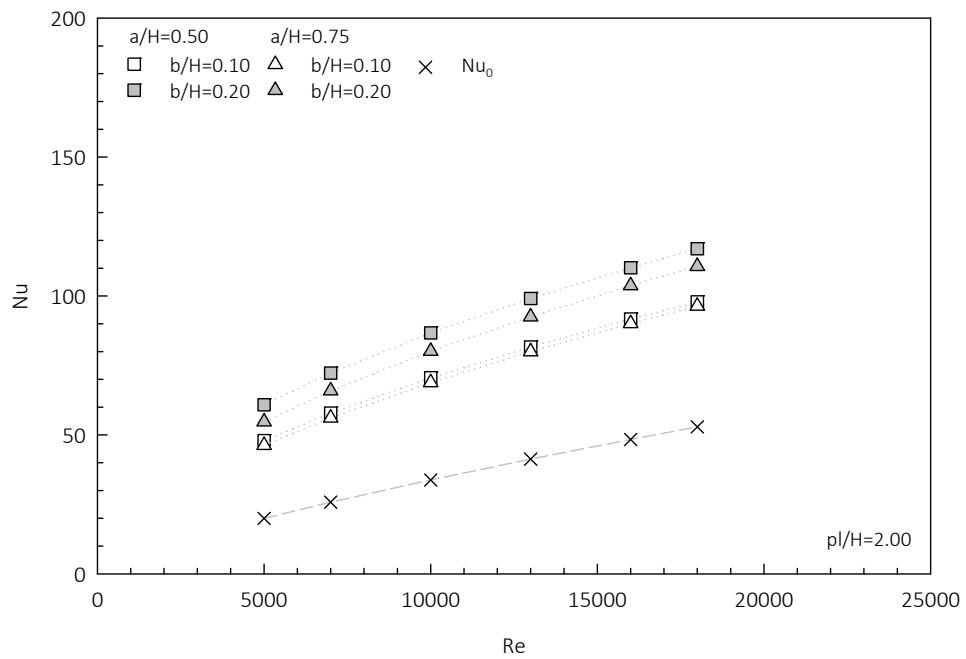


Figure 5.6 Variations of experimental Nu with Re at  $p/H=2.00$

### 5.1.4 Experimental thermo-hydraulic performance

For condition of the same pumping power, the thermo-hydraulic performances for experiment of the wavy baffle channel were evaluated for a range of Reynolds number from 5,000 to 18,000. The results on thermo-hydraulic performance are presented in Figure 5.7 and 5.8. The thermal performance obviously declined with increasing Reynolds number. Considering the thermo-hydraulic results for each fixed relative longitudinal pitch, thermal performance increased with reducing the relative baffle height from 0.2 to 0.1 and also increased with an increment in the relative amplitude from 0.50 to 0.75. These experimental results were collected for comparing with the numerical solutions in the subsequent validation section.

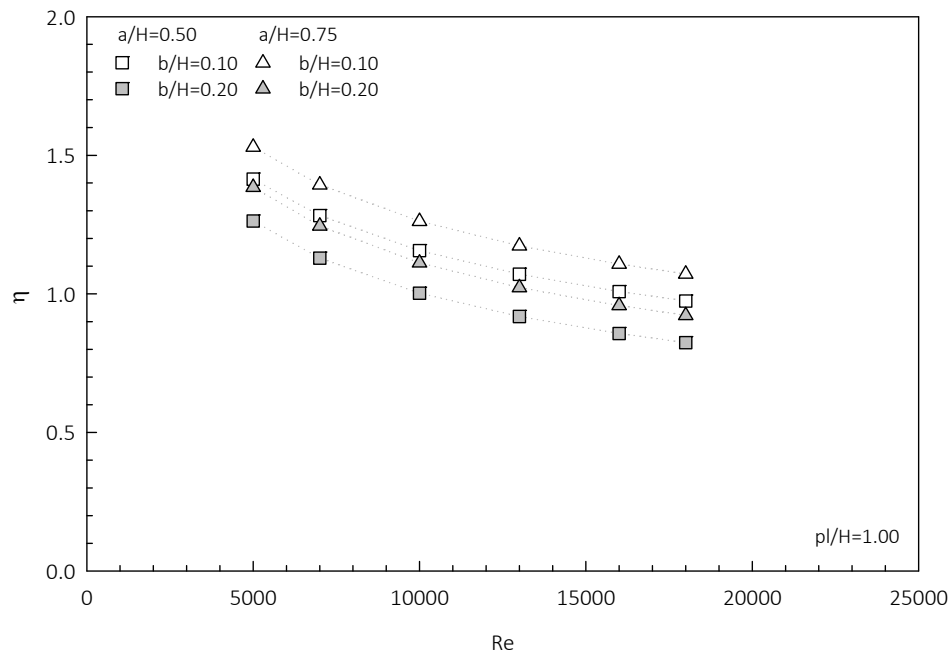


Figure 5.7 Variations of experimental  $\eta$  with Re at  $p/H=1.00$

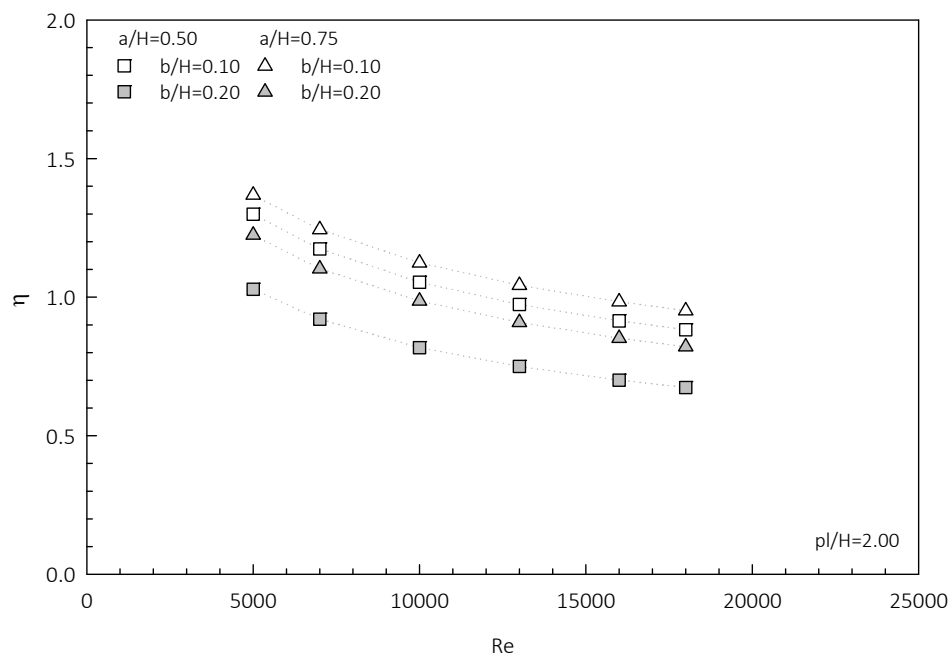


Figure 5.8 Variations of experimental  $\eta$  with Re at  $p/H=2.00$

## 5.2 Verification of numerical simulation

### 5.2.1 Grid refinement study

The grid resolution used for the numerical model was based on successive grid refinement experiments. The main parameter specified the grid resolution of numerical model was the edge size of following geometries: the wavy baffle's curve, the baffle's height, the baffle's longitudinal pitch, and the deduced channel's height. To check for grid independence, first, the grid resolution was refined from 60,000 (coarse) to 200,000 (fine) elements by adjusting the edge size of the defined geometries. Next, the smooth channel's numerical simulations were conducted at a given Reynolds number of 10,000 using those refined grid models. Then, the numerical solutions compiled from the grid refinement study were determined and reported in Table 5.2.

The absolute errors of the predicted friction factors and Nusselt numbers compared to the Blasius and Dittus-Boelter correlations are presented in Figure 5.9 and Figure 5.10, respectively. The averaged  $y^+$  values are also presented in Figure 5.11. According to the grid refinement study, the results of friction factor and Nusselt number for candidate case: 3, 4, 5, 6, and 7 were not significantly different to each other. However, there were obviously differences for the averaged  $y^+$  values. As the grid resolution had become finer, the  $y^+$  values had reduced. The values for the case: 5, 6, and 7 were not significantly different. Hence, to reduce the computational efforts, the grid resolution of case no. 5 (107,066 elements) was deliberately selected

for meshing the numerical model. In addition, for turbulent flows, the first grid that normal to the wall surface was required to be within the laminar sublayer of the boundary layer. It should exhibit the  $y^+$  values of less than 1.0. Corresponding to the averaged  $y^+$  value obtained from the refinement, the selected grid resolution was sufficiently fine for achieving the desired computational accuracy.

**Table 5.2** Grid refinement study at Re=10,000

Case	No. of Elements	$\Delta P$ (Pa)	f	Nu	Ave. $y^+$
1	59,126	-7.8066	0.0341	34.1387	2.5801
2	65,518	-7.6553	0.0334	33.5542	1.8005
3	75,106	-7.6241	0.0333	33.4635	1.1961
4	87,890	-7.6092	0.0332	33.4409	0.8569
5	107,066	-7.5986	0.0331	33.4302	0.6012
6	135,360	-7.6049	0.0332	33.4198	0.6012
7	188,000	-7.6073	0.0332	33.4194	0.6013

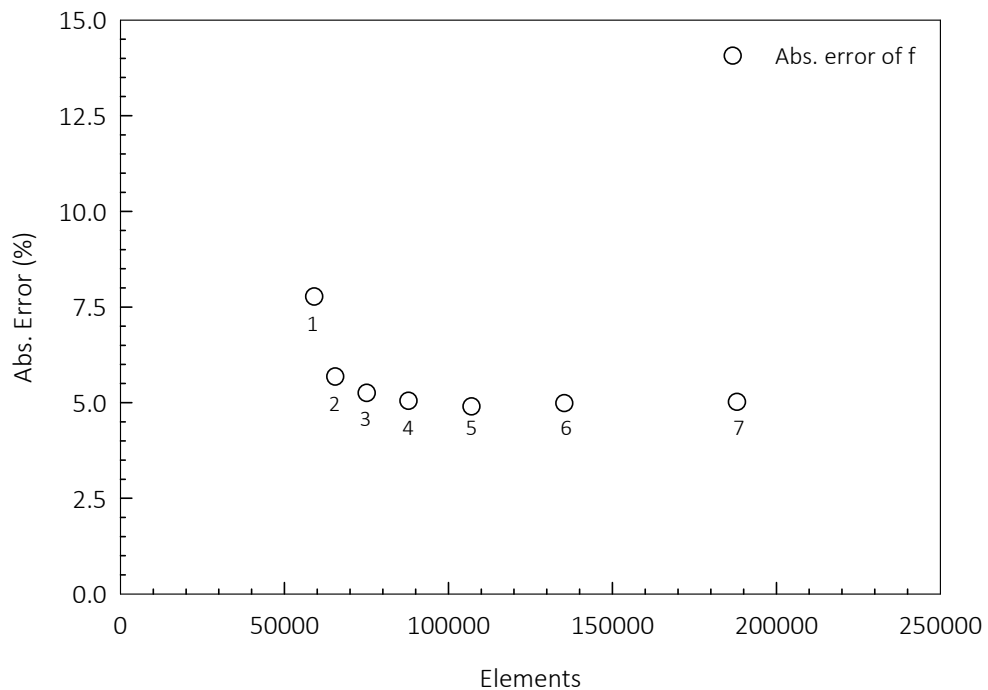


**Figure 5.9** Absolute error of f from grid refinement study

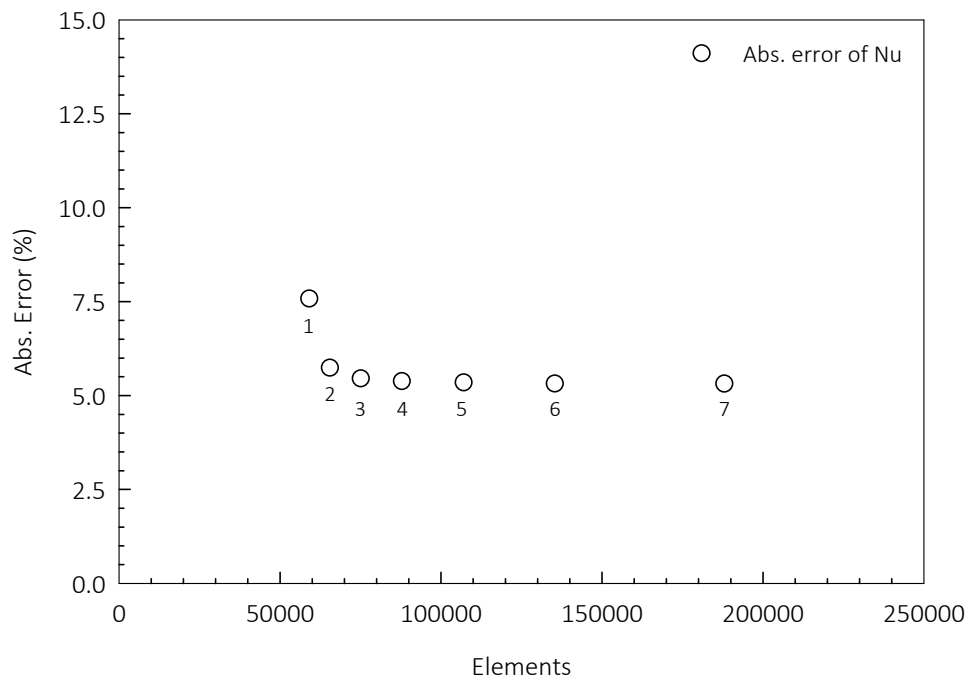


Figure 5.10 Absolute error of Nu from grid refinement study

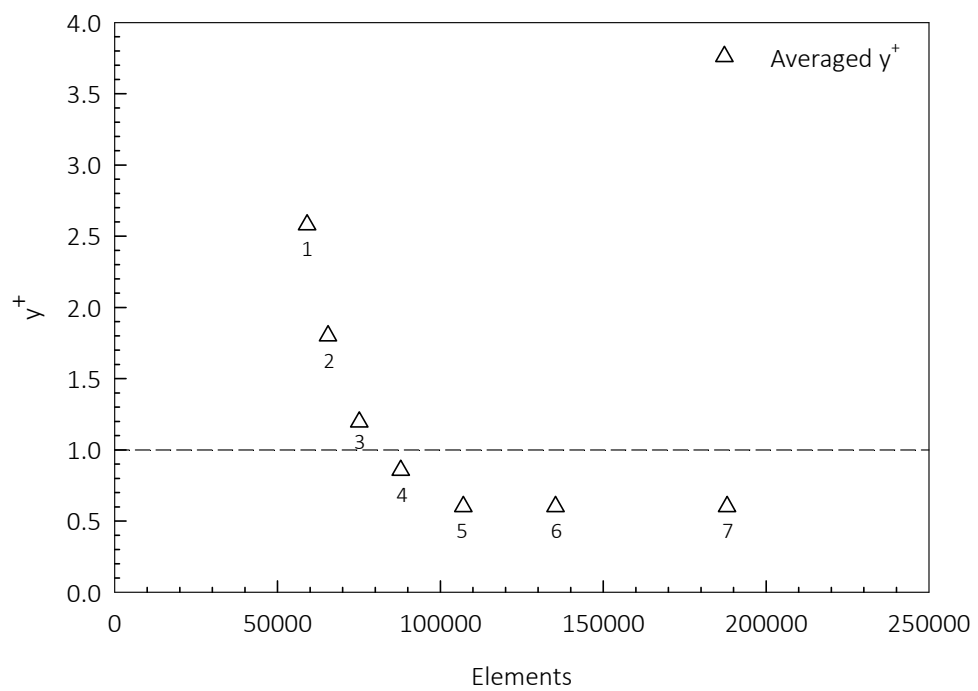


Figure 5.11 The  $y^+$  values from grid refinement study

### 5.2.2 Estimation of grid convergence index

The results of grid information and the calculated grid convergence index are presented in Table 5.3. Since the magnitude of friction factor was small, the different pressure values for each periodic module were used instead. As a result, the GCI for each finer grid resolution was reduced. This result indicated that the numerical solutions were within the asymptotic range of convergence. Since the GCI for both different pressure and Nusselt number of case no. 5 was not significant different to the case no. 6. Due to the cost and time of computations, the grid resolution of case no. 5 was selected with the acceptable level of accuracy.

**Table 5.3** Grid convergence index

Case	No. of Elements	GCI (%)	
		$\Delta P$	Nu
1	59,126	-	-
2	65,518	43.24	167.02
3	75,106	8.91	25.90
4	87,890	4.26	6.46
5	107,066	3.03	3.05
6	135,360	1.82	2.98
7	188,000	0.66	0.13

### 5.2.3 Verification of smooth channel for numerical simulation

To verify the numerical model, the computations were performed to quantify the friction factor ( $f_0$ ) and Nusselt number ( $Nu_0$ ) for numerical smooth channel at Reynolds number ranging from 5,000 to 18,000. Then, the computed  $f_0$  and  $Nu_0$  values were qualified with the calculations from the prominent classical correlations as expressed in the previous chapter at the same given Reynolds numbers. The predicted  $f_0$  were compared with the Blasius and Petukhov correlations. The predicted  $Nu_0$  were compared with the Dittus-Boelter and Gnielinski correlations.

Comparisons of predicted and correlation values of the friction factor and Nusselt number were presented in Figure 5.12 and 5.13, respectively. As a result, the predicted values for numerical smooth channel were in reasonably agreement with those classical correlations. The predicted friction factor had maximum deviations of 6.70% and 5.49% compared to the Blasius and Petukhov correlations, respectively. For Nusselt number, the maximum deviations were found to be 9.64% and 19.71% compared to the Dittus-Boelter and Gnielinski, respectively. Consequently, the numerical solutions based on the verification results were reliable.

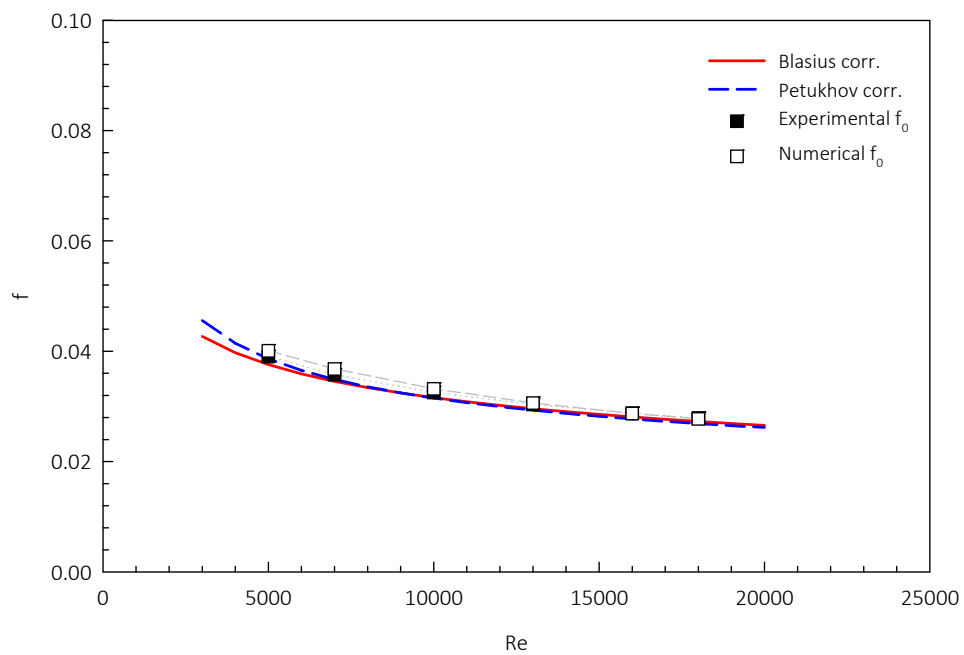


Figure 5.12 Comparison of predicted  $f_0$  and corresponding correlations

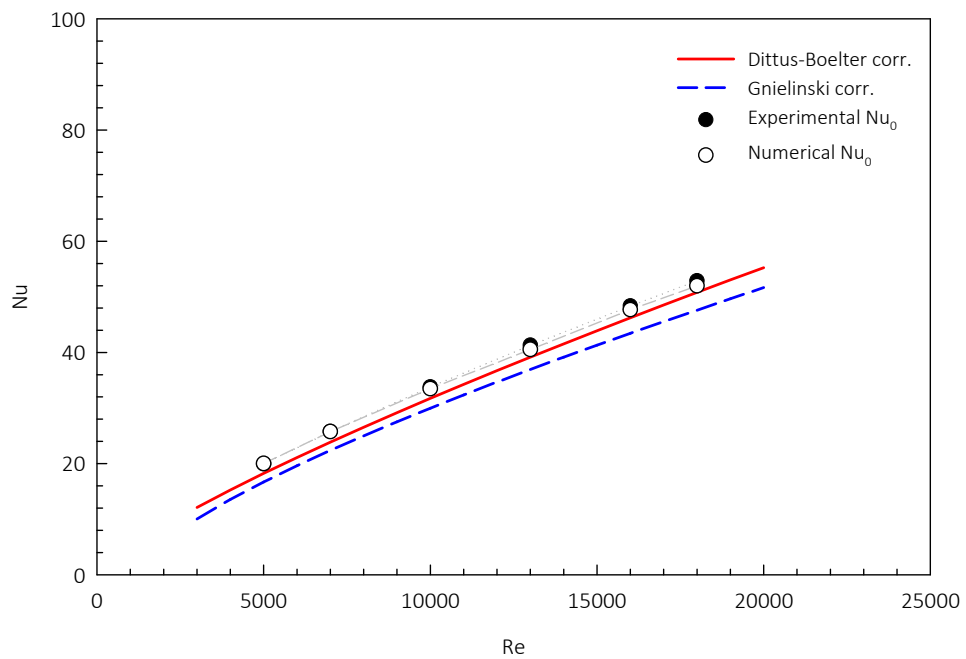


Figure 5.13 Comparison of predicted  $Nu_0$  and corresponding correlations

### 5.3 Validation of numerical simulation

In order to validate the numerical model, the experimental data were required for comparison. Therefore, a set of experiments was preliminary conducted. The experimental data were used to compare with the predicted values from numerical simulation. For comparison purpose, the numerical simulation was carried out under the same condition of a constant surface heat flux on the top wall. The following sections detail this validation process.

#### 5.3.1 Comparison of friction characteristics

The comparisons of predicted friction factor with experimental friction factor are presented in Figure 5.14 and 5.15. The predicted friction factors obtained from numerical solutions were in reasonable agreement with the friction factors compiled from the preliminary experiment. The maximum deviation of the predicted friction factor compared with the experimental data was 9.32% corresponding to the baffle 'a/H=0.50 b/H=0.20 p/H=1.00'.

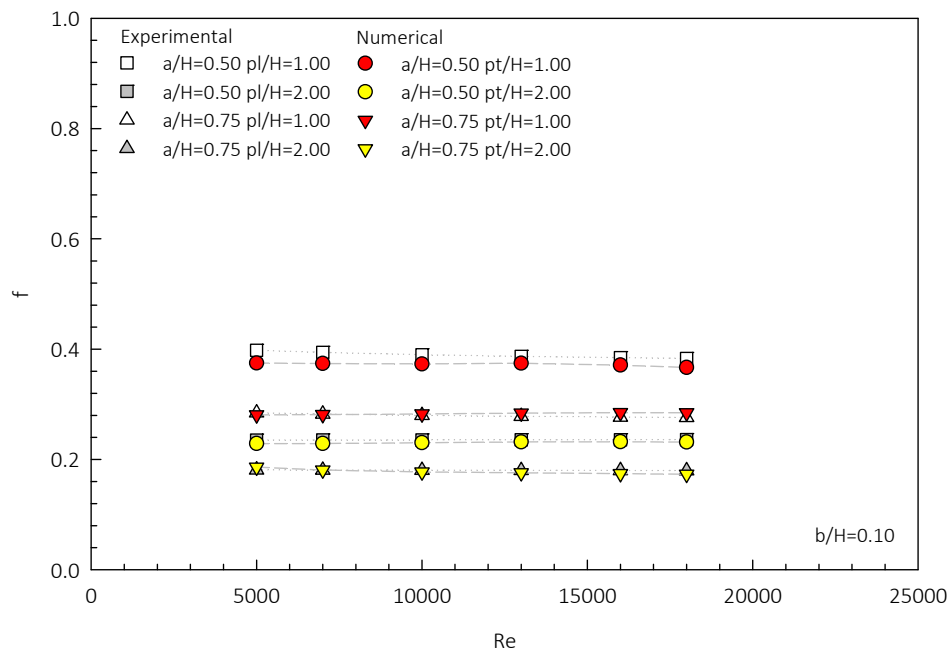


Figure 5.14 Comparison of experimental and numerical  $f$

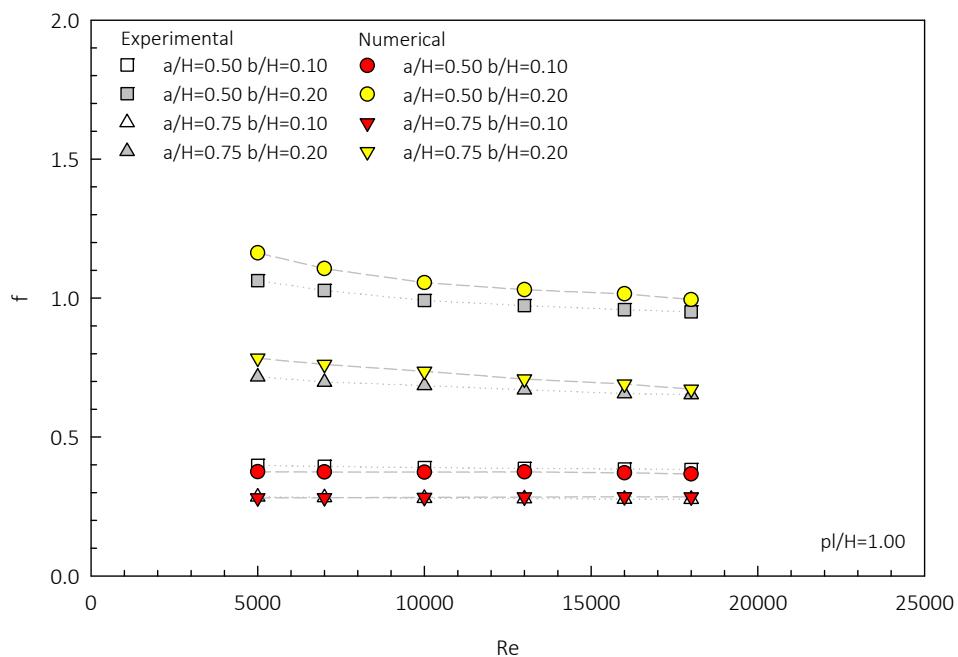


Figure 5.15 Comparison of experimental and numerical  $f$

### 5.3.2 Comparison of heat transfer characteristics

The comparisons of predicted Nusselt number with experimental friction factor are presented in Figure 5.16 and 5.17. The predicted Nusselt numbers attained from numerical solutions were in reasonable agreement with the Nusselt numbers compiled from the prior experiment. However, the maximum deviation of the predicted Nusselt number compared with the experimental data was 5.98% corresponding to the baffle 'a/H=0.50 b/H=0.10 p/H=2.00'. Consequently, the numerical solutions based on the validation results were acceptable.

The constructed numerical model was entirely verified and validated. The model could be used to represent the specified problem of interest. Next, the numerical computations with various flow rates and different geometric parameters were performed to investigate the fluid flow and heat transfer characteristics in the sinusoidal wavy baffle channel. Chapter 6 presents and discusses the numerical results of various baffles' arrangements on the key quantifying performance factors using the air as a working fluid. Chapter 7 presents and discusses the effects of various particle sizes and volume fraction on the given key performance factors for the proposed baffle's geometry using  $Al_2O_3$ -water as a working fluid.

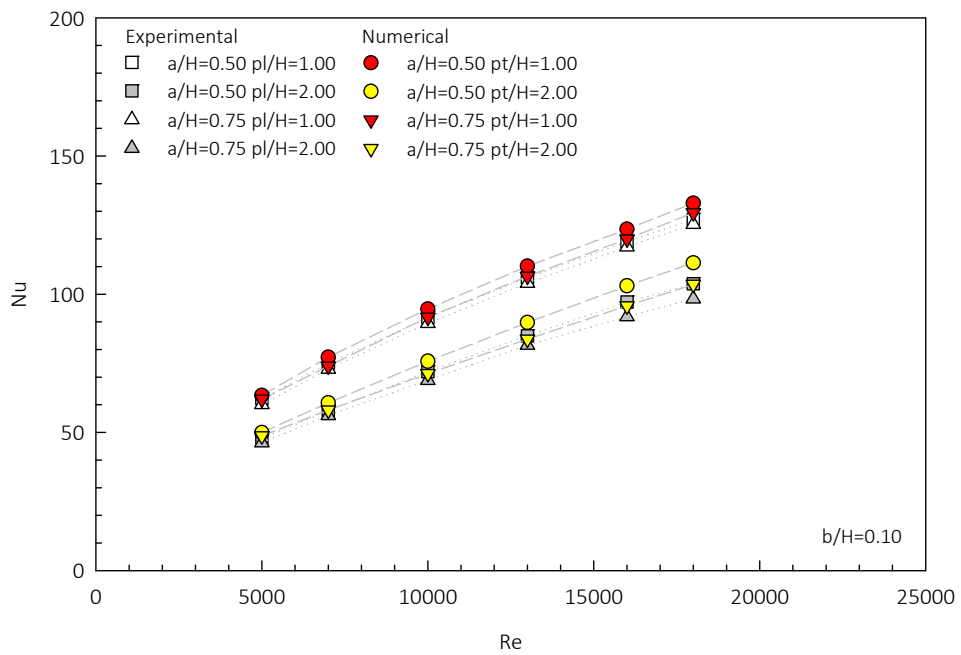


Figure 5.16 Comparison of experimental and numerical Nu

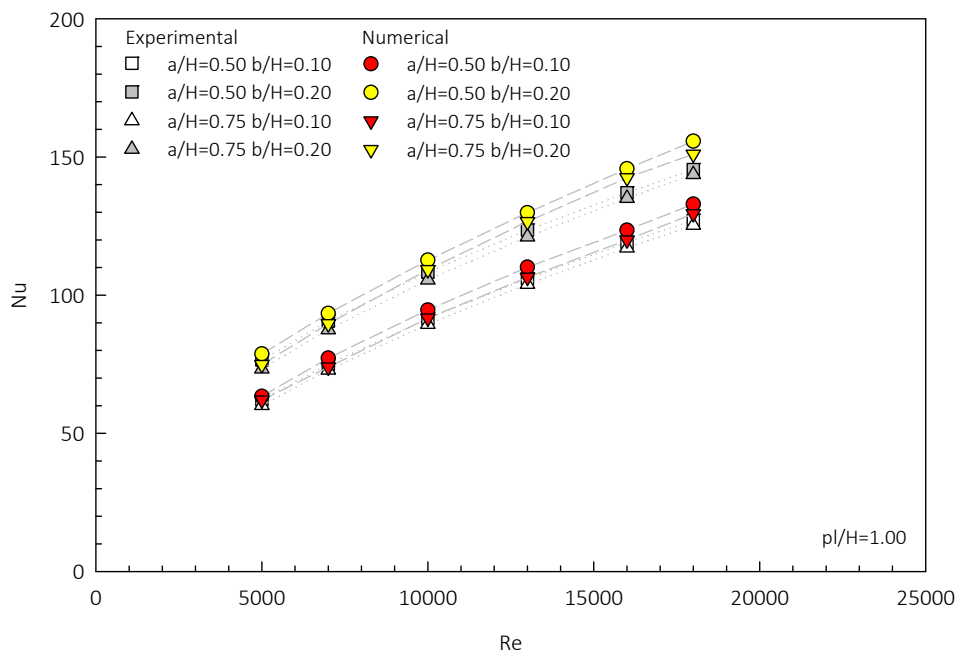


Figure 5.17 Comparison of experimental and numerical Nu

## CHAPTER 6

# NUMERICAL INVESTIGATION OF AIR FLOW

This chapter describes and discusses the effects of baffle geometry, arrangement, and flow conditions on the flow and heat transfer characteristics. First, the flow topology and coherent structure are explained to investigate the flow characteristics of the baffle channel. Then, the evaluated key performance factors with respect to smooth channel are reported to ascertain the degree of enhancement in pressure loss and heat transfer rate. The assessed thermal performances at the same pumping power are included. Finally, the development of empirical correlations related to flow condition and geometric parameters are introduced to predict the performance factors.

### 6.1 The baffle channel computation of air flow

Subsequent to the verification and validation stages in Chapter 5, the numerical simulations were conducted to investigate the fluid flow and heat transfer characteristics in the sinusoidal wavy baffle channel. For the air flow study, the numerical model was developed under the following assumptions:

- Steady three-dimensional fluid flow and heat transfer.
- Turbulent and incompressible flow.
- Constant thermophysical properties
- Negligible body forces.
- Negligible viscous dissipation.
- Negligible radiation heat transfer.
- No thermal energy sources within the fluid.

The range of geometric parameters, flow condition, and thermal condition considered in the numerical investigation of air flow is organized in Table 6.1. The periodic and thermal boundary conditions were applied to the computational domain which was previously illustrated in Figure 4.2 and 4.3. Since an assumption in the air flow study was constant thermophysical properties, therefore the air properties were based on the inlet temperature (300K). The required channel characteristic, solid wall and the air properties are summarized in Table 6.2.

**Table 6.1** Geometric parameters and flow condition of air flow

<b>Geometric parameters</b>	<b>Values</b>
Relative amplitude, $a/H$	0.25, 0.50, 0.75, 1.00
Relative height, $b/H$	0.05, 0.10, 0.15
Relative longitudinal pitch, $pL/H$	0.5, 1.0, 1.5
Relative transverse pitch, $pt/H$	1.0
Channel height, $H$	0.02 m
Hydraulic diameter, $D_h$	0.04 m
<b>Flow and thermal conditions</b>	<b>Values</b>
Working fluid	Air
Reynolds number, $Re$	5,000 – 18,000
Surface heat flux, $q_s$	1,000 W/m <sup>2</sup>

**Table 6.2** Reference values used in computations of air flow [93]

<b>Channel characteristic</b>	
Hydraulic diameter, $D_h$	0.04 m
<b>Aluminum properties (300K)</b>	
Density, $\rho$	2702 kg/m <sup>3</sup>
Specific heat at constant pressure, $c_p$	903 J/kg·K
Thermal conductivity, $k$	237 W/m <sup>2</sup> ·K
<b>Air properties (300K, 1atm)</b>	
Density, $\rho$	1.1614 kg/m <sup>3</sup>
Specific heat at constant pressure, $c_p$	1006.43 J/kg·K
Thermal conductivity, $k$	0.0263 W/m <sup>2</sup> ·K
Dynamic viscosity, $\mu$	1.846×10 <sup>-5</sup> kg/m·s
Kinematic viscosity, $\nu$	1.589×10 <sup>-5</sup> m <sup>2</sup> /s
Prandtl number, $Pr$	0.707
Inlet temperature, $T_{in}$	300 K

The turbulence model used in the computations was the RNG  $k-\varepsilon$  turbulence model with the enhanced wall treatment option. Note that, the numerical schemes for discretization as presented previously in Table 4.2 were employed to solve for the numerical solutions. The required input for the computations was the mass flow rate specified from the observed Reynolds number. The specified mass flow rates for the air flow study are listed in Table 6.3. The numerical simulations were computed iteratively until all of monitoring residuals had

reached the given convergence criteria. Consequently, the numerical simulations were considered to be solved.

**Table 6.3** Specified mass flow rates in computation of air flow

Reynolds number	Mass flow rate: kg/s
5,000	$4.6150 \times 10^{-4}$
7,000	$6.4610 \times 10^{-4}$
10,000	$9.2300 \times 10^{-4}$
13,000	$11.9990 \times 10^{-4}$
16,000	$14.7680 \times 10^{-4}$
18,000	$16.6140 \times 10^{-4}$

The numerical simulations were carried out for various flow conditions and different geometric parameters specified earlier in Table 6.1. The essential output values were read out from the numerical solutions to calculate the key performance factors which were friction factor, Nusselt number, and the thermo-hydraulic performance. Moreover, the flow topology analysis and coherent structure was also introduced to explain the flow behaviors. For the flow topology analysis, the baffle channel was cut into cross-sectional transverse planes along the flow direction (the x-axis) on the dimensionless  $x/H$  locations as depicted in Figure 6.1. For the purpose of presentation, the location of nominated transverse plane was begun at a crest of a baffle and ended at another crest of a consecutive baffle in the upward zone. The velocity gradient tensors on each transverse plane were calculated. The streamlines and the streamsurfaces were developed based on the velocity gradient tensors. For coherent structure, the Q criterion was used as the vortex detection scheme.

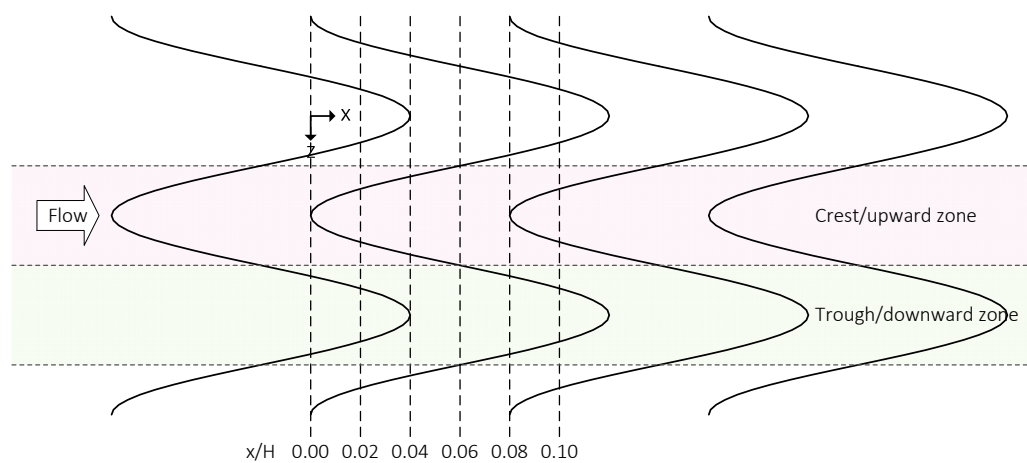


**Figure 6.1** Locations of cross-sectional transverse plane of interest

## 6.2 Flow characteristics of air

This section presents the effects of the geometric parameters on the pressure loss and the flow characteristics. The friction factors of the air flow in the baffle channel were individually determined at Reynolds number ranging from 5,000 to 18,000. The friction factor was calculated from the read out pressure drop across the periodic module along the streamwise direction (the x-axis). Then, the friction factor ratio was estimated with respect to the smooth channel at the same Reynolds number.

### 6.2.1 Effects of Reynolds number and longitudinal pitch

Typically, for a fully developed turbulent flow in the channel, the friction factor decreased slightly with increasing Reynolds number due to the destruction of the viscous sublayer. The values of friction factor for the baffle channel were markedly higher than for the smooth channel at a given range of Reynolds numbers as expected. So, the friction factor ratio was presented to ascertain the degree of pressure loss enlargement. The effects of Reynolds number and  $p/H$  on the friction factor ratio for the baffles having  $b/H=0.05$ , 0.10, and 0.15 are presented in Figure 6.2, 6.3, and 6.4, respectively. The friction factor ratio increased considerably with increasing Reynolds number. It indicated that the increasing rate of friction factor for the baffle channel was noticeably higher than for the smooth channel.

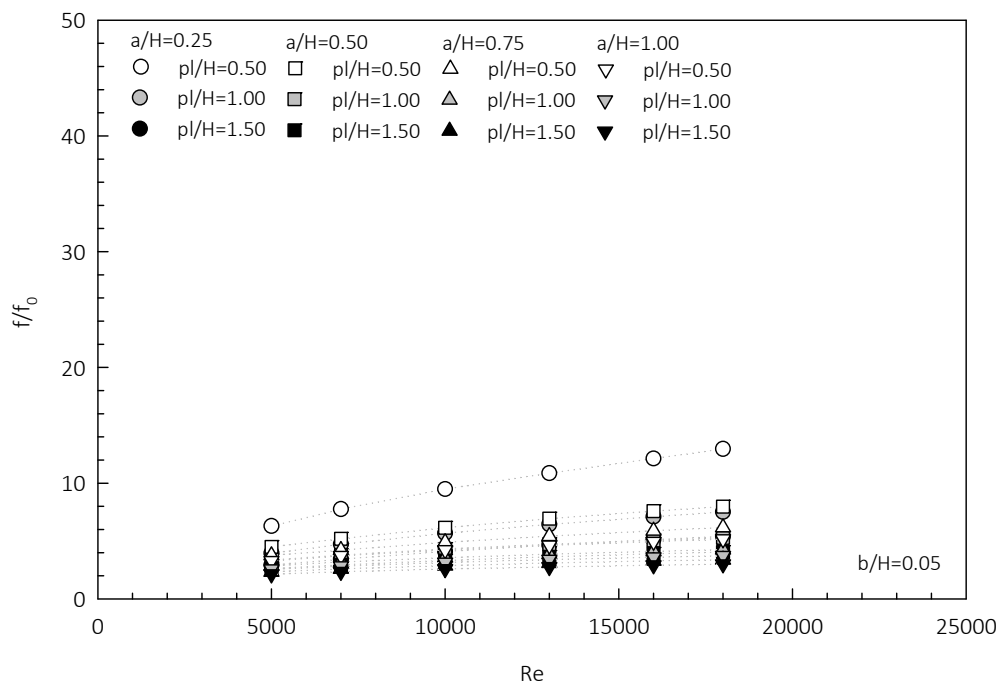
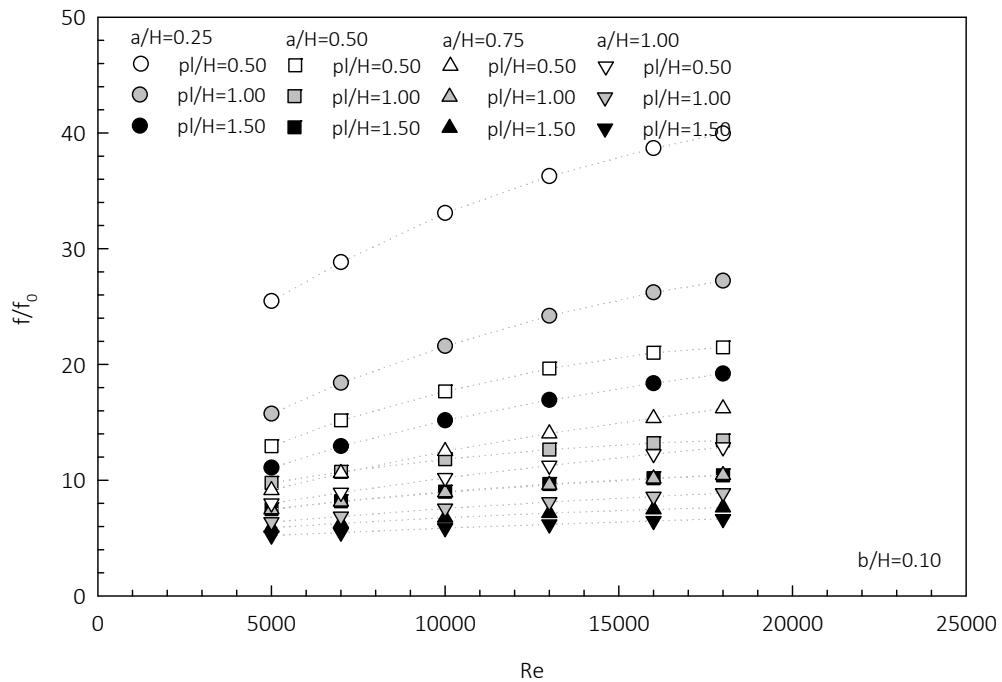
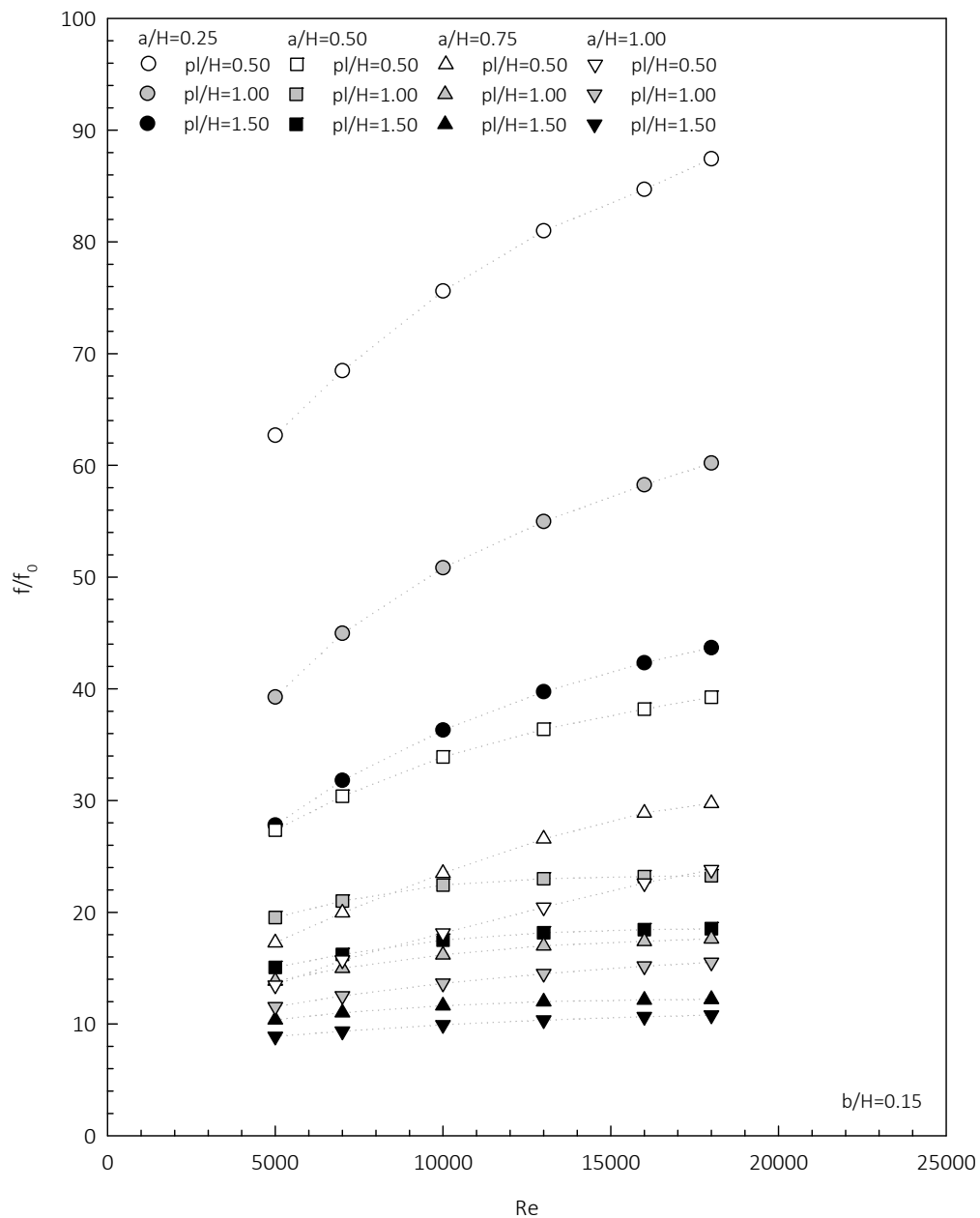


Figure 6.2 Variation of  $f/f_0$  with Re for varied  $p/H$  at  $b/H=0.05$



**Figure 6.3** Variation of  $f/f_0$  with  $Re$  for varied  $p/H$  at  $b/H=0.10$

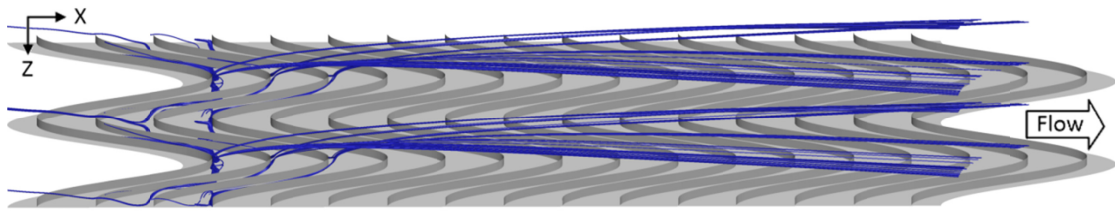
Considering results of the baffles having  $b/H=0.05$  (Figure 6.2), for the case  $p/H=0.50$ , the friction factor ratio of the same amplitude increased noticeably with increasing Reynolds number. However, for the cases  $p/H=1.00$  and  $1.50$ , the friction factor ratio increased slightly with increasing Reynolds number. With an expansion of longitudinal pitch, the friction factor ratio dropped considerably due to expanded area between the consecutive baffles which reduced the pressure drop across the pitch interval. The results of the baffles having  $b/H=0.10$  and  $0.15$  as shown in Figure 6.3 and 6.4 also gave the similar effects for the friction factor ratio. Nevertheless, they provided greatly higher values due to their higher blockage ratios. According to the numerical results, the values of friction factor ratio of the baffle channel within a given range of Reynolds numbers were 2.13 – 87.43 times compared with the smooth channel.



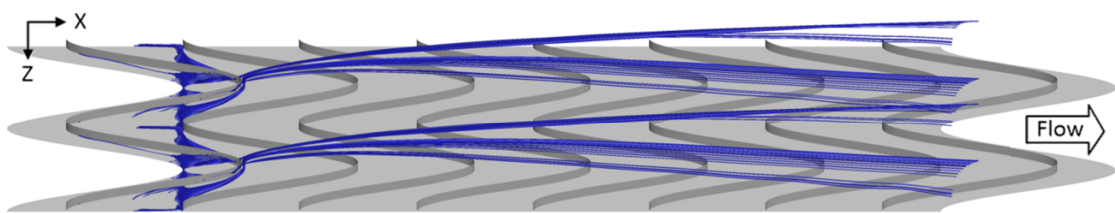
**Figure 6.4** Variation of  $f/f_0$  with  $Re$  for varied  $p/H$  at  $b/H=0.15$

Figure 6.5a, b, and c present the streamlines of impinging flow released from the crest of baffle 'a/H=0.75 b/H=0.10' at  $Re=10,000$  for varied longitudinal pitches:  $p/H=0.50$ ,  $1.00$ , and  $0.50$ , respectively. In upward zone, at the area in front of the crest of each baffle, the main flow's streamlines were separated along the profile of the baffle. The separated streamlines combined with the others and lifted up at the trough of the next baffle in downward zone. Considering the case  $p/H=1.50$  (Figure 6.5c), the flow streamed across about six modules (approximately  $9H$ ) and impinged into the area in front of the crest of seventh consecutive baffle in upward zone. After impinging, the flow was separated, combined with the others, and streamed up again

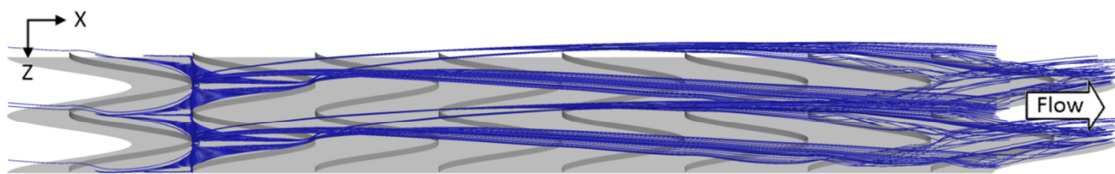
in downward zone. It was observed that, this flow pattern was repeated continuously along the baffle channel. The narrower pitches also produced similar flow patterns except that the impinging lengths were extended longer than the wider pitches.



(a) ' $a/H=0.75$   $b/H=0.10$   $pL/H=0.50$ '



(b) ' $a/H=0.75$   $b/H=0.10$   $pL/H=0.50$ '



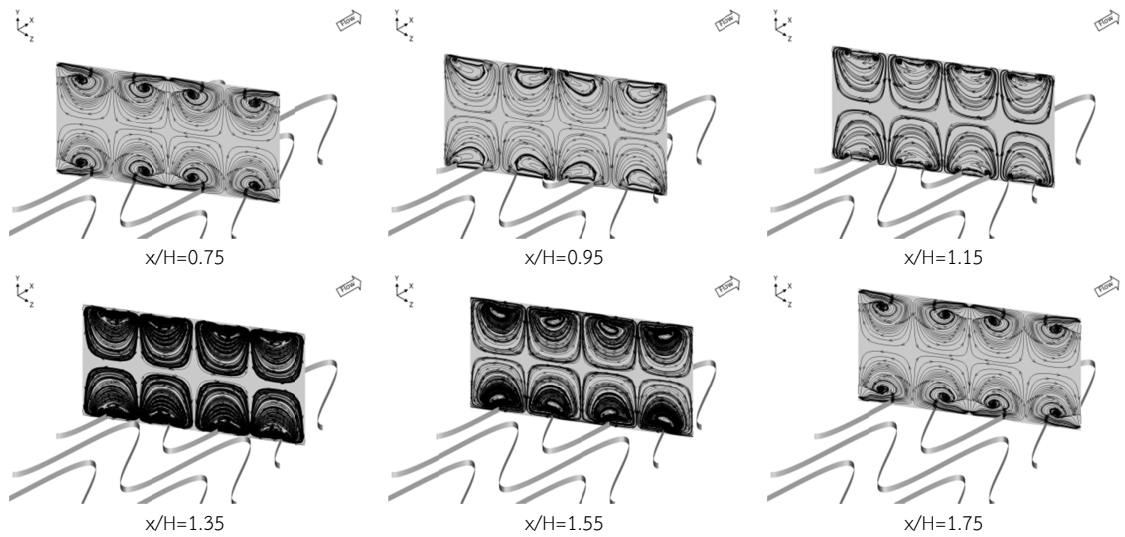
(c) ' $a/H=0.75$   $b/H=0.10$   $pL/H=1.50$ '

**Figure 6.5** Streamlines released from the crest of baffles at  $Re=10,000$

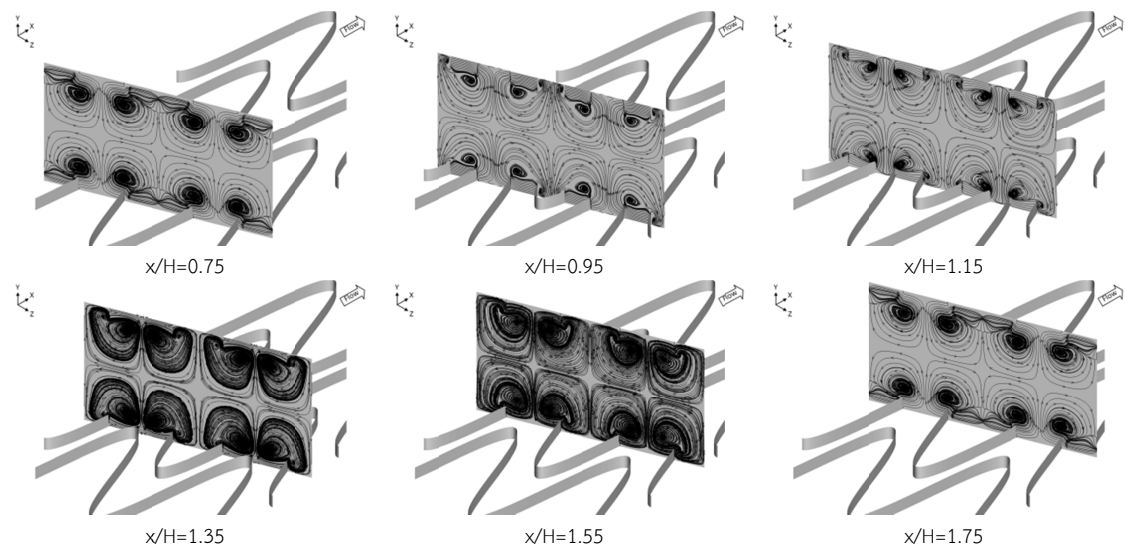
### 6.2.2 Effects of baffle height

Figure 6.6a, b, and c present the secondary flow patterns on the nominated transverse planes of the baffle ' $a/H=0.75$   $pL/H=1.00$ ' at  $Re=10,000$  for varied baffle heights:  $b/H=0.05$ ,  $0.10$  and  $0.15$ , respectively. Considering the case  $b/H=0.05$  (Figure 6.6a), in upward zone, at the crest of baffle, the main flow was forced to escape along the wave of the baffle. Therefore, the main flow was separated and the secondary flow was occurred. It was observed that, the secondary flow behaved in pattern of counter rotating vortex pair. The vortex pair was impinged to the area behind the crest of baffle. Simultaneously, in downward zone, the separated flow was lifted up and combined with the other separated flows at the area in front of the trough of baffle. A part of streamed up flow was induced downward and reattached to the area behind the crest of other baffle in upward zone. These flow

patterns happened continuously in the baffle channel. The other baffle heights also provided the similar flow behaviors except that the strength of counter rotating vortex pair seemed stronger.

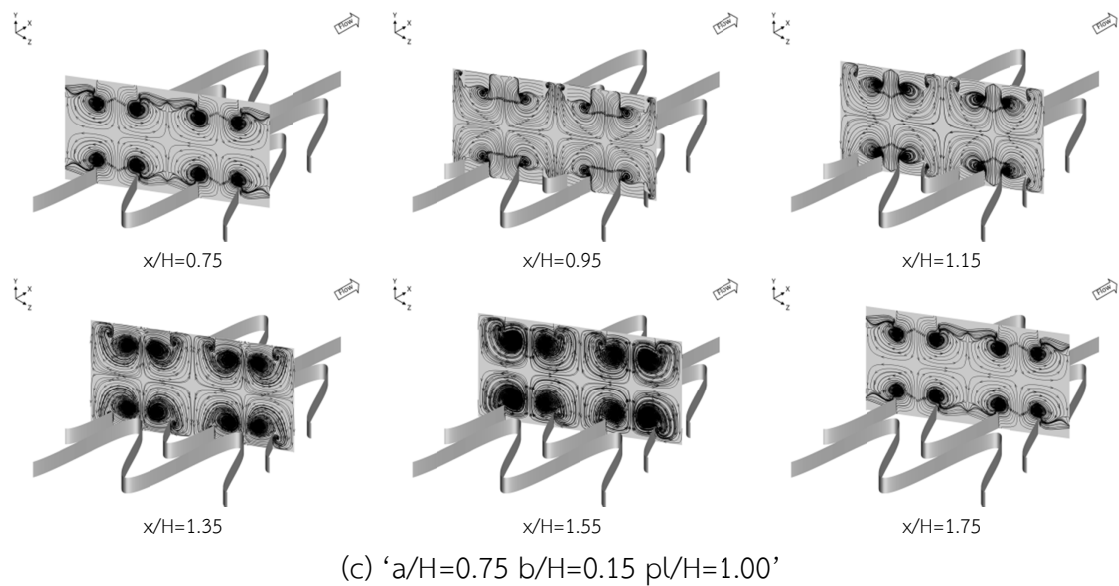


(a) ' $a/H=0.75$   $b/H=0.05$   $p/H=1.00$ '



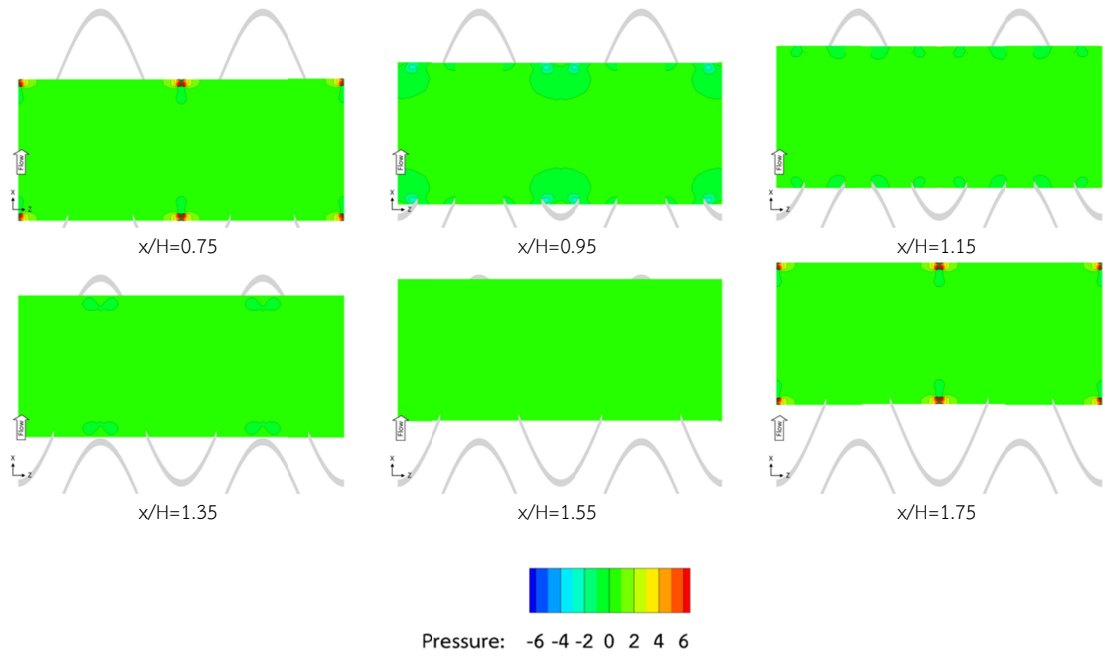
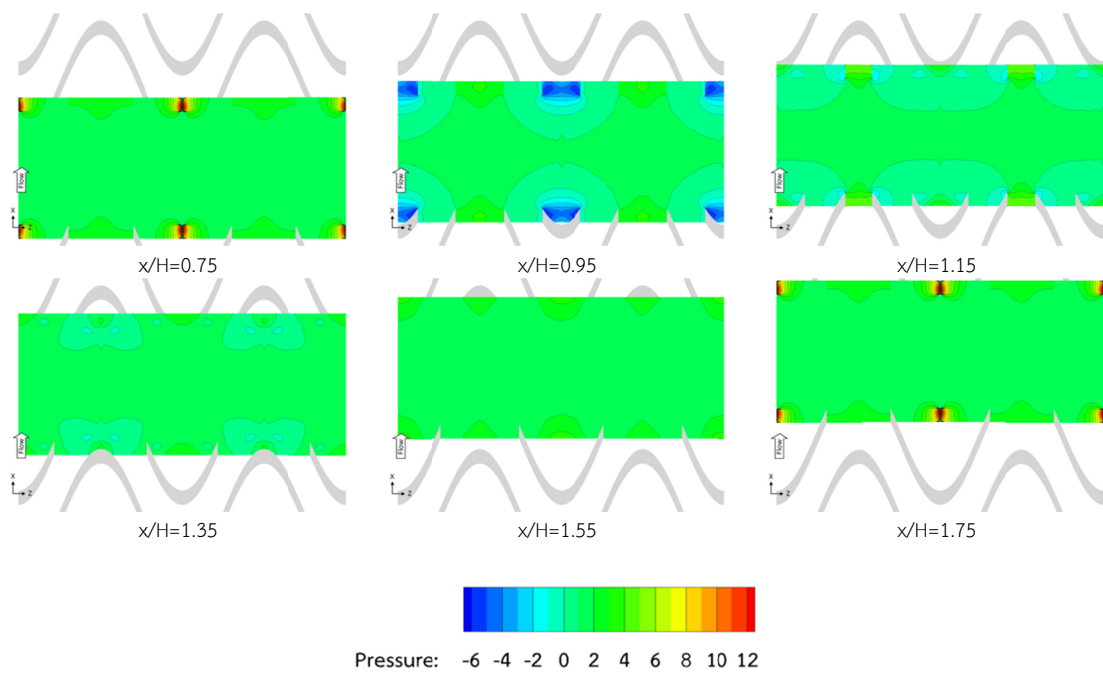
(b) ' $a/H=0.75$   $b/H=0.10$   $p/H=1.00$ '

Figure 6.6 Secondary flow patterns for varied  $b/H$  at  $Re=10,000$



**Figure 6.6** Secondary flow patterns for varied  $b/H$  at  $Re=10,000$  (cont'd)

Figure 6.7a, b, and c present the pressure distributions on the nominated transverse planes of the baffle 'a/H=0.75 pL/H=1.00' at  $Re=10,000$  for varied baffle heights:  $b/H=0.05$ ,  $0.10$  and  $0.15$ , respectively. These pressure contours were plotted to observe the region where the high pressure gradient existed. Considering the case  $b/H=0.10$  (Figure 6.7b), in upward zone, the highest positive pressure (red color) occurred in the area in front of the crest of baffle which was the stagnation point. The main flow had hit the crest of baffle. Behind the crest of baffle, the negative pressure (blue color) was presented. The negative pressure induced the counter rotating vortex pair to impinge to the heat surface area behind that baffle. With extending the baffle height, these pressure gradients became greater which indicated by the blue area was expanded while the green area (zero gradient) was reduced.

(a) ' $a/H=0.75$   $b/H=0.05$   $pL/H=1.00$ '(b) ' $a/H=0.75$   $b/H=0.10$   $pL/H=1.00$ '**Figure 6.7** Pressure distribution for varied  $b/H$  at  $Re=10,000$

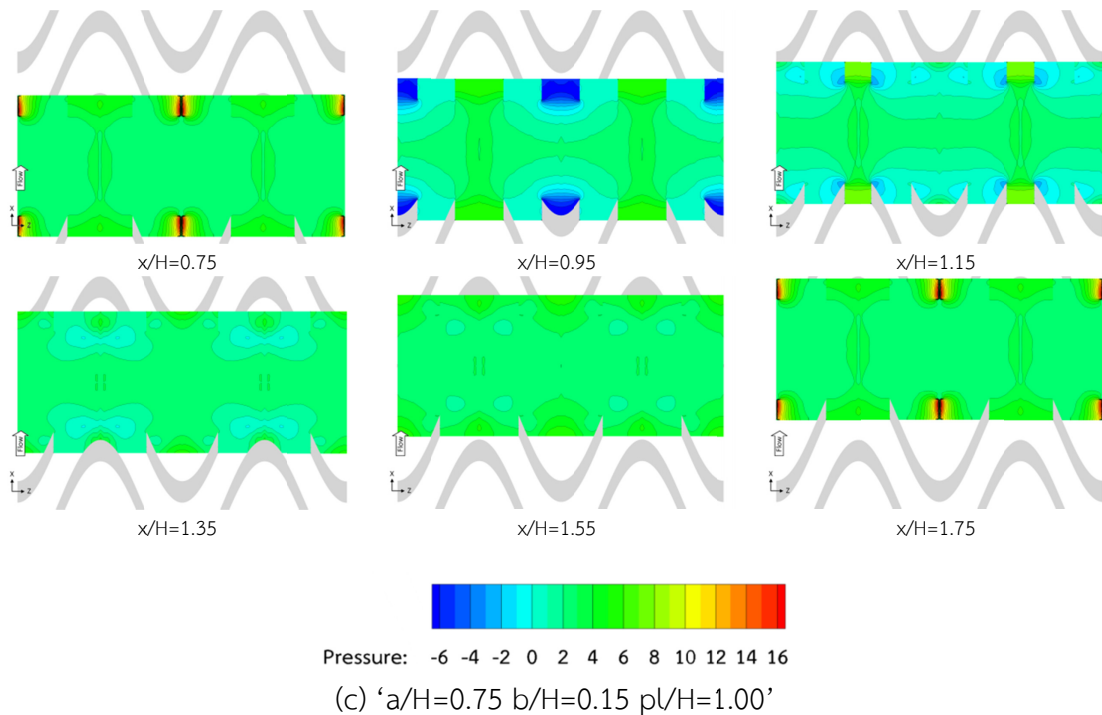
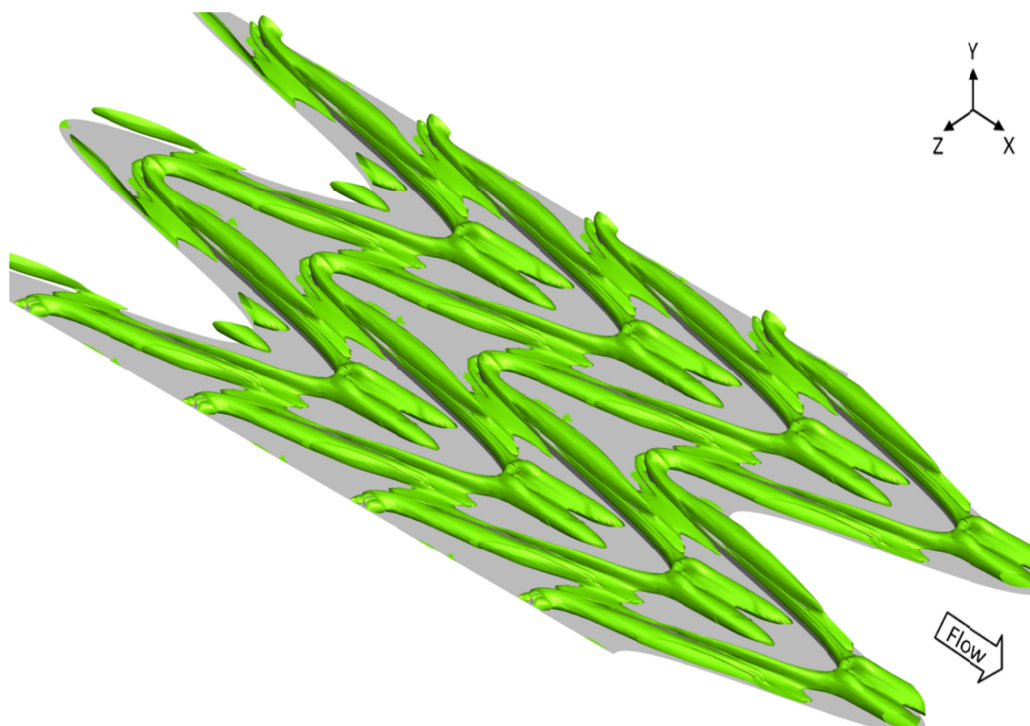
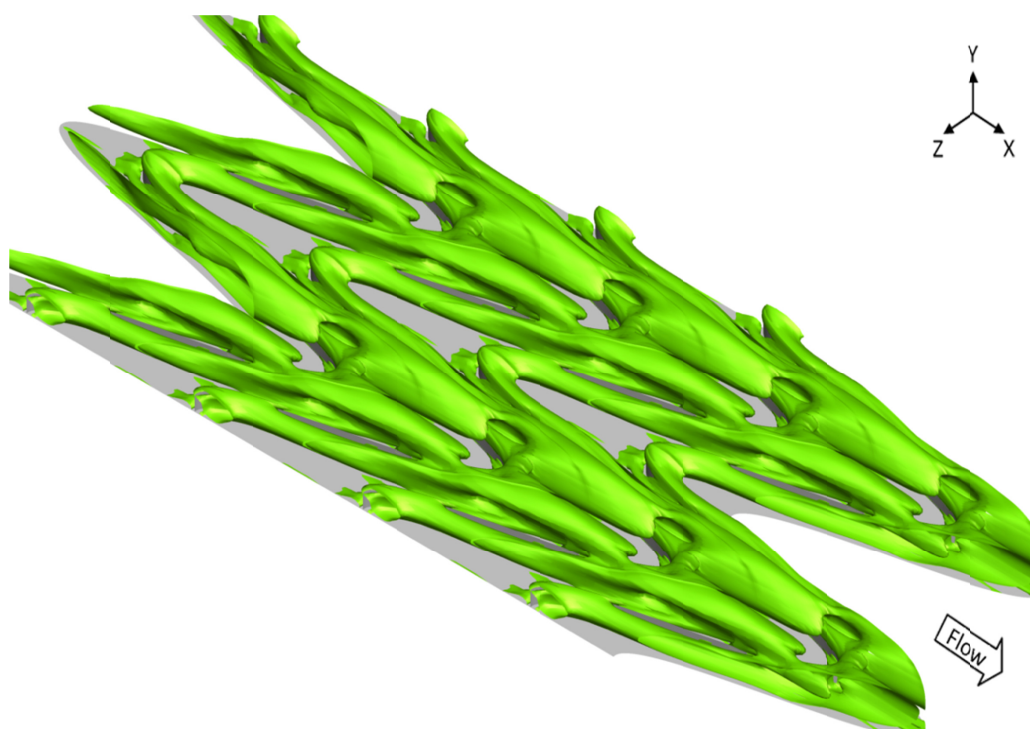


**Figure 6.7** Pressure distribution for varied  $b/H$  at  $Re=10,000$  (cont'd)

Figure 6.8a, b, and c present the  $Q$  isosurface of the baffle 'a/H=0.75 p/H=1.00' at  $Re=10,000$  for varied baffle heights:  $b/H=0.05$ , 0.10 and 0.15, respectively. The  $Q$  isosurface was used to visualize the coherent structure or the vorticity field. The location of high vorticity was indicated by the green isosurface tube. Inside the green tube, the secondary flow was recirculated continuously. The recirculation tube represented the secondary flow structure resulting from the existence of baffles. Considering the case  $b/H=0.05$  (Figure 6.8a), the isosurface tube existed along the profile of the baffles. In upward zone, the main flow was separated at the crest of baffle. The secondary flow recirculated in streamwise direction along the isosurface tube. In downward zone, at the trough of baffle, the isosurface combined with the others and lifted across that baffle. These  $Q$  isosurface patterns also occurred continuously along the baffle channel. With extending the baffle height, the isosurface tube became bigger which indicated that the vorticity inside the recirculation tube was more intensified.

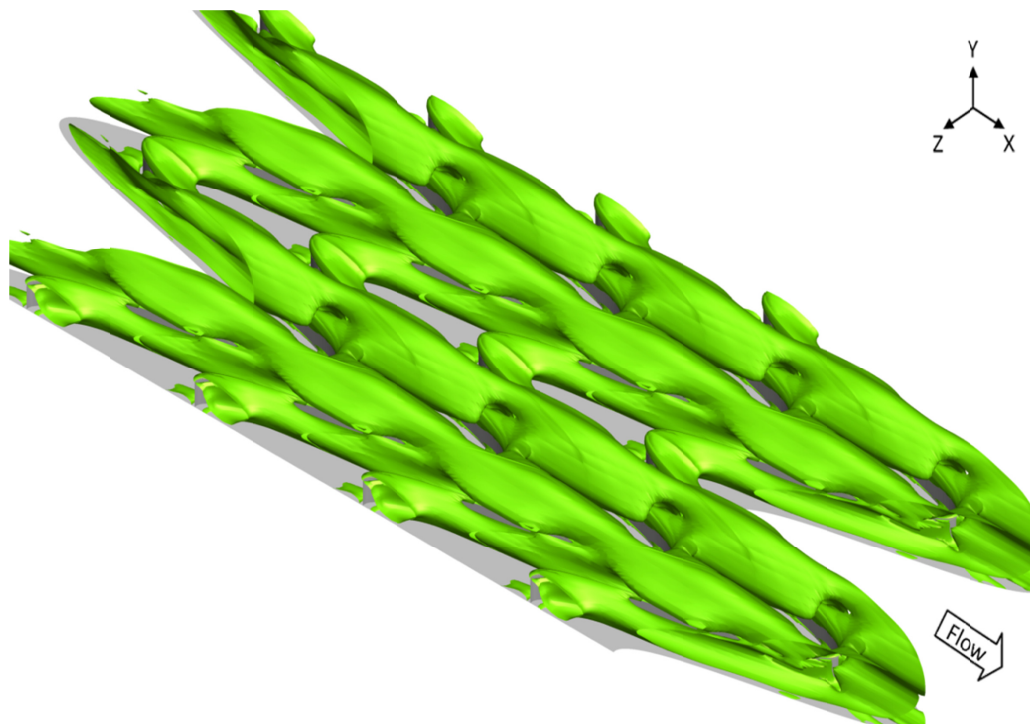


(a) ' $a/H=0.75$   $b/H=0.05$   $p/H=1.00$ '



(b) ' $a/H=0.75$   $b/H=0.10$   $p/H=1.00$ '

**Figure 6.8** The Q isosurface for varied  $b/H$  at  $Re=10,000$



(c) 'a/H=0.75 b/H=0.15 p/H=1.00'

**Figure 6.8** The Q isosurface for varied b/H at Re=10,000 (cont'd)

The effects of extending baffle height on the friction factor ratio are exemplified in Figure 6.9, 6.10, and 6.11. The friction factor ratio of the baffles having b/H=0.05 and 0.10 increased slightly with increasing Reynolds number. For the case b/H=0.15, the friction factor ratio increased considerably with an increase in Reynolds number. The extension of baffle height gave a result in rapid increase of the friction factor ratio for each given Reynolds number. This is because of the strength of induced vortex pair from the secondary flow that impinged on the area behind each wave of the baffle depended on the blockage ratio. The stronger impingement from greater baffle height could persuade more pressure loss across the baffles. These behaviors are evidently presented in Figure 6.12 to 6.15. According to numerical results, the lowest friction factor ratio was found to be 2.13 times corresponding to the baffle 'a/H=1.00 b/H=0.05 p/H=1.50' at Re=5,000. The highest friction factor ratio was found to be 87.43 times corresponding to the baffle 'a/H=0.25 b/H=0.15 p/H=0.50' at Re=18,000.

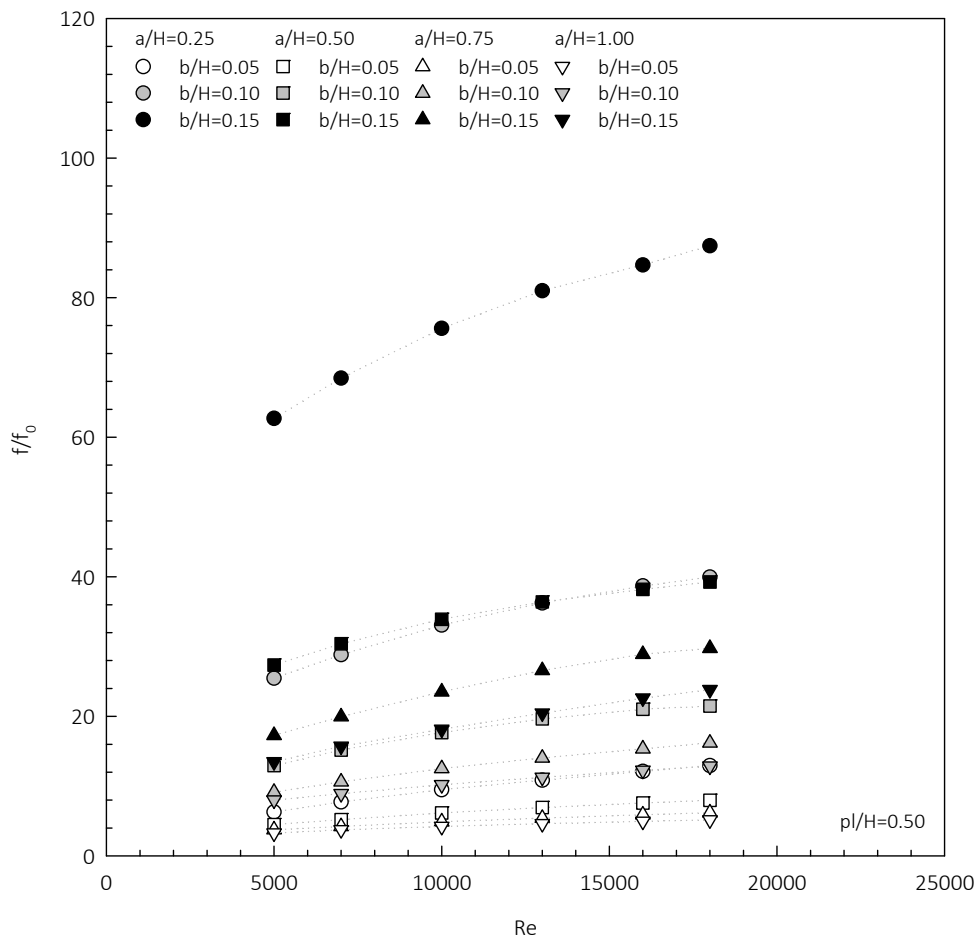


Figure 6.9 Variation of  $f/f_0$  with  $Re$  for varied  $b/H$  at  $pL/H=0.50$

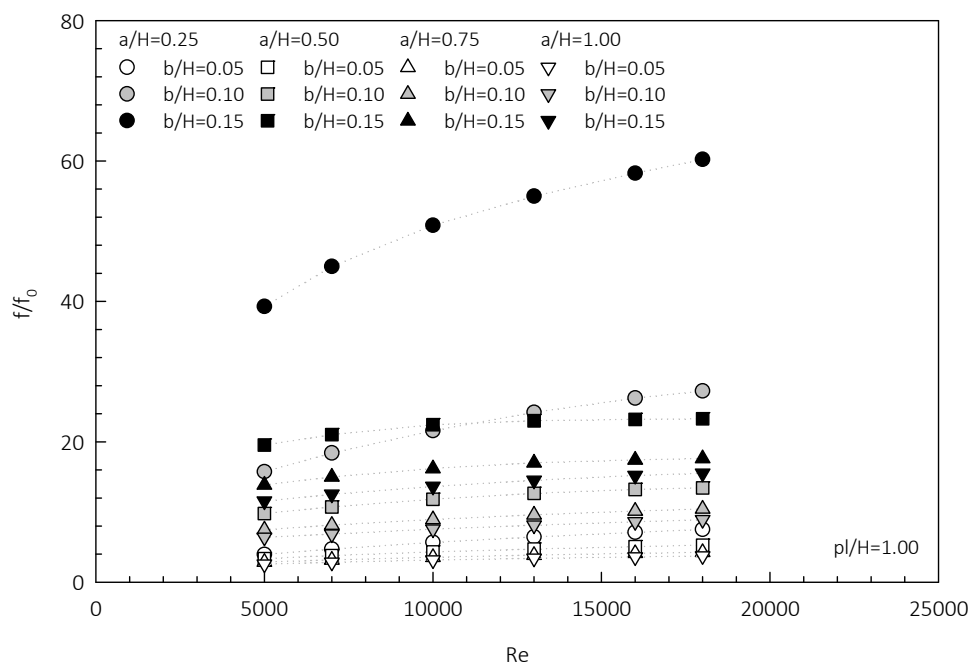


Figure 6.10 Variation of  $f/f_0$  with  $Re$  for varied  $b/H$  at  $pL/H=1.00$

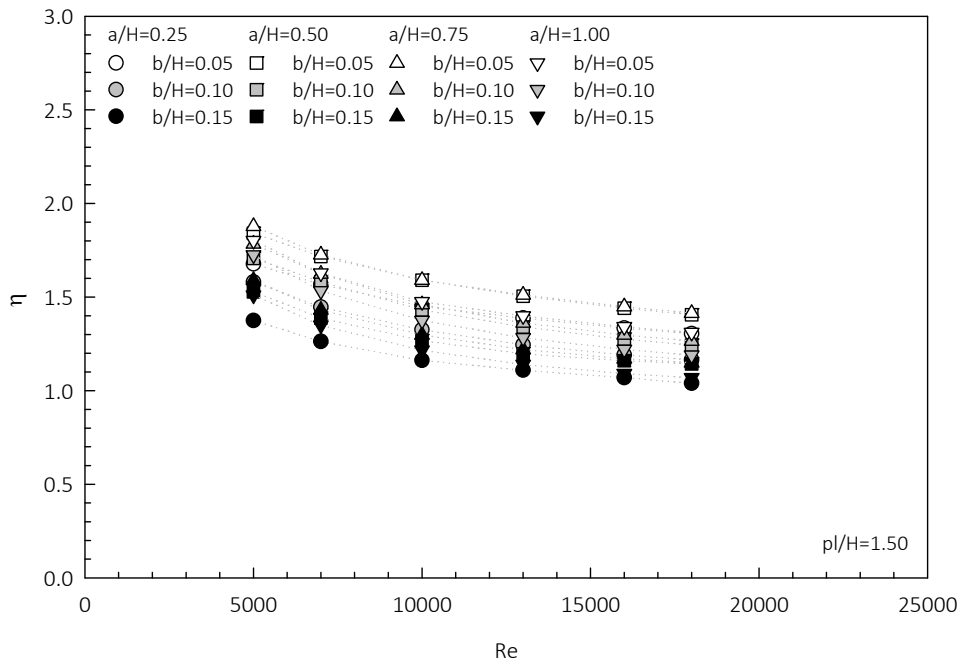


Figure 6.11 Variation of  $f/f_0$  with  $Re$  for varied  $b/H$  at  $pl/H=1.50$

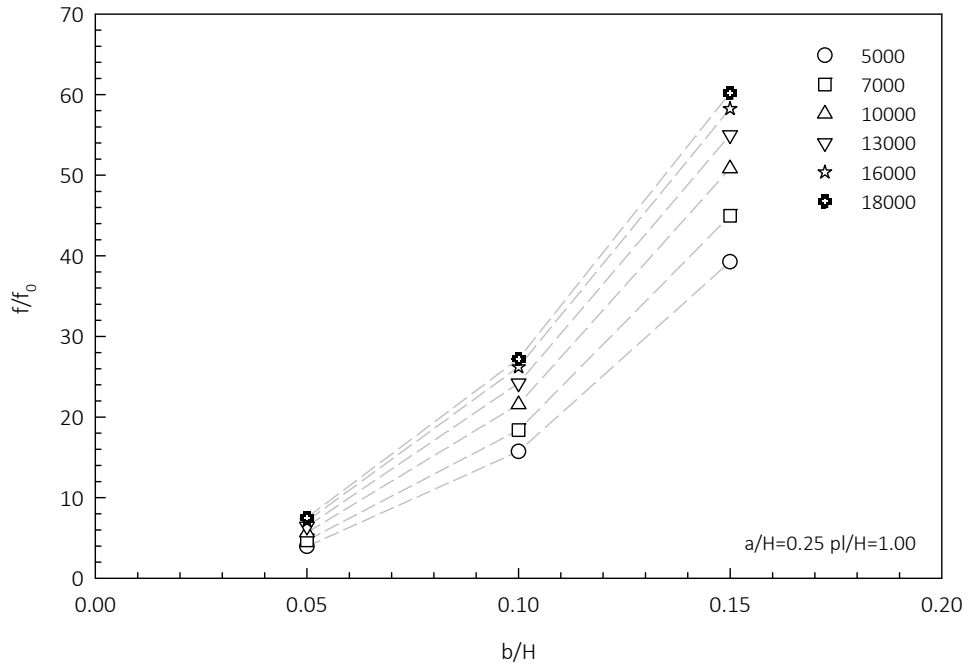


Figure 6.12 Variation of  $f/f_0$  with  $b/H$  for various  $Re$  at  $a/H=0.25$

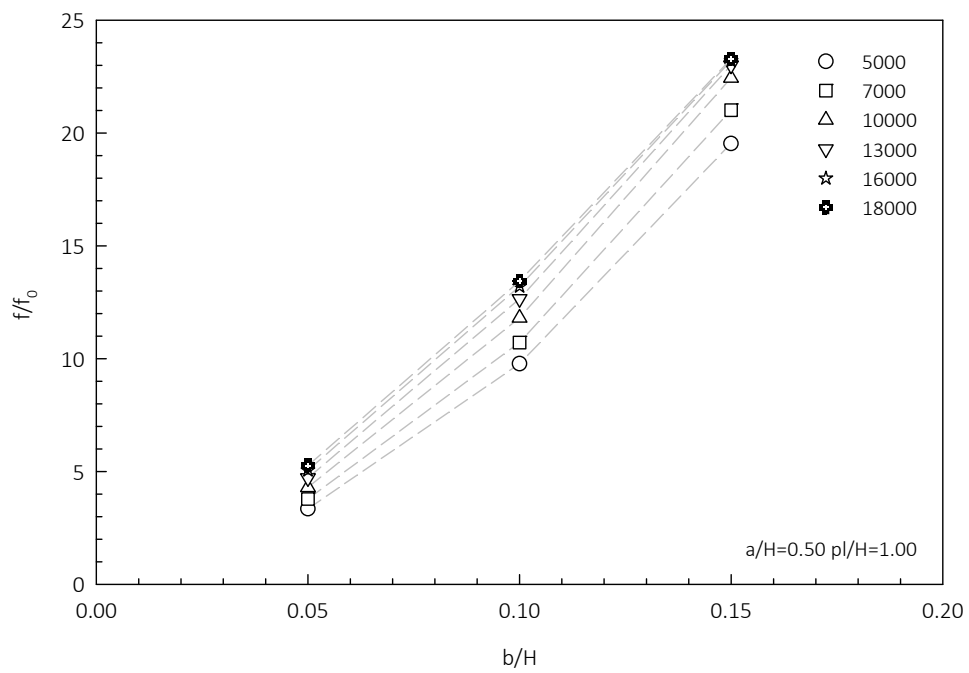


Figure 6.13 Variation of  $f/f_0$  with  $b/H$  for various  $Re$  at  $a/H=0.50$

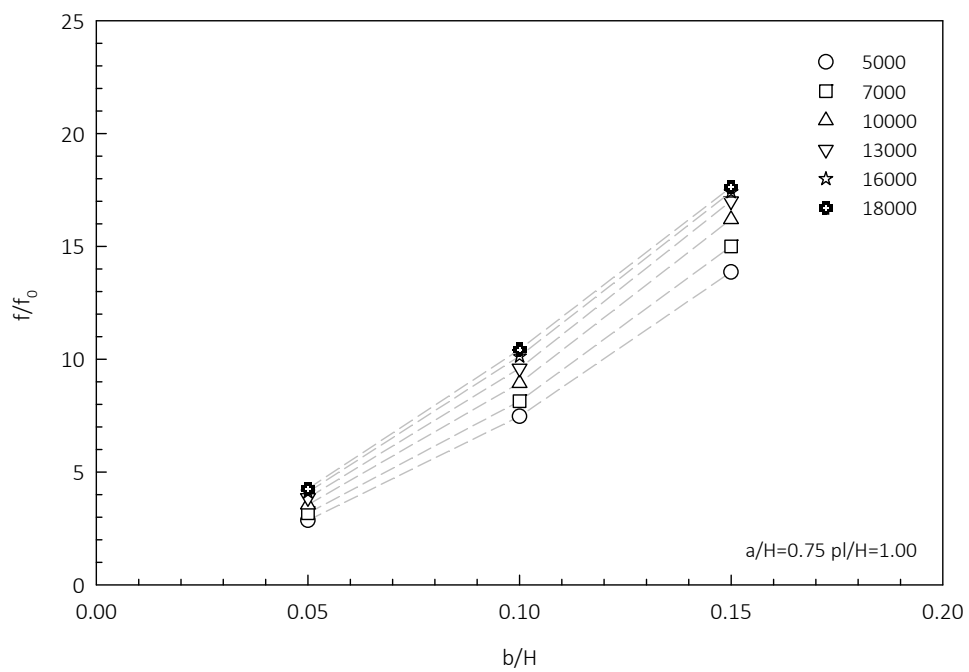


Figure 6.14 Variation of  $f/f_0$  with  $b/H$  for various  $Re$  at  $a/H=0.75$

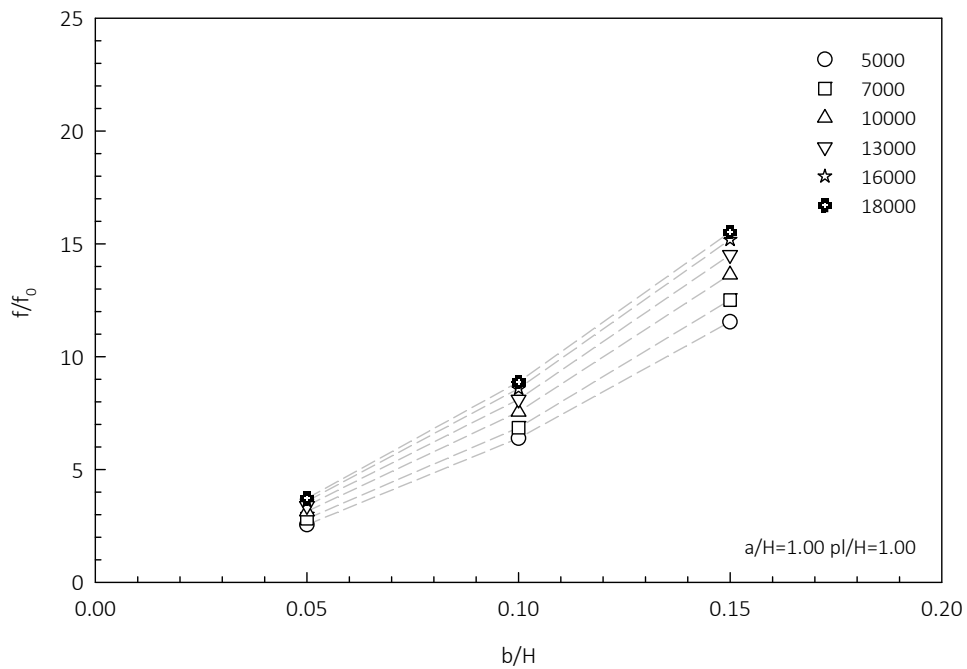
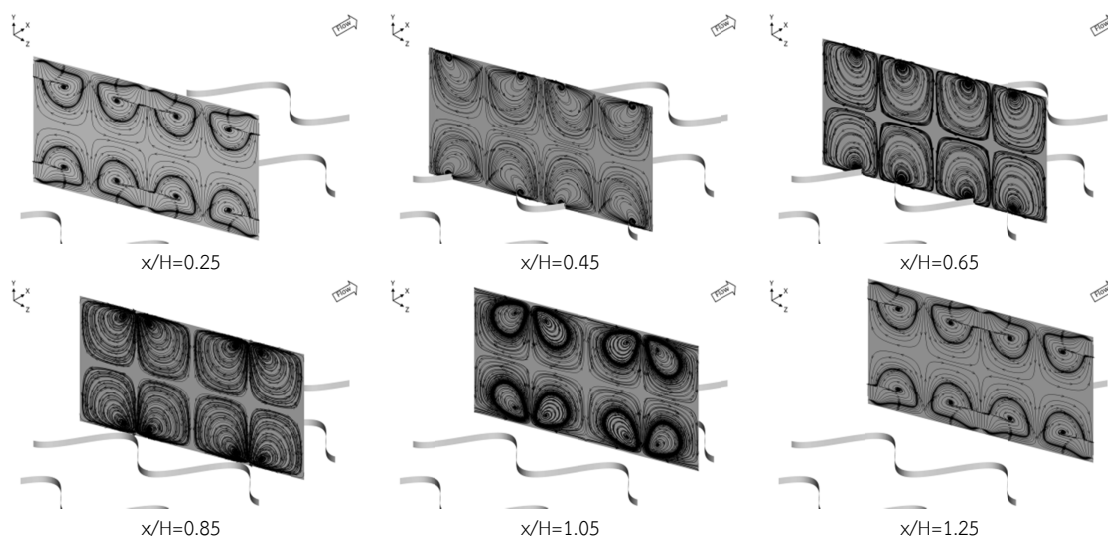


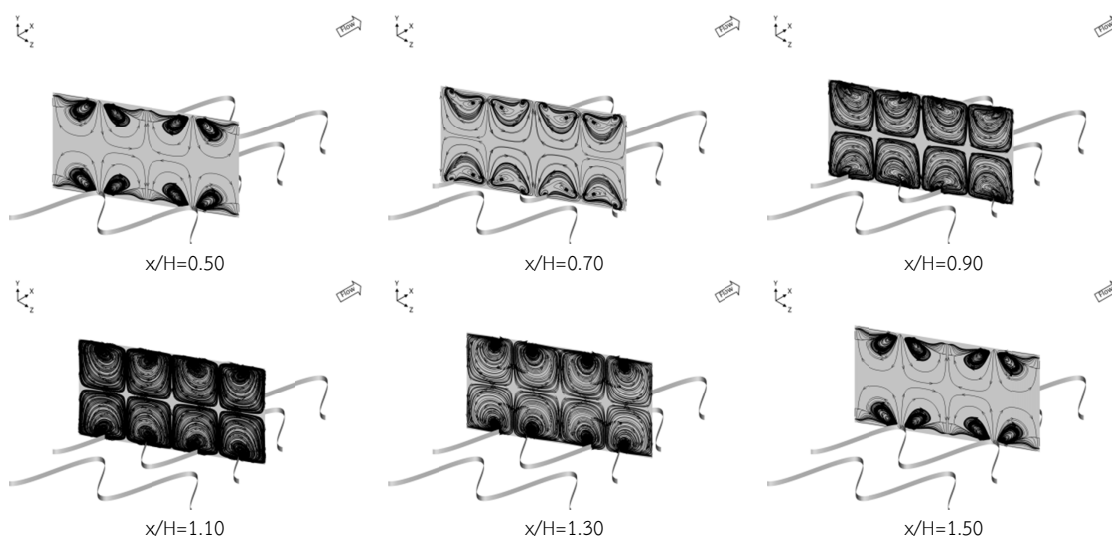
Figure 6.15 Variation of  $f/f_0$  with  $b/H$  for various  $Re$  at  $a/H=1.00$

### 6.2.3 Effects of baffle amplitude

Figure 6.16a, b, c, and d present the secondary flow patterns on the transverse planes of the baffle ' $b/H=0.10$   $p/H=1.00$ ' at  $Re=10,000$  for varied baffle amplitudes:  $a/H=0.25$ ,  $0.50$ ,  $0.75$ , and  $1.00$ , respectively. Considering the case  $a/H=0.25$  (Figure 6.16a), in upward zone, at the crest of baffle, it was appeared that the main flow was also forced to escape along the profile of baffle. The secondary flows also occurred in pattern of counter rotating vortex pairs. They were induced downward and impinged to the area behind the crest of baffle. Simultaneously, in downward zone, the separated flow was also lifted up and combined with the other flows at the area in front of the trough of baffle. These secondary flow behaviors were occurred continuously in the baffle channel. The other baffle amplitudes also provided similar flow characteristics except that the strength of counter rotating vortex pair looked weaken.



(a) ' $a/H=0.25$   $b/H=0.05$   $p/H=1.00$ '



(b) ' $a/H=0.50$   $b/H=0.10$   $p/H=1.00$ '

**Figure 6.16** Secondary flow patterns for varied  $a/H$  at  $Re=10,000$

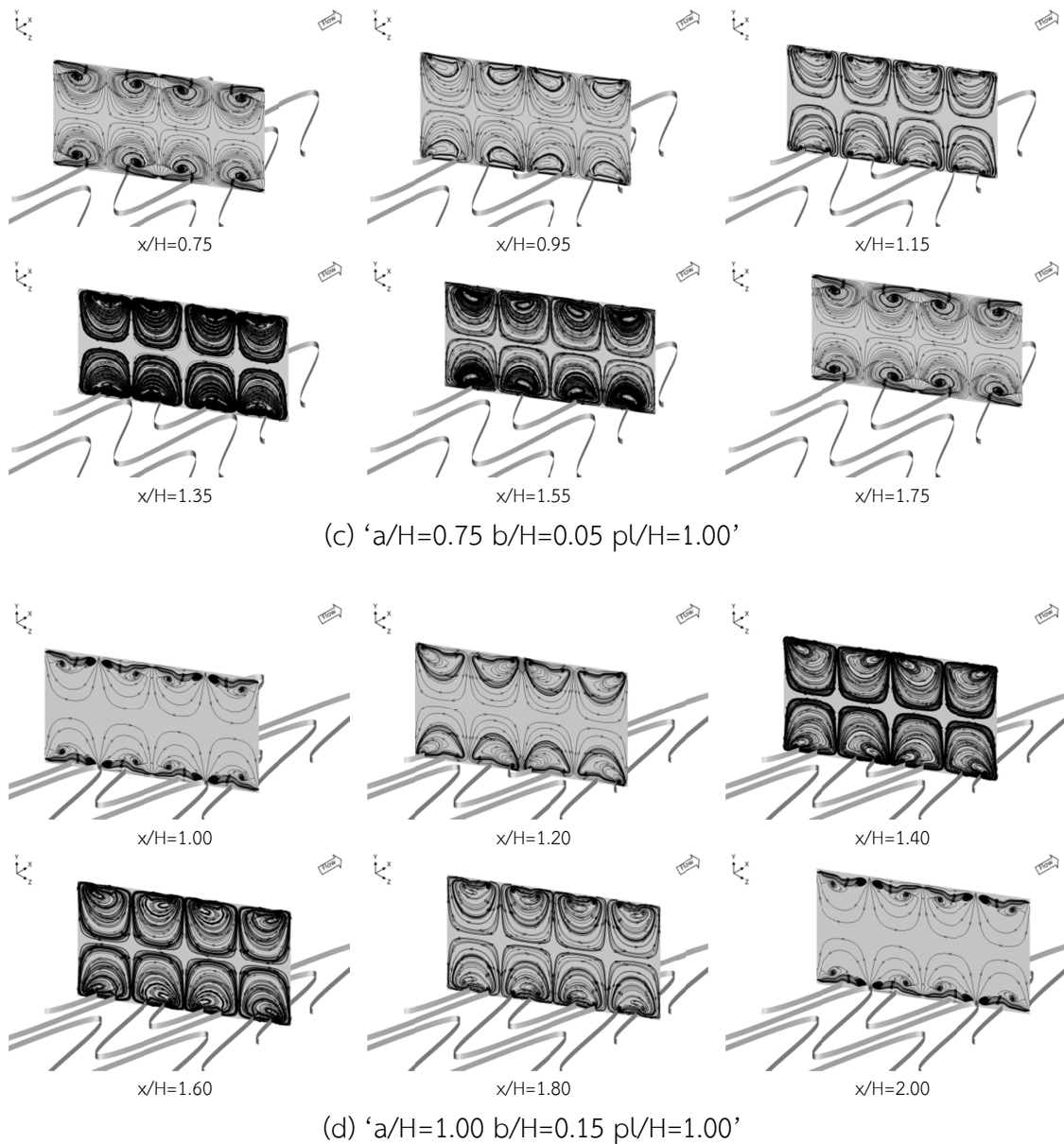
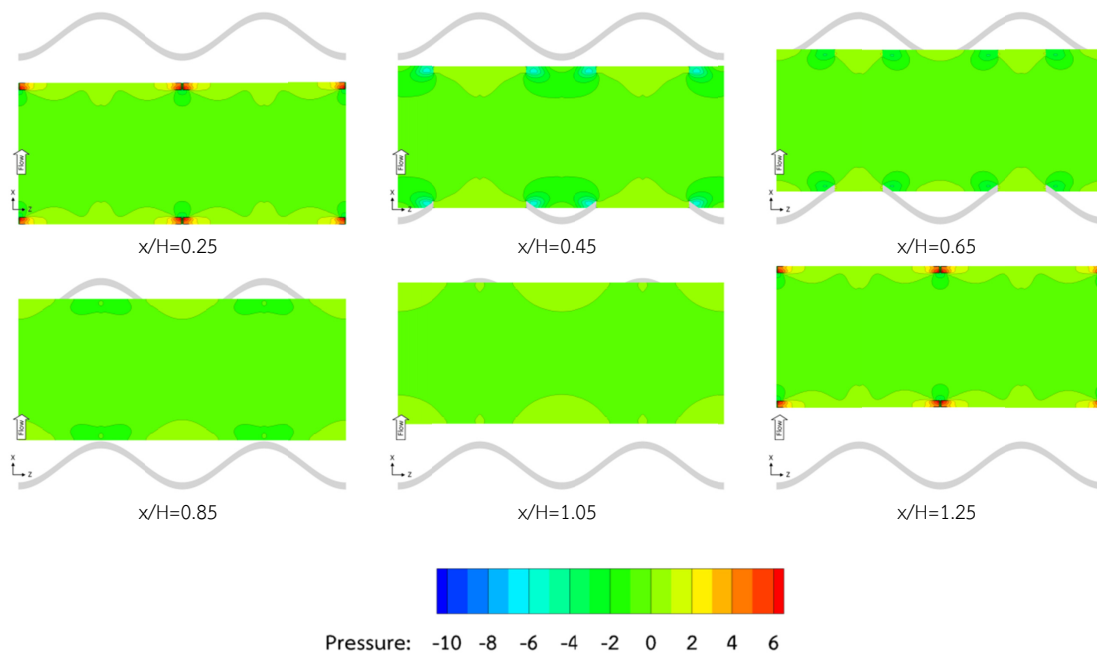
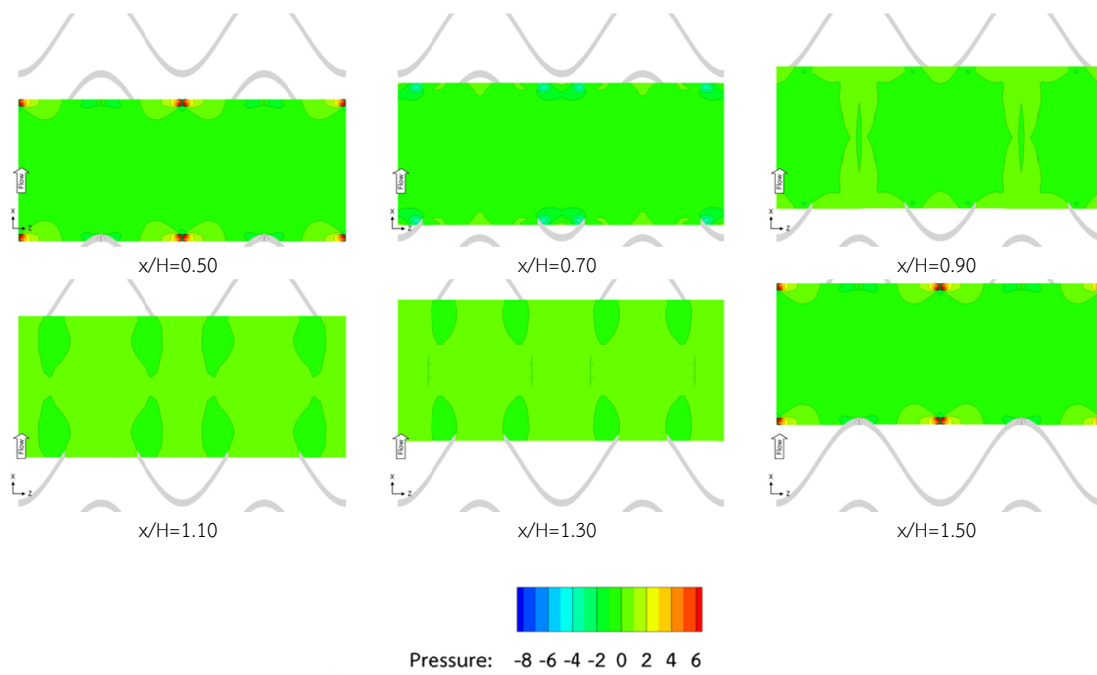


**Figure 6.16** Secondary flow patterns for varied  $a/H$  at  $Re=10,000$  (cont'd)

Figure 6.17a, b, c, and d present the pressure distributions on the nominated transverse planes of the baffle ' $b/H=0.10$   $p/H=1.00$ ' at  $Re=10,000$  for varied baffle amplitudes:  $a/H=0.25$ ,  $0.50$ ,  $0.75$ , and  $1.00$ , respectively. Considering the case  $a/H=0.25$  (Figure 6.17a), in upward zone, the highest positive pressure (red color) also happened in the stagnation point which was the flow separation region (in front of the crest of the baffle). Behind the crest of the baffle, the negative pressure (blue color) was occurred. The counter rotating vortex pair was impinged to that heat surface area. However, an increment of the baffle amplitude had little influence on the pressure gradient. It was also observed that, the pressure gradient reduced with increasing amplitude.

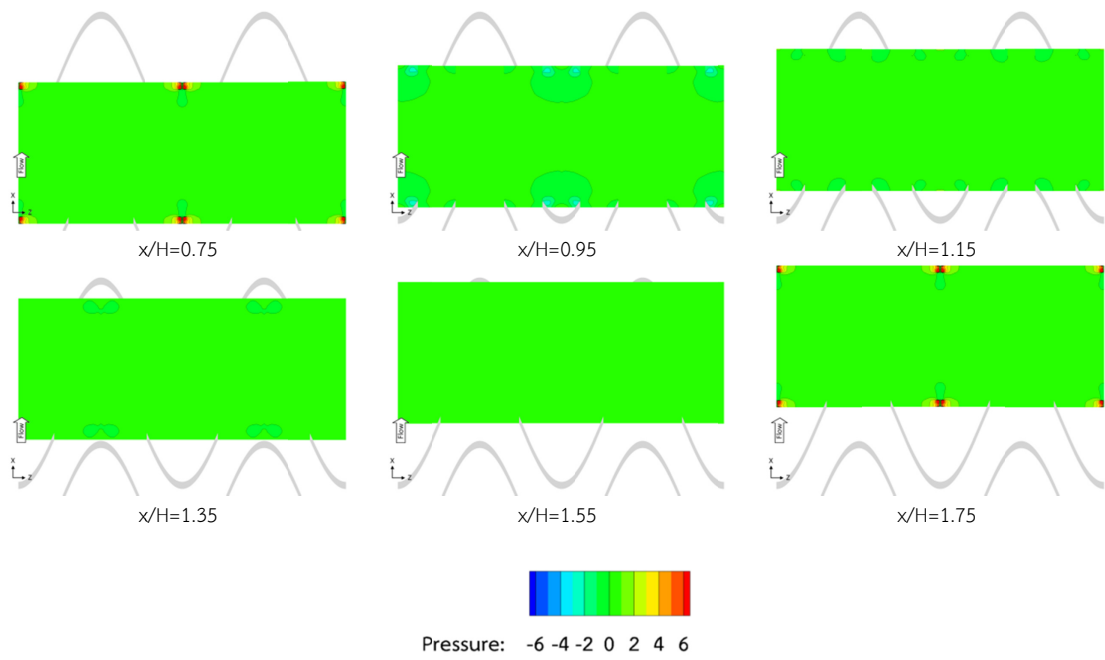


(a) ' $a/H=0.25$   $b/H=0.05$   $pL/H=1.00$ '

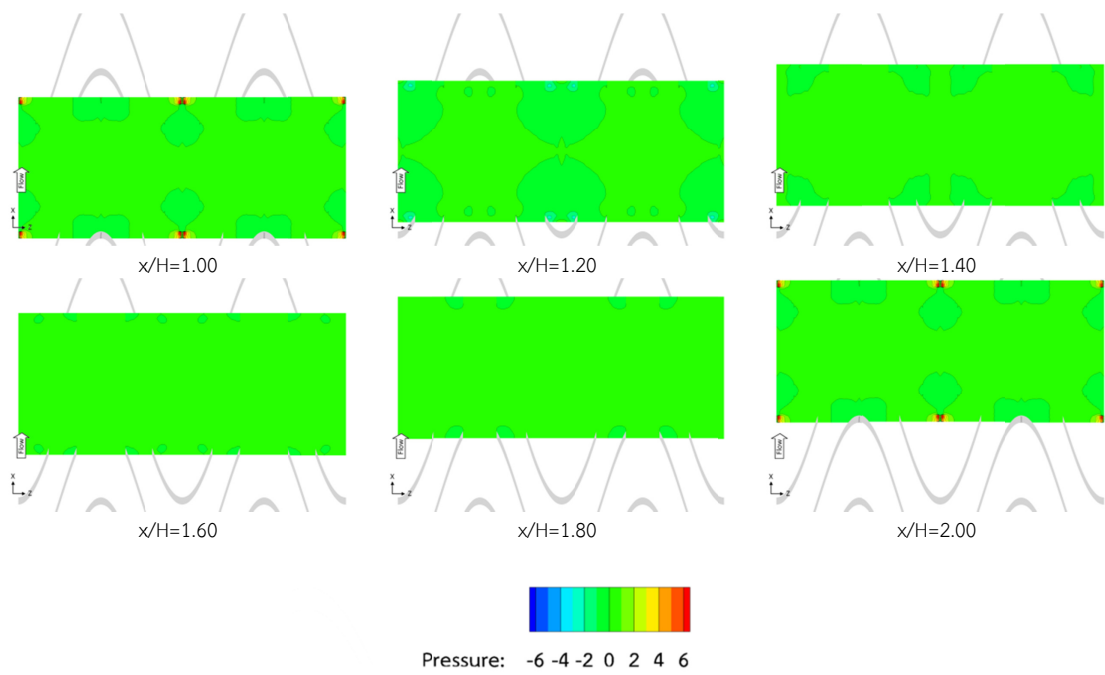


(b) ' $a/H=0.50$   $b/H=0.10$   $pL/H=1.00$ '

Figure 6.17 Pressure distribution for varied  $a/H$  at  $Re=10,000$



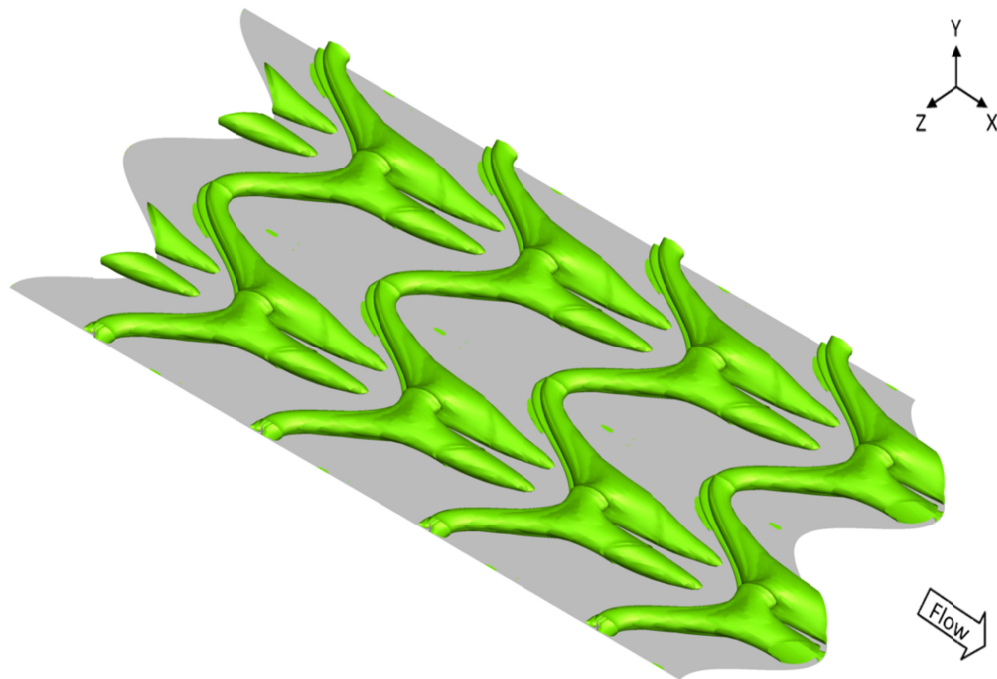
(c) 'a/H=0.75 b/H=0.05 pL/H=1.00'



(d) 'a/H=1.00 b/H=0.15 pL/H=1.00'

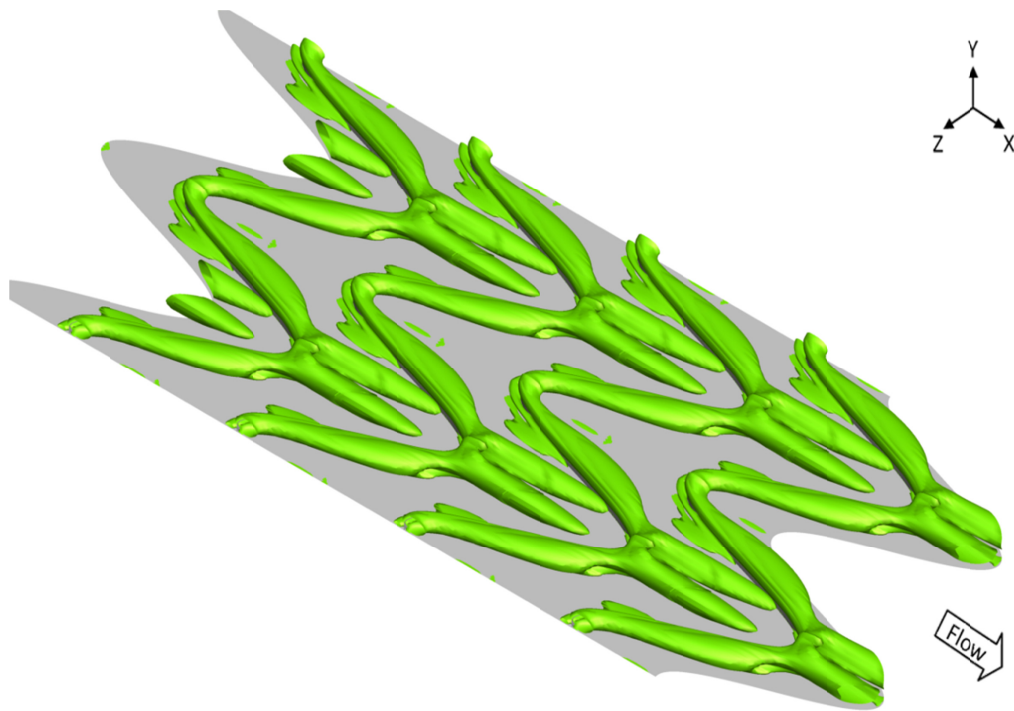
Figure 6.17 Pressure distribution for varied a/H at Re=10,000 (cont'd)

Figure 6.18a, b, c, and d present the  $Q$  isosurfaces of the baffle ' $b/H=0.10$   $pL/H=1.00$ ' at  $Re=10,000$  for varied baffle amplitudes:  $a/H=0.25$ ,  $0.50$ ,  $0.75$ , and  $1.00$ , respectively. Considering the case  $a/H=0.25$  (Figure 6.18a), in upward zone, the  $Q$  isosurface tube also located along the wave of baffles. The main flow was also separated at the crest of baffle. The secondary flow recirculated in streamwise direction along the recirculation tube. In downward zone, at the trough of baffle, the isosurface tube also combined with the others and lifted across the baffles. These  $Q$  isosurface patterns had sustained continuously along the baffle channel. With increasing baffle amplitude, the  $Q$  isosurface tube became smaller. However, it also combined with the adjacent isosurface tubes which created the persistent vorticity structure.

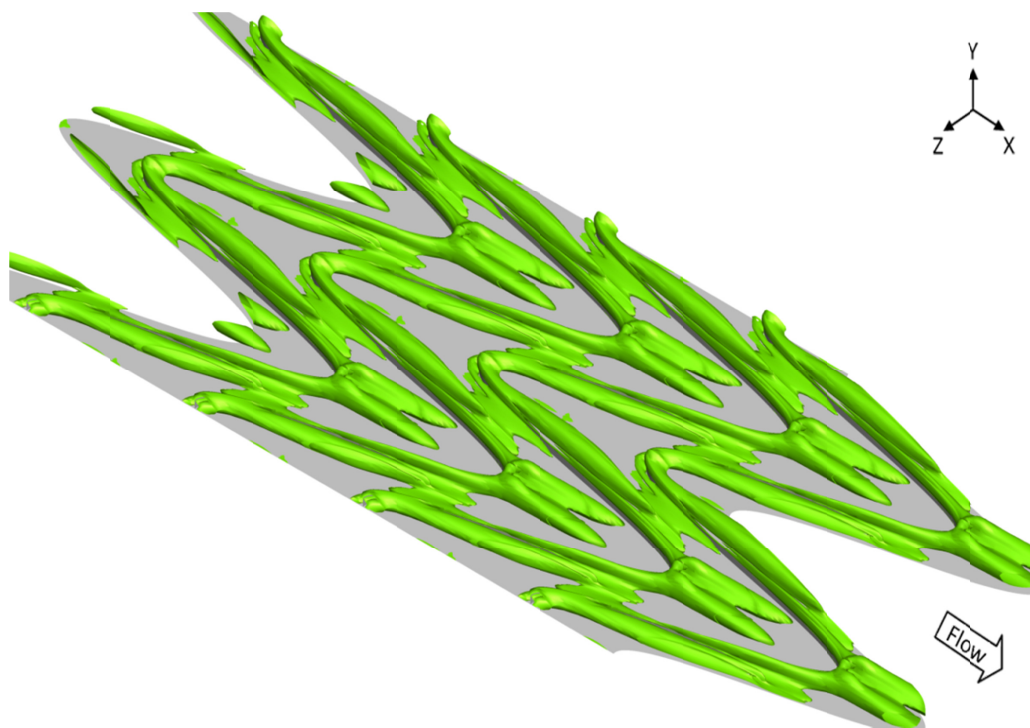


(a) ' $a/H=0.25$   $b/H=0.05$   $pL/H=1.00$ '

**Figure 6.18** The  $Q$  isosurface for varied  $a/H$  at  $Re=10,000$

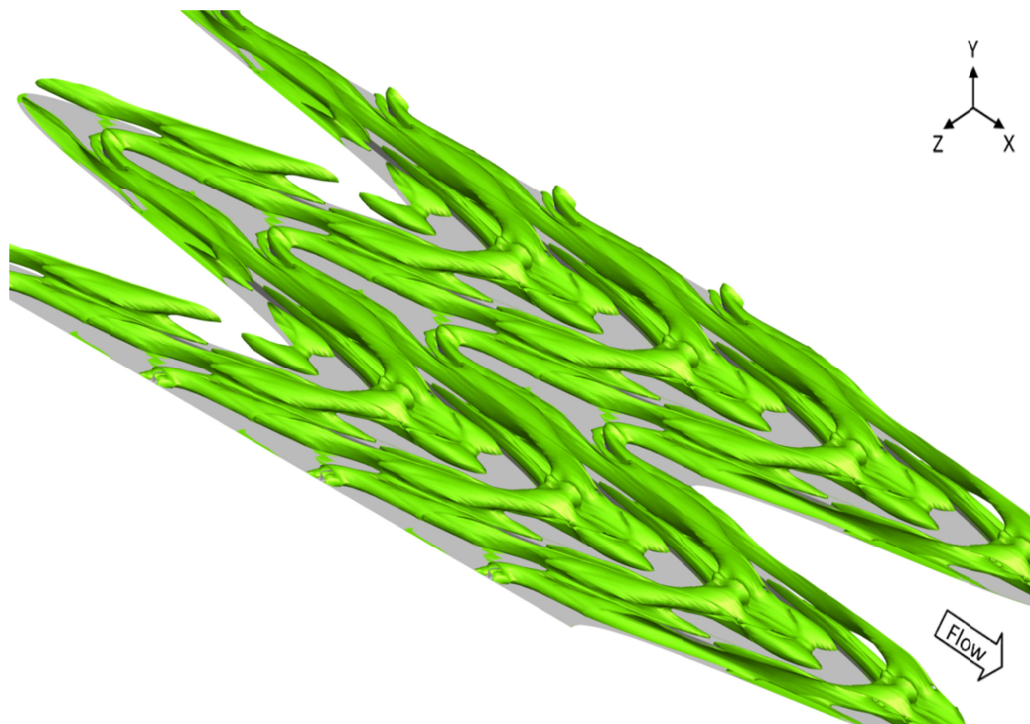


(b) 'a/H=0.50 b/H=0.10 p/H=1.00'



(c) 'a/H=0.75 b/H=0.05 p/H=1.00'

Figure 6.18 The Q isosurface for varied a/H at Re=10,000 (cont'd)



(d) ' $a/H=1.00$   $b/H=0.15$   $p/H=1.00$ '

**Figure 6.18** The Q isosurface for varied  $a/H$  at  $Re=10,000$  (cont'd)

Considering the effects of baffle amplitude on the friction factor ratio, Figure 6.19, 6.20, and 6.21 present the results of the baffles having  $b/H=0.05$ ,  $0.10$ , and  $0.15$ , respectively. With the increment of amplitudes, for the case  $b/H=0.05$ , the friction factor ratio reduced slightly. For higher blockage ratio cases:  $b/H=0.10$  and  $0.15$ , the friction factor ratio also decreased noticeably. Therefore, the increment of amplitudes had an effect in significantly reduced the pressure loss for each given Reynolds number. The strength of the flow impingement also reduced with increasing amplitude. Consequently, depending on Reynolds number and the baffle height, the higher amplitude provided considerably lower pressure loss.

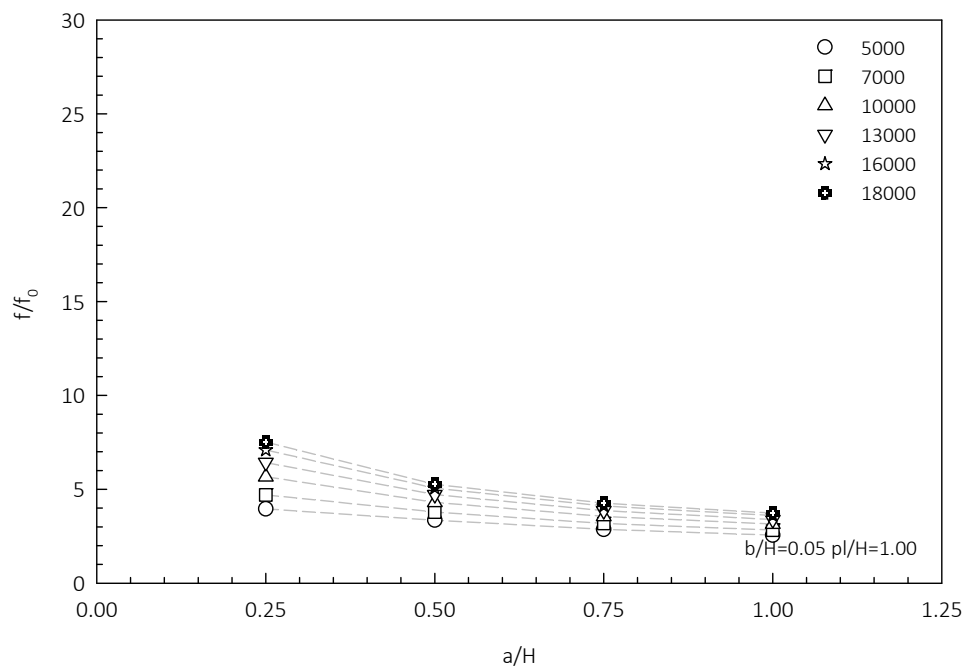


Figure 6.19 Variation of  $f/f_0$  with  $a/H$  for various  $Re$  at  $b/H=0.05$

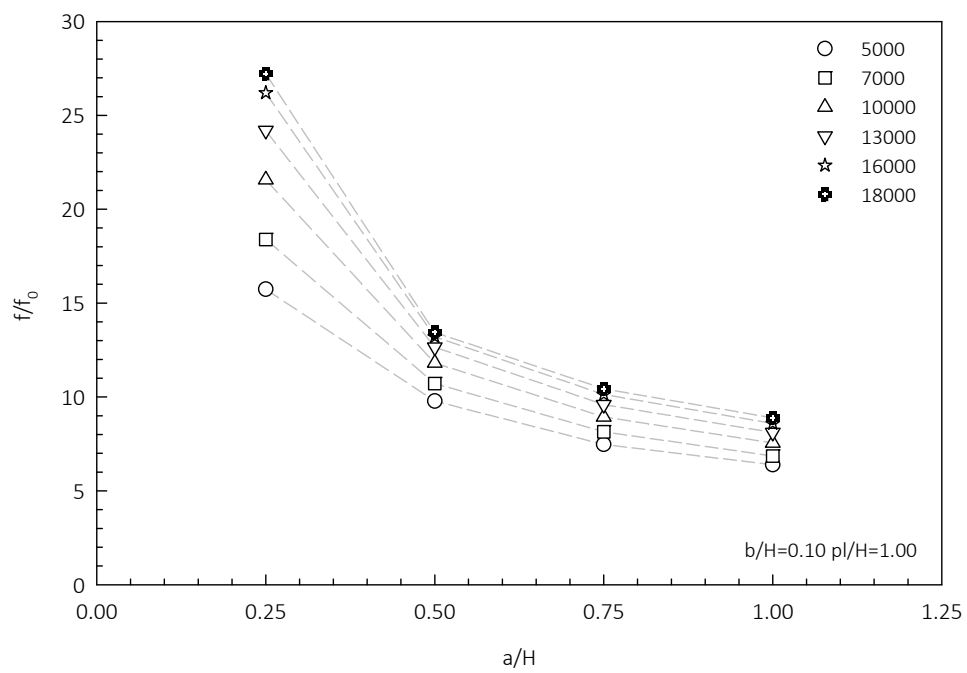


Figure 6.20 Variation of  $f/f_0$  with  $a/H$  for various  $Re$  at  $b/H=0.10$

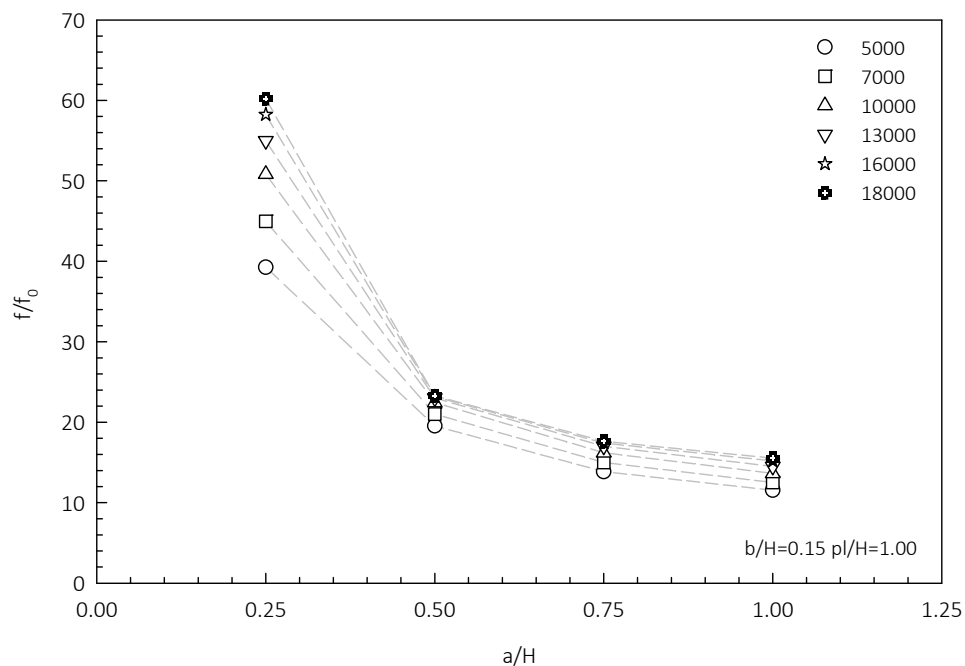


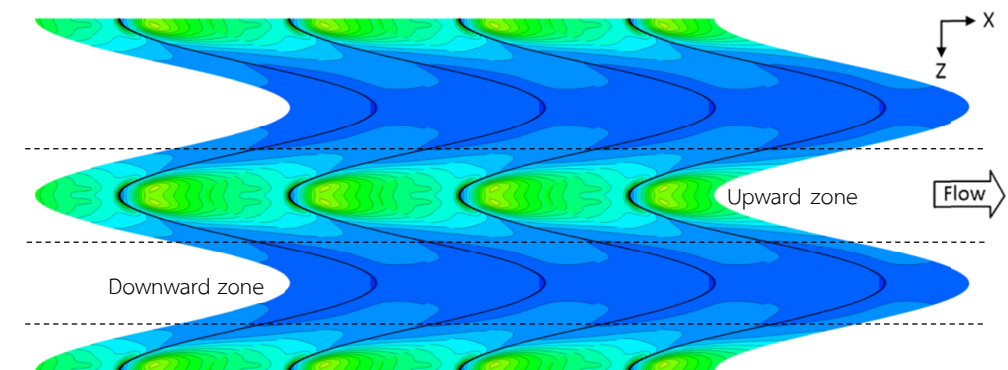
Figure 6.21 Variation of  $f/f_0$  with  $a/H$  for various  $Re$  at  $b/H=0.15$

### 6.3 Heat transfer characteristics of air flow

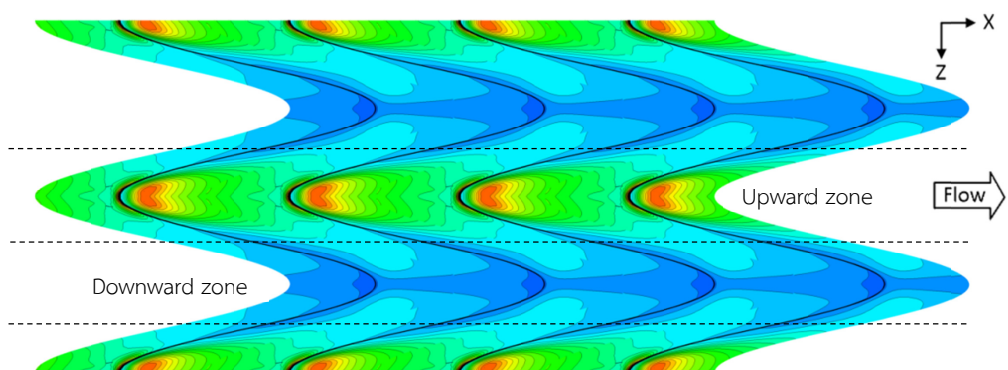
This section presents the effects of the geometric parameters on heat transfer characteristics. The heat transfer coefficients of the air flow in the baffle channel were individually determined at Reynolds number ranging from 5,000 to 18,000. The area-weighted averaged Nusselt number was calculated regarding to heat surface area. Then, the Nusselt number ratio was also estimated with respect to the smooth channel at the same Reynolds number.

#### 6.3.1 Effects of Reynolds number and longitudinal pitch

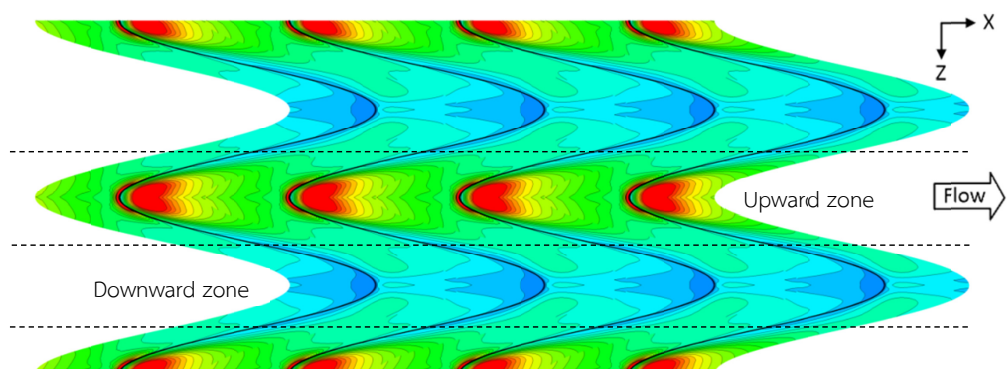
The results of Nusselt number contours of the baffle ' $a/H=0.75$   $b/H=0.5$   $p/H=1.00$ ' at different Reynolds number of 5,000, 10,000, and 16,000 are presented in Figure 6.22a, b, and c, respectively. Considering  $Re=5,000$ , the Nusselt numbers on the region along the downward zone were low (indicated by dark blue color). The Nusselt numbers on the region along the upward zone were higher (indicated by the light blue, green, and yellow colors). With increasing Reynolds number to 10,000 and 16,000, the Nusselt numbers increased. It was evidently observed by the increase in yellow, orange, and red areas along the upward zone and the reduction in blue area along the downward zone. Consequently, the averaged Nusselt number increased with increasing Reynolds number.



(a) Re=5,000



(b) Re=10,000



(c) Re=16,000

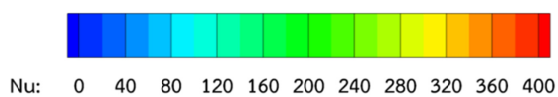


Figure 6.22 Nu contours of varied Re

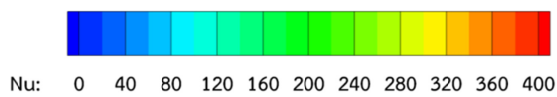
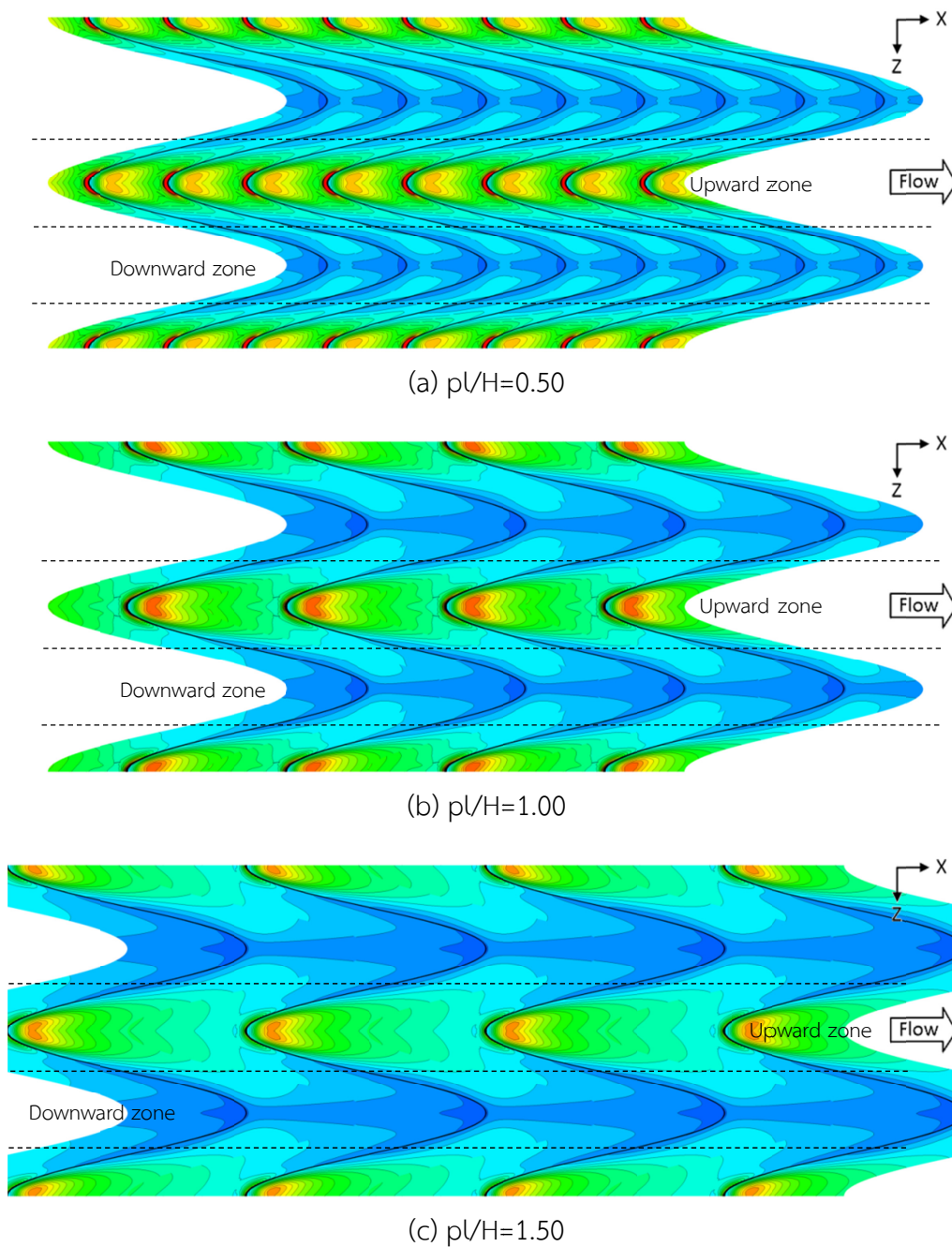


Figure 6.23 Nu contour of varied  $p/H$

The effects of baffles having  $p/H=0.50$ ,  $1.00$ , and  $1.50$  on the Nusselt number contours at  $Re=10,000$  are illustrated in Figure 6.23a, b, and c, respectively. The narrower pitch ( $p/H=0.50$ ) gave higher Nusselt number than the wider pitches:  $p/H=1.00$  and  $1.50$ . This may be due to the strength of secondary flow impingement and reattachment of more packed baffles ( $p/H=0.50$ ) was higher than the wider ones. The flow impingement conveyed the lower air temperature to the area of higher temperature. This temperature difference resulted in higher Nusselt number especially in front of the crest of each baffle in upward zone which had strong flow impingement.

For fully developed turbulent flow in the channel, typically, the Nusselt number moderately increased with an increase of Reynolds number due to the reduction of the viscous sublayer. The Nusselt numbers for the baffle channel were considerably greater than for the smooth channel at a given range of Reynolds numbers. This may be due to the main flow separation, the secondary flow reattachment/impingement, and the vortex pair generation induced by the presence of baffles. This occurrence had enhanced the heat transfer rate. The effects of Reynolds numbers and longitudinal pitches on the Nusselt number ratio for the baffles having  $b/H=0.05$ ,  $0.10$ , and  $0.15$  are presented in Figure 6.24 to 6.26, respectively. The Nusselt number ratio reduced slightly with increasing Reynolds number. Moreover, the Nusselt number ratio also decreased with an expansion of longitudinal pitches.

Considering results of the baffles having  $b/H=0.05$  (Figure 6.24), the Nusselt number ratio of the same amplitude reduced gradually with increasing Reynolds number. However, with expanding  $p/H$ , the Nusselt number ratio decreased dramatically due to falling in the strength of impingement behind each wave of baffles. For the cases:  $b/H=0.10$  and  $0.15$  as shown in Figure 6.25 and 6.26, respectively, also gave the similar results for the Nusselt number ratio. However, it provided relatively greater values due to its higher blockage ratio. According to the numerical results, the values of Nusselt number ratio of the baffle channel within a given range of Reynolds numbers were found to be  $1.89 - 5.88$  times compared with the smooth channel.

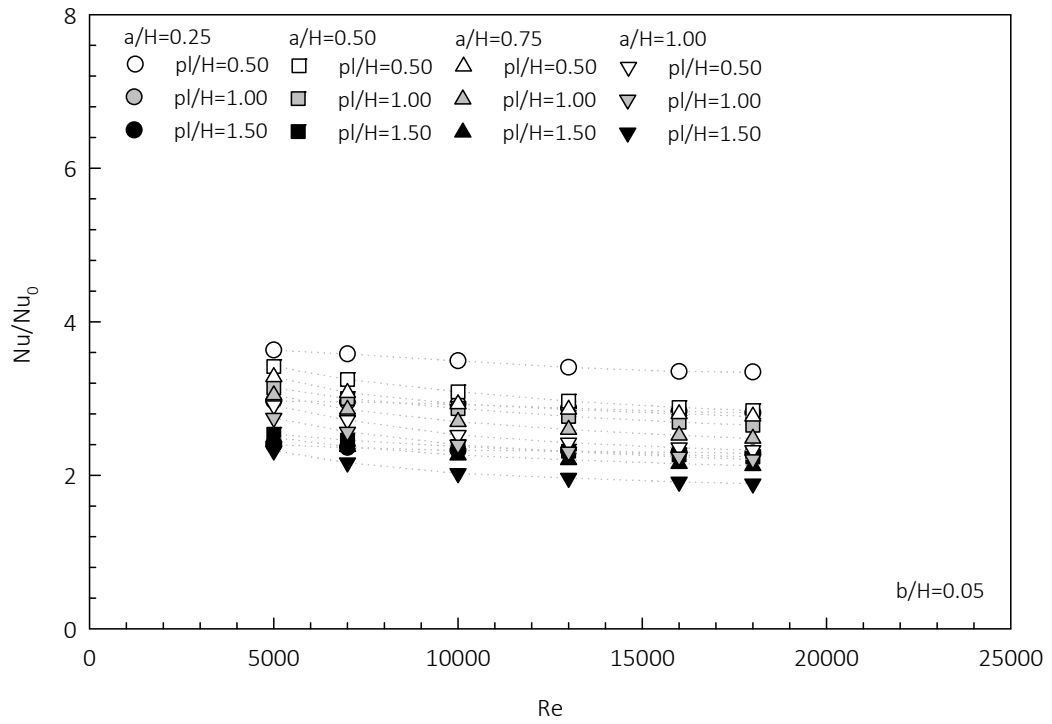


Figure 6.24 Variation of  $Nu/Nu_0$  with  $Re$  for varied  $p/H$  at  $b/H=0.05$

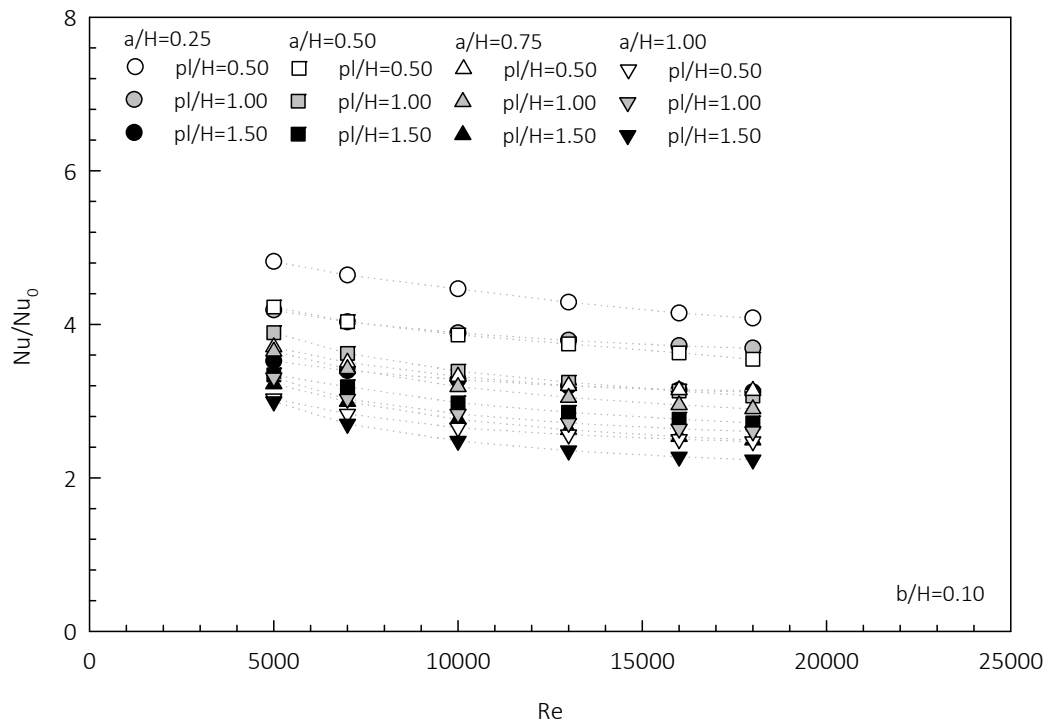


Figure 6.25 Variation of  $Nu/Nu_0$  with  $Re$  for varied  $p/H$  at  $b/H=0.10$

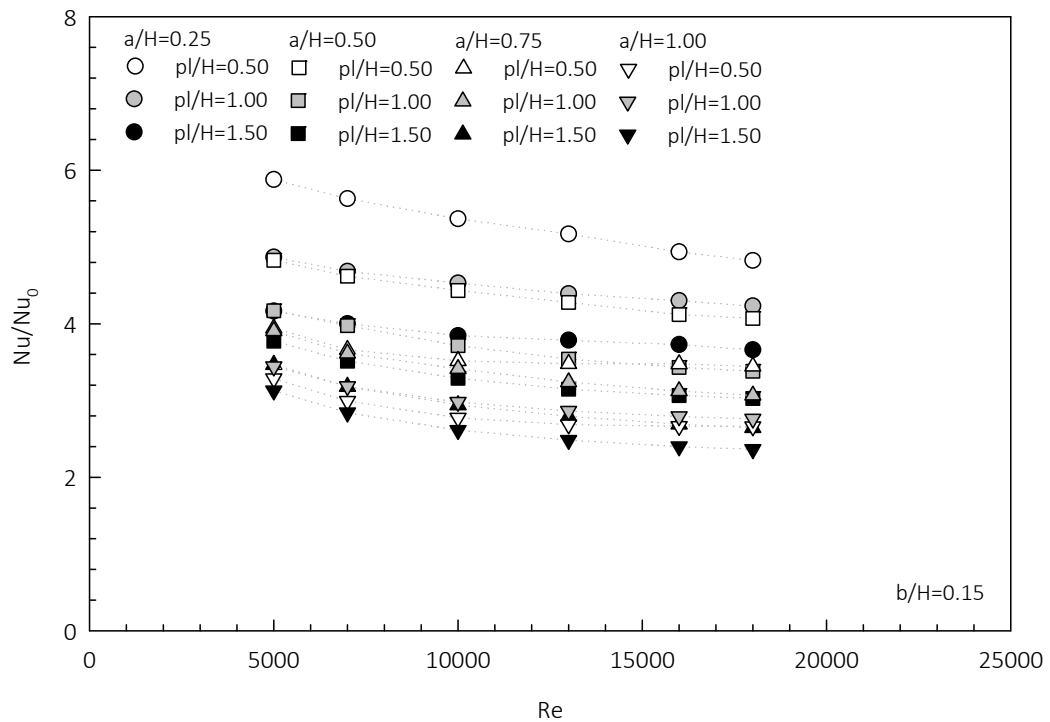
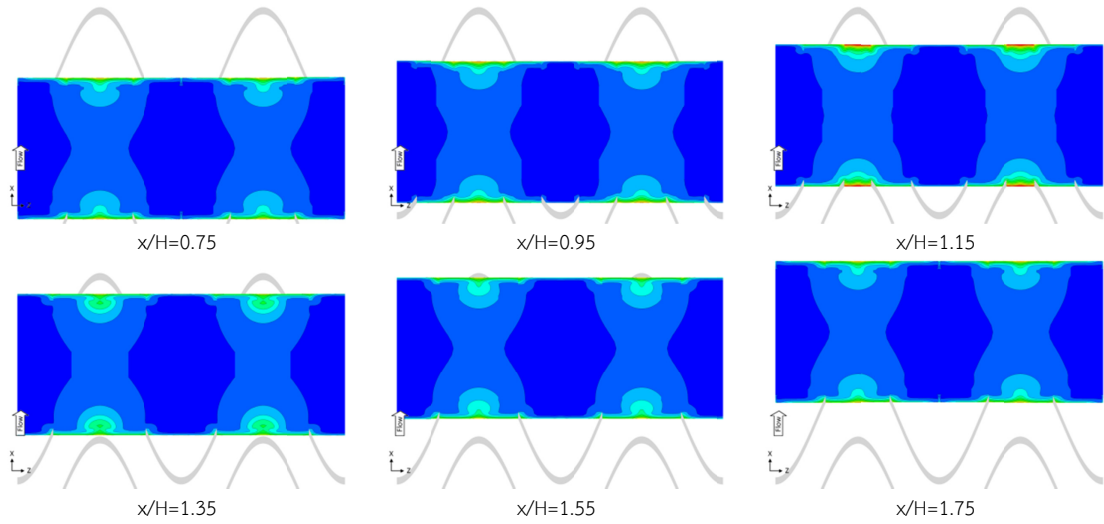
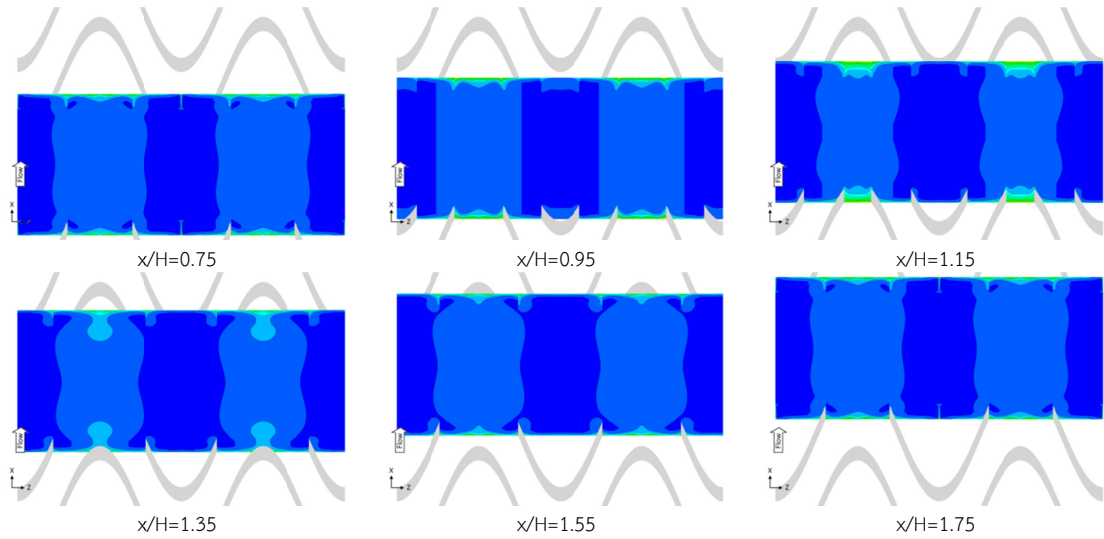


Figure 6.26 Variation of  $Nu/Nu_0$  with  $Re$  for varied  $p/H$  at  $b/H=0.15$

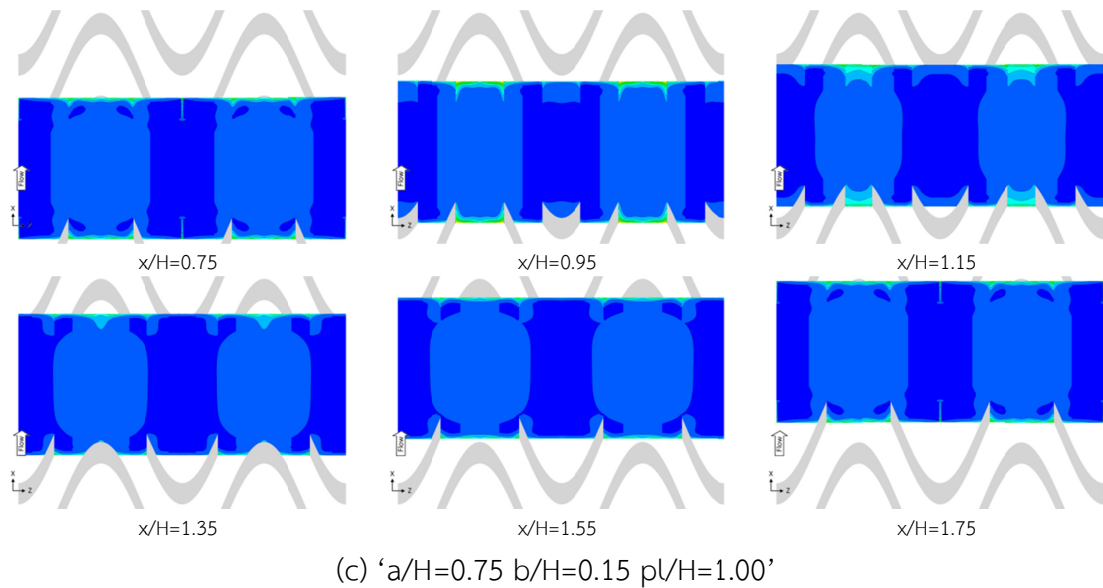
### 6.3.2 Effects of baffle height

Figure 6.27a, b, and c present the temperature distributions on the nominated transverse planes of the baffle 'a/H=0.75 p/H=1.00' at  $Re=10,000$  for varied baffle heights:  $b/H=0.05$ , 0.10 and 0.15, respectively. For the case  $b/H=0.05$ , the high temperature occurred in the region of downward zone (indicated by light blue, green, yellow, and red areas). The convective heat transfer in this region was low due to the low temperature gradient between the air fluid and the heat surface. In upward zone of baffle, the air fluid temperature was low which caused the high temperature gradient to the heat surface. Therefore, the convective heat transfer in this region was higher. With expanding the baffle height, the air fluid temperature became lower which caused higher temperature gradient and also enhanced the heat transfer.

(a) ' $a/H=0.75$   $b/H=0.05$   $p/H=1.00$ '(b) ' $a/H=0.75$   $b/H=0.10$   $p/H=1.00$ '

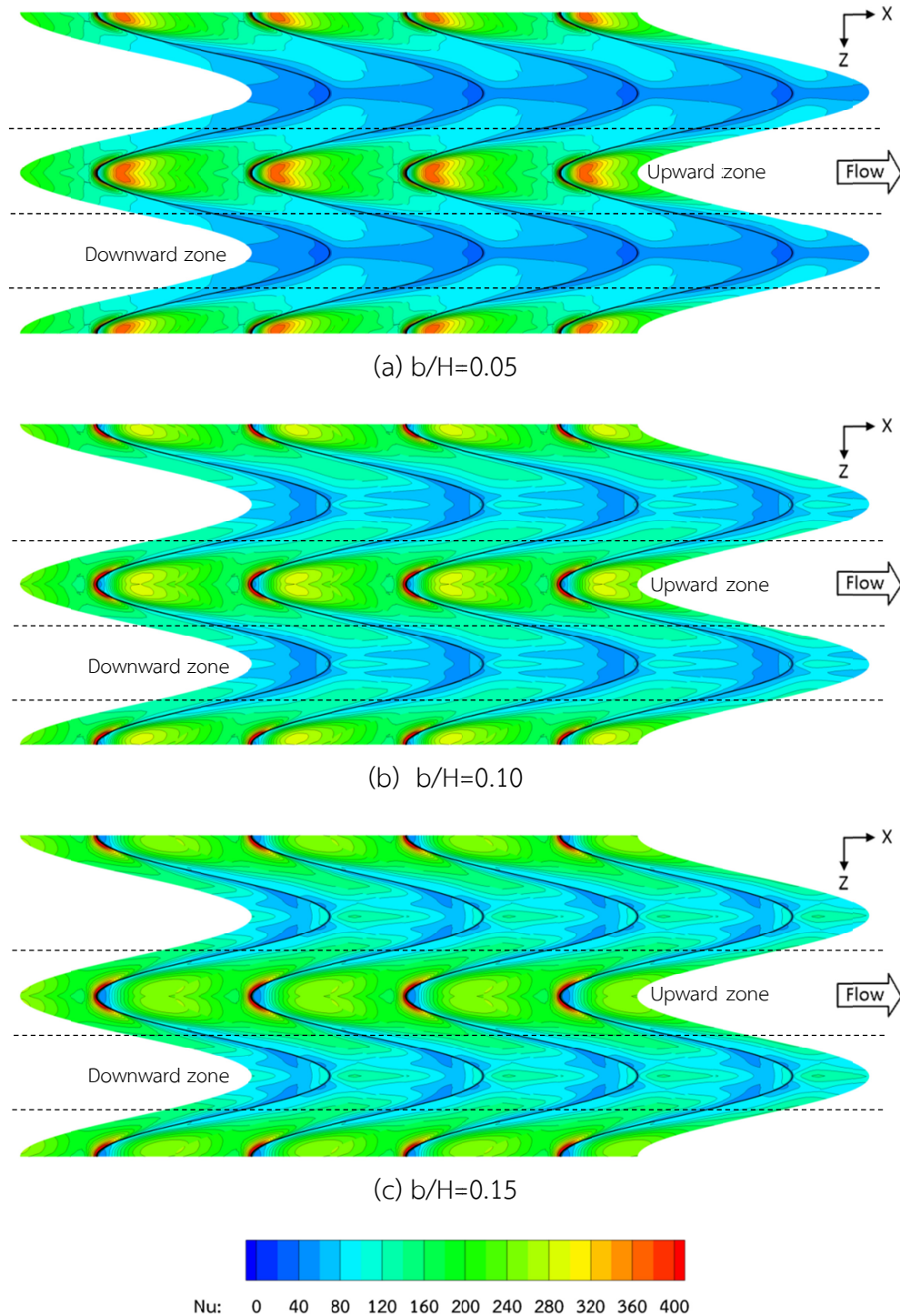
Temperature: 300 308 316 324 332 340

Figure 6.27 Temperature distributions for varied  $b/H$  at  $Re=10,000$



**Figure 6.27** Temperature distributions for varied  $b/H$  at  $Re=10,000$  (cont'd)

Figure 6.28a, b, and c, present the Nusselt number contours at  $Re=10,000$  for the baffle 'a/H=0.75 pL/H=1.00' with varied baffle heights:  $b/H=0.05$ , 0.10, and 0.15, respectively. Considering the case  $b/H=0.05$  (Figure 6.28a), the Nusselt numbers on the region along downward zone were also lower (blue regions) than Nusselt numbers on the region along upward zone of baffles (green, yellow, and orange colors). With extending baffle height to 0.10 and 0.15, the blue regions reduced whereas the green and yellow regions enlarged which indicate the increasing in Nusselt numbers. Moreover, it was observed that, the extending baffle height provided substantial Nusselt number especially in front of the crest of baffles which indicated by the red regions. Consequently, the averaged Nusselt number also increased with extending baffle height.



**Figure 6.28** Nu contour of varied  $b/H$  at  $Re=10,000$

The effects of varied baffle height:  $b/H=0.05$ ,  $0.10$ , and  $0.15$  on the Nusselt number ratios at  $Re=10,000$  are presented in Figure 6.29, 6.30, and 6.31, respectively. The Nusselt number ratio decreased gradually with increasing Reynolds number. The extending baffle height gave a result in significant increase of the Nusselt number ratio for each given Reynolds number. This may be due to the influence of the

blockage ratio on the strengths of the flow impingement and the vortex pair behind each wave of baffles.

The vortex pair induced the lower air temperature from the core flow to the heat surface area and also reduced the thermal boundary layer. This occurrence resulted in higher temperature gradient close to the surface wall and enhanced the heat transfer rate. This behavior was presented apparently in Figure 6.32, 6.33, 6.34, and 6.35 corresponding to the baffles:  $a/H=0.25$ , 0.50, 0.75, and 1.00, respectively. It was also observed that, for the case  $a/H=0.25$ , the Nusselt number ratio increased considerably with extending baffle height. With an increment of amplitude, the enhancement of Nusselt number ratio declined. According to numerical results, the lowest Nusselt number ratio was found to be 1.89 times corresponding to the baffle ‘ $a/H=1.00$   $b/H=0.05$   $p/H=1.50$ ’ at  $Re=5,000$ . The highest Nusselt number ratio was found to be 5.88 times corresponding to the baffle ‘ $a/H=0.25$   $b/H=0.15$   $p/H=0.50$ ’ at  $Re=18,000$ .

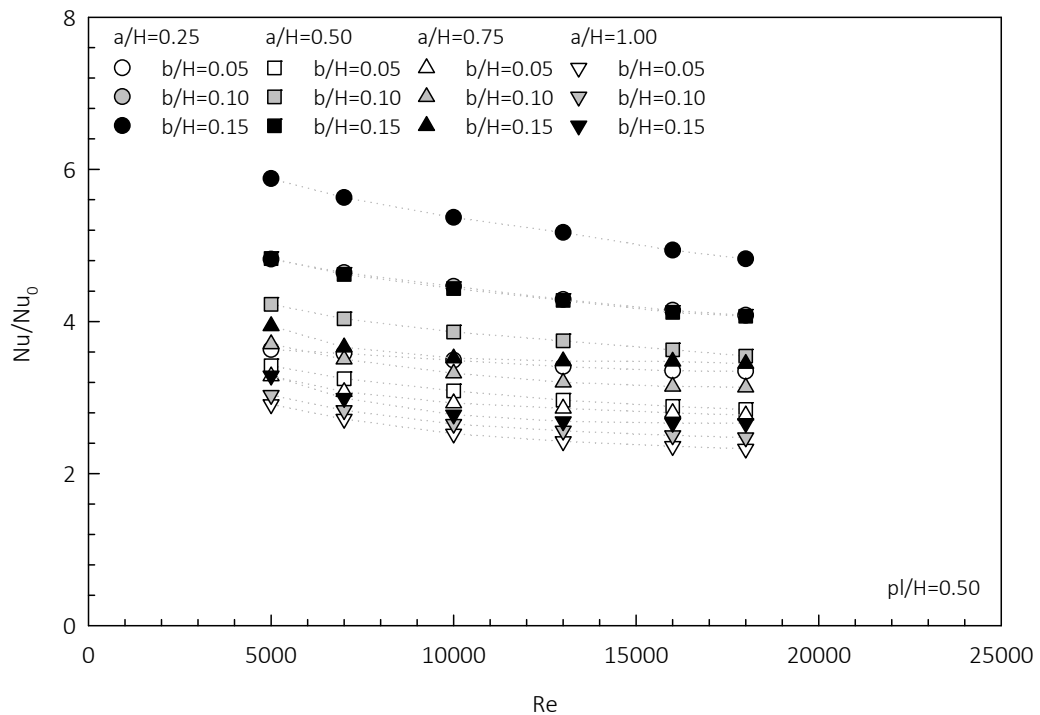


Figure 6.29 Variation of  $Nu/Nu_0$  with  $Re$  for varied  $b/H$  at  $p/H=0.50$

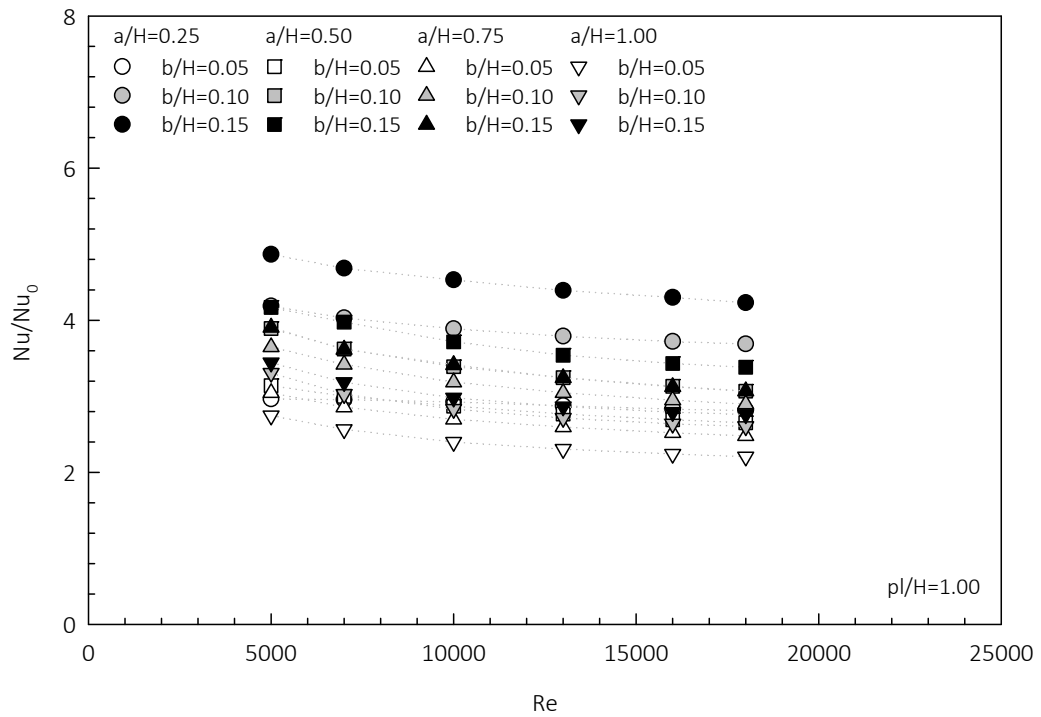


Figure 6.30 Variation of  $Nu/Nu_0$  with  $Re$  for varied  $b/H$  at  $p/H=1.00$

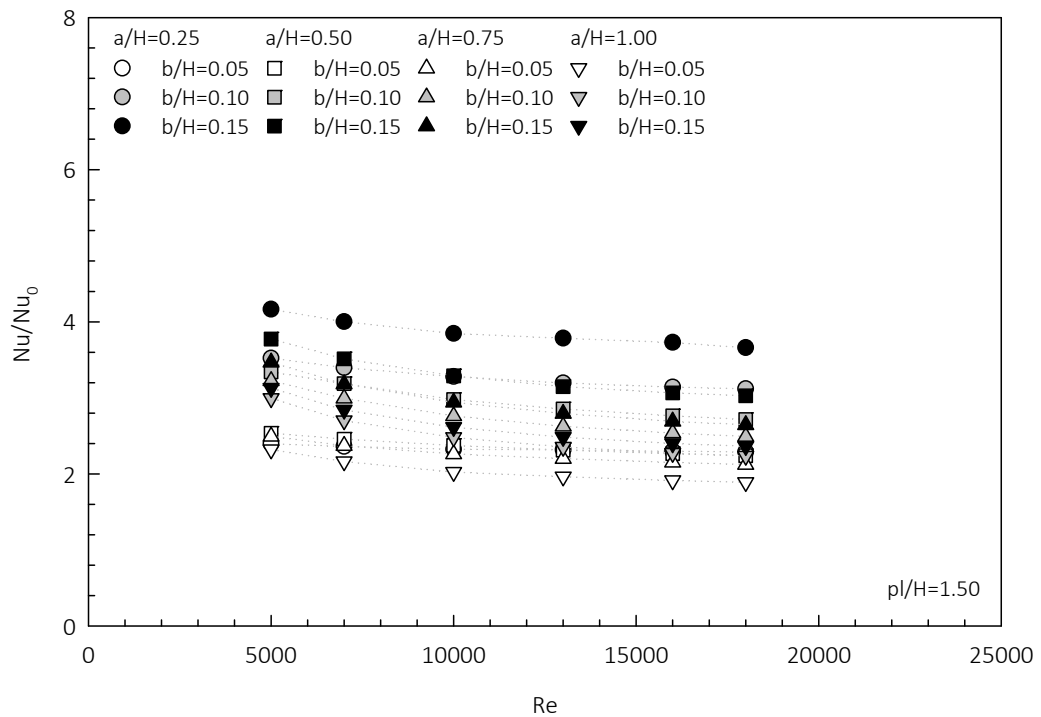


Figure 6.31 Variation of  $Nu/Nu_0$  with  $Re$  for varied  $b/H$  at  $p/H=1.50$

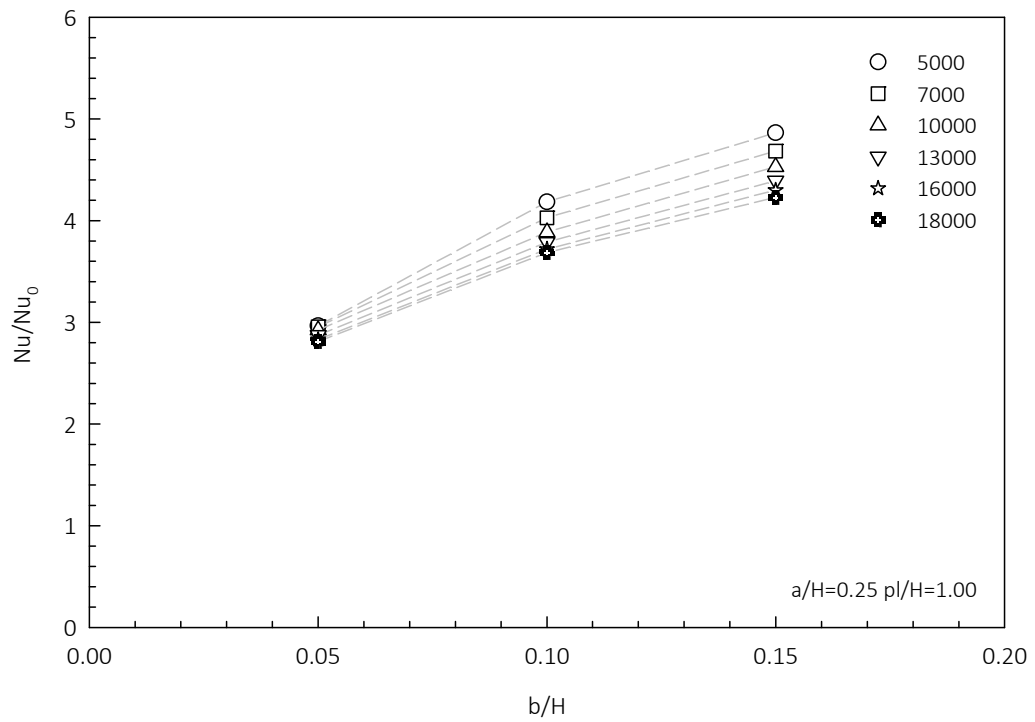


Figure 6.32 Variation of  $Nu/Nu_0$  with  $b/H$  for various Re at  $a/H=0.25$

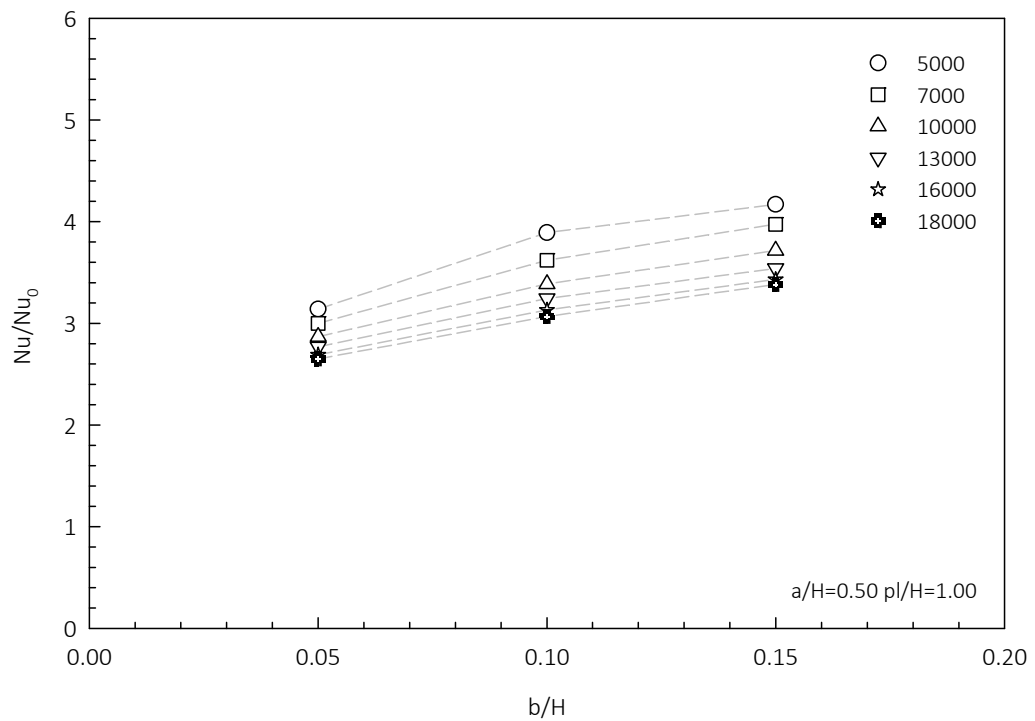


Figure 6.33 Variation of  $Nu/Nu_0$  with  $b/H$  for various Re at  $a/H=0.50$

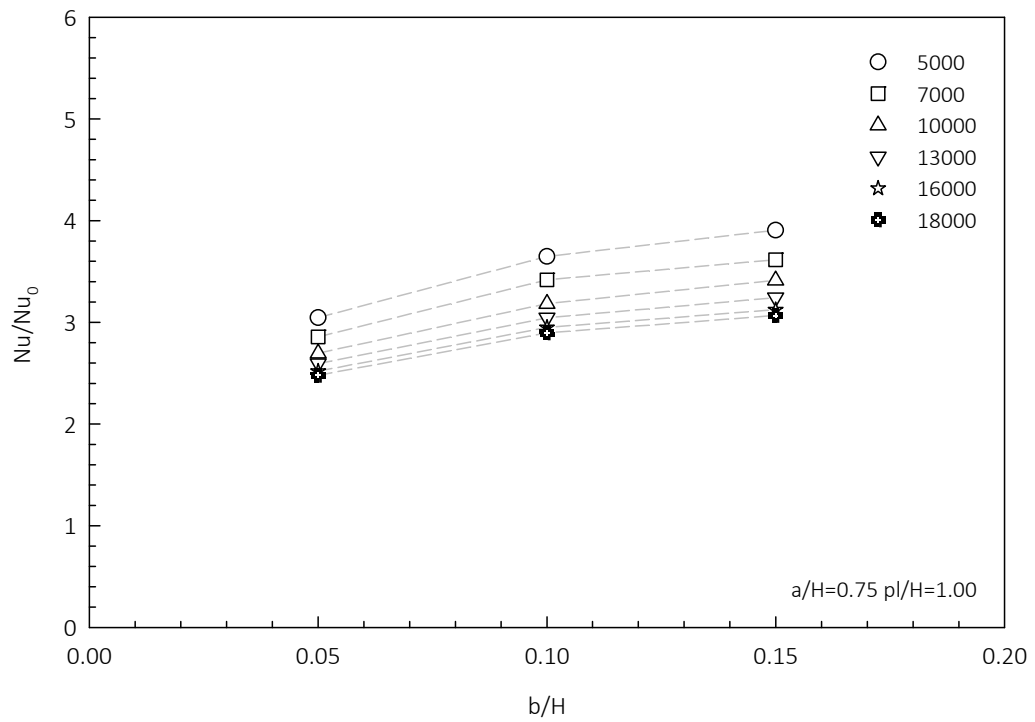


Figure 6.34 Variation of  $Nu/Nu_0$  with  $b/H$  for various  $Re$  at  $a/H=0.75$

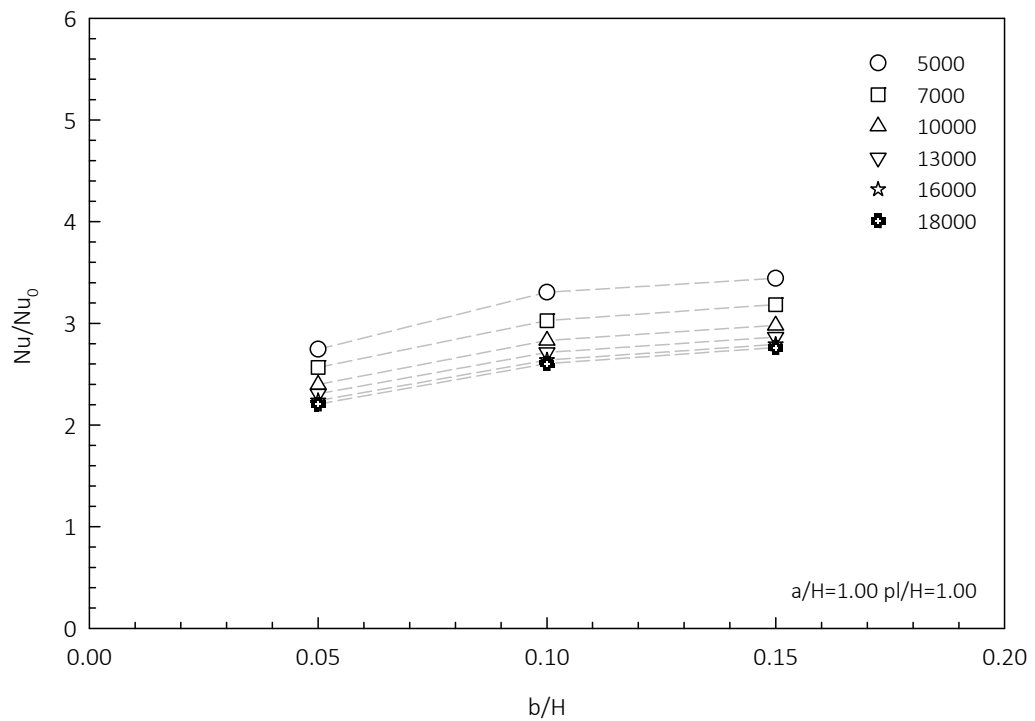


Figure 6.35 Variation of  $Nu/Nu_0$  with  $b/H$  for various  $Re$  at  $a/H=1.00$

### 6.3.3 Effects of baffle amplitude

Figure 6.36a, b, c, and d present the temperature distributions on the nominated transverse planes of the baffle 'b/H=0.10 pL/H=1.00' at Re=10,000 for varied baffle amplitudes: a/H=0.25, 0.50, 0.75, and 1.00, respectively. Considering the case a/H=0.25, the high temperature also happened in the region of upward zone (indicated by light blue, green, yellow, and red areas). Because of the low temperature gradient between the air and heat surface, the convective heat transfer in this region was low. The high temperature gradient to the surface occurred at upward zone of baffle since the air temperature in this region was low. Therefore, the convective heat transfer in this zone was greater. With increasing the baffle amplitude, the air temperature became higher at downward zone which caused lower temperature gradient and also reduced the convective heat transfer.

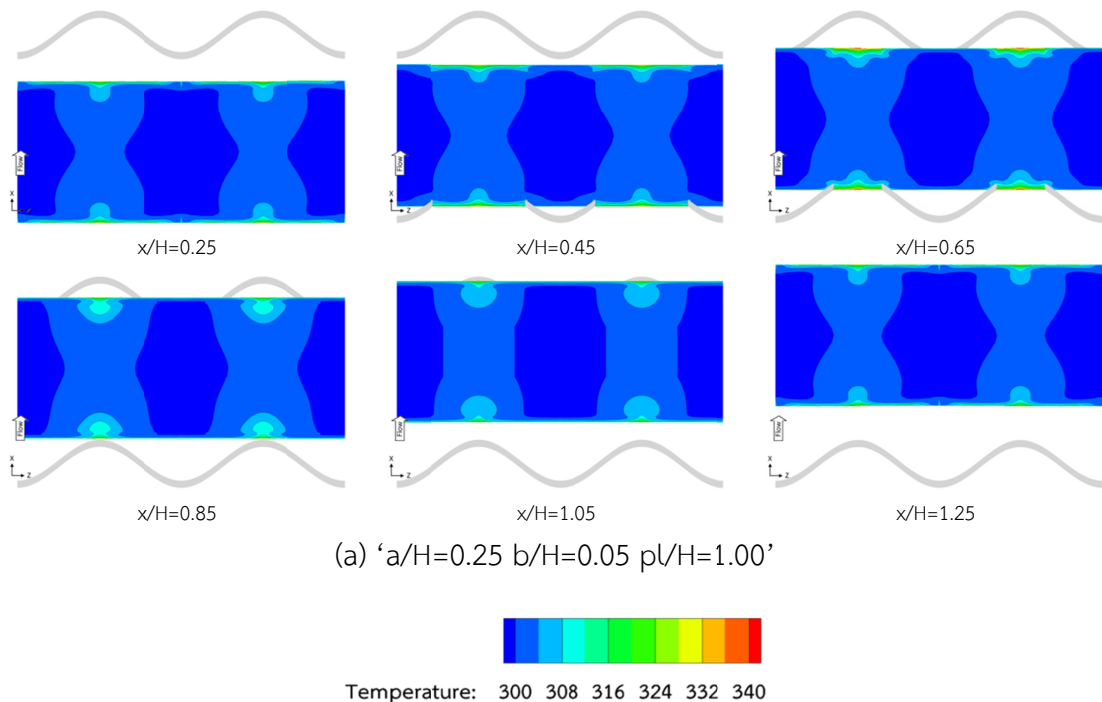
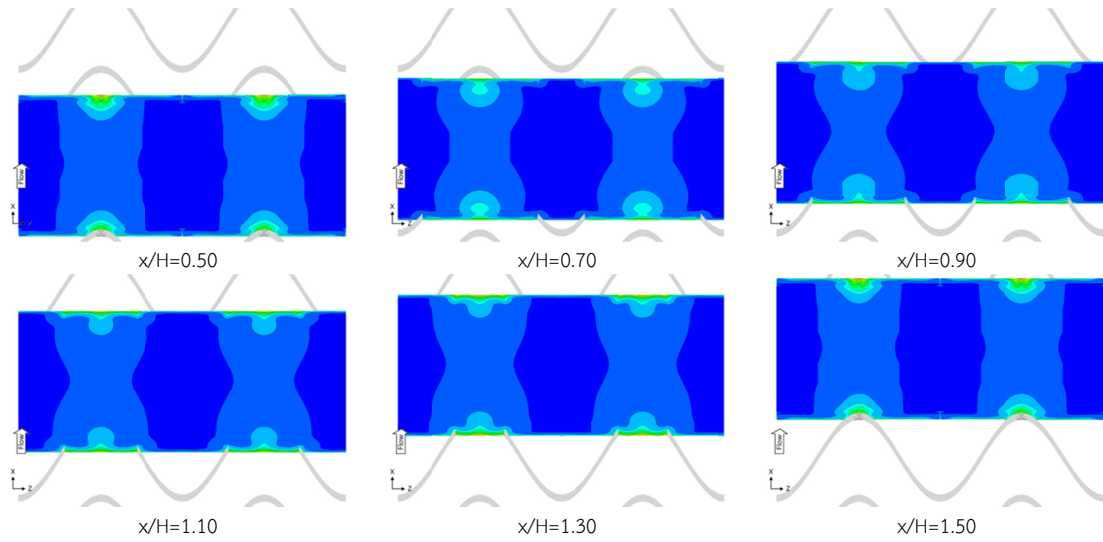
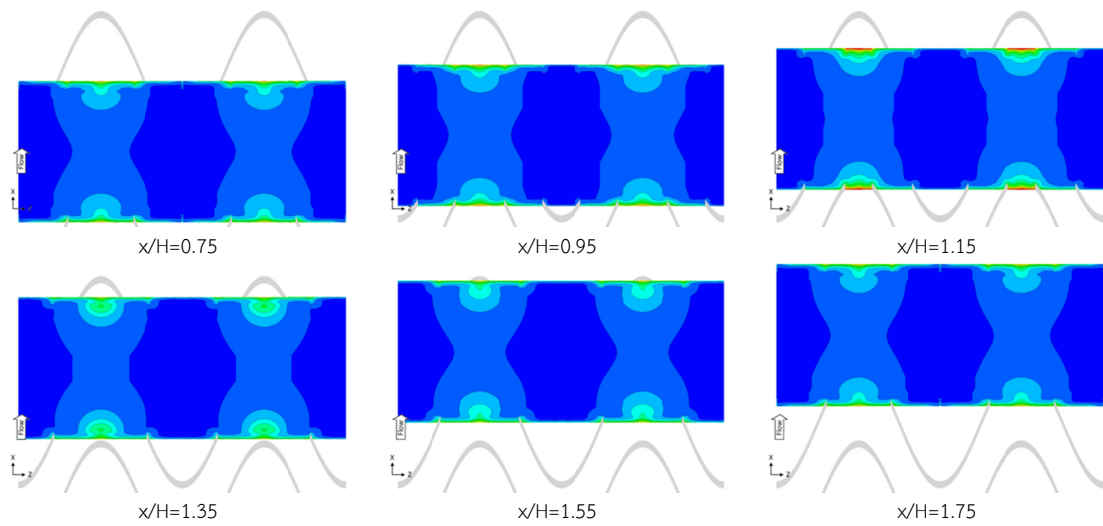
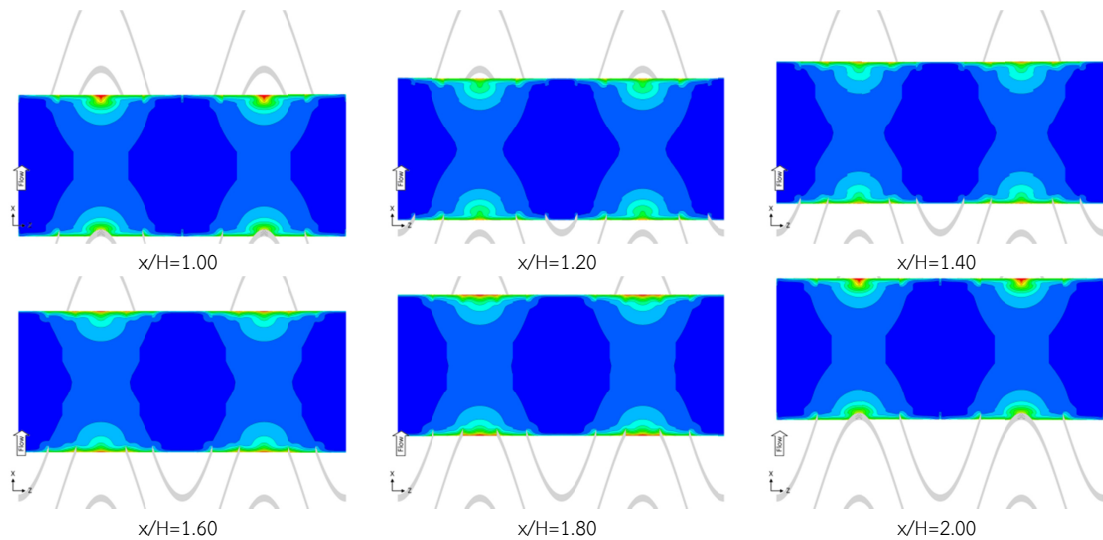


Figure 6.36 Temperature distribution for varied a/H at Re=10,000

(b) ' $a/H=0.50$   $b/H=0.10$   $pL/H=1.00$ '(c) ' $a/H=0.75$   $b/H=0.05$   $pL/H=1.00$ '

Temperature: 300 308 316 324 332 340

Figure 6.36 Temperature distribution for varied  $a/H$  at  $Re=10,000$  (cont'd)



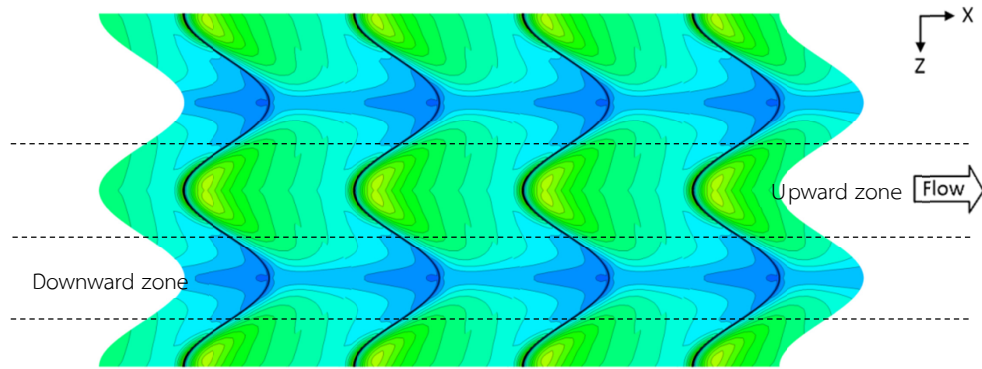
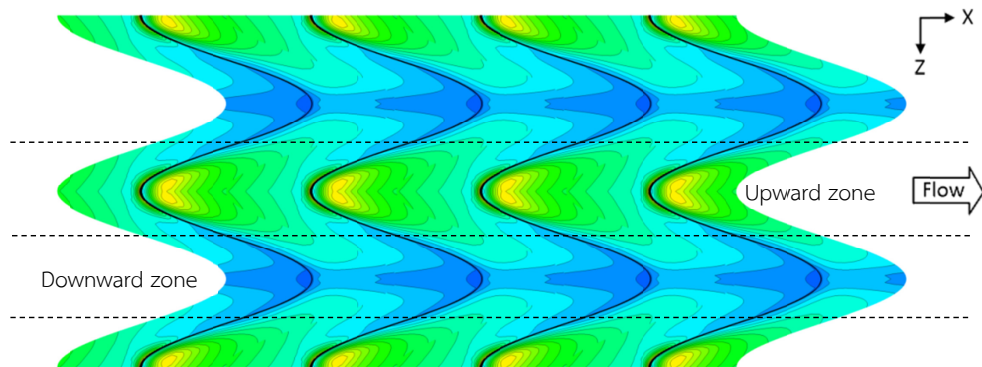
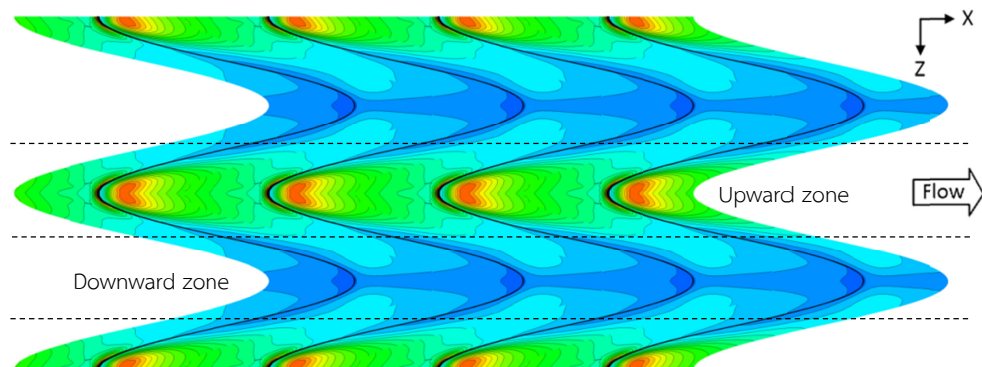
(d) 'a/H=1.00 b/H=0.15 pL/H=1.00'



Temperature: 300 308 316 324 332 340

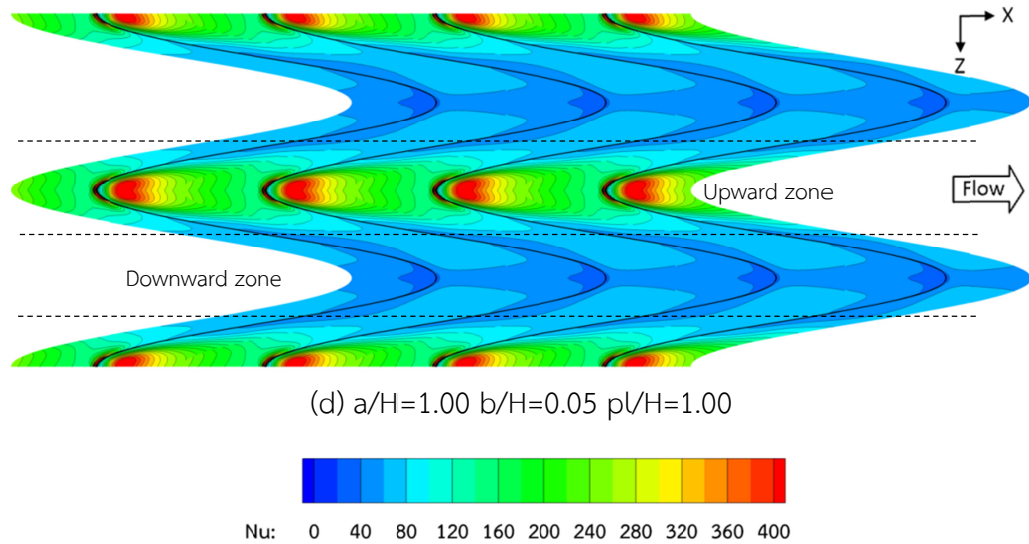
**Figure 6.36** Temperature distribution for varied  $a/H$  at  $Re=10,000$  (cont'd)

Figure 6.37a, b, c, and d, present the Nusselt number contours at  $Re=10,000$  for the baffle 'b/H=0.05 pL/H=1.00' with varied baffle amplitudes:  $a/H=0.25, 0.50, 0.75,$  and  $1.00,$  respectively. First, considering the case  $a/H=0.05,$  the Nusselt numbers on the region along the downward zone were also lower (blue regions) than Nusselt numbers on the region along the upward zone (green and yellow colors). The blue regions were also small compared with the green regions. This result indicated that, the surface temperatures at the area in front of the trough of baffle were high whereas the temperatures behind the crest of baffle were lower. With an increment of baffle amplitude to  $0.50, 0.75,$  and  $1.00,$  the blue regions expanded whereas the green and yellow regions reduced. However, behind the crest of each baffle, the red region occurred and enlarged with increasing amplitude which indicates the increasing in Nusselt numbers. Moreover, it was observed that, there was still substantial high Nusselt number in front of the crest of each baffle. Consequently, the averaged Nusselt number decreased with increasing the baffle amplitude.

(a)  $a/H=0.25$   $b/H=0.05$   $pL/H=1.00$ (b)  $a/H=0.50$   $b/H=0.05$   $pL/H=1.00$ (c)  $a/H=0.75$   $b/H=0.05$   $pL/H=1.00$ 

Nu: 0 40 80 120 160 200 240 280 320 360 400

Figure 6.37 Nu contour of varied  $a/H$  at  $Re=10,000$



**Figure 6.37** Nu contour of varied  $a/H$  at  $Re=10,000$  (cont'd)

Figure 6.38, 6.39, and 6.40 present the Nusselt number ratio of the baffle  $p/H=1.00$  with varied baffle amplitudes having  $b/H=0.05$ ,  $0.10$ , and  $0.15$ , respectively. Considering the case  $b/H=0.05$  (Figure 6.38a), the Nusselt number ratio decreased slightly with an increment of amplitude from  $0.50$  to  $1.00$ . The higher amplitude gave lower Nusselt number ratio. This was due to the reduction of the strength of secondary flow reattachment/impingement in the downward zone. However, the baffle  $a/H=0.25$  provided lower Nusselt number ratio at low Reynolds number compared with the baffle  $a/H=0.50$ .

For the baffles:  $b/H=0.10$  and  $0.15$  (Figure 6.39 and 6.40), the Nusselt number ratio decreased gradually with an increment of baffle amplitude. This may be due to the strength of secondary flow impingement downward zone was also reduced with increasing amplitude. According to the numerical results, the highest Nusselt number ratio was found to be  $4.86$  at the baffle ' $a/H=0.25$   $b/H=0.15$   $p/H=1.00$ '.

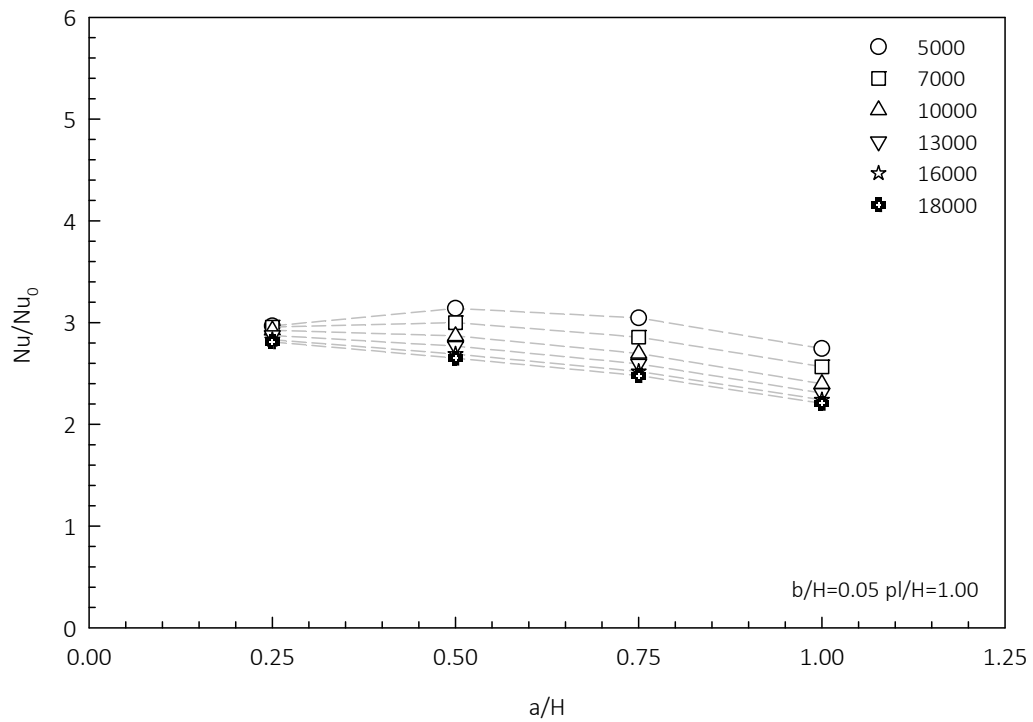


Figure 6.38 Variation of  $Nu/Nu_0$  with  $a/H$  for various  $Re$  at  $b/H=0.05$

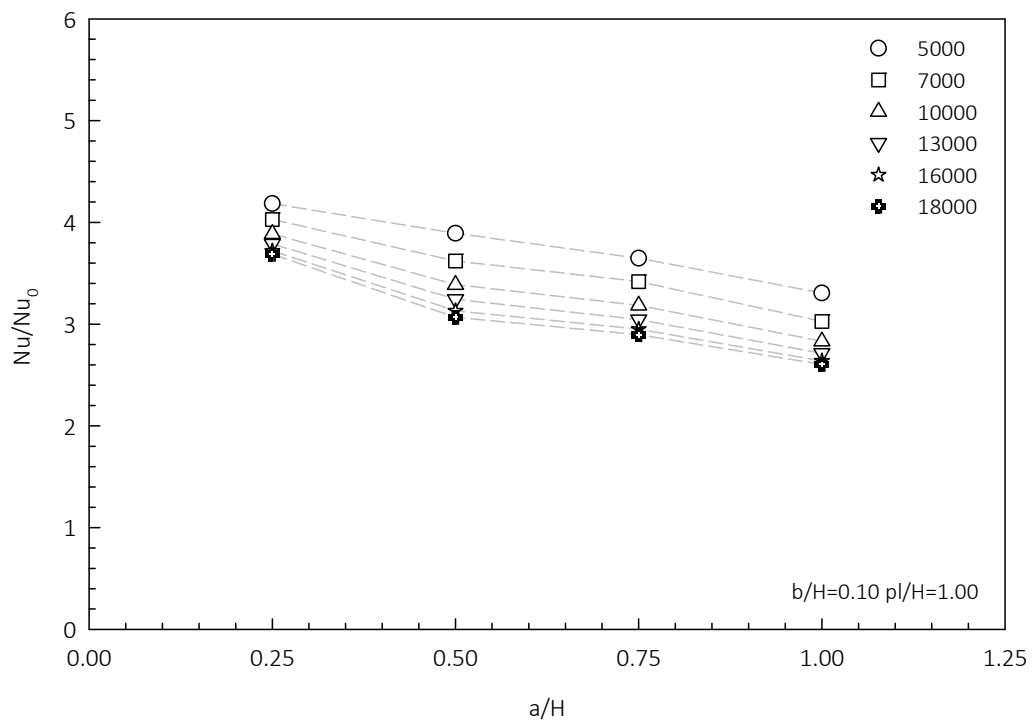
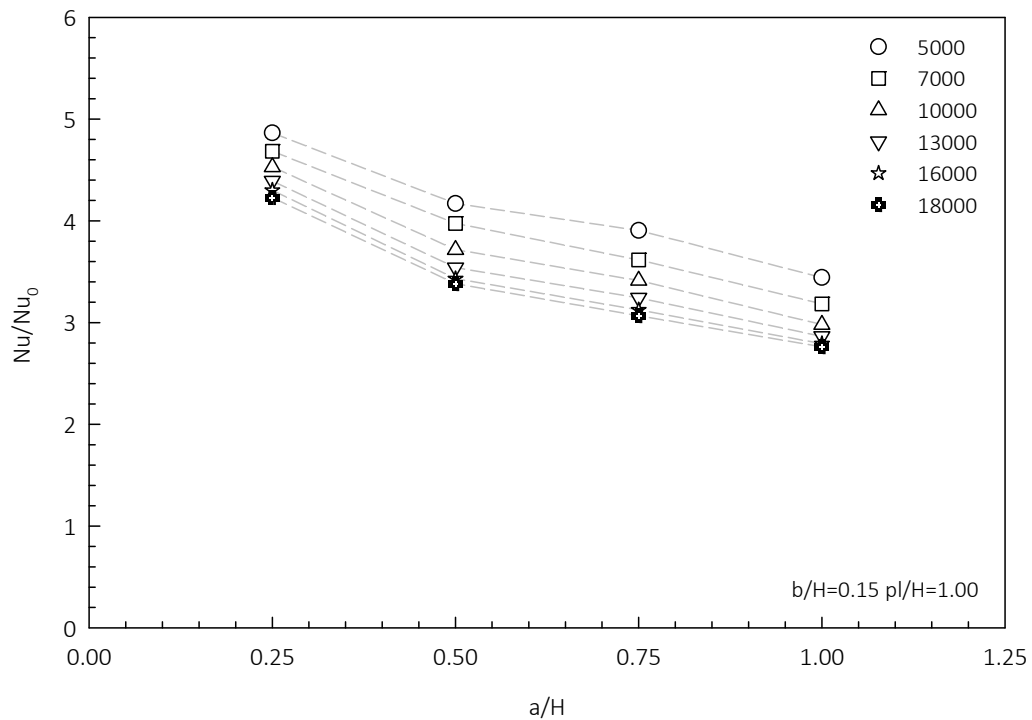


Figure 6.39 Variation of  $Nu/Nu_0$  with  $a/H$  for various  $Re$  at  $b/H=0.10$



**Figure 6.40** Variation of  $Nu/Nu_0$  with  $a/H$  for various  $Re$  at  $b/H=0.15$

## 6.4 Thermo-hydraulic performance of air flow

This section presents the effects of the geometric parameters on the thermo-hydraulic performance. Assumed the same pumping power, the thermo-hydraulic performance was individually evaluated for a range of Reynolds number from 5,000 to 18,000.

### 6.4.1 Effects of Reynolds number and longitudinal pitch

Figure 6.41 to 6.43 present the effects of Reynolds number and longitudinal pitch on the thermo-hydraulic performance for varied baffle height:  $b/H=0.05$ ,  $0.10$ , and  $0.15$ , respectively. As a result, the thermal performance decreased considerably with increasing Reynolds number. It was also observed that, for most cases, the  $p/H=1.00$  provided the better thermal performance than  $p/H=0.50$  and  $1.50$ . Moreover, for most cases, the values of thermo-hydraulic performances at a given range of Reynolds number were noticeably higher than unity. Therefore, the sinusoidal wavy baffle channel in the present study can potentially improve the thermal performance with respect to the smooth channel.

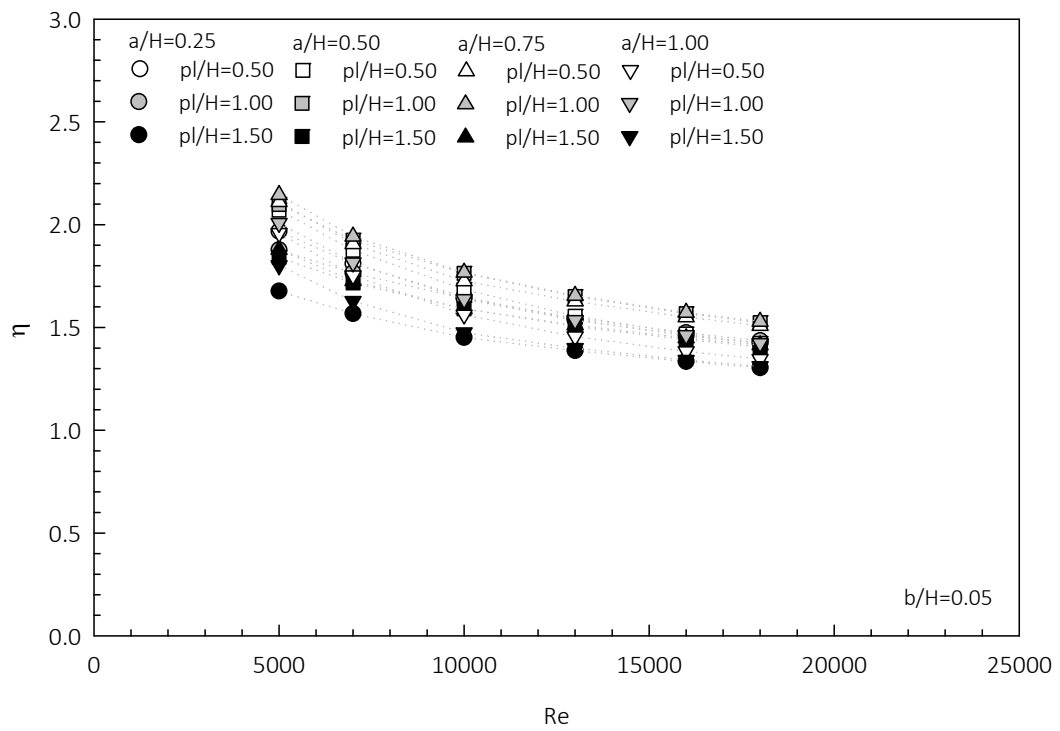


Figure 6.41 Variation of  $\eta$  with  $Re$  for varied  $p/H$  at  $b/H=0.05$

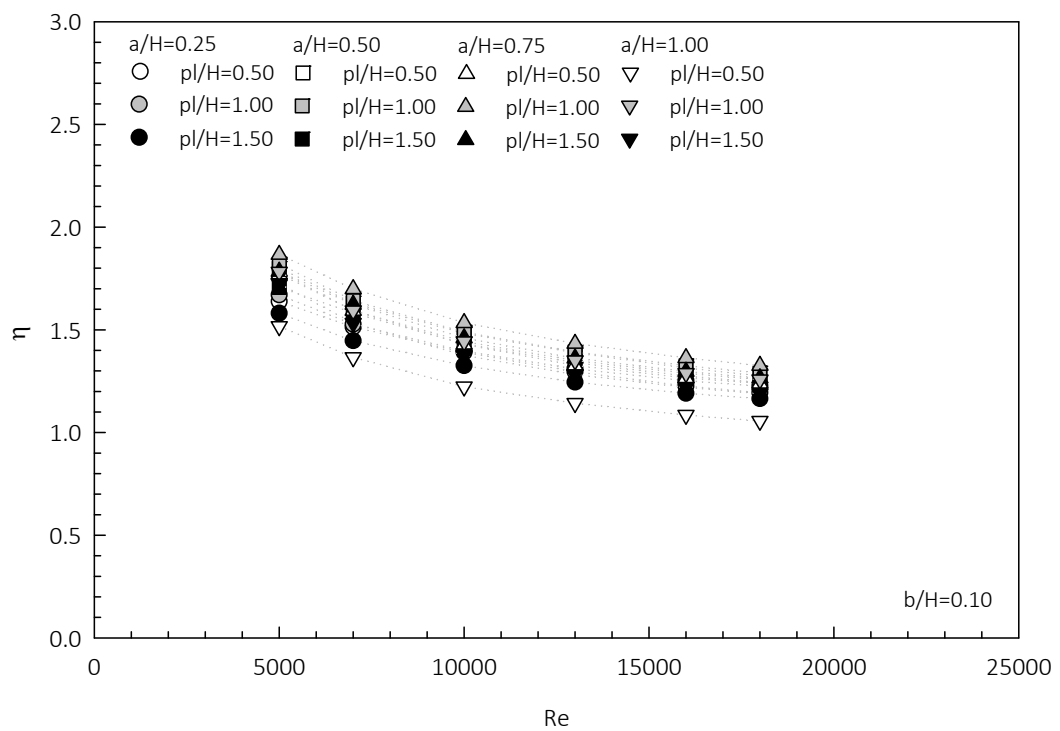


Figure 6.42 Variation of  $\eta$  with  $Re$  for varied  $p/H$  at  $b/H=0.10$

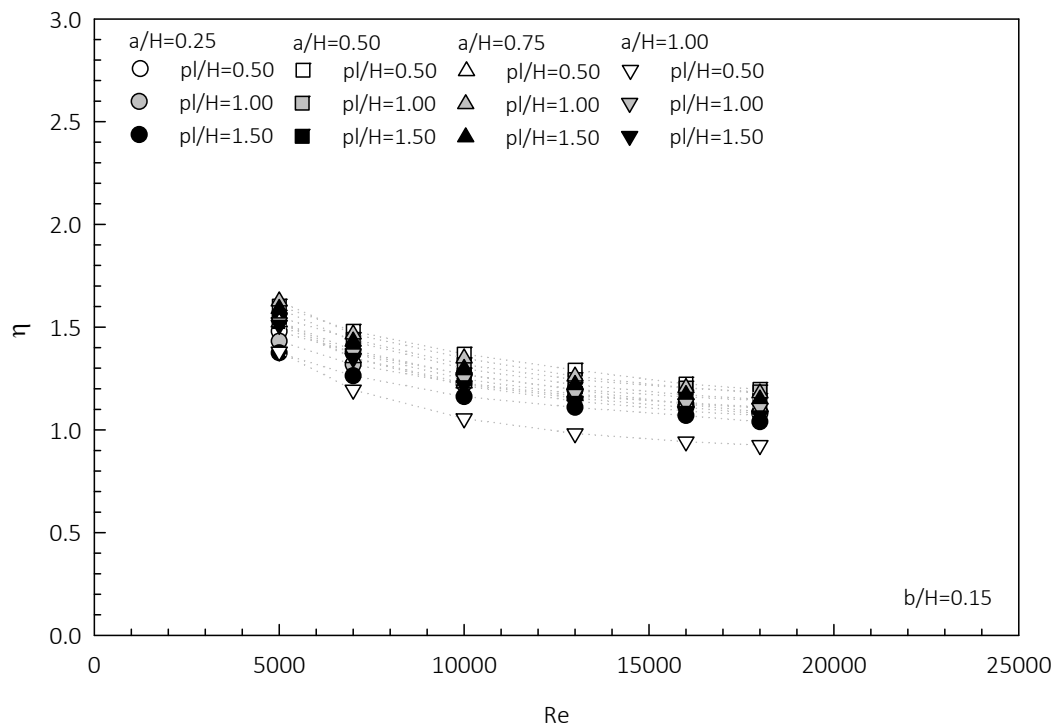


Figure 6.43 Variation of  $\eta$  with Re for varied  $p/H$  at  $b/H=0.15$

#### 6.4.2 Effects of baffle height

Figure 6.44 to 6.47 present the thermo-hydraulic performances of varied baffle heights having various amplitudes:  $a/H=0.25$ ,  $0.50$ ,  $0.75$ , and  $1.00$ , respectively. As a result, the thermal performance decreased markedly with extending baffle height for each given Reynolds number. This was due to the influence of the blockage ratio on the friction factor was more than the enlargement of heat transfer rate. According to the numerical results, the maximum thermal performance was found to be  $2.15$  corresponding to the baffle ' $a/H=0.75$   $b/H=0.50$   $p/H=1.00$ ' at a given Reynolds number of  $5,000$ .

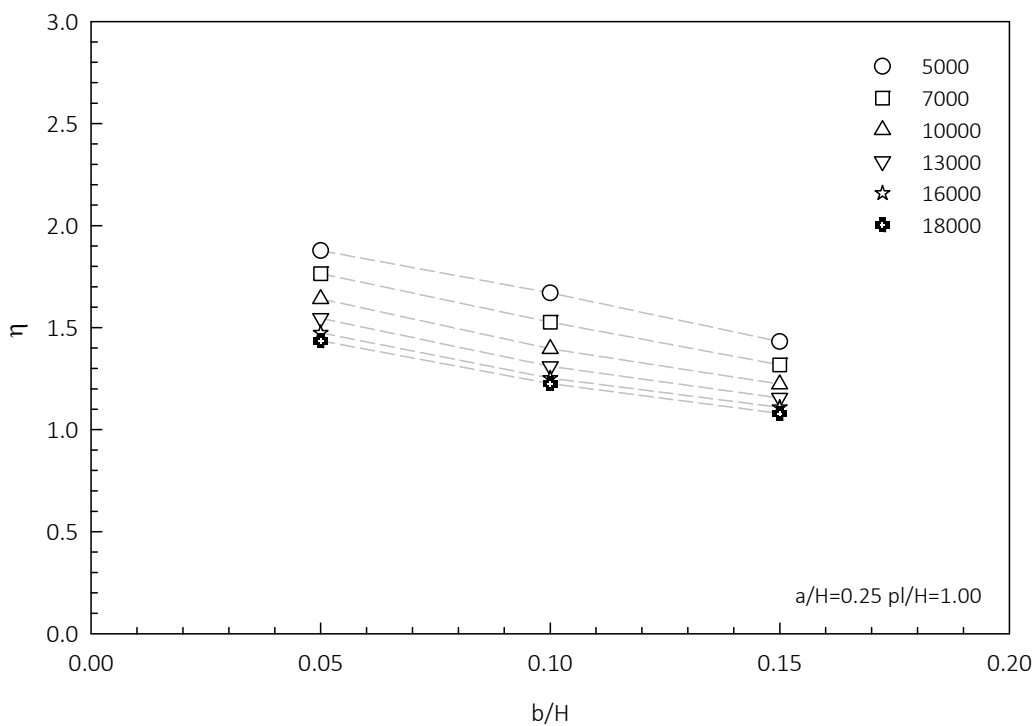


Figure 6.44 Variation of  $\eta$  with  $b/H$  for various  $Re$  at  $a/H=0.25$

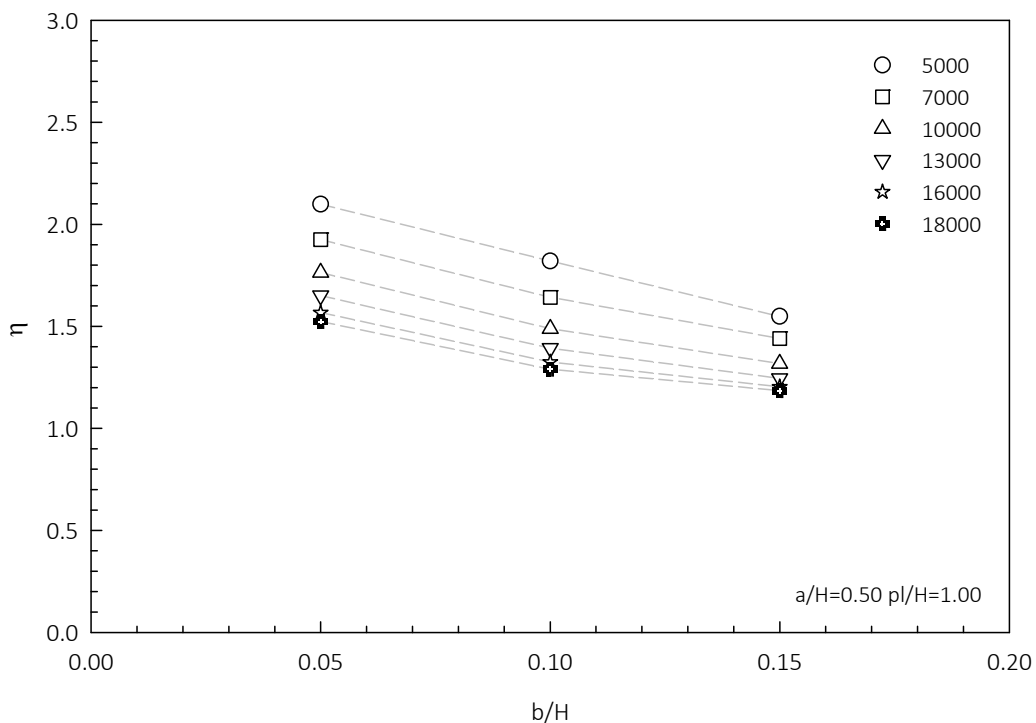


Figure 6.45 Variation of  $\eta$  with  $b/H$  for various  $Re$  at  $a/H=0.50$

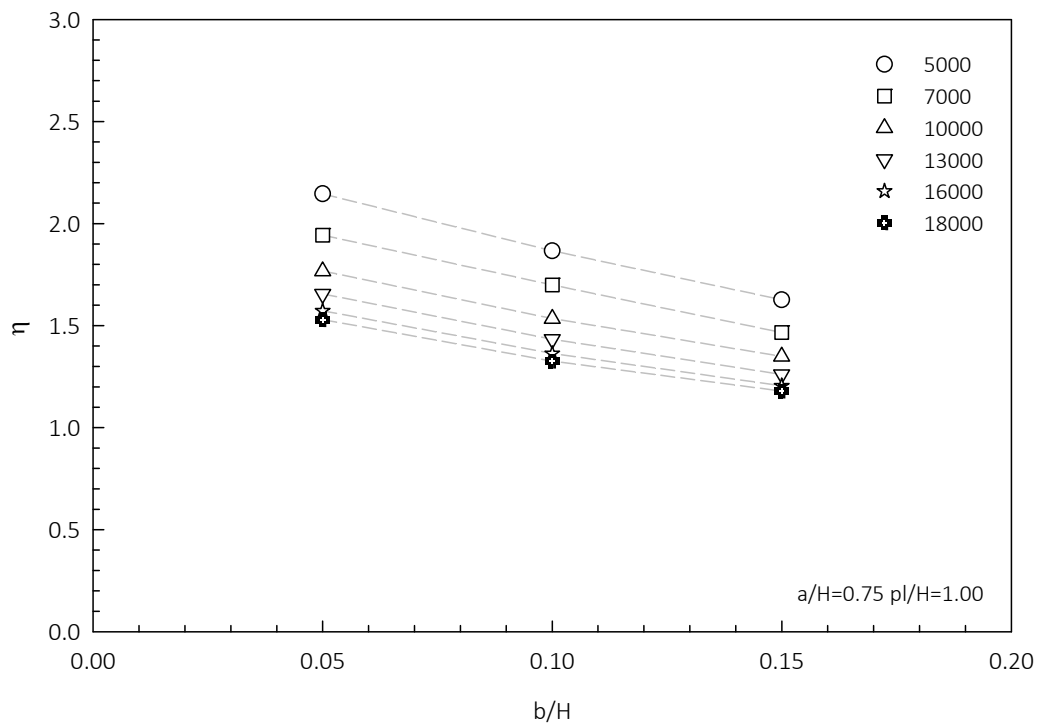


Figure 6.46 Variation of  $\eta$  with  $b/H$  for various  $Re$  at  $a/H=0.75$

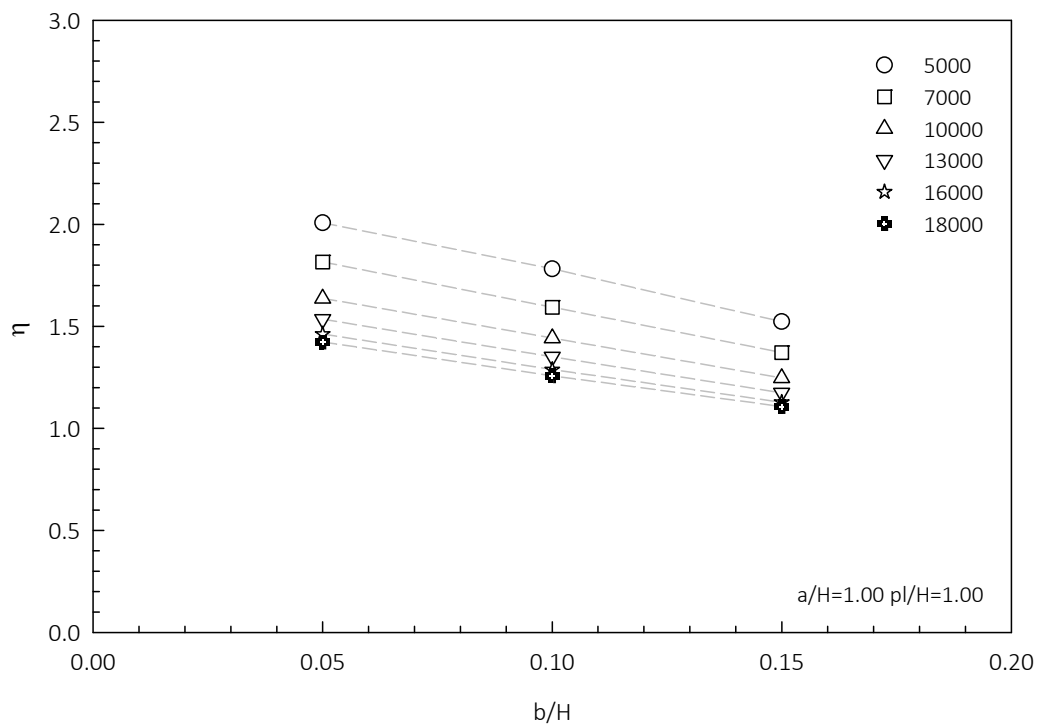


Figure 6.47 Variation of  $\eta$  with  $b/H$  for various  $Re$  at  $a/H=1.00$

### 6.4.3 Effects of baffle amplitude

Figure 6.48, 6.49, and 6.50 present the thermo-hydraulic performances of varied amplitudes having baffle height:  $b/H=0.05$ ,  $0.10$ , and  $0.15$ , respectively. Considering the case  $b/H=0.05$ , the thermal performance increased gradually with increasing  $a/H$  from  $0.25$  to  $0.50$ . The thermal performance increased slightly from  $a/H=0.50$  until reached  $a/H=0.75$  and then decreased slightly at  $a/H=1.00$ . The other baffle heights also delivered the similar results. The reason could be the effect of the lower heat transfer in the downward zone was more than the heat transfer enhancement in the upward zone combined with the reduction of pressure loss due to the increasing amplitude. According to the numerical result, depending on Reynolds number, the maximum thermal performances were found to be  $1.53 - 2.15$  corresponding to the baffle ‘ $a/H=0.75$   $b/H=0.05$   $p/H=1.00$ ’.

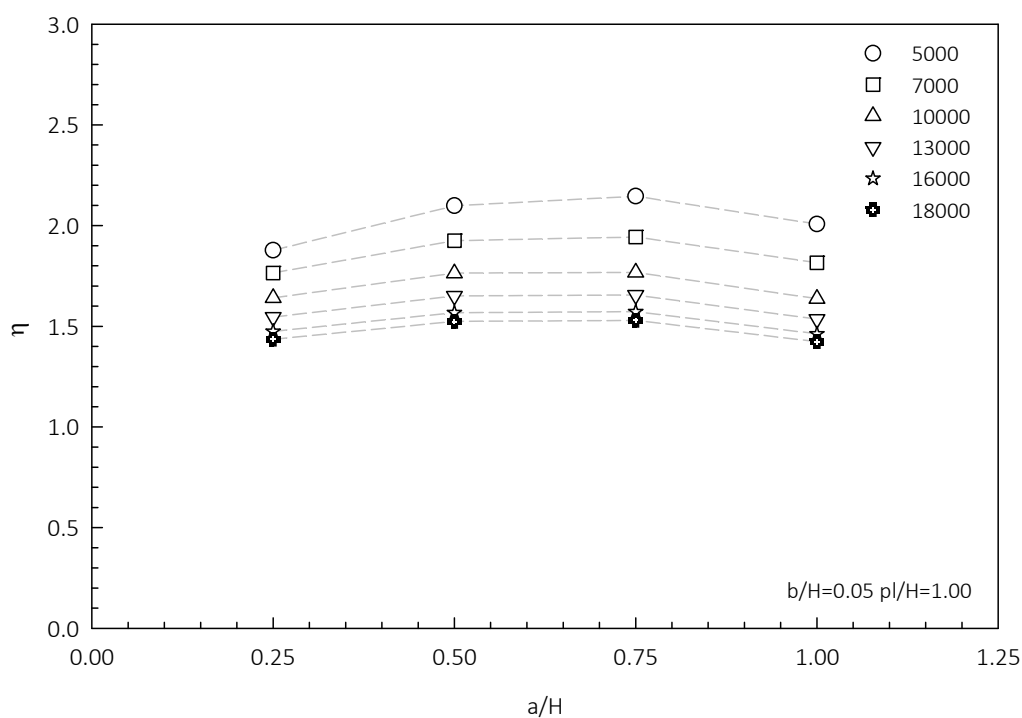


Figure 6.48 Variation of  $\eta$  with  $a/H$  for various  $Re$  at  $b/H=0.05$

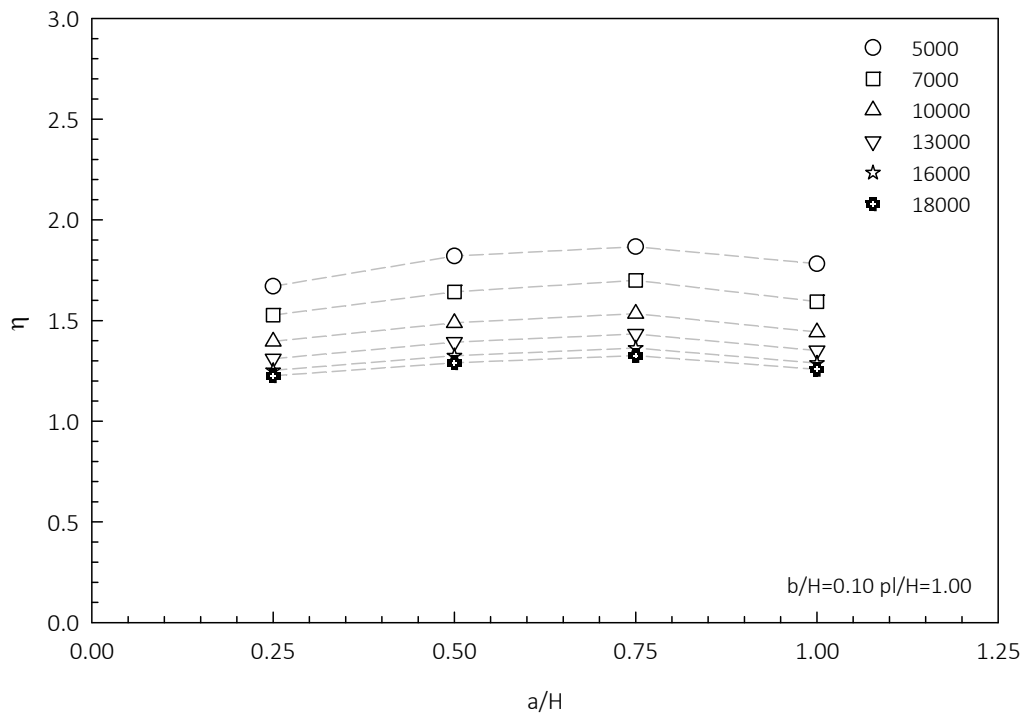


Figure 6.49 Variation of  $\eta$  with  $a/H$  for various  $Re$  at  $b/H=0.10$

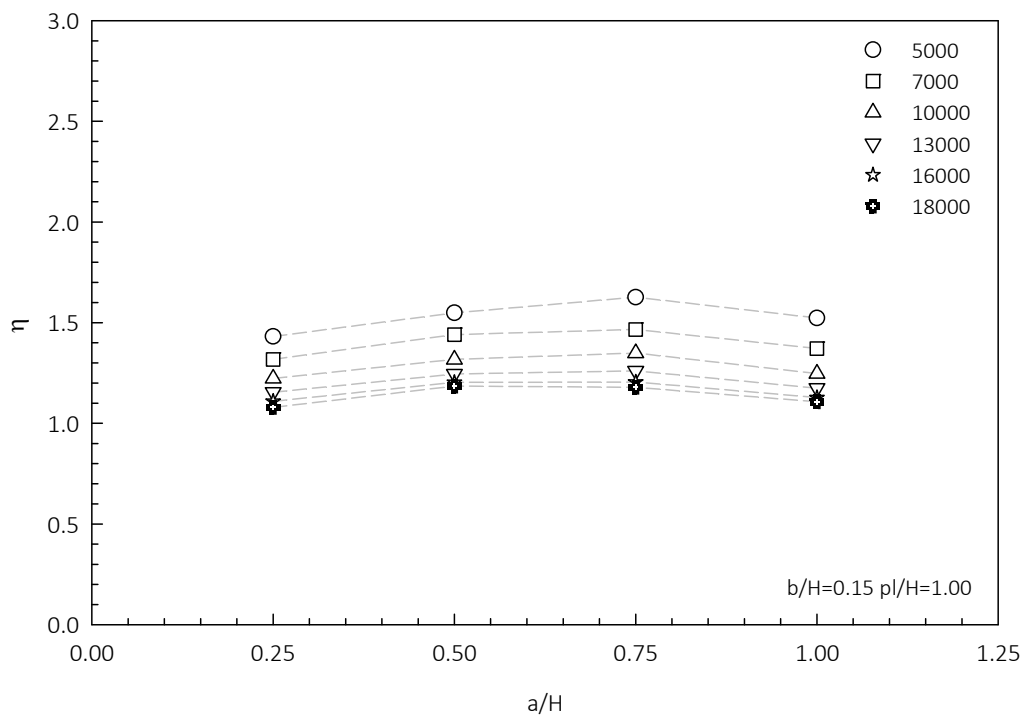


Figure 6.50 Variation of  $\eta$  with  $a/H$  for various  $Re$  at  $b/H=0.15$

## 6.5 Empirical correlations of air flow

For the present study, the correlations for prediction of the friction factor, the Nusselt number, and the thermo-hydraulic performance were developed using linear regression analysis. Based on the obtained numerical outputs for the range of observed values, the friction factor, the Nusselt number, and the thermo-hydraulic performance as functions of Reynolds number and geometric parameters which were relative height ( $b/H$ ), relative longitudinal pitch ( $pl/H$ ), and relative amplitude ( $a/H$ ) were approximated as the following equations, respectively.

$$f = 4.0949 \text{Re}^{0.0714} (b/H)^{1.5188} (pl/H)^{-0.5914} e^{(0.1329 \ln(a/H)^2 - 0.5421 \ln(a/H))} \quad (6.1)$$

$$\text{Nu} = 0.3774 \text{Re}^{0.6553} (b/H)^{0.2738} (pl/H)^{-0.2036} e^{(-0.1398 \ln(a/H)^2 - 0.4367 \ln(a/H))} \quad (6.2)$$

$$\eta = 8.0259 \text{Re}^{-0.2519} (b/H)^{-0.2325} (pl/H)^{-0.0064} e^{(-0.1841 \ln(a/H)^2 - 0.2560 \ln(a/H))} \quad (6.3)$$

The predicted values of the friction factor, the Nusselt number, and the thermo-hydraulic performance from the correlation equations (Equations 6.1 – 6.3) were compared with the obtained numerical data. These comparisons are presented in Figure 6.51, 6.52, and 6.53, respectively. The predicted friction factor and Nusselt number were well agreed with the numerical values within  $\pm 20\%$  deviations. The predicted thermo-hydraulic performance was in good agreement with the numerical values within  $\pm 15\%$  deviations. Therefore, these correlations can reasonably predict the values of the Nusselt number, and the thermo-hydraulic performance in the range of observed parameters.

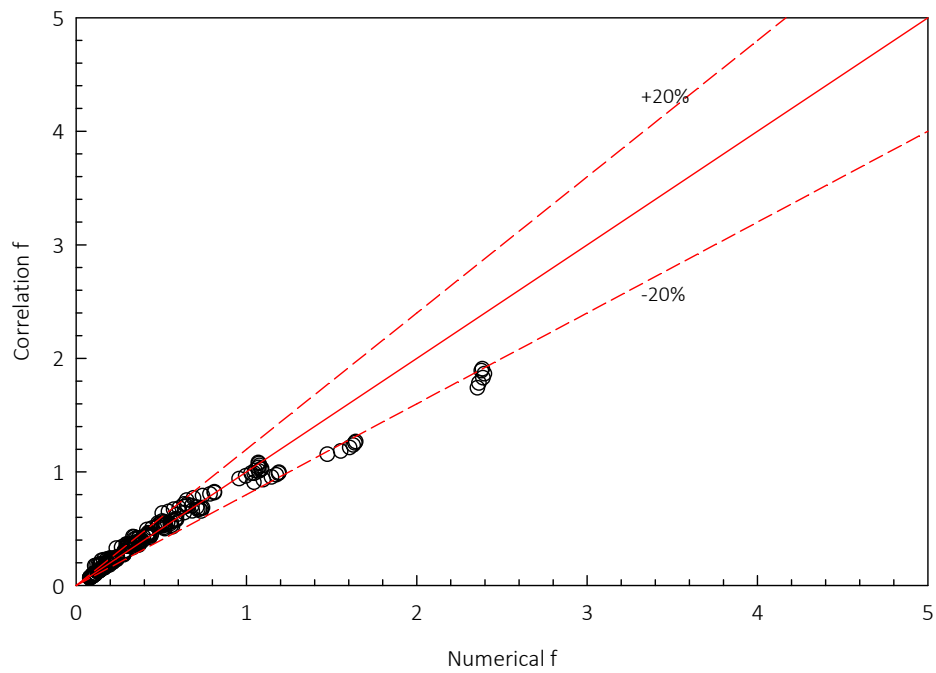


Figure 6.51 Comparison of correlation and numerical  $f$

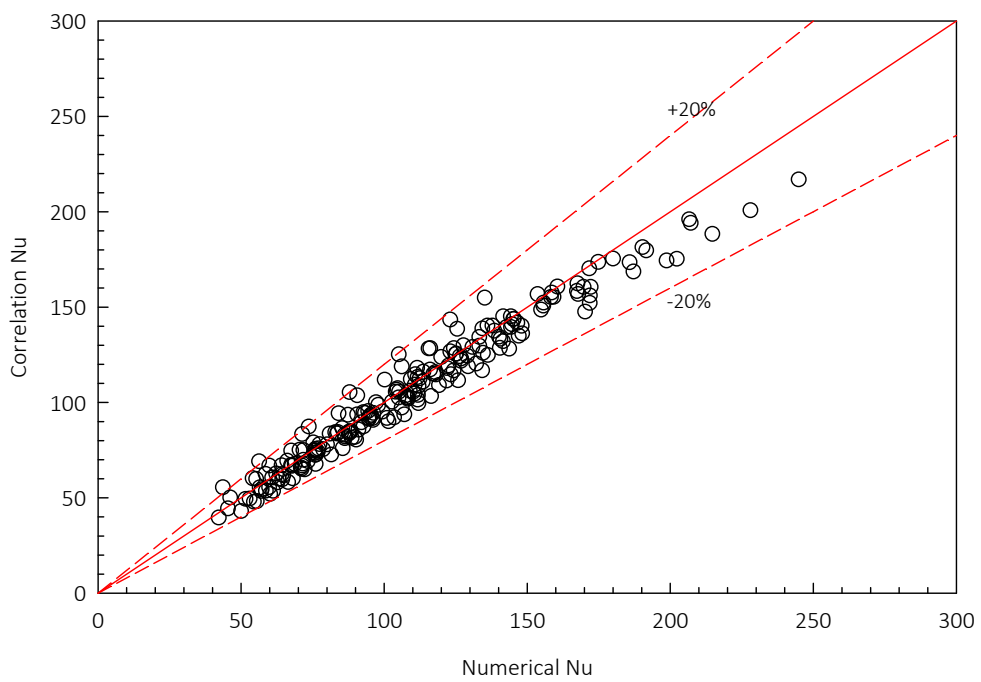


Figure 6.52 Comparison of correlation and numerical  $Nu$

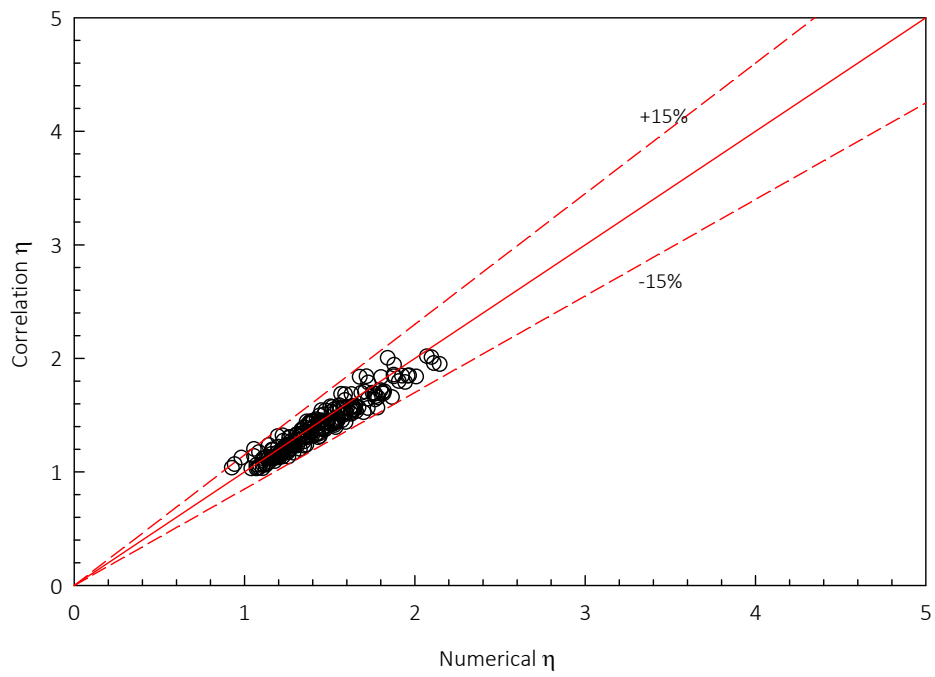


Figure 6.53 Comparison of correlation and numerical  $\eta$

## CHAPTER 7

# NUMERICAL INVESTIGATION OF NANOFUID FLOW

This chapter describes and discusses the effects of water and a nanofluid on the flow and heat transfer characteristics in the sinusoidal wavy baffle channel corresponding to the proposed baffle 'a/H=0.75 b/H=0.05 p/H=1.00'. This baffle geometry was selected due to its highest thermo-hydraulic performance achieved in the previous chapter.

### 7.1 The baffle channel computation of nanofluid flow

In the present study, the numerical simulations were carried out for the proposed optimum baffle geometry: 'a/H=0.75 b/H=0.05 p/H=1.00' using water and Al<sub>2</sub>O<sub>3</sub>-water nanofluid as working fluids with varied nanoparticle sizes and varied volume fractions at the observed range of Reynolds number 5,000 to 18,000. For the nanofluid flow study, the numerical simulation was developed under the following assumptions:

- Steady three-dimensional fluid flow and heat transfer.
- Turbulent and incompressible flow.
- Single-phase fluid flow
- Negligible body forces.
- Negligible viscous dissipation.
- Negligible radiation heat transfer.
- No thermal energy sources within the fluid.

The range of nanofluid parameters, the baffle geometry, channel characteristic, flow condition, and thermal condition are summarized in Table 7.1. Additionally, in the numerical simulation, the nanofluid was considered as Newtonian fluid and treated as a single-phase fluid. The properties of base fluid and Al<sub>2</sub>O<sub>3</sub> are presented in Table 7.2. The results and discussions presented hereafter focus on the effects of nanoparticle sizes, volume fractions, and Reynolds number on the flow and heat transfer characteristics in the periodical fully-developed turbulent regime.

**Table 7.1** Study parameters and flow conditions of nanofluid flow

Study parameters	Values
Proposed baffle geometry	'a/H=0.75 b/H=0.05 p/H=1.00'
Channel height, H	0.02 m
Hydraulic diameter, $D_h$	0.04 m
Nanoparticle size, $d_p$	30, 50, 80 nm
Nanoparticle volume fraction, $\phi$	1, 3, 5 %
Flow and thermal conditions	Values
Reynolds number, Re	5,000 – 18,000
Working fluid	Water, Al <sub>2</sub> O <sub>3</sub> -water nanofluid
Surface heat flux, $q_s$	10,000 W/m <sup>2</sup>

**Table 7.2** Reference values used in computations of nanofluid flow [93]

Thermophysical property	H <sub>2</sub> O	Al <sub>2</sub> O <sub>3</sub> (Solid)
Density, $\rho$	998.2 kg/m <sup>3</sup>	3,970 kg/m <sup>3</sup>
Specific heat at constant pressure, $c_p$	4,182 J/kg·K	765 J/kg·K
Thermal conductivity, k	0.606 W/m <sup>2</sup> ·K	40.0 W/m <sup>2</sup> ·K
Dynamic viscosity, $\mu$	0.001003 kg/m·s	-
Prandtl number, Pr	6.9909	-
Temperature reference, $T_{ref}$	293 K	293

## 7.2 Flow characteristics of nanofluid

This section presents the effects of water and Al<sub>2</sub>O<sub>3</sub>-water nanofluid on the pressure loss and flow characteristics. The results of friction factor for smooth channel using water and for the proposed baffle channel using Al<sub>2</sub>O<sub>3</sub>-water nanofluid are presented in Figure 7.1. Similar to air flow results, for periodical fully-developed turbulent flow in the channel, the friction factors of base fluid and nanofluid decreased slightly with increasing Reynolds number as expected. The values of friction factor for the baffle channel using Al<sub>2</sub>O<sub>3</sub>-water were markedly higher than for the smooth channel using water at given range of Reynolds number.

Considering the effect of nanoparticle sizes for a constant volume concentration, the change in nanoparticle diameters from 30nm to 80nm had a little effect on the friction factor. For the range of observed Reynolds number, the values of friction factor for the same volume fraction were not significant different. Considering the effect of nanoparticle volume fractions for the same nanoparticle diameter, the friction factor increased with an increment in volume concentration from 1% to 5%. Since the pressure drop is dependent on the density and viscosity of

fluid, the addition of volume fraction also increases the density and viscosity of nanofluids. Moreover, the volume concentration has a strong influence on the mass density of nanofluid. Consequently, the increase in nanoparticle volume fraction caused an enlargement of pressure drop and also the friction factor.

The values of friction factor ratio for given different nanoparticle sizes and volume fractions are presented in Figure 7.2. The friction factor ratio increased with an increase in Reynolds number. The increment in volume concentration also had the friction factor ratio increased. According to numerical solutions, the values of friction factor ratio of the proposed baffle channel using  $\text{Al}_2\text{O}_3$ -water were 2.51 - 4.10 times with respect to the smooth channel using water.

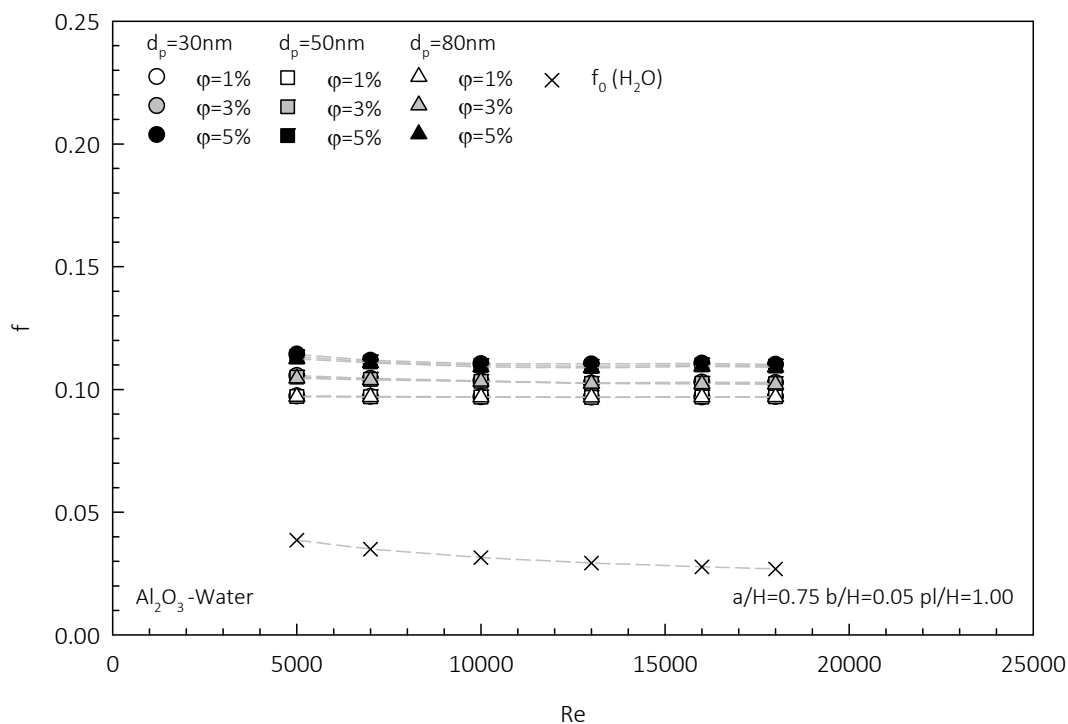


Figure 7.1 Variation of  $f$  with  $Re$  for varied  $d_p$  and  $\phi$

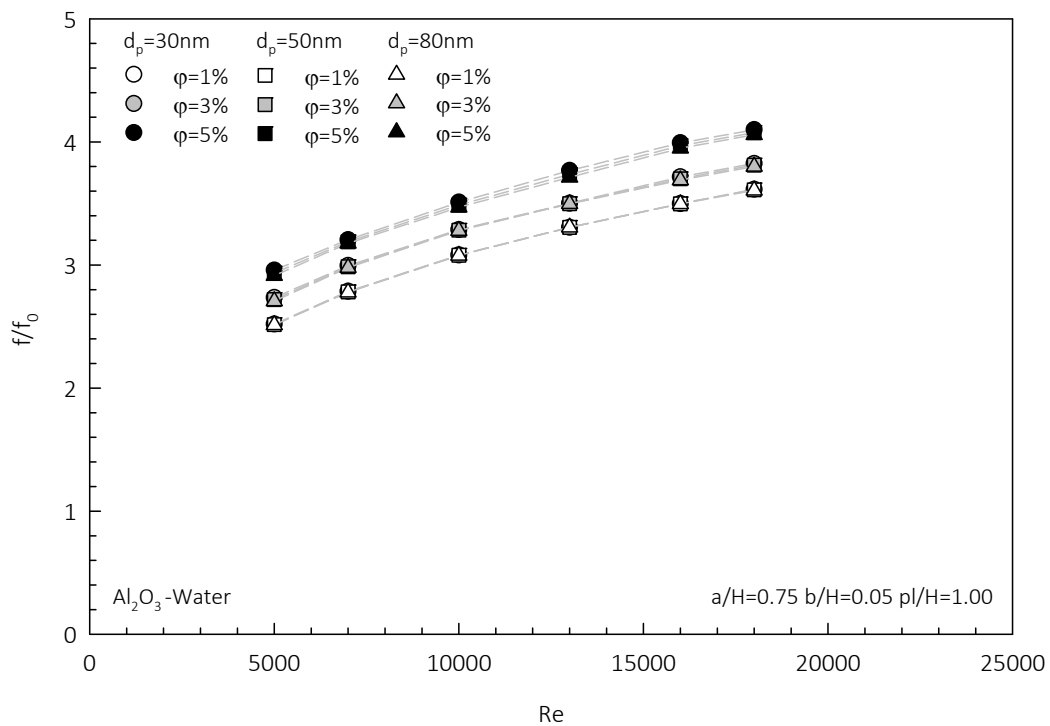
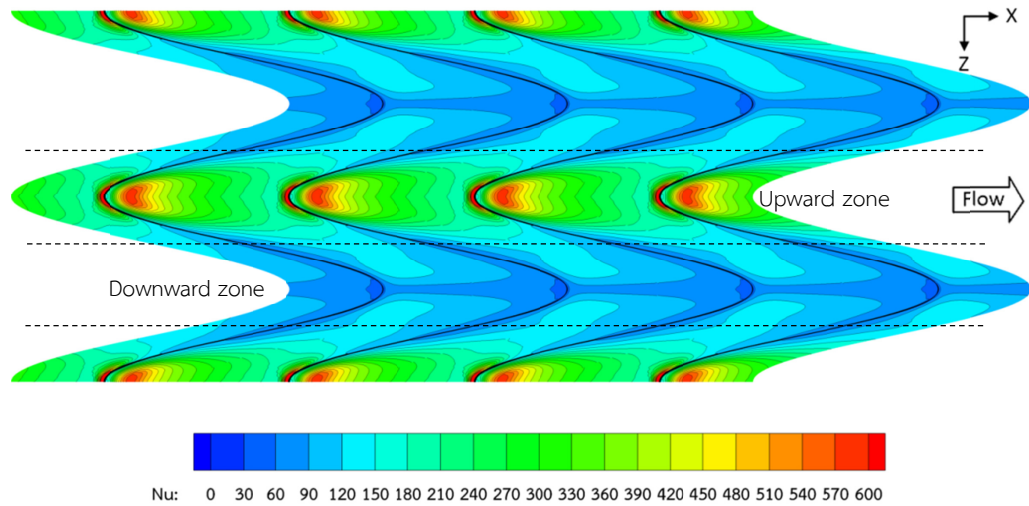


Figure 7.2 Variation of  $f/f_0$  with Re for varied  $d_p$  and  $\phi$

### 7.3 Heat transfer characteristics of nanofluid flow

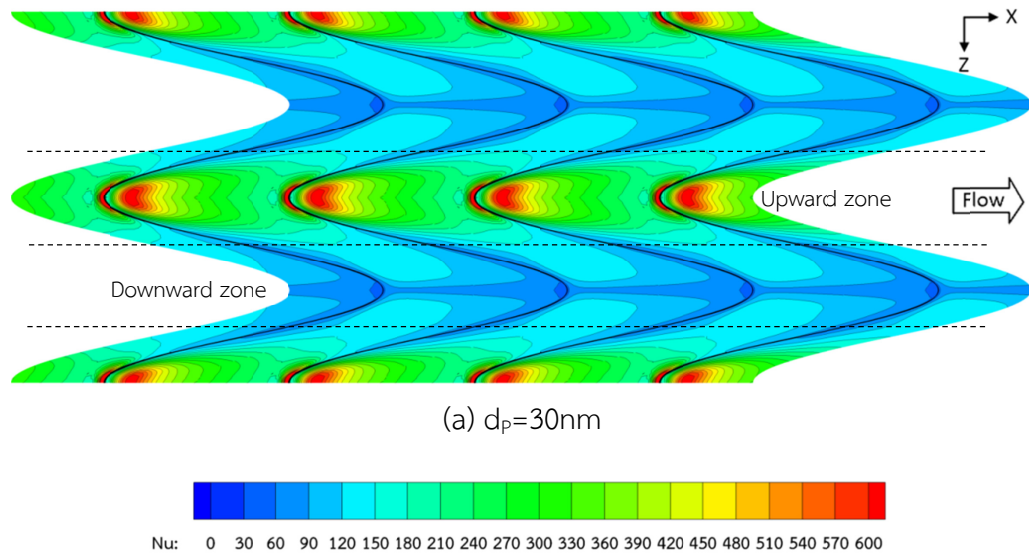
This section presents the effects of water and  $\text{Al}_2\text{O}_3$ -water nanofluid on heat transfer characteristics. The heat transfer coefficients of water and  $\text{Al}_2\text{O}_3$ -water nanofluid in the proposed baffle channel were individually determined at Reynolds number ranging from 5,000 to 18,000. The area-weighted averaged Nusselt number was calculated regarding to heat surface area. Then, the Nusselt number ratio was also calculated with respect to the smooth channel using water at the same Reynolds number.

Figure 7.3 presents the Nusselt number contour of water as the base fluid at  $\text{Re}=10,000$ . The pattern of Nusselt number contour of the water flow was similar to the air flow except that its values were greatly higher due to its higher thermal conductivity and higher convective heat transfer coefficient. This Nusselt number contour was used as a base case for comparing with the results of a nanofluid flow.



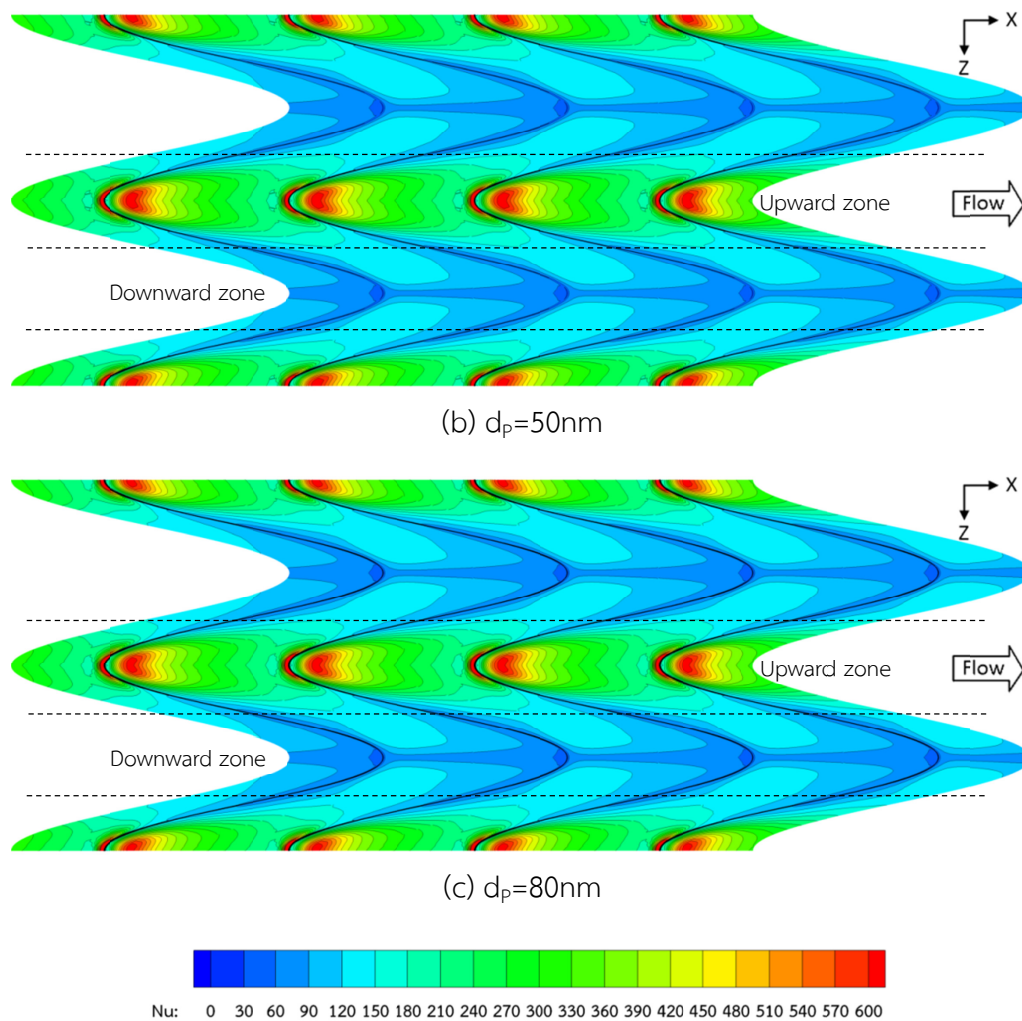
**Figure 7.3** Nu contour of water as base fluid at  $Re=10,000$

Figure 7.4a, b, and c present the Nusselt number contours at  $Re=10,000$  for  $Al_2O_3$ -water nanofluid with varied particle sizes:  $d_p=30, 50,$  and  $80nm$ , respectively. As a result, the Nusselt number contours of  $Al_2O_3$ -water nanofluid had similar pattern as the water. However, the  $Al_2O_3$ -water nanofluid provided higher Nusselt number as indicated by more light blue area in the downward zone. Particularly for the case  $\phi=1\%$ , with increasing particle size, the patterns of the Nusselt number contours were not apparently different. Therefore, the particle size also had a little effect on heat transfer coefficient.



(a)  $d_p=30nm$

**Figure 7.4** Nu contours of varied  $d_p$  at  $\phi=1\%$



**Figure 7.4** Nu contours of varied  $d_p$  at  $\phi=1\%$  (cont'd)

Figure 7.5a, b, and c present the Nusselt number contours at  $Re=10,000$  for  $Al_2O_3$ -water nanofluid with varied volume fractions:  $\phi=1, 3,$  and  $5\%$  respectively. The Nusselt number contours of  $Al_2O_3$ -water nanofluid with volume fraction of  $1\%$  had similar pattern as the water. With adding volume fraction, in the downward zone, the blue area reduced whereas the light blue and green areas expanded. The green, yellow, and red areas in the upward zone also increased. Consequently, the Nusselt number increased apparently with adding volume fraction.

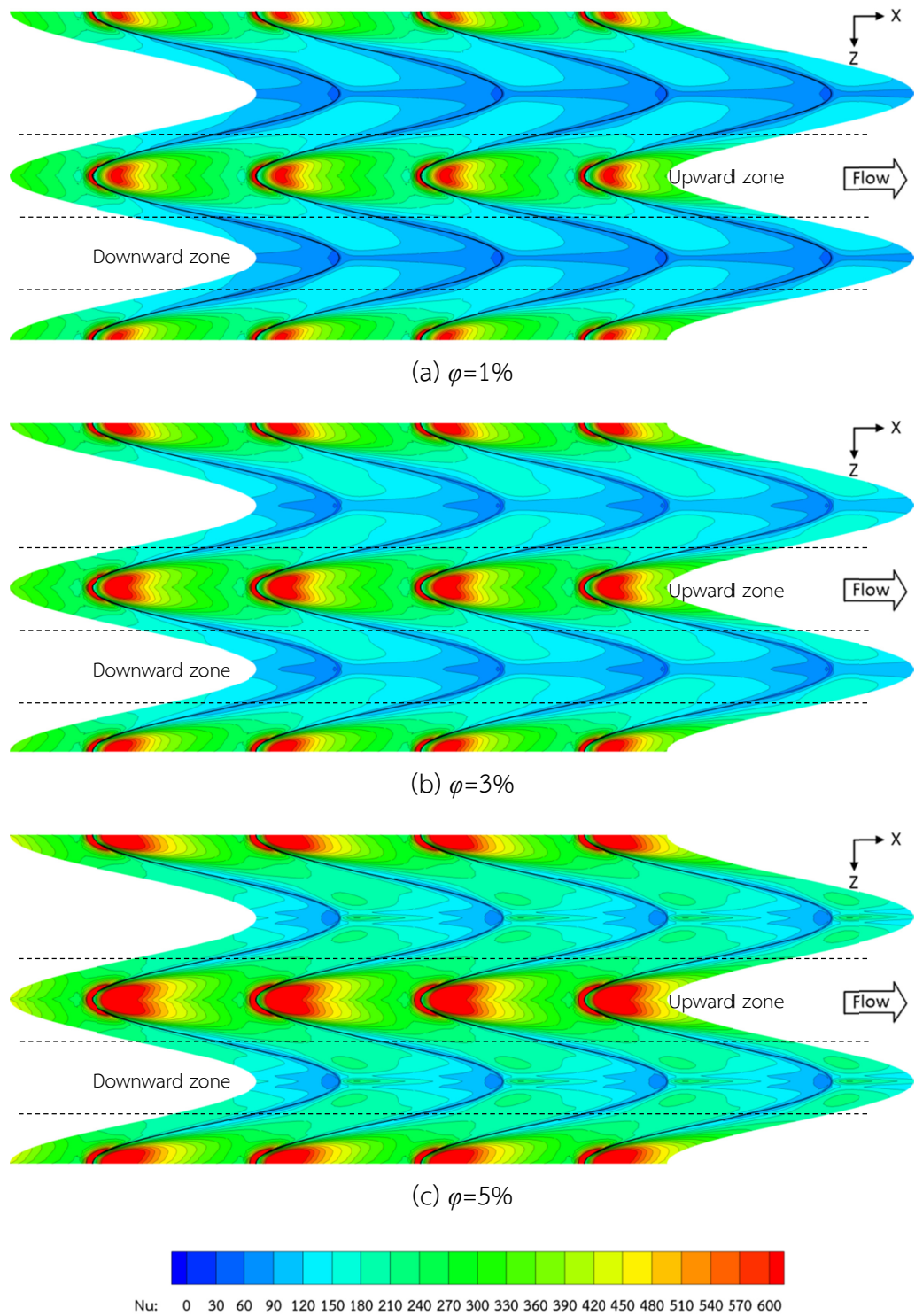


Figure 7.5 Nu contours of varied  $\varphi$  at  $d_p=30\text{nm}$

The results of averaged Nusselt number for smooth channel using water and for the proposed baffle channel using  $\text{Al}_2\text{O}_3$ -water nanofluid are presented in Figure 7.6. Similar to air flow results, the Nusselt numbers of base fluid and nanofluid increased substantially with increasing Reynolds number. The values of averaged

Nusselt number for the proposed baffle channel using  $\text{Al}_2\text{O}_3$ -water were noticeably greater than for the smooth channel using water at given range of Reynolds numbers.

Considering the effect of nanoparticle sizes for the same volume concentration, increasing nanoparticle diameters from 30nm to 80nm had reduced the Nusselt number. Considering the effect of particle volume fractions for the same particle size, the Nusselt number increased with an addition in volume concentration from 1% to 5%. It was observed that, with reducing nanoparticle size, the Nusselt number increased moderately at volume fraction of 3% and 5%. However, at the volume fraction of 1%, the Nusselt number increased slightly with shrinking nanoparticle diameters.

The possible reason for the augmentation in heat transfer may be due to the nanoparticles suspended in the fluid had increased the thermal conductivity of the nanofluid. The energy exchange process caused by the chaotic movement of nanoparticles and the thermal dispersion also involved. The mixing effects of nanoparticles near the wall, the flow reattachment/impingement, and the destruction of boundary layer thickness resulted from presence of the baffles may be attributed to the larger enhancement in convective heat transfer coefficient compared to enhancement in thermal conductivity. Furthermore, the heat transfer enhancement of nanofluids may be related to the reduction of viscosity and so thinner the laminar sublayer since the boundary layer thickness is proportional to the fluid viscosity. Consequently, the improvement of Nusselt number was obviously perceived.

The values of Nusselt number ratio for different particle sizes and volume fractions are presented in Figure 7.7. The Nusselt number ratio decreased gradually with increasing Reynolds number. The Nusselt number also increased with reducing nanoparticle diameter. The adding volume concentration had increased the Nusselt number ratio. According to numerical results, the values of Nusselt number ratio of the proposed baffle channel using  $\text{Al}_2\text{O}_3$ -water were 2.02 - 3.84 times with respect to the smooth channel using water.

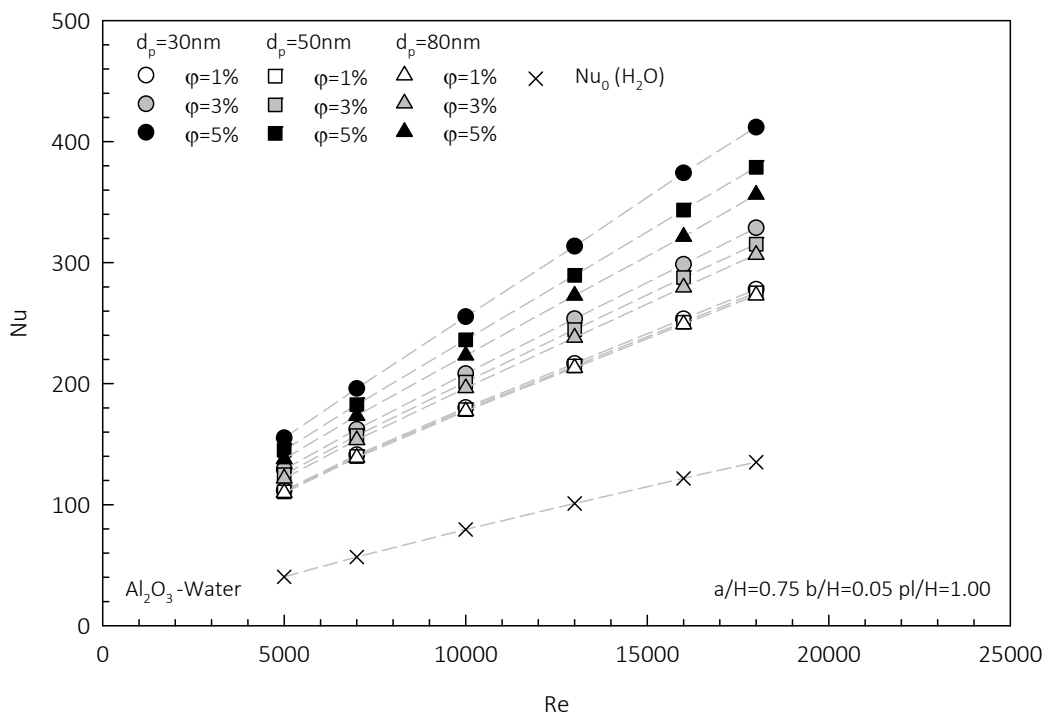


Figure 7.6 Variation of Nu with Re for varied  $d_p$  and  $\varphi$

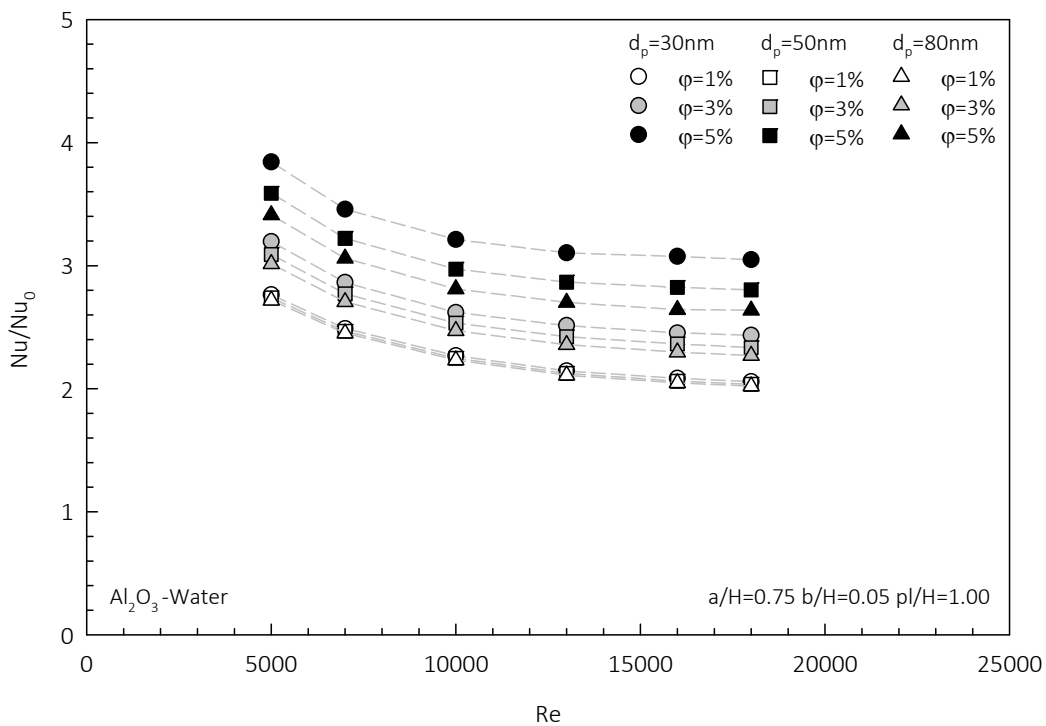


Figure 7.7 Variation of Nu/Nu<sub>0</sub> with Re for varied  $d_p$  and  $\varphi$

#### 7.4 Thermo-hydraulic performance of nanofluid flow

The effects of  $\text{Al}_2\text{O}_3$ -water nanofluid having different nanoparticle sizes and volume fractions on thermo-hydraulic performance are presented and discussed in this section. By assumed the constant pumping power, the thermo-hydraulic performances were individually evaluated for a given range of Reynolds number from 5,000 to 18,000.

The results of thermo-hydraulic performance for the proposed optimum baffle channel using  $\text{Al}_2\text{O}_3$ -water nanofluid are presented in Figure 7.8. Similar to the air flow results, the thermal performance of  $\text{Al}_2\text{O}_3$ -water nanofluid decreased moderately with increasing Reynolds number. However, the values of thermo-hydraulic performance for different nanoparticle sizes and volume fractions were higher than unity at given Reynolds numbers. For the volume fraction of 1%, the thermal performance slightly dropped with increasing particle diameter. For the volume fraction of 3 and 5%, with decreasing particle diameter, the thermo-hydraulic performance markedly increased. According to the numerical results, depending on Reynolds number, the maximum thermo-hydraulic performance were found to be 1.90 – 2.68 corresponding to nanoparticle size of 30nm and volume fraction 5% for the baffle ‘ $a/H=0.75$   $b/H=0.05$   $p/H=1.00$ ’.

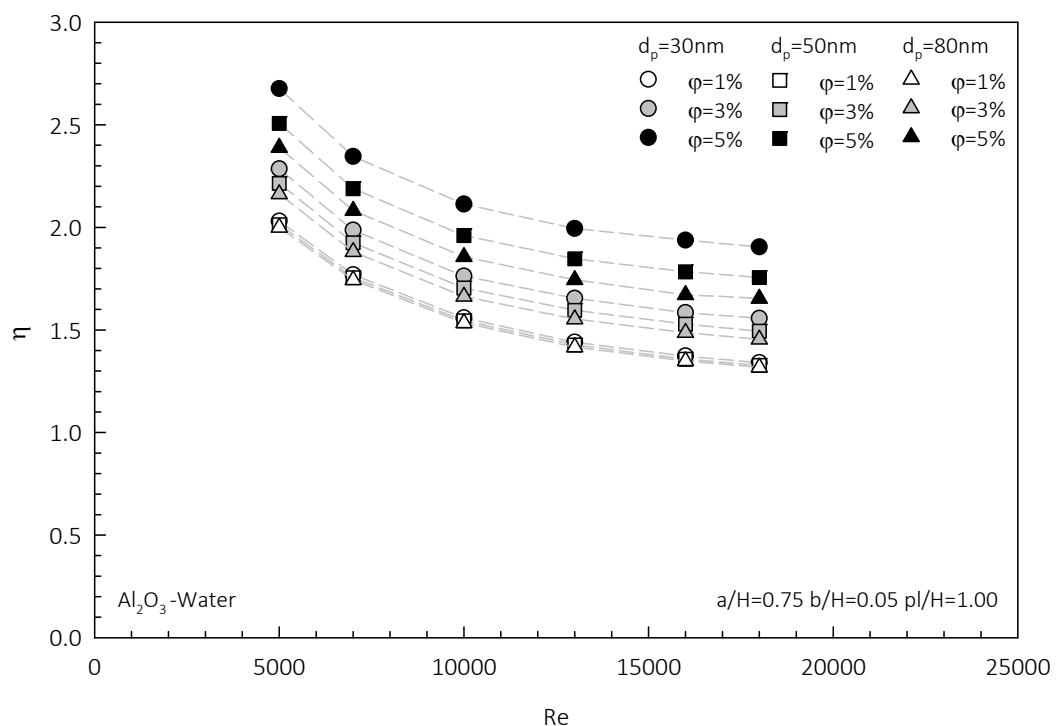


Figure 7.8 Variation of  $\eta$  with Re for varied particle sizes and volume fractions

## 7.5 Empirical correlation of nanofluid flow

For the study on the proposed optimum baffle: 'a/H=0.75 b/H=0.05 pL/H=1.00' using Al<sub>2</sub>O<sub>3</sub>-water nanofluid, the correlations for prediction of the friction factor, the Nusselt number, and the thermo-hydraulic performance were developed using multiple linear regression analysis. Based on the obtained numerical solutions for the range of observed values, the friction factor, the Nusselt number, and the thermo-hydraulic performance as functions of Reynolds number and nanofluid parameters which were nanoparticle size ( $d_p$ ) and nanoparticle volume fraction ( $\phi$ ) were approximated as the following equations, respectively.

$$f = 0.3165 \text{Re}^{-0.0155} d_p^{-0.0064} e^{(0.0463 \ln(\phi)^2 + 0.4335 \ln(\phi))} \quad (7.1)$$

$$\text{Nu} = 4.2160 \text{Re}^{0.7279} d_p^{-0.0727} e^{(0.1317 \ln(\phi)^2 + 1.1858 \ln(\phi))} \quad (7.2)$$

$$\eta = 341.4284 \text{Re}^{-0.3011} d_p^{-0.0705} e^{(0.1162 \ln(\phi)^2 + 1.0413 \ln(\phi))} \quad (7.3)$$

The predicted values of the friction factor, the Nusselt number, and the thermo-hydraulic performance from the correlation equations (Equations 7.1 – 7.3) were compared with the obtained numerical solutions. These comparisons are presented in Figure 7.9, 7.10, and 7.11, respectively. The predicted friction factor was in good agreement with the numerical values within  $\pm 5\%$ . The predicted Nusselt number and thermo-hydraulic performance were well agreed with the numerical values within  $\pm 10\%$  deviations, respectively. Therefore, these correlations can reasonably predict the values of the friction factor, Nusselt number, and the thermo-hydraulic performance in the range of observed parameters.

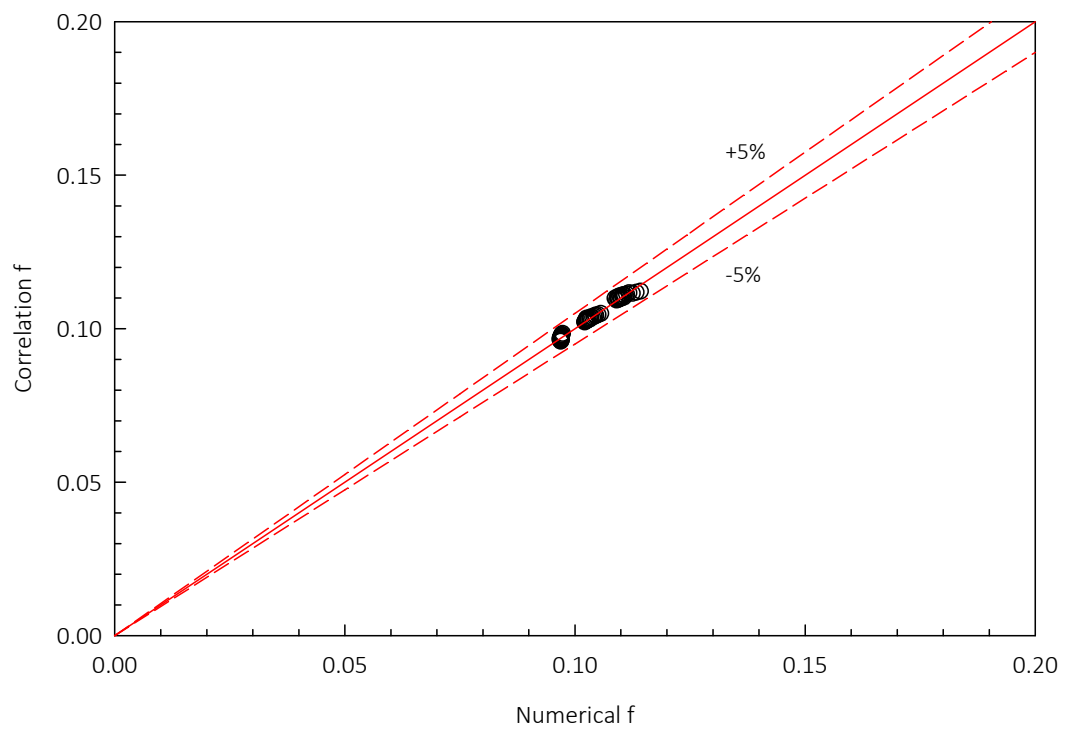


Figure 7.9 Comparison of correlation and numerical f

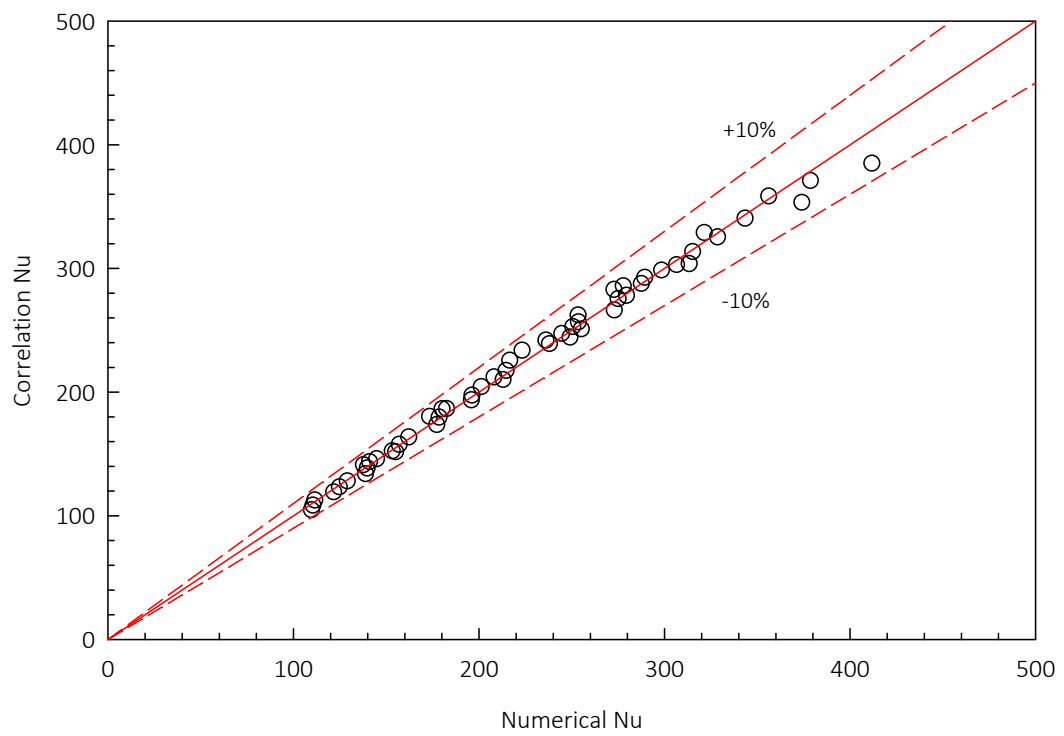
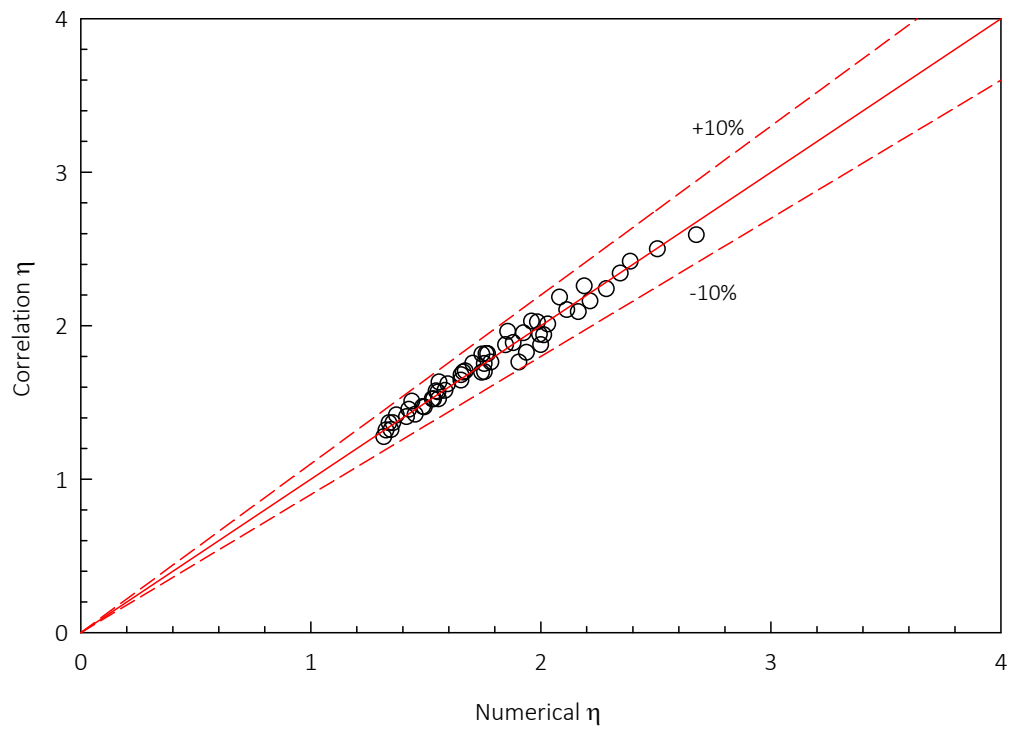


Figure 7.10 Comparison of correlation and numerical Nu



**Figure 7.11** Comparison of correlation and numerical  $\eta$

## CHAPTER 8

# CONCLUSIONS AND SUGGESTIONS

The main objective of the present study was to investigate the fluid flow and heat transfer characteristics of a channel with sinusoidal wavy baffles using air, water and  $\text{Al}_2\text{O}_3$ -water nanofluid as working fluids. A three-dimensional steady-state turbulent flow model was developed with an assumption of periodical fully developed turbulent flow. A constant surface heat flux as thermal boundary condition was applied on the top and bottom walls in the baffle channel. The computational domain was mapped into the physical domain to create the numerical model. Grid structure was specified and generated. The RNG  $k-\varepsilon$  turbulence model was employed in the numerical simulation. By applying the finite volume method, the numerical simulation was iteratively solved using the SOU and QUICK schemes. The numerical solutions were verified with grid refinement study and grid convergence index method. The numerical solutions were also compared with the well-known smooth channel correlations. The numerical simulation was validated with the experimental data obtained from preliminary experiment. For the air flow, the numerical simulations were carried out to investigate the effect of varied geometric parameters and flow conditions on the key quantifying performance factors. Then, the investigation of water and  $\text{Al}_2\text{O}_3$ -water nanofluid were conducted to examine the effects of varied particle sizes and volume fractions on the thermal performance using the proposed baffle attained from the optimum solution of the air flow computation.

### 8.1 Conclusions

The computational results for numerical simulation of sinusoidal wavy baffle channel leads to the following major conclusions:

According to validation and verification process, the numerical model provided reliable and adequate accuracy to predict the heat transfer enhancement capability of the baffle channel. The flow topology analysis and coherent structure helped to gain a better understanding of the characteristics of fluid flow and heat transfer enhancement in the sinusoidal wavy baffle channel.

In general, Nusselt number gradually increased whereas friction factor slightly decreased with increasing Reynolds number as expected. The increment of longitudinal pitch considerably reduced both heat transfer coefficient and pressure loss. The Nusselt number increased significantly with extending the baffle height. However, the friction factor also increased noticeably due to the strength of vortex

pair that induced the secondary flow impingement and reattachment. An increment of the baffle amplitude led to significant reduction in friction factor whereas Nusselt number declined slightly.

Depending on Reynolds number, the maximum thermal performance is found to be 1.53 – 2.15 corresponding to the baffle 'a/H=0.75 b/H=0.05 p/H=1.00'. According to developed correlations for the baffle geometric parameters and flow conditions, the influence of Reynolds number, the baffle height, and the baffle amplitude are most significant, respectively.

By applying the proposed optimum baffle 'a/H=0.75 b/H=0.05 p/H=1.00' using the water and Al<sub>2</sub>O<sub>3</sub>-water nanofluid as working fluids, the nanoparticle sizes had a little influence on friction factor for the same volume fraction. However, the friction factor increased moderately with adding volume fraction. Nusselt number increased substantially with increasing volume fraction and improved moderately with reducing nanoparticle sizes. The thermo-hydraulic performance also increased with decreasing nanoparticle size. The addition of volume fraction had strong influence on the thermal performance.

According to the numerical solutions, depending on Reynolds number, the maximum thermo-hydraulic performance was found to be 1.90 – 2.68 corresponding to nanoparticle size of 30nm and volume fraction 5% for the proposed optimum baffle channel.

## 8.2 Suggestions for future work

An unsteady three-dimensional flow model should be introduced to the numerical simulation of sinusoidal wavy baffle channel which can allow more details of the flow and heat transfer characteristics to be more accurately observed.

The use of LES (Large Eddy Simulation) or DNS (Direct Numerical Simulation) should also be considered.

The two-phase model should be introduced to the numerical simulation of nanofluids to compare the results with the single-phase model.

There are also needs for careful and well-planned experiments to provide suitable measuring data for validate and verify the numerical simulation.

## REFERENCES

- [1] Warren M. Rohsenow, James P. Hartnett and Yong I. Cho. **Handbook of Heat Transfer**. 3rd ED. New York : McGraw-Hill, Inc. 1998.
- [2] Ralph L. Webb, Nae-Hyun Kim. **Principles of Enhanced Heat Transfer**. 2nd ED. London : CRC Press 2005.
- [3] Das S. K., Choi S. U. S. and Patel H. E. "Heat transfer in nanofluids - A review." **Heat Transfer Engineering.**, vol. 27, no. 10, 2006. pp. 3-19
- [4] Bhushan B., Singh R. "A review on methodology of artificial roughness used in duct of solar air heaters." **Energy.**, vol. 35, 2010. pp. 202-212
- [5] Verma S. K., Prasad B. N. "Investigation for the optimal thermohydraulic performance of artificially roughened solar air heaters." **Renewable Energy.**, vol. 20, 2000. pp. 19-36
- [6] Karwa R., Solanki S. C. and Saini J. S. "Thermo-hydraulic performance of solar air heaters having integral chamfered rib roughness on absorber plates." **Energy.**, vol. 26, 2001. pp. 161-176
- [7] Momin A. M. E., Saini J. S. and Solanki S. C. "Heat transfer and friction factor in solar air heater duct with v-shaped rib roughness on absorber plate." **International Journal of Heat and Mass Transfer.**, vol. 45, 2002. pp. 3383-3396
- [8] Bhagoria J. L., Saini J. S. and Solanki S. C. "Heat transfer coefficient and friction factor correlations for rectangular solar air heater duct having transverse wedge shaped rib roughness on the absorber plate." **Renewable Energy.**, vol. 25, 2002. pp. 341-369
- [9] Lau S. C., Cervantes J., Han J. C., Rudolph R. J. and Flannery K. "Measurements of wall heat (mass) transfer for flow through blockages with round and square holes in a wide rectangular channel." **International Journal of Heat and Mass Transfer.**, vol. 46, no. 2, 2003. pp. 3991-4001
- [10] Karwa R. "Experimental studies of augmented heat transfer and friction in asymmetrically heated rectangular ducts with ribs on the heated wall in transverse, inclined, v-continuous and v-discrete pattern." **International Communications in Heat and Mass Transfer.**, vol. 30, no. 2, 2003. pp. 241-250
- [11] Sahu M. M., Bhagoria J. L. "Augmentation of heat transfer coefficient by using 90° broken transverse ribs on absorber plate of solar air heater." **Renewable Energy.**, vol. 30, 2005. pp. 2057-2073
- [12] Aharwal K. R., Gandhi B. K. and Saini J. S. "Experimental investigation on heat transfer enhancement due to a gap in an inclined continuous rib

- arrangement in a rectangular duct of solar air heater." **Renewable Energy.**, vol. 33, 2008. pp. 585-596
- [13] Saini S. K., Saini R. P. "Development of correlations for nusselt number and friction factor for solar air heater with roughened duct having arc-shaped wire as artificial roughness." **Solar Energy.**, vol. 82, 2008. pp. 1118-1130
- [14] Promvong P., Thianpong C. "Thermal performance assessment of turbulent channel flows over different shaped ribs." **International Communications in Heat and Mass Transfer.**, vol. 35, 2008. pp. 1327-1334
- [15] Bopche S. B., Tandale M. S. "Experimental investigation on heat transfer and friction characteristics of a turbulator roughened solar air heater duct." **International Journal of Heat and Mass Transfer.**, vol. 52, 2009. pp. 2834-2848
- [16] Promvong P. "Heat transfer and pressure drop in a channel with multiple 60° v-baffles." **International Communications in Heat and Mass Transfer.**, vol. 37, 2010. pp. 835-840
- [17] Afanasiev V. N., Chudnovsky Y. P. and Leontiev A. I. "Experimental study of vortex heat transfer enhancement mechanisms." **Experimental Thermal and Fluid Science.**, vol. 7, no. 2, 1993. pp. 137
- [18] Bilen K., Akyol U. and Yapici S. "Heat transfer and friction correlations and thermal performance analysis for a finned surface." **Energy Conversion and Management.**, vol. 42, 2001. pp. 1071-1083
- [19] Chandra P. R., Alexander C. R. and Han J. C. "Heat transfer and friction behaviors in rectangular channels with varying number of ribbed walls." **International Journal of Heat and Mass Transfer.**, vol. 46, 2003. pp. 481-495
- [20] Karmare S. V., Tikekar A. N. "Heat transfer and friction factor correlation for artificially roughened duct with metal grit ribs." **International Journal of Heat and Mass Transfer.**, vol. 50, 2007. pp. 4342-4351
- [21] Saini R. P., Verma J. "Heat transfer and friction factor correlations for a duct having dimple-shape artificial roughness for solar air heater." **Energy.**, vol. 33, 2008. pp. 1277-1287
- [22] Chang S. W., Chiang K. F., Yang T. L. and Huang C. C. "Heat transfer and pressure drop in dimpled fin channels." **Experimental Thermal and Fluid Science.**, vol. 33, 2008. pp. 23-40
- [23] Yu R., Chaoyi W. and Shusheng Z. "Transitional flow and heat transfer characteristics in a rectangular duct with stagger-arrayed short pin fins." **Chinese Journal of Aeronautics.**, vol. 22, 2009. pp. 237-242

- [24] Fiebig M. "Embedded vortices in internal flow: Heat transfer and pressure loss enhancement." **International Journal of Heat and Fluid Flow.**, vol. 16, 1995. pp. 376-388
- [25] Gentry M. C., Jacobi A. M. "Heat transfer enhancement by delta-wing vortex generators on a flat plate: Vortex interactions with the boundary layer." **Experimental Thermal and Fluid Science.**, vol. 14, 1997. pp. 231-242
- [26] Gentry M. C., Jacobi A. M. "Heat transfer enhancement by delta-wing-generated tip vortices in flat-plate and developing channel flows." **Transactions of The ASME, Journal of Heat Transfer.**, vol. 124, no. 6, 2002. pp. 1158-1168
- [27] Kim E., Yang J. S. "An experimental study of heat transfer characteristics of a pair of longitudinal vortices using color capturing technique." **International Journal of Heat and Mass Transfer.**, vol. 45, 2002. pp. 3349-3356
- [28] Dupont F., Gabillet C. and Bot P. "Experimental study of the flow in a compact heat exchanger channel with embossed-type vortex generators." **Transactions of the ASME, Journal of Fluids Engineering.**, vol. 125, no. 4, 2003. pp. 701-709
- [29] Joardar A., Jacobi A. M. "Impact of leading edge delta-wing vortex generators on the thermal performance of a flat tube, louvered-fin compact heat exchanger." **International Journal of Heat and Mass Transfer.**, vol. 48, no. 8, 2005. pp. 1480-1493
- [30] Joardar A., Jacobi A. M. "Heat transfer enhancement by winglet-type vortex generator arrays in compact plain-fin-and-tube heat exchangers." **International Journal of Refrigeration.**, vol. 31, no. 1, 2008. pp. 87-97
- [31] Jaurker A. R., Saini J. S. and Gandhi B. K. "Heat transfer and friction characteristics of rectangular solar air heater duct using rib-grooved artificial roughness." **Solar Energy.**, vol. 80, 2006. pp. 895-907
- [32] Layek A., Saini J. S. and Solanki S. C. "Second law optimization of a solar air heater having chamfered rib-groove roughness on absorber plate." **Renewable Energy.**, vol. 32, 2007. pp. 1967-1980
- [33] Varun, Saini R. P. and Singal S. K. "Investigation of thermal performance of solar air heater having roughness elements as a combination of inclined and transverse ribs on the absorber plate." **Renewable Energy.**, vol. 33, 2008. pp. 1398-1405
- [34] Promvong P., Chompookham T., Kwankaomeng S. and Thianpong C. "Enhanced heat transfer in a triangular ribbed channel with longitudinal vortex

- generators." **Energy Conversion and Management.**, vol. 51, 2010. pp. 1242-1249
- [35] Patankar S. V., Liu C. H. and Sparrow E. M. "Fully developed flow and heat-transfer in ducts having streamwise-periodic variations of cross-sectional area." **Transactions of the ASME, Journal of Heat Transfer.**, vol. 99, 1977. pp. 180-186
- [36] Webb G. W., Ramadhyani S. "Conjugate heat transfer in a channel with staggered ribs." **International Journal of Heat and Mass Transfer.**, vol. 28, 1985. pp. 1679-1687
- [37] Cheng C. H., Huang W. H. "Numerical prediction for laminar forced convection in parallel-plate channels with transverse fin arrays." **Numerical Heat Transfer Part A: Application.**, vol. 16, 1989. pp. 77-100
- [38] Cheng C. H., Huang W. H. "Predicting thermal conductivity of liquid suspensions of nanoparticles (nanofluids) based on rheology." **International Journal of Heat and Mass Transfer.**, vol. 34, 1991. pp. 2739-2749
- [39] Biswas G., Chattopadhyay H. "Heat transfer in a channel with built-in wing-type vortex generators." **International Journal of Heat and Mass Transfer.**, vol. 35, no. 4, 1992. pp. 803-814
- [40] Brockmeier U., Guentermann T. and Fiebig M. "Performance evaluation of a vortex generator heat transfer surface and comparison with different high performance surfaces." **International Journal of Heat and Mass Transfer.**, vol. 36, no. 10, 1993. pp. 2575-2587
- [41] Zhu J. X., Mitra N. K. and Fiebig M. "Effects of longitudinal vortex generators on heat transfer and flow loss in turbulent channel flows." **International Journal of Heat and Mass Transfer.**, vol. 36, no. 9, 1993. pp. 2339-2347
- [42] Zhu J. X., Fiebig M. and Mitra N. K. "Numerical investigation of turbulent flows and heat transfer in a rib-roughened channel with longitudinal vortex generators." **International Journal of Heat and Mass Transfer.**, vol. 38, no. 3, 1995. pp. 495-501
- [43] Biswas G., Deb P. and Biswas S. "Generation of longitudinal streamwise vortices - A device for improving heat exchanger design." **Transactions of the ASME, Journal of Heat Transfer.**, vol. 116, no. 3, 1994. pp. 588-597
- [44] Biswas G., Mitra N. K. and Fiebig M. "Heat transfer enhancement in fin-tube heat exchangers by winglet type vortex generators." **International Journal of Heat and Mass Transfer.**, vol. 37, no. 2, 1994. pp. 283-291
- [45] Biswas G., Torii K., Fujii D. and Nishino K. "Numerical and experimental determination of flow structure and heat transfer effects of longitudinal

- vortices in a channel flow." **International Journal of Heat and Mass Transfer.**, vol. 39, no. 16, 1996. pp. 3441-3451
- [46] Lopez J. R., Anand N. K. and Fletcher L. S. "Heat transfer in a three-dimensional channel with baffles." **Numerical Heat Transfer Part A: Application.**, vol. 30, 1996. pp. 189-205
- [47] Guo Z., Anand N. K. "Three dimensional heat transfer in a channel with a baffle in the entrance region." **Numerical Heat Transfer Part A: Application.**, vol. 31, 1997. pp. 21-35
- [48] Yang Y. T., Hwang C. Z. "Calculation of turbulent flow and heat transfer in a porous-baffled channel." **International Journal of Heat and Mass Transfer.**, vol. 46, no. 5, 2003. pp. 771-780
- [49] Bazdid-Tehrani F., Naderi-Abadi M. "Numerical analysis of laminar heat transfer in entrance region of a horizontal channel with transverse fins." **International Communication in Heat and Mass Transfer.**, vol. 31, no. 2, 2004. pp. 211-220
- [50] Mousavi S. S., Hooman K. "Heat and fluid flow in entrance region of a channel with staged baffles." **Energy Conversion and Management.**, vol. 47, 2006. pp. 2011-2019
- [51] Chaube A., Sahoo P. K. and Solanki S. C. "Analysis of heat transfer augmentation and flow characteristics due to rib roughness over absorber plate of a solar air heater." **Renewable Energy.**, vol. 31, 2006. pp. 317-331
- [52] Wu J. M., Tao W. Q. "Investigation on laminar convection heat transfer in fin-and-tube heat exchanger in aligned arrangement with longitudinal vortex generator from the viewpoint of field synergy principle." **Applied Thermal Engineering.**, vol. 27, 2007. pp. 2609-2617
- [53] Wu J. M., Tao W. Q. "Numerical study on laminar convection heat transfer in a rectangular channel with longitudinal vortex generator part A: Verification of field synergy principle." **International Journal of Heat and Mass Transfer.**, vol. 51, no. 5-6, 2008. pp. 1179-1191
- [54] Wu J. M., Tao W. Q. "Numerical study on laminar convection heat transfer in a channel with longitudinal vortex generator part B: Parametric study of major influence factors." **International Journal of Heat and Mass Transfer.**, vol. 51, no. 13-14, 2008. pp. 3683-3692
- [55] Chu P., He Y. L. and Tao W. Q. "Three-dimensional numerical study of flow and heat transfer enhancement using vortex generators in fin-and-tube heat exchangers." **Transactions of the ASME, Journal of Heat Transfer.**, vol. 131, no. 9, 2009. pp. 091903

- [56] Chu P., He Y. L., Lei Y. G., Tian L. T. and Li R. "Three-dimensional numerical study on fin-and-oval-tube heat exchanger with longitudinal vortex generators." **Applied Thermal Engineering.**, vol. 29, no. 5-6, 2009. pp. 859-876
- [57] Promvong P., Kwankaomeng S. "Periodic laminar flow and heat transfer in a channel with 45° staggered v-baffles." **International Communications in Heat and Mass Transfer.**, vol. 37, 2010. pp. 841-849
- [58] Promvong P., Jedsadaratanachai W. and Kwankaomeng S. "Numerical study of laminar flow and heat transfer in square channel with 30° inline angled baffle turbulators." **Applied Thermal Engineering.**, vol. 30, 2010. pp. 1292-1303
- [59] Vajjha R. S., Das D. K. "Experimental determination of thermal conductivity of three nanofluids and development of new correlations." **International Journal of Heat and Mass Transfer.**, vol. 52, 2009. pp. 4675-4682
- [60] Wang X. Q., Mujumdar A. S. "Heat transfer characteristics of nanofluids: A review." **International Journal of Thermal Sciences.**, vol. 46, 2007. pp. 1-19
- [61] Keblinski P., Phillpot S. R., Choi S. U. S. and Eastman J. A. "Mechanisms of heat flow in suspensions of nano-sized particles (nanofluids)." **International Journal of Heat and Mass Transfer.**, vol. 45, 2002. pp. 855-863
- [62] Koo J., Kleinstreuer C. "Laminar nanofluid flow in micro-heat sinks." **International Journal of Heat and Mass Transfer.**, vol. 48, no. 13, 2005. pp. 2652-2661
- [63] Chandrasekar M., Suresh S. and Chandra Bose A. "Experimental investigations and theoretical determination of thermal conductivity and viscosity of Al<sub>2</sub>O<sub>3</sub>/water nanofluid." **Experimental Thermal and Fluid Science.**, vol. 34, 2010. pp. 210-216
- [64] Longo G. A., Zilio C. "Experimental measurement of thermophysical properties of oxide-water nano-fluids down to ice-point." **Experimental Thermal and Fluid Science.**, vol. 35, 2011. pp. 1313-1324
- [65] Chen H., Witharana S., Jin Y., Kim C. and Ding Y. "Laminar forced convection flows in horizontal channel with transverse fins placed in entrance regions." **Particuology.**, vol. 7, 2009. pp. 151-157
- [66] Nguyen C. T., Desgranges F., Roy G., Galanis N., Mare' T., Boucher S. and Angue Mintsa H. "Temperature and particle-size dependent viscosity data for water-based nanofluids - hysteresis phenomenon." **International Journal of Heat and Fluid Flow.**, vol. 28, 2007. pp. 1492-1506

- [67] Corcione M. "Empirical correlating equations for predicting the effective thermal conductivity and dynamic viscosity of nanofluids." **Energy Conversion and Management.**, vol. 52, 2011. pp. 789-793
- [68] Pak B. C., Cho Y. I. "Hydrodynamic and heat transfer study of dispersed fluids with submicron metallic oxide particles." **Experimental Heat Transfer.**, vol. 11, no. 2, 1998. pp. 151-170
- [69] Xuan Y., Li Q. "Investigation on convective heat transfer and flow features of nanofluids." **Transactions of The ASME, Journal of Heat Transfer.**, vol. 125, no. 1, 2003. pp. 151-155
- [70] Zhou D. W. "Heat transfer enhancement of copper nanofluid with acoustic cavitation." **International Journal of Heat and Mass Transfer.**, vol. 47, 2004. pp. 3109-3117
- [71] Yang Y., Zhang G., Grulke E. A., Anderson W. B. and Wu G. "Heat transfer properties of nanoparticle-in-fluid dispersions (nanofluids) in laminar flow." **International Journal of Heat and Mass Transfer.**, vol. 48, 2005. pp. 1107-1116
- [72] Wen D., Ding Y. "Formulation of nanofluids for natural convective heat transfer application." **International Journal of Heat and Fluid Flow.**, vol. 26, 2005. pp. 855-864
- [73] Heris S. Z., Esfahany M. N. and Etemad S. G. "Experimental investigation of convective heat transfer of Al<sub>2</sub>O<sub>3</sub>/water nanofluid in circular tube." **International Journal of Heat and Fluid Flow.**, vol. 28, 2007. pp. 203-210
- [74] Duangthongsuk W., Wongwises S. "Effect of thermo-physical properties models on the prediction of the convective heat transfer coefficient for low concentration nanofluids." **International Communications in Heat and Mass Transfer.**, vol. 35, no. 10, 2008. pp. 1320-1326
- [75] Duangthongsuk W., Wongwises S. "Heat transfer enhancement and pressure drop characteristics of TiO<sub>2</sub>-water nanofluid in a double-tube counter flow heat exchanger." **International Journal of Heat and Mass Transfer.**, vol. 52, no. 7-8, 2009. pp. 2059-2067
- [76] Williams W., Buongiorno J. and Hu L. W. "Experimental investigation of turbulent convective heat transfer and pressure loss of alumina/water and zirconia/water nanoparticle colloids (nanofluids) in horizontal tubes." **Transactions of The ASME, Journal of Heat Transfer.**, vol. 130, no. 4, 2008. pp. 042412-1-7
- [77] Fotukian S. M., Esfahany M. N. "Experimental study of turbulent convective heat transfer and pressure drop of dilute CuO/water nanofluid inside a circular

- tube." **International Communications in Heat and Mass Transfer.**, vol. 37, 2010. pp. 214-219
- [78] Sajadi A. R., Kazemi M. H. "Investigation of turbulent convective heat transfer and pressure drop of TiO<sub>2</sub>/water nanofluid in circular tube." **International Communications in Heat and Mass Transfer.**, vol. 38, 2011. pp. 1474-1478
- [79] Syam Sundar L., Sharma K. V. "Turbulent heat transfer and friction factor of Al<sub>2</sub>O<sub>3</sub> nanofluid in circular tube with twisted tape inserts." **International Journal of Heat and Mass Transfer.**, vol. 53, 2010. pp. 1409-1416
- [80] Wongcharee K., Eiamsa-ard S. "Enhancement of heat transfer using CuO/water nanofluid and twisted tape with alternate axis." **International Communications in Heat and Mass Transfer.**, vol. 38, 2011. pp. 742-748
- [81] Salman B. H., Mohammed H. A. and Kherbeet A. S. "Heat transfer enhancement of nanofluids flow in microtube with constant heat flux." **International Communications in Heat and Mass Transfer.**, vol. 39, 2012. pp. 1195-1204
- [82] Mohammed H. A., Al-Shamani A. N. and Sheriff J. M. "Thermal and hydraulic characteristics of turbulent nanofluids flow in a rib-groove channel." **International Communications in Heat and Mass Transfer.**, vol. 39, 2012. pp. 1584-1594
- [83] Abbasian Arani A. A., Amani J. "Experimental study on the effect of TiO<sub>2</sub>-water nanofluid on heat transfer and pressure drop." **Experimental Thermal and Fluid Science.**, vol. 42, 2012. pp. 107-115
- [84] Lotfi R., Saboonhi Y. and Rashidi A. M. "Numerical study of forced convective heat transfer of nanofluids: Comparison of different approaches." **International Communications in Heat and Mass Transfer.**, vol. 37, 2010. pp. 74-78
- [85] Akbari M., Galanis N. and Behzadmehr A. "Comparative analysis of single and two-phase models for CFD studies of nanofluid heat transfer." **International Journal of Thermal Sciences.**, vol. 50, 2011. pp. 1343-1354
- [86] Joel H. Ferziger, Milovan Perić. **Computational Methods for Fluid Dynamics.** 3rd ED. Berlin : Springer 2002. ISBN 3-540-42074-6.
- [87] David C. Wilcox. **Turbulence Modeling for CFD.** 2nd ED. La Cañada Flintridge : DCW Industries, Inc. 2002.
- [88] Henk K. Versteeg, Weeratunge Malalasekera. **An Introduction to Computational Fluid Dynamics.** Essex : Pearson Education 2007.
- [89] Suhas V. Patankar. **Numerical Heat Transfer and Fluid Flow.** New York : McGraw-Hill, Inc. 1980.

- [90] Vajjha R. S., Das D. K. "Measurement of thermal conductivity of three nanofluids and development of new correlations." **International Journal of Heat and Mass Transfer.**, vol. 52, 2009. pp. 4675-4682
- [91] Roache P. J. "Perspective: A method for uniform reporting of grid refinement studies." **Transactions of the ASME, Journal of Fluids Engineering.**, vol. 116, 1994. pp. 405-413
- [92] Roache P. J. "Quantification of uncertainty in computational fluid dynamics." **Annual Review of Fluid Mechanics.**, vol. 29, 1997. pp. 123-160
- [93] F. P. Incropera et al. **Fundamentals of Heat and Mass Transfer.** 6th ED. Hoboken : John Wiley & Sons (Asia) 2007.
- [94] Winterton R. H. S. "Where did the Dittus and Boelter equation come from?" **International Journal of Heat Mass Transfer.**, vol. 41, no. 4-5, 1998. pp. 809-810
- [95] Sutthichai Panwong. "**Heat transfer characteristics in a channel fitted with S-baffles.**" Master Thesis. Faculty of Engineering, King Mongkut's Institute of Technology Ladkrabang. 2014.

## APPENDIX

## APPENDIX A

AN EXAMPLE OF USER DEFINED FUNCTION (UDF) FOR  
NANOFLUID

```

/*****
UDF for specifying properties of nanofluid
*****/

#include "udf.h"
#define n_vf 0.01
#define dp 30.0e-9
#define kbf 0.6
#define knp 40.0
#define kappa 1.381e-23
#define rhof 998.2
#define rhop 3970.0
#define cpf 4182.0
#define cpp 765.0
#define temp_ref 293.0
#define M 18.01528
#define N 6.022e23
#define pi 3.141592
#define mu_f 0.001003

DEFINE_PROPERTY(cell_conductivity,c,t)
{
    real knf, f, beta, kstatic, kbrow;
    real temp = C_T(c,t);
    real nf = n_vf;

    if (nf>0.0)
    {
        f = ((2.8217e-2)*n_vf + 3.917e-3)*(temp/temp_ref) + (-3.0669e-2)*n_vf -
3.91123e-3;
        beta = 8.4407*pow((100.0*n_vf),-1.07304);
        kstatic = kbf*((knp + 2.0*kbf - 2.0*(kbf-knp)*n_vf) / (knp + 2.0*kbf +
(kbf-knp)*n_vf));
        kbrow = f*(5.0e4)*beta*n_vf*rhof*cpf*sqrt((kappa*temp)/(rhop*dp));
        knf = kstatic+kbrow;
    }
    Else
    {

```

```

        f = ((2.8217e-2)*n_vf + 3.917e-3)*(temp/temp_ref) + (-3.0669e-2)*n_vf -
3.91123e-3;
        beta = 0.0;
        kstatic = kbf*((knp + 2.0*kbf - 2.0*(kbf-knp)*n_vf) / (knp + 2.0*kbf +
(kbf-knp)*n_vf));
        kbrow = f*(5.0e4)*beta*n_vf*rhof*cpf*sqrt((kappa*temp)/(rhof*dp));
        knf = kstatic+kbrow;
    }
    return knf;
}

```

```

DEFINE_PROPERTY(cell_viscosity,c,t)

```

```

{
    real df, mu_eff;
    real temp = C_T(c,t);

    df = 0.1*pow((6.0*M/(N*pi*rhof)),(1.0/3.0));
    mu_eff = mu_f/(1.0-34.87*pow((dp/df),-0.3)*pow(n_vf,1.03));

    return mu_eff;
}

```

```

DEFINE_PROPERTY(cell_density,c,t)

```

```

{
    real rho_eff;
    rho_eff = ((1.0-n_vf)*rhof)+(n_vf*rhop);

    return rho_eff;
}

```

```

DEFINE_SPECIFIC_HEAT(cell_cp, T, Tref, h, yi)

```

```

{
    real rho_eff, cp_eff;
    rho_eff = ((1.0-n_vf)*rhof)+(n_vf*rhop);
    cp_eff = (((1.0-n_vf)*rhof*cpf)+(n_vf*rhop*cpp))/rho_eff;
    *h = cp_eff*(T-Tref);

    return cp_eff;
}

```

```
}  
/*****  
End of code  
*****/
```

## APPENDIX B

AUTHOR PUBLICATION

### International journal

- [1] Noothong W., Suwannapan S., Thianpong C., and Promvong P. “Enhanced Heat Transfer in a Heat Exchanger Square–Duct with Discrete V–Finned Tape Inserts” has been accepted by **Chinese Journal of Chemical Engineering** in 2014-05-22 and will be published in 2015.
- [2] Promvong P., Noothong W., Thianpong C. “Numerical Heat Transfer Investigation in Solar Air Heater Channel with Wavy-Baffles” **Advanced Materials Research** vol. 1051, 2014. pp. 808-812

### International conference

- [1] Noothong W., Chinaruk Thianpong C., Promvong P. “Effect of Amplitude of S-Baffles on Heat Transfer Enhancement in a Channel” **1st International Symposium on Technology for Sustainability**, Bangkok, Thailand, January, 2012. pp. 443-446
- [2] Noothong W., Promvong P. “Effect of Wavy-Baffle Height on Thermal Behaviors in a Channel” **International Conference on Engineering, Applied Sciences, and Technology**, Bangkok, Thailand, November, 2012. pp.171-175

## AUTHOR BIOGRAPHY

<b>Name</b>	Mr.Watcharin Noothong
<b>Date of Birth</b>	26 June 1976
<b>Place of Birth</b>	Bangkok, Thailand
<b>Address</b>	100/40 Srinakarin Rd., Bangmuang, Muangsamutprakan, Samutprakan 10270
<b>Education</b>	1997: B.Eng. in Electrical Engineering Mahidol University, Nakhon Pathom, Thailand 2003: M.Eng. in Manufacturing Management (International Program) Mahanakorn University of Technology, Bangkok, Thailand
<b>Experiences</b>	2003 – Present: Lecturer Department of Mechanical Engineering Mahanakorn University of Technology, Bangkok, Thailand